191(4), 2022

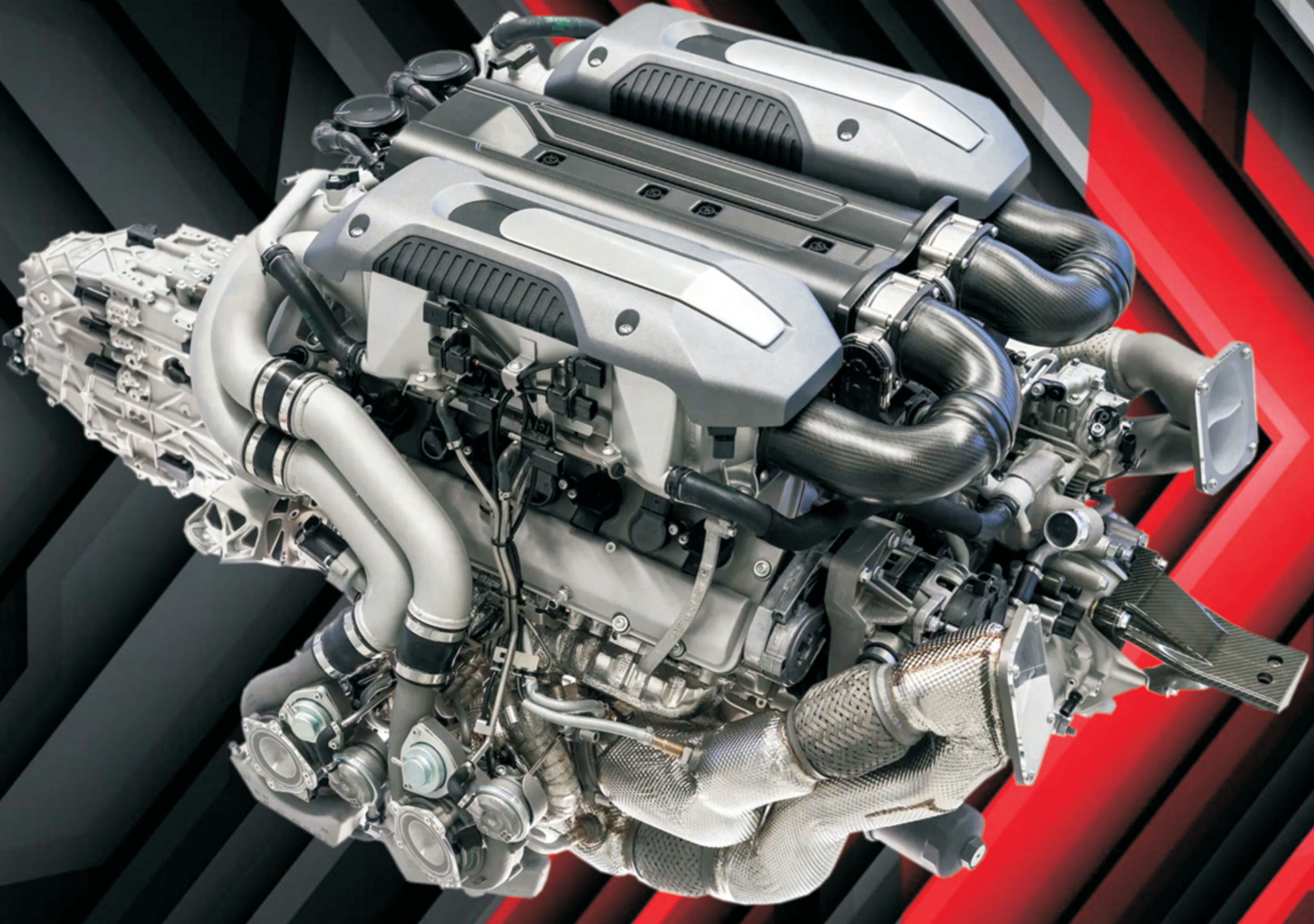

COMBUSTION ENGINES

PTNSS

Wrocław University of Science and Technology

X INTERNATIONAL
CONGRESS ON COMBUSTION ENGINES

POLISH SCIENTIFIC SOCIETY OF COMBUSTION ENGINES

June 18th-20th, 2023

congress.ptnss.pl

Wrocław University of Science and Technology
Faculty of Mechanical Engineering
27 Wybrzeże Wyspiańskiego Street, 50-370 Wrocław, Poland

Due to the dynamic development of machine and vehicle powertrains, the "Combustion Engines" scientific journal, while retaining its historical title, currently publishes works related not only to internal combustion engines, but also other powertrains, including hybrid drives, electric drives and fuel cells.

COMBUSTION ENGINES
A Scientific Magazine

2022, 191(4)

Year LXI

PL ISSN 2300-9896
PL eISSN 2658-1442

Publisher:
Polish Scientific Society of Combustion Engines
60-965 Poznan, pl. M. Skłodowskiej-Curie 5, Poland
tel.: +48 61 6475966, fax: +48 61 6652204
E-mail: sekretariat@ptnss.pl
WebSite: http://www.ptnss.pl
Papers available on-line: http://combustion-engines.eu

Contents

Publisher:

Polish Scientific Society of Combustion Engines
60-965 Poznan, pl. M. Sklodowskiej-Curie 5, Poland
tel.: +48 61 6475966, fax: +48 61 6652204
E-mail: sekretariat@ptnss.pl
WebSite: http://www.ptnss.pl

Subscriptions
Send subscription requests to the Publisher's address.
Cost of a single issue PLN 40.

Preparation for print
ARS NOVA Publishing House
60-782 Poznan, ul. Grunwaldzka 17/10A

Circulation: 80 copies

Printing and binding

Zakład Poligraficzny Moś i Łuczak, sp. j.,
Poznań, ul. Piwna 1

The journal is under the patronage of the Transport Committee of the Polish Academy of Sciences

The journal is registered and listed in the Polish and international database

Papers published in the *Combustion Engines* quarterly receive 70 points as stated by the Notification of the Minister of Science and Education dated 1 December 2021.

Declaration of the original version
The original version of the Combustion Engines journal is the printed version.

Cover
I – Bugatti Chiron quad-turbocharged 8.0 dm^3 W16 engine
(www.motor1.com);
background *(black and red abstraction – www.peakpx.com)*

IV – Bugatti Chiron W16 Engine cross-section
(www.ehfcv.com)

Article citation info:
STOECK, T. Problems of regeneration of modern piezoelectric fuel injectors. *Combustion Engines*. 2022, **191**(4), 3-8.
https://doi.org/10.19206/CE-146700

Tomasz STOECK

Combustion Engines
Polish Scientific Society of Combustion Engines

Problems of regeneration of modern piezoelectric fuel injectors

ARTICLE INFO

Received: 10 January 2022
Revised: 13 February 2022
Accepted: 14 February 2022
Available online: 5 March 2022

The paper presents a method of testing piezoelectric fuel injectors in modern common rail systems, which allows them to be repaired almost to the full extent. The obtained results indicate that this process can be effectively carried out, even taking into account the existing technological limitations. The most important stages of the implemented activities are specified, first of all the scope of required maintenance activities in the pre- and post-assembly stages, as well as the types of diagnostic tests carried out on separate test benches. Although the presented analysis concerns a specific example, individual conclusions and observations can be applied to fuel injectors from other manufacturers, in which the actuator is not replaceable.

Key words: *common rail system, piezoelectric fuel injector, diagnostic tests, regeneration process*

1. Introduction

There is an increased demand for the regeneration of piezoelectric fuel injectors on the market of maintenance services. Although this technology does not play a dominant role in modern common rail systems, in which solutions with a solenoid operated valve predominate, the percentage of its use is systematically growing [1, 19]. This is due to the optimal shaping of the high-pressure direct fuel injection strategy, implemented with a highly flexible and multiple division of the dosed fuel during a single diesel engine cycle. This is essential from the point of view of reducing fuel consumption as well as reducing noise emissions and the toxicity of exhaust fumes [13, 21, 22]. Due to the above considerations, piezoelectric fuel injectors are offered by all major manufacturers of fuel injection equipment. Moreover, the increasing access to spare parts as well as specialized accessories and diagnostic devices significantly increased their repair possibilities.

At present, the most important problem is the issue of the crystal stack, usually placed inside the main body, which effectively eliminates its replacement, e.g. Bosch, Denso, Delphi [4, 6, 18]. The exception to this rule is the products of Siemens VDO Continental, which is a world leader in the field of PCR (Piezo Common Rail) systems, in which the actuator is screwed to the upper part of the fuel injector with a nut. As a result, disassembly of this element is not difficult, as it is similar to the use of a classic solenoid [5, 26]. In other cases, it is possible to revitalize the stack, i.e. remove micro-short circuits between individual layers by means of a current signal of a specific amplitude. However, this process has no effect on mechanical damage, and additionally it must be carried out on specially dedicated test benches, e.g. DS2R, CRU2r, CRU4R [24]. The high precision of individual actuators makes them the most susceptible to damage components of common rail systems in difficult operating conditions.

The tests were mainly aimed at assessing the possibility of repairing the third generation piezoelectric fuel injector, taking into account and using cognitive techniques that will enable its full efficiency to be restored. For this reason, a range of maintenance and repair activities was proposed, implemented at individual stages of this process, taking into account the difficulties and technological limitations. The methodology is distinguished by the use of equipment that is not used in the manufacturer's standard procedures.

2. Methods

2.1. Test object

The tests were carried out on a Bosch CRI3-16 piezoelectric fuel injector, which was removed from the 3.0 TDI (Turbo Direct Injection) engine of a Volkswagen Touareg passenger car with an operational mileage of 262 thousand km.

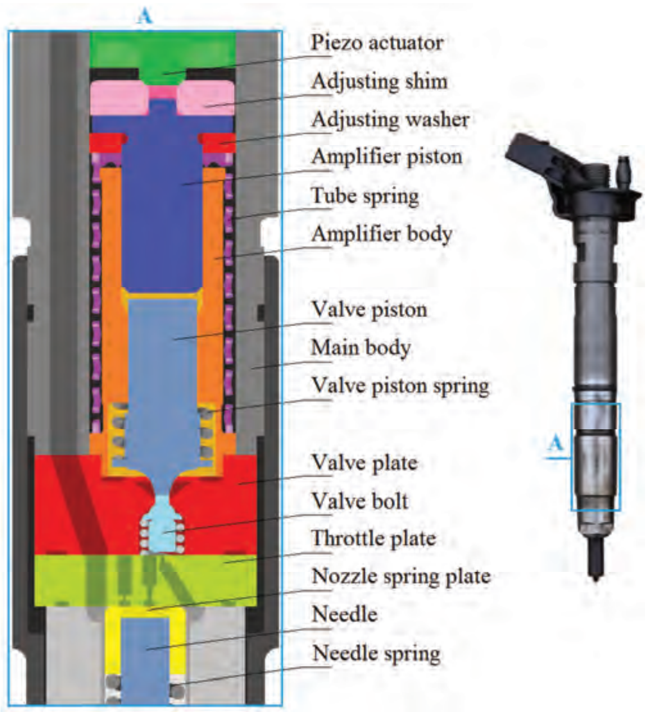

Fig. 1. Bosch CRI3-16 fuel injector design: own study based on [20]

This type of fuel injector belongs to the third generation CRS3 (Common Rail System) systems, operating at working pressure up to 160 MPa [9]. Figure 1 shows the most important elements of the internal structure, specifying the control valve assembly and the hydraulic amplifier. Other characteristic features include the triangular cross-section of the needle in the guiding part, providing space for free fuel flow. Moreover, compared to solenoid solutions, the high pressure feed connector is positioned centrally rather than laterally, which simplifies the upper part of the main body. For this reason, the overflow connector is located next to the flange with the electrical connection [12].

2.2. Test beds

During the regeneration of the fuel injector, the following apparatus and dedicated instrumentation were used, which included:
– 12PSB test bench with a complete Stardex kit (Fig. 2),
– Mega Tester V3 piezoelectric actuator tester,
– Bass BP-3605 fuel injector pressure tester,
– Yizhan 13MP HDMI VGA microscope camera,
– Polsonic Sonic 9, Bene YesWeCan 3L ultrasonic cleaners,
– IP54 electronic micrometer,
– Facom E.316A200S electric torque wrench,
– GRS Tools POWER HONE diamond grinder,
– vices, grips and workshop tools.

Fig. 2. 12PSB test bench with Stardex kit

2.3. Research plan

Figure 3 shows an in-house test plan which only partially overlaps with Bosch's procedures. Due to the available equipment, checking the piezoelectric actuator and the state of tightness can be carried out in the initial stages. The detection of a failure results in the suspension of the regeneration process or the exclusion of the fuel injector from thermochemical cleaning and preliminary flow measurements on the test bench. In addition, washing in ultrasonic baths takes place after microscopic inspection and applies only to those components that will not be replaced. Differences may also apply to the correction of fuel dosage, as the manufacturer assumes top-down adjustment by means of coding or by earlier disassembly of the nozzle and changing the thickness of the needle washer (not shown in Fig. 1). The latter method results from the frictional wear of the plunger and barrel assembly, which is one of the most frequently detected failures in common rail fuel injectors [2, 3, 8]. However, this process can be extended in the situations when other irregularities are found during the tests.

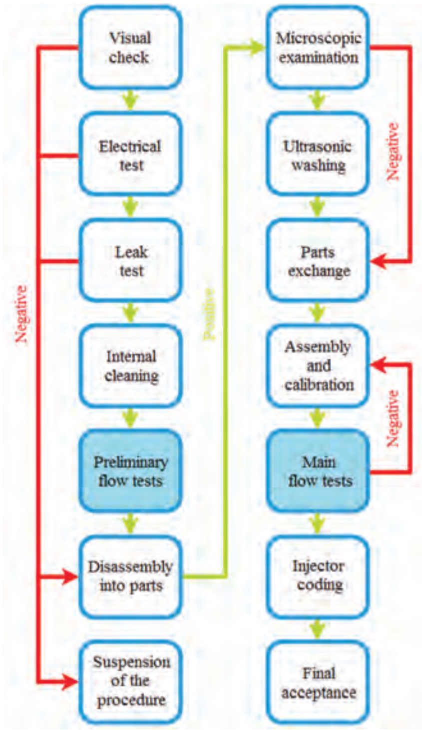

Fig. 3. Research plan

3. Analysis results and discussion

3.1. Preliminary tests

The inspection of the tested fuel injector did not reveal any external defects or incompleteness of its components. Therefore, electrical measurements were performed using the Mega Tester V3 (Fig. 4). The data presented in Table 1 show that the piezoelectric actuator was functional, as the values of all parameters were within the nominal ranges. The main difference compared to Siemens VDO Continental products is the lack of necessity to control GAP, i.e. the size of the gap between the crystal stack and the hydraulic valve lifter [15].

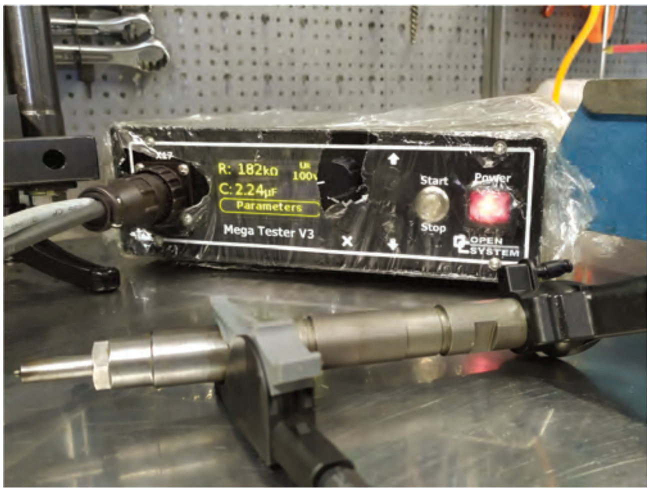

Fig. 4. Testing piezoelectric actuator with the Mega Tester V3

Table 1. Results of the electric tests

Type of parameter	Nominal range	Result
Piezo actuator resistance, R [kΩ]	150–210	182
Piezo actuator initial capacitance, C [μF]	1.5–3.3	2.24
Continuous resistance test, R_C [kΩ]	150–210	182–183
Piezo actuator insulation resistance, R_I [MΩ]	10–∞	∞

In the next step, the tightness of the fuel injector was checked on the Bass BP-3605 tester (Fig. 5). At a pressure of 40–50 MPa, no leaks were found in the area of the nozzle and the overflow connector. This proves that the nozzle and the nut are kept tight, as well as the valve assembly. At this stage, it is possible to test the quality of fuel atomisation, but it is necessary to provide a control impulse from an additional diagnostic device, e.g. AZ0222-CRR, SRN.101.540, AZ0134-13. This test is carried out optionally, mainly in the case of suspected obstruction of the exit holes, changes in their geometry, bad condition of the tip, etc.

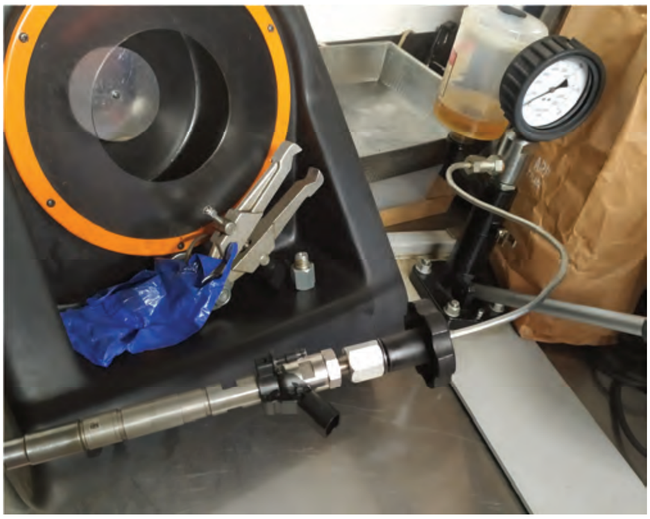

Fig. 5. The fuel injector leak test on the Bass BP-3605 tester

In accordance with the adopted test plan, the CRI3-16 fuel injector was subjected to thermochemical cleaning. In this process, as in the preliminary flow measurements, a 12PSB test bench with a Stardex kit was used (Fig. 6).

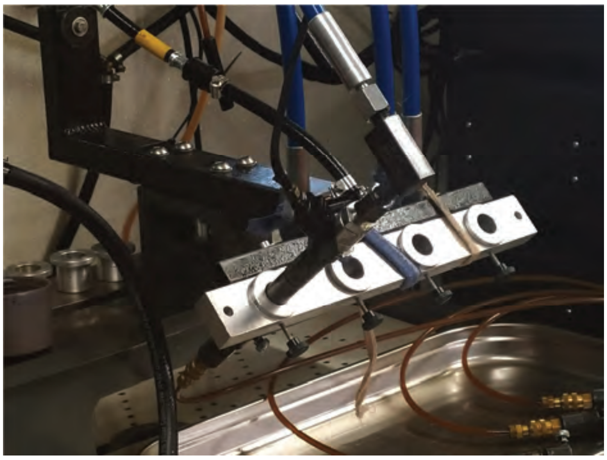

Fig. 6. View of the fuel injector during flow measurements

The results presented in Table 2 show that a negative result of the measurements was obtained at full load. A disturbance in the fuel supply after the maximum pressure and control time have been set, may suggest a problem in the operation of the actuator group. Despite the fact that the criteria specified by the manufacturer were met for the remaining operating points, the values of fuel injection doses also seem to be slightly underestimated. It would be premature to indicate possible causes, at least until the fuel injector is disassembled and the individual components are inspected. Nevertheless, improper cooperation of the plunger and barrel assembly should be ruled out, as wearing of the needle in the nozzle would be visible in the idle and pre-injection tests [10, 25].

Table 2. Results of the preliminary fuel injector flow test

Test name	Injection pressure, p_{inj} [MPa]	Nozzle opening times, t [μs]	Injection dosage, d [ml/min]	
			Nominal range	Result
Maximum Load	160	550	46.2±6.5	39.4
Emission Point	80	465	18.7±4.3	18.0
Pre-injection	120	170	1.8±1.5	1.2
Idle	25	525	3.1±2.7	3.1

In organoleptic tests and under high microscopic magnification, corrosion centres were revealed on parts that were in direct contact with the fuel, e.g. on the throttle and valve plates (Fig. 7a). Traces of frictional wear were also observed on some working surfaces, in particular on those from the hydraulic booster (Fig. 7b). As a result, it was decided that the the above actuator assemblies would be replaced completely. Moreover, taking into account the operational mileage over 200,000 km, a new nozzle was used, similarly to the regeneration of fuel injectors from other manufacturers [23]. It should be emphasised, however, that the technical condition of the needle and the nozzle did not raise any major objections (Fig. 8). The remaining components were bathed in ultrasonic cleaners and then thoroughly dried with compressed air.

a) b)

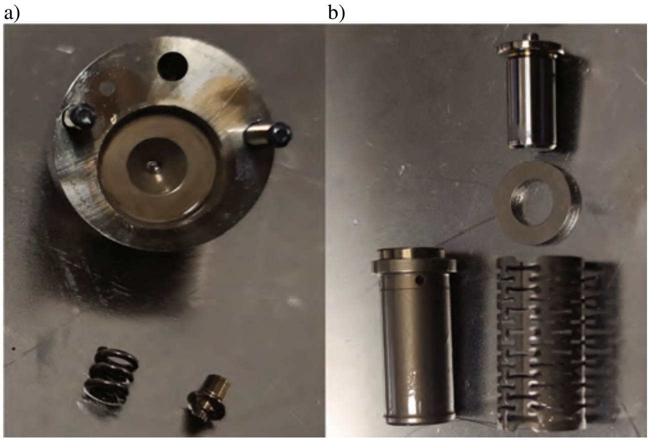

Fig. 7. Exemplary parts of the valve group a) amplifier module b)

The data presented in the literature show that the properties of piezoelectric crystals deteriorate with long-term operation [7, 16, 17]. As a result of the ageing process, the response to the electric impulse changes, thus reducing the elongation of the actuator and the impact on the moving parts of the injector [14]. This means that the actions taken may turn out to be insufficient, because even with the valve replaced, an increased amount of fuel will be transferred to the overflow.

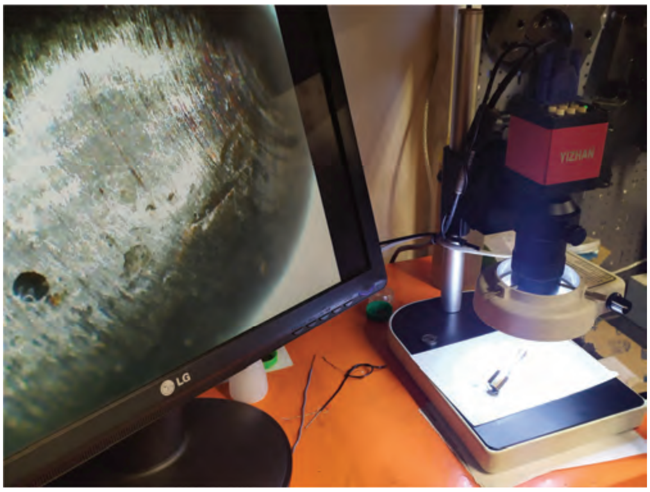

Fig. 8. Microscopic inspection of the nozzle tip

Fig. 9. Measurement of the adjusting shim thickness after grinding

Fig. 10. Assembly of the hydraulic booster

Taking into account the results of preliminary tests, it was decided that the stack length compensation would be ensured by grinding the front surface of the adjusting shim of the hydraulic booster by 0.2 mm (Fig. 9). In turn, the assembly of this assembly required venting and pressing in the presence of oil (Fig. 10 and 11). In this way, falsification of the measurements on the test bench, i.e. the occurrence of the so-called zero doses, is prevented.

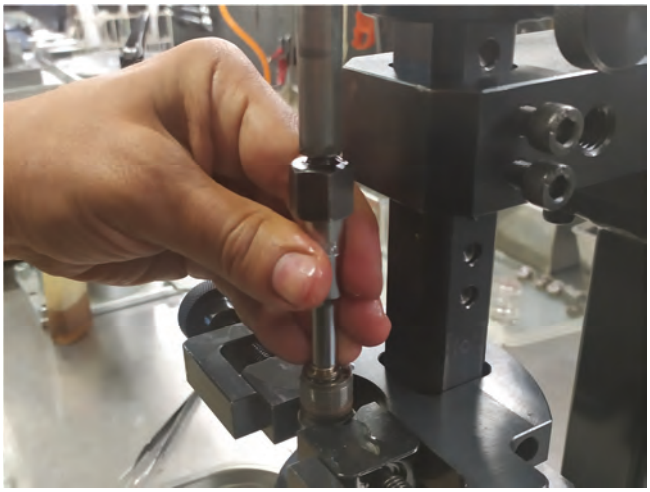

Fig. 11. Pressing step in the presence of oil

3.2. Main tests

Table 3 shows the results of the main tests that were carried out after the fuel injector was regenerated. This process should be assessed positively, as the fuel injection doses within the required limits were obtained at all operating points. Moreover, their values were increased compared to the initial state, which proves that the damage was correctly verified and the actions taken were right.

Table 3. Results of the main fuel injector flow test

Test name	Injection pressure, p_{inj} [MPa]	Nozzle opening times, t [μs]	Injection dosage, d [ml/min]	
			Nominal range	Result
Maximum load	160	550	46.2±6.5	43.2
Emission point	80	465	18.7±4.3	19.4
Pre-injection	120	170	1.8±1.5	1.6
Idle	25	525	3.1±2.7	4.2

It is also worth noting that in some cases, compensation for the loss resulting from the ageing of the crystal stack may be limited only to assigning a new ISA (German: Injektor-Spannungs-Abgleich) code. It consists in finding a higher threshold voltage at which the actuator will open the valve through the hydraulic booster assembly and raise the needle in the nozzle. As a result, coding the piezoelectric fuel injector, i.e. shifting its operation range, becomes a kind of corrective action [11], supplementing the information on the correction of fuel dosage IMA (German: Injektor-Mengen-Abgleich). The procedure is carried out automatically on the same diagnostic stand that was used in flow tests.

4. Conclusions

The proposed method allows the regeneration of common rail piezoelectric fuel injectors, as shown in a specific example. Due to the extended scope of maintenance and diagnostics, as well as easier access to spare parts, this process is not limited only to the stages of cleaning, testing and assigning new codes. This also applies to the replacement of the plunger and barrel assembly for selected reference numbers, treated in recent years as the first and, in principle, the only stage of repair. Of course, the necessary condition for the effectiveness of the activities carried out is the technical condition of the actuator itself, which, unlike other control and actuator elements, is still not replaceable. By making this technology available on the market of maintenance services market, the repair will be completely full-spectrum, as is the case with Siemens VDO Continental products.

Acknowledgements

The paper was created thanks to the cooperation with AUTO NEXT SERWIS car service company based in Szczecin (Prawobrzeże Quarter), which provided test benches, apparatus and accessories used in the regeneration process of the tested fuel injector.

Nomenclature

C	piezo actuator initial capacitance
CRI	common rail injector
CRS	common rail system
d	injection dosage
GAP	space between the piezo actuator and the injector hydraulic valve pusher
IMA	correction of injector doses
ISA	injector voltage correction
PCR	piezo common rail system
p_{inj}	injection pressure
R	piezo actuator resistance
R_C	continuous resistance test
R_I	piezo actuator insulation resistance
t	nozzle opening times

Bibliography

[1] AMBROSIO, S., FERRARI, A., MANCARELLA, A. at al. Comparison of the emissions, noise, and fuel consumption comparison of direct and indirect piezoelectric and solenoid injectors in a low-compression-ratio diesel engine. *Energies*. 2019, **4023**(12). https://doi.org/10.3390/en12214023

[2] COSTA DE MACÊDO NETO, J., ANUNCIAÇÃO BRITO DE OLIVEIRA, M., BARREDA DEL CAMPO, E.R. at al. Failure in fuel injector nozzles used in diesel engines. *Journal of Mechanics Engineering and Automation*. 2015, **5**, 237-240. https://doi.org/10.17265/2159-5275/2015.04.005

[3] CHOMIK, Z., ŁAGOWSKI, P. The analysis of mechanical damage of common rail injectors. *Journal of Research and Applications in Agricultural Engineering*. 2019, **64**(1), 13-20.

[4] CHOPRA, S., ACHARI, P., KULKARNI, V. Current market techniques used to reduce CO_2 emissions from diesel engines. *International Journal of Scientific Engineering and Applied Science*. 2016, **2**(12), 84-93.

[5] EGGER, K., WARGA, J., KLÜGL, W. New common rail injection system with piezo actuation for diesel passenger cars. *MTZ Worldwide*. 2002, **63**(9), 14-17. https://doi.org/10.1007/BF03227566

[6] HAGEN, J., HERRMANN, O.E., WEBER, J. et al. Better diesel combustion by further injector improvement. *Auto Tech Review*. 2016, **5**(9), 28-35. https://doi.org/10.1365/s40112-016-1198-4

[7] HAO, S., HUANG, Y., ZHANG, S. Research on the drive system of piezoelectric injector. *Advances in Engineering Research*. 2017, **100**, 98-102. https://doi.org/10.2991/icmeim-17.2017.19

[8] IGNACIUK, P., GIL, L. Damages to injectors in diesel engines. *Advances in Science and Technology Research Journal*. 2014, **21**(8), 58-61. https://doi.org/10.12913/22998624.1091880

[9] JOCANOVIĆ, M.T., KARANOVIĆ, V.V., KNEŽEVIĆ, D.M. et al. Diesel fuel filtration problems with modern common rail injection systems. *Vojnotehnički Glasnik/ Military Technical Courier*. 2017, **65**(4), 968-933. https://doi.org/10.5937/vojtehg65-11577

[10] JUŚCIŃSKI, S., PIEKARSKI, W., CHOMIK, Z. Analysis of injection systems types used in agricultural machines. *Agricultural Engineering*. 2017, **21**(4), 37-46. https://doi.org/10.1515/agriceng-2017-0034

[11] KACZOROWSKI, M., PILEWSKI, Z. Kodowanie IMA/ ISA wtryskiwaczy piezoelektrycznych. *Bosch Autospec*. 2017, **66**(4), 7-9.

[12] KACZOROWSKI, M., PILEWSKI, Z. Wtryskiwacze piezoelektryczne – pionierzy wysokich ciśnień do 2500 barów. *Bosch Autospec*. 2017, **65**(3), 7-10.

[13] KOTEN, H., GUNES, E.C., GUNER, K. Piezo-actuated common rail injector structure and efficient design. *Journal of Energy Systems*. 2018, **2**(3), 97-114. https://doi.org/10.30521/jes.453560

[14] KRIVTSOV, S.N., KRIVTSOVA, T.I. Variations in health of piezoelectric elements of the Common Rail electric hydraulic nozzles in the operating conditions. *IOP Conference Series: Materials Science and Engineering*. 2021, **1061**, 1-8. https://doi.org/10.1088/1757-899X/1061/1/012022

[15] MEGA TESTER V3. Software instruction manual version 3.0. *The private company "Open System"*. 2019, Khmelnitsky.

[16] NOURAEI, H., BEN-MRAD, R., SINCLAIR, A.N. Development of a piezoelectric fuel injector. *IEEE Transactions on Vehicular Technology*. 2016, **65**(3), 1162-1170. https://doi.org/10.1109/TVT.2015.2410136

[17] PAYRI, R., GIMENO, J., MATA, C. et al. Rate of injection measurements of a direct-acting piezoelectric injector for different operating temperatures. *Energy Conversion and Management*. 2017, **154**, 387-393. https://doi.org/10.1016/j.enconman.2017.11.029

[18] POGULYAEV, Y.D., BAITIMEROV, R.M., ROZHDESTVENSKII, Y.V. Detailed dynamic modeling of common rail piezo injector. *Procedia Engineering*. 2015, **129**, 93-98. https://doi.org/10.1016/j.proeng.2015.12.014

[19] RAHUL, T.L. Recent trends in internal combustion engine. *International Research Journal of Engineering and Technology*. 2020, **7**(4), 924-930.

[20] SALVADOR, F.J., PLAZAS, A.H., GIMENO, J. et al. Complete modelling of a piezo actuator last generation injector for diesel injection systems. *International Journal of Engine Research*. 2012, **15**(1), 3-19. https://doi.org/10.1177/1468087412455373

[21] SATKOSKI, C.A., SHAVER, G.M., MORE, R. et al. Dynamic modeling of a piezoelectric actuated fuel injector. *Proceedings of the 2009 IFAC Workshop on Engine and Powertrain Control, Simulation and Modeling IFP*. 2009, 235-240. https://doi.org/10.3182/20091130-3-FR-4008.0048

[22] SENOUSY, M.S., LI, F.X., MUMFORD, D. et al. Thermo-electro-mechanical performance of piezoelectric stack actuators for fuel injector applications. *Journal of Intelligent Material Systems and Structures*. 2009, **20**, 387-399. https://doi.org/10.1177/1045389X08095030

Tomasz Stoeck, DEng. – Faculty of Mechanical Engineering and Mechatronics, West Pomeranian University of Technology in Szczecin, Poland.

e-mail: *tstoeck@wp.pl*

[23] STOECK, T. Application of the experimental design technique in fuel dose adjustment of common rail injector. *Combustion Engines*. 2019, **179**(4), 210-215. https://doi.org/10.19206/CE-2019-435

[24] STOECK, T. Method for testing modern common rail piezoelectric fuel injectors. *Combustion Engines*. 2021, **186**(3), 31-36. https://doi.org/10.19206/CE-140246

[25] STOECK, T. Methodology of testing common rail fuel injectors witch the use of Gauss`s formulas. *Combustion Engines*. 2021, **184**(1), 11-15. https://doi.org/10.19206/CE-133505

[26] STOECK, T., ABRAMEK, K.F., OSIPOWICZ, T. Simplified methodology for testing common rail piezoelectric injectors taking into account reference characteristics. *Engineering Review*. 2021, **41**(2), 54-61. https://doi.org/10.30765/er.1475

Article citation info:
DZIUBEK, M., GRYGIER, D. Comparative analysis of construction materials used for fastening elements of six-point safety belts in rally cars. *Combustion Engines*. 2022, **191**(4), 9-14. https://doi.org/10.19206/CE-146697

Mateusz DZIUBEK
Dominika GRYGIER

Combustion Engines
Polish Scientific Society of Combustion Engines

Comparative analysis of construction materials used for fastening elements of six-point safety belts in rally cars

ARTICLE INFO

Received: 29 December 2021
Revised: 21 January 2021
Accepted: 14 February 2021
Available online: 5 March 2022

Safety belts are one of the most significant elements of car equipment classified as passive safety. This paper provides a comparative material analysis of critical components of a trusted manufacturer's six-point harness used in motorsports racing with commercially available imitation belts. Despite the FIA certification labels, the imitation belts are characterized by extremely poor quality in the selection of materials for components such as the snap hooks and the locking sleeves in the central fastening mechanism, posing a real hazard to unaware belt users.

Key words: *six-point safety belt, failure, motorsport, passive safety*

1. Introduction

Seat belts are one of the most crucial components of passive safety [26]. As a critical feature of the six-point belts used in high-performance sports cars, it is essential to ensure the safety of the driver and/or passenger under high acceleration and overload conditions. The sets of three pairs of belts – shoulder, lap and crotch belts – are equipped on one side with buckles fastened in a central locking mechanism and on the other side with a snap hook, which is connected to the body of the vehicle at the mounting points [1]. Sports seat belts must meet rigorous standards, including the FIA 8853-2016 standard set by the International Automobile Federation [7]. At the same time, FIA homologation for belts is valid for five years from the year of manufacture, after which time belts cannot be used in professional motorsport. Unfortunately on the market appeared a number of substitutes and replicas of belts fully imitating certified six-point safety belts with sewn-on labels that confirm compliance with the FIA standard and specify the specific year of the end of the homologation.

Sport seat belts have two main purposes. The first is increased safety. Due to their design, they provide better protection during an accident than civilian belts. This is associated with the greater number of belts and the fact that sports belts are tightened firmly on the human body without any slack. This keeps the body properly supported during an accident and reduces the risk of hitting interior components. The second role of the sport six-point harness is to stabilize the body position in the seat while driving. During sports competitions, there are significant overloads, such as during braking and turn taking [14]. For this reason, driving a performance car in regular belts would cause the body to move cumbersomely on the seat, which would be a hazardous condition for efficient maneuvering of the vehicle. The use of sport harnesses eliminates this inconvenience, making car steering more comfortable and precise [17, 25].

The elements that attach the belts to the body of the vehicle, i.e. snap hooks, are one of the most crucial elements in sports seat belts, being responsible for transferring all loads. Snap hooks, buckles, clasps, and centre fastening mechanisms should be made from medium-carbon steels in the normalized or quenched and tempered state, or high-strength micro-alloyed steels. Selection of such materials makes the elements characterized by relatively high strength while maintaining adequate toughness. The use of fine-grained tempered martensite microstructure materials is a well-established practice in the automotive industry for many years [3, 9, 15].

Seat belt failure cases described in the literature focus on damage of the polymer fibres subject to degradation processes [10, 11], disintegration of the fastener mechanisms [6, 8, 21] or poor quality of the attachment points to the vehicle body [12]. In addition, an extensive part of the available research results describe medical aspects of post-accident injuries and accident statistics related to passive safety [5, 13, 19, 20, 22, 23]. The referenced articles describe cases of failures that result from many different factors. Most of these relate to the degradation processes of the polymers used in fastener components. Long-term functioning in unfavourable environmental conditions (elevated temperature, exposure to ultraviolet radiation, exposure to oxygen) results in gradual deterioration of the material's mechanical properties. In the end, the conclusions of these analyses usually come down to an improvement of the material selection or construction process, which must take into account nonstandard conditions of use. At the same time, a utilitarian feature of these analyses is their potential usefulness in forensic science. At the same time, the analysis presented in the following represents a different type of failure case, i.e., deliberate lowering of the quality of the material in order to increase the potential profits of the company under the pretext of selling replica belts with the FIA standard.

2. Subject of the study and methodology

The purpose of this study was a comparative analysis of the materials used for the snap hooks securing six-point sport harness belts and selected central fastening mechanisms components. The tests were conducted on three sets of belts, one set being the original set from a well-known and verified manufacturer, while the other two sets were imitations of the same company's product. Each harness tested (original or imitation) had an appropriate label with the information required by FIA Standard 8853-2016 (Fig. 1): (1) the FIA standard number; (2) the manufacturer's name, which may be replaced by a logo; (3) the unique serial number of the harness; (4) the homologation number; (5) the year of the expiry date; (6) (optionally) the information about adaptation to the FRH system.

The morphology of the microstructure in the nital-etched state was observed using light and electron microscopy methods. It was analysed using a Phenom XL scanning electron microscope (Eindhoven, Netherlands) and a Nikon Eclipse MA 200 light metallographic microscope (Tokyo, Japan) equipped with a Nikon DS-Fi5 CCD camera. SEM observations were conducted using material contrast (BSE detector, back-scattered electrons) under 15 kV accelerating voltage conditions. Additional microscopic observations were made in the picral-etched state, which reveals the distribution and morphology of the iron carbides without etching the grain boundaries.

The chemical composition of the material of snap hooks was determined by optical emission spectroscopy using a Leco GDS-500A glow discharge analyser (St. Joseph, MI, USA).

Hardness measurements were performed using the Vickers method in accordance with PN-EN ISO 6507-1:2018-5, taking a series of five or ten measurement points for each measurand (depending on measurement stability) to determine the standard deviation. Measurements with a load of 49.03 N (HV5) and 294.2 N (HV30) were made using a Zwick/Roell ZHV30/zwickiLine hardness tester (Ulm, Germany).

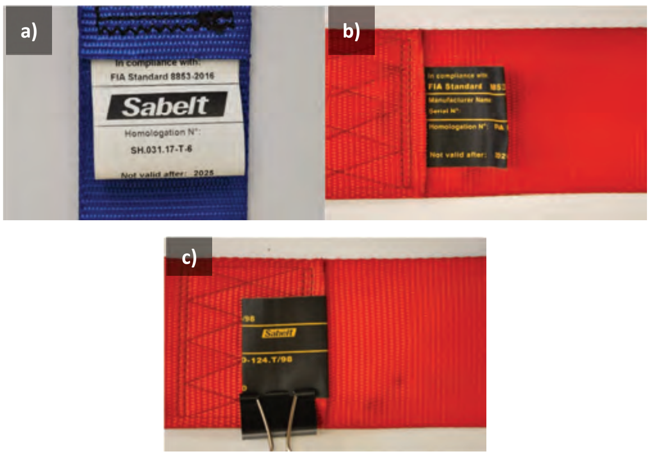

Fig. 1. Manufacturers' labels sewn onto the six-point harnesses containing information regarding compliance with the FIA standard and temporary homologation: a) original belt; b) c) imitations of the original belt

3. Results and Discussion

3.1. Comparative material tests of snap hooks

It was found that the snap hooks were made of two different grades of steel with various microstructure morphology and hardness. The original component was made of medium-carbon steel of grade C50 according to PN-EN ISO 683-1:2018-09. At the same time, it is characterized by the microstructure of tempered martensite, which indicates that the heat treatment process was carried out (Fig. 2a, Fig. 3a).

In case of the snap hook coming from the belt imitating the original one, it was made of low-carbon steel for cold forming of DC04 grade according to PN-EN 10130:2009 standard. It is characterized by a ferritic-pearlitic microstructure with locally occurring precipitations of tertiary cementite at grain boundaries (Fig. 2bc, Fig. 3bc). According to PN-EN 10130:2009, the mechanical properties of such steel are guaranteed for only six months after the product is made at the factory available to the customer, which is due to the aging processes occurring in this type of steel. The presence of tertiary cementite in excessive amounts reduce the toughness of steel, especially if it is located at the ferrite grain boundaries [2, 18]. For this reason, its amount, size and morphology are strictly controlled in the automotive low carbon steels in order to achieve a precipitation strengthening effect instead of a deterioration of the mechanical properties (mainly decrease in toughness) [4, 16, 24, 27].

The significant divergence in the chemical composition (primarily in carbon content) and the form of microstructure translates into the results of hardness measurements – 482.1 ±2.3 HV30 for the original element and 105.6 ±1.0 HV30 for the snap hook from belts imitating the original ones.

Table 1. Results of spectral analysis of the chemical composition of snap hook from original belts

Object	Chemical composition [wt.%]				
	C	Mn	Si	P	S
original component	0.502	0.732	0.201	0.014	0.001

Table 2. Results of spectral analysis of the chemical composition of snap hook from belts imitating the original

Object	Chemical composition [wt.%]				
	C	Mn	Si	P	S
imitation component	0.071	0.248	0.002	0.011	0.003

Table 3. Results of HV30 hardness measurements of snap hook from original belts

Object	Hardness measurements [HV30]				
original component	482.0	478.9	480.3	479.6	481.6
	486.5	483.3	484.7	482.2	481.8
		average ±SD		**482.1**	**±2.3**

Table 4. Results of HV30 hardness measurements of snap hook from belts imitating the original

Object	Hardness measurements [HV30]				
imitation component	103.9	105.8	103.6	105.7	106.1
	106.3	106.1	106.2	105.4	106.5
		average ±SD		**105.6**	**±1.0**

Conducting a comparative qualitative assessment of the morphology of the two types of microstructures, it is important to point out the diametrical differences that are reflected in the contrasting behaviour of the two types of snap hooks:

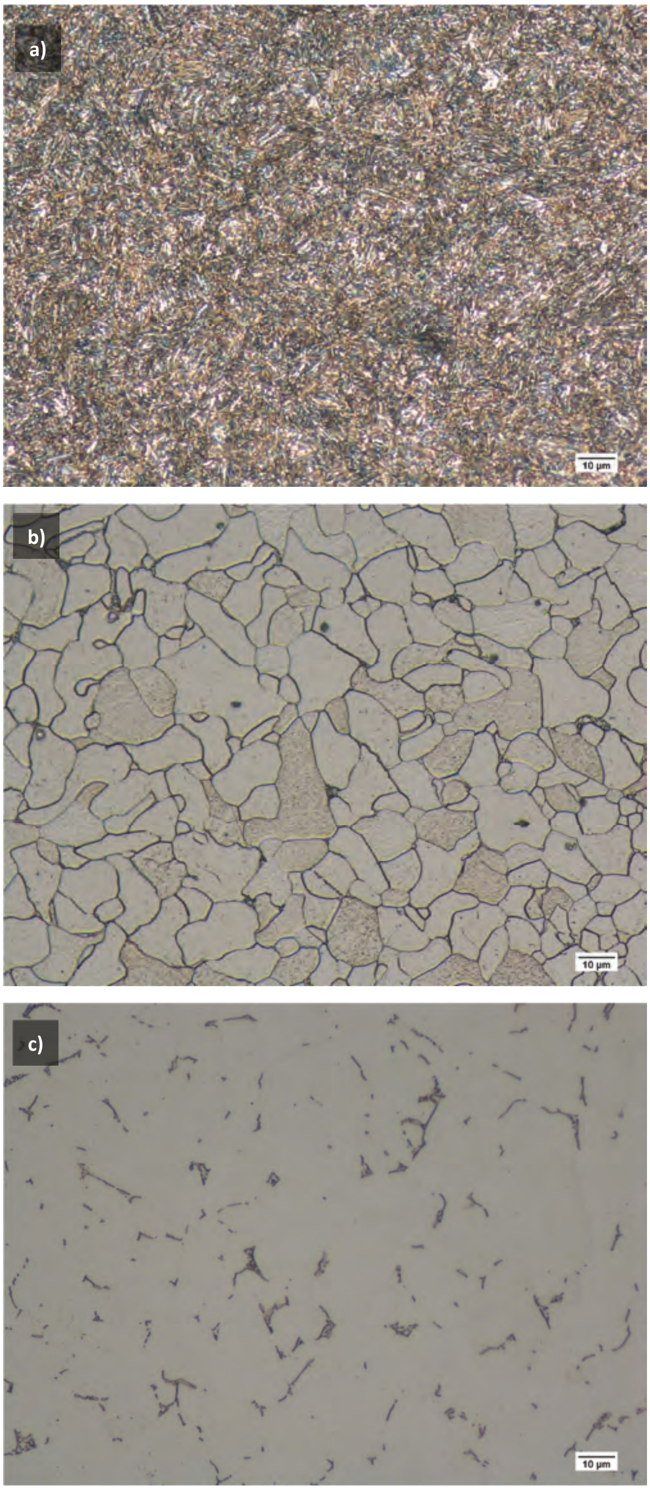

Fig. 2. Snap hook: a) original with tempered martensite microstructure; b) c) imitating original with ferritic microstructure with minor amount of pearlite colonies and presence of tertiary cementite at grain boundaries (micrograph c) in picral-etched state to visualize the extensive amount of cementite)

– the tempered martensite microstructure in the original component in contrast to the ferritic microstructure with a minor amount of pearlite colonies and tertiary cementite precipitations at grain boundaries in the imitation original component translate into the dissimilar material strengthening mechanisms;
– the degree of refinement of the microstructure of the compared elements, which results in a different grain boundary strengthening effect of the material in favour of the original snap hook (Fig. 3a vs Fig. 3c);
– the presence of undesirable precipitations of tertiary cementite at grain boundaries in DC04 steel, which locally forms a continuous network, thus providing a privileged site for accelerated crack growth and propagation;

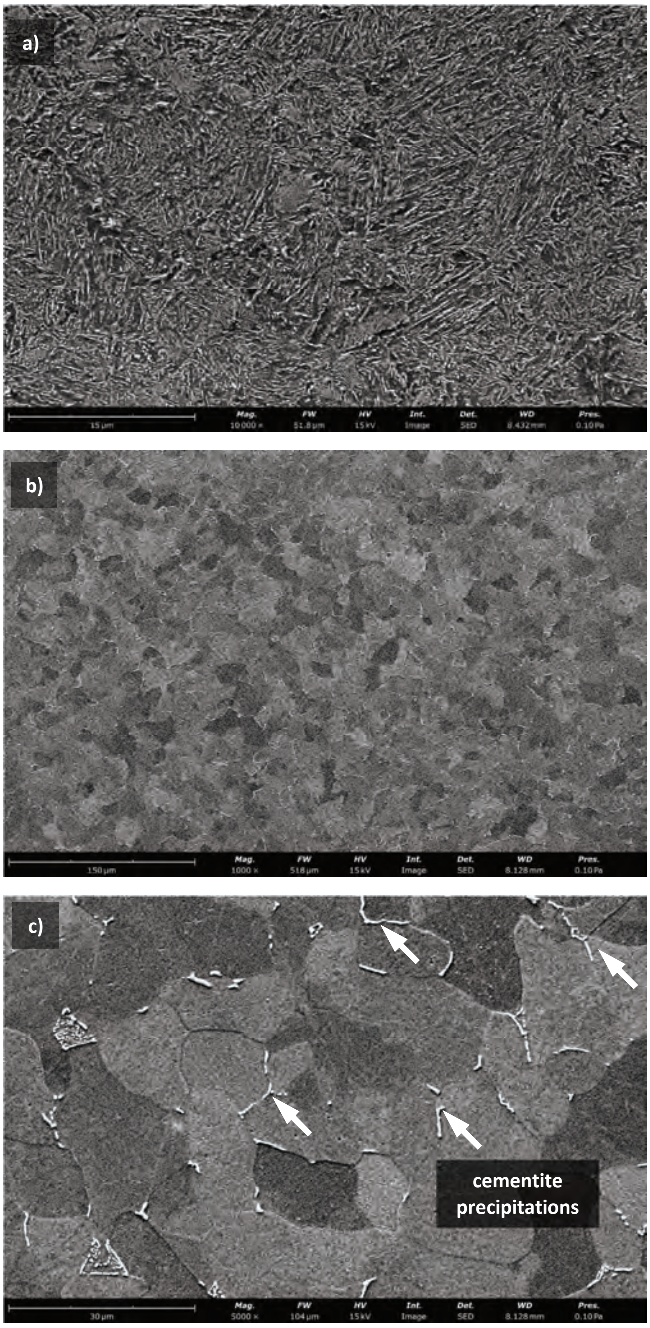

Fig. 3. Snap hook: a) original with tempered martensite microstructure; b) imitating original with ferritic microstructure with minor amount of pearlite colonies; c) numerous tertiary cementite precipitations visible at grain boundaries (indicated by arrows); SEM (BSE)

– the general purpose of the two identified steels, where C50 in the quenched and tempered condition is intended for highly stressed parts (components in general mechanical engineering and vehicle construction) and DC04 for metal forming (automotive industry, the domestic appliances sector, metal furniture, shaft processing, radiators, ventilators, tubes and small profiles).

According to PN-EN 10130:2009, DC04 steel has a maximum tensile strength of 270–350 MPa. In contrast, C50 grade steel in the quenched and tempered state according to PN-EN ISO 683-1:2018-09 has a tensile strength of 750–900 MPa. These differences are depicted by the almost five times higher hardness of the original snap hook than that of the replica.

3.2. Comparative material tests of central fastening mechanism components

A recurring defect of imitation seat belts is the tendency for the central fastening mechanism to jam, making it extremely difficult for the driver and/or passenger to safely and quickly exit the vehicle. The reason for this phenomenon is the deformation of the set of locking sleeves of the seat belt tongues in the central mechanism (Fig. 4). Their size and construction make it impossible to perform chemical composition analysis by GDS methods.

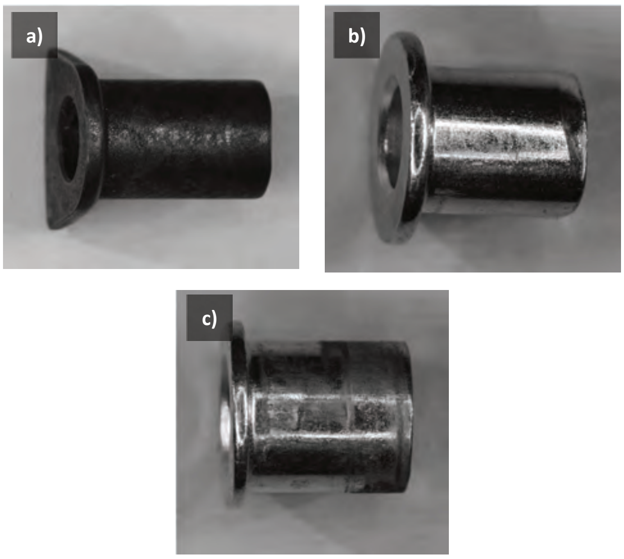

Fig. 4. The central fastening sleeve, which causes the mechanism to jam in the event of an accident, making it difficult to release the safety belts: a) original belts; b) c) imitation of original belts

The original sleeve is characterised by a tempered martensite microstructure with numerous visible porosities and shrinkage microcavities (Fig. 5a). Their presence is an evidence of the casting nature of sleeve production. However, the number and distribution of voids reduce the quality of the material. They provide an easy path for crack propagation. Due to the morphology of the microstructure, the material can be classified as a medium carbon steel for heat treatment.

The sleeves installed in the central fasteners of the belts imitating the original ones are characterised by a microstructure of ferritic-pearlitic morphology with a locally visible deformation texture resulting from the plastic forming process of the details. This texture translates into anisotropy of the mechanical properties of the sleeve. The number of pearlite colonies is relatively small and their distribution is not band-shaped. The ratio of the proportion of pearlite to ferrite grains makes it possible to classify the material in the family of low-carbon steels for metal forming.

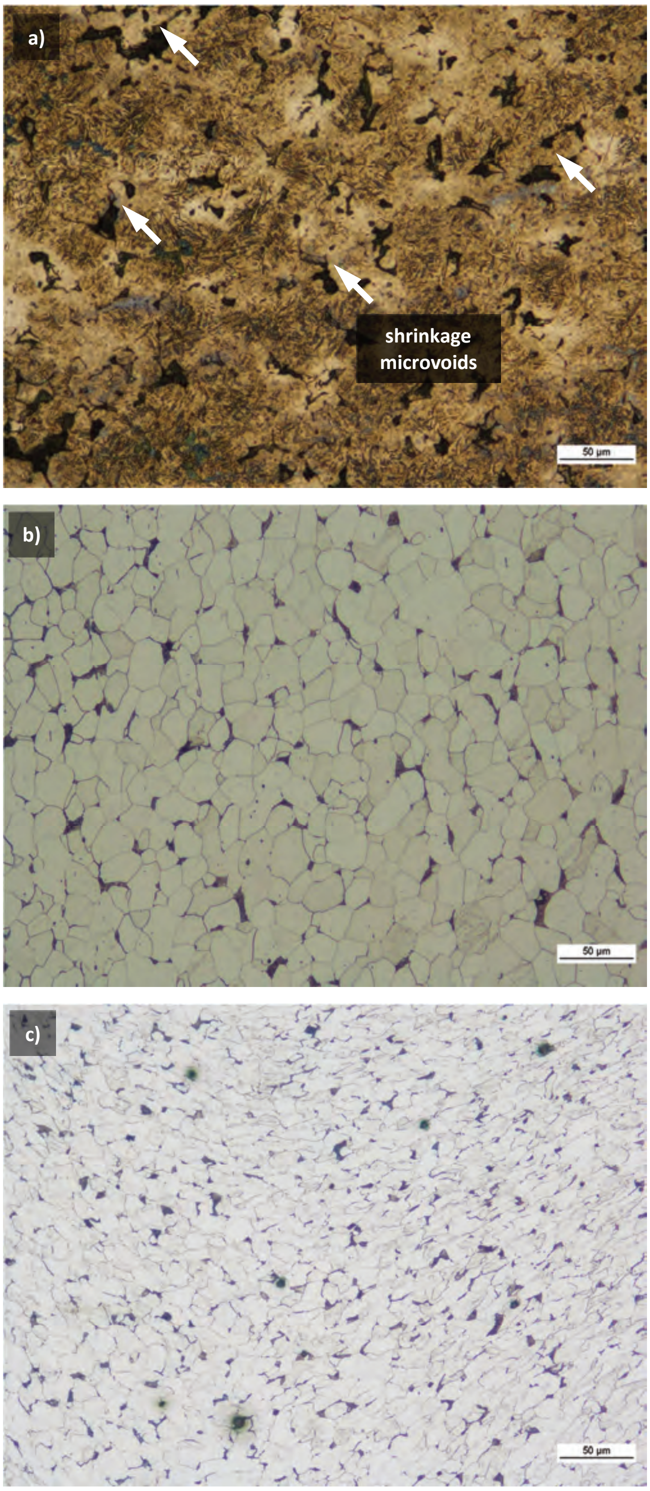

Fig. 5. Sleeve of the central fastener: a) the original with tempered martensite microstructure with visible numerous porosities and shrinkage microcavities; b) c) an imitation of the original with ferritic-pearlitic microstructure with visible locally occurring deformation grain texture resulting from the metal forming process of the workpiece

The obtained hardness results confirm and illustrate the differences in the materials used for the central fastener elements. In the case of the original part, a hardness of 353.6 ±57.8 HV5 was obtained, while the components imitating the original ones had a hardness of 168.7 ±1.8 HV5 and 229.6 ±9.4 HV5, respectively. The high standard deviation in the case of the original sleeve is due to the presence of numerous porosities and shrinkage microcavities.

The differences in manufacturing technology (cast steel vs steel), microstructure morphology and design are reflected in the different behaviour of components when subjected to external forces during a potential accident/impact. Due to the use of low-carbon steel, non-original parts are plastically deformed, causing the central fastening mechanism to jam. The original component used is heat-treated and has up to twice the hardness, but the amount of voids and porosity reduces the quality of the material applied, which can also result in cracking and blocking of the central fastening mechanism.

Table 5. Results of HV5 hardness measurements of sleeve from original belts

Object	Hardness measurements [HV5]				
original component	305.0	298.0	326.1	450.0	352.4
	439.2	410.8	313.6	311.4	329.8
		average ±SD		**353.6**	**±57.8**

Table 6. Results of HV5 hardness measurements of sleeve A from belts imitating the original

Object	Hardness measurements [HV5]				
imitation component A	171.7	168.9	167.7	168.3	166.9
		average ±SD		**168.7**	**±1.8**

Table 7. Results of HV5 hardness measurements of sleeve B from belts imitating the original

Object	Hardness measurements [hv5]				
imitation component B	225.5	234.5	242.7	227.7	214.8
		average ±SD		**229.6**	**±9.4**

4. Conclusions

On the basis of the test results obtained, it must be stated that the observed differences in materials illustrate the extreme quality in the selection and manufacture of all sets of belts, which is directly related to the safety, health and life of their users. The differences are visible in the applied constructional solutions, selected steel grades, manufacturing technology, microstructure morphology, and achieved material hardness.

For both of the imitation sports belt harness components considered (snap hooks and central fastening mechanism sleeves), the selection of used materials differed significantly from the original belts of the verified manufacturer. It was found that:

– the original snap hook has seven times higher carbon content (C: 0.502 wt%) in relation to the imitation (C: 0.071 wt%), where carbon is the basic element determining the mechanical properties of unalloyed steels;
– the components used are characterized by different microstructure morphology due to the extremely different heat treatment processes performed;
– the different degree of strengthening of the materials is illustrated by the hardness results, where the original component shows higher hardness (snap hook: 482.1 ±2.3 HV30; sleeve: 353.6 ±57.8 HV5) in relation to the imitation (snap hook: 105.6 ±1.0 HV30; sleeve A: 168.7 ±1.8 HV5; sleeve B: 229.6 ±9.4 HV5).

The analysed belts imitating the original ones are not able to meet the requirements of the FIA 8853-2016 standard. Unfortunately, at the same time the user of such belts is not able to visually assess their quality, as the belts are equipped with appropriate labels confirming their homologation. Only during the purchase stage can the credibility of the product be evaluated on the basis of the content of the advertisement or confidence in the dealer. At the same time, the results of the research are also intended to raise consumer awareness of the risks associated with the purchase of passive safety equipment from unreliable sources or/and at discounted prices, which entails real threats to life and health. Moreover, they are the base and starting point for the planned further research: verification of the belts in sledge crush tests with a dummy.

Nomenclature

FIA Fédération Internationale de l'Automobile
FRH frontal head restraint
GDS glow discharge spectrometry
SEM scanning electron microscope
BSE backscattered electron

Bibliography

[1] ACAR, B.S. Passive prevention systems in automobile safety. *International Encyclopedia of Transportation*. 2021, 406-414. https://doi.org/10.1016/B978-0-08-102671-7.10111-3

[2] BENSCOTER, A.O., BRAMFITT, B.L. Metallography and microstructures of low-carbon and coated steels. *Metallography and Microstructures – ASM International*. 2004, 588-607. https://doi.org/10.31399/asm.hb.v09.a0003761

[3] BILLUR, E. Hot formed steels. *Automotive Steels*. 2017, 387-411. https://doi.org/10.1016/B978-0-08-100638-2.00012-2

[4] BIN, W., ZHENYU, L., XIAOGUANG, Z. et al. Precipitation behavior of nanoscale cementite in hypoeutectoid steels during ultra fast cooling (UFC) and their strengthening effects. *Materials Science and Engineering: A*. 2013, **575**, 189-198. https://doi.org/10.1016/j.msea.2013.02.071

[5] BOWMAN, E.J., HARRIS, D.A., BROWN, T.H. Scrotal injury following restrained impact: A risk of misnavigation. *Injury Extra*. 2007, **38**(9), 314-316. https://doi.org/10.1016/j.injury.2006.12.025
[6] DUNN, R.F., MCSWAIN, R.H., MILLS, T. et al. Failure of plastic press release buttons in automobile seat belts. *Engineering Failure Analysis*. 2005, **12**(1), 81-98. https://doi.org/10.1016/j.engfailanal.2004.05.003
[7] FEDERATION INTERNATIONALE DE L'AUTOMOBILE FIA 8853-2016 – Safety Harnesses. 2016.
[8] FREEMAN, M.D. Traffic Injury Investigation. *Forensic Epidemiology*. 2016, 315-330. https://doi.org/10.1016/B978-0-12-404584-2.00012-4
[9] HALL, J.N., FEKETE, J.R. Steels for auto bodies. *Automotive Steels*. 2017, 19-45. https://doi.org/10.1016/B978-0-08-100638-2.00002-X
[10] HENSHAW, J.M., WOOD, V., HALL, A.C. Failure of automobile seat belts caused by polymer degradation. *Engineering Failure Analysis*. 1999, **6**(1), 13-25. https://doi.org/10.1016/S1350-6307(98)00026-0
[11] HENSHAW, J.M., WOOD, V., HALL, A.C. Failure of automobile seat belts caused by polymer degradation. *Failure Analysis Case Studies II*. 2001, 317-329. https://doi.org/10.1016/B978-0-08-043959-4.50033-X
[12] LI, Y., PENG, H., RONG, B. et al. Analysis and Improvement for the failure of seat belt anchor of a car based on simulation and experiment. *Proceedings of the FISITA 2012 World Automotive Congress*. 2013, **197**, 717-731. https://doi.org/10.1007/978-3-642-33805-2_59
[13] LICHTENSTEIN, M.J., BOLTON, A., WADE, G. Body mass as a determinant of seat belt use. *The American Journal of the Medical Sciences*. 1989, **297**(4), 233-237. https://doi.org/10.1097/00000441-198904000-00007
[14] MERKISZ, J., PIELECHA, I., MARKOWSKI, J. Operating parameters of high performance vehicle engines. *Combustion Engines*. 2007, **131**(4), 3-18. https://doi.org/10.19206/CE-117313
[15] DE MOOR, E., SPEER, J.G. Bainitic and quenching and partitioning steels. *Automotive Steels*. 2017, 289-316. https://doi.org/10.1016/B978-0-08-100638-2.00010-9
[16] NAGATA, M.T., SPEER, J.G., MATLOCK, D.K. Effect of deformation on cementite precipitation during overaging of low-carbon sheet steel. *Scripta Materialia*. 2001, **44**(6), 899-903. https://doi.org/10.1016/S1359-6462(00)00696-5
[17] PATALAK, J.P., HARPER, M.G., WEAVER, A.A. et al. Estimated crash injury risk and crash characteristics for motorsport drivers. *Accident Analysis & Prevention*. 2020, **136**, 105397. https://doi.org/10.1016/j.aap.2019.105397
[18] PERO-SANZ ELORZ, J.A., QUINTANA HERNÁNDEZ, M.J., VERDEJA GONZÁLEZ, L.F. Solid-state transformations in the Fe-C system. *Solidification and Solid-State Transformations of Metals and Alloys*. 2017, 255-324. https://doi.org/10.1016/B978-0-12-812607-3.00008-5
[19] PORTER, R.S., ZHAO, N. Patterns of injury in belted and unbelted individuals presenting to a trauma center after motor vehicle crash: seat belt syndrome revisited. *Annals of Emergency Medicine*. 1998, **32**(4), 418-424. https://doi.org/10.1016/S0196-0644(98)70169-6
[20] RIVARA, F.P., THOMPSON, D.C., CUMMINGS, P. Effectiveness of primary and secondary enforced seat belt laws. *American Journal of Preventive Medicine*. 1999, **16**(1), 30-39. https://doi.org/10.1016/S0749-3797(98)00113-5
[21] ROBERTS, A., PARTAIN, M., BATZER, S. et al. Failure analysis of seat belt buckle inertial release. *Engineering Failure Analysis*. 2007, **14**(6), 1135-1143. https://doi.org/10.1016/j.engfailanal.2006.11.059
[22] SIRIWARDENA, A.K. Seat-belt aortic injury. *European Journal of Vascular Surgery*. 1990, **4**(6), 649-650. https://doi.org/10.1016/S0950-821X(05)80825-4
[23] VAUGHN, M.G., SALAS-WRIGHT, C.P., PIQUERO, A.R. Buckle up: non-seat belt use and antisocial behavior in the United States. *Annals of Epidemiology*. 2012, **22**(12), 825-831. https://doi.org/10.1016/j.annepidem.2012.09.010
[24] WANG, B., LIU, Z., ZHOU, X. et al. Precipitation behavior of nanoscale cementite in 0.17% carbon steel during ultra fast cooling (UFC) and thermomechanical treatment (TMT). *Materials Science and Engineering: A*. 2013, **588**, 167-174. https://doi.org/10.1016/j.msea.2013.09.012
[25] WIDSTROM, L., BLUSTIN, J.M. Motor sports. Sports-related fractures, dislocations and trauma. 2020, 901-906. https://doi.org/10.1007/978-3-030-36790-9_63
[26] WRÓBEL, R., SIERZPUTOWSKI, G., HALLER, P. et al. The vehicle driver safety prediction system. *Combustion Engines*. https://doi.org/10.19206/CE-142950
[27] ZHAO, M.-C., HUANG, X.-F., ATRENS, A. Role of second phase cementite and martensite particles on strength and strain hardening in a plain C-Mn steel. *Materials Science and Engineering: A*. 2012, **549**, 222-227. https://doi.org/10.1016/j.msea.2012.04.040

Mateusz Dziubek, MEng. – Faculty of Mechanical Engineering, Wroclaw University of Science and Technology.
e-mail: *mateusz.dziubek@pwr.edu.pl*

Dominika Grygier, DSc., DEng. – Faculty of Mechanical Engineering, Wroclaw University of Science and Technology.
e-mail: *dominika.grygier@pwr.edu.pl*

Article citation info:
BIENIEK, A., GRABA, M., MAMALA, J. et al. Energy consumption of a passenger car with a hybrid powertrain in real traffic conditions. *Combustion Engines*. 2022, **191**(4), 15-22. https://doi.org/10.19206/CE-142555

Andrzej BIENIEK
Mariusz GRABA
Jarosław MAMALA
Krzysztof PRAŻNOWSKI
Krystian HENNEK

Combustion Engines
Polish Scientific Society of Combustion Engines

Energy consumption of a passenger car with a hybrid powertrain in real traffic conditions

ARTICLE INFO

Received: 21 July 2021
Revised: 31 August 2021
Accepted: 23 September 2021
Available online: 5 December 2021

The analysis of energy consumption in a hybrid drive system of a passenger car in real road conditions is an important factor determining its operational indicators. The article presents energy consumption analysis of a car equipped with an advanced Plug-in Hybrid Electric Drive (PHEV), driving in real road conditions on a test section of about 51 km covered in various environmental conditions and seasons. Particular attention was paid to the energy consumption resulting from the cooperation of two independent drive units, analyzed in terms of the total energy expenditure. The energy consumption obtained from fuel and energy collected from the car's batteries for each run over the total distance of 12 500 km was summarized. The instantaneous values of energy consumption for the hybrid drive per kilometer of distance traveled in car's real operating conditions range from 0.6 to 1.4 MJ/km, with lower values relating to the vehicle operation only with electric drive. The upper range applies to the internal combustion engine, which increases not only the energy expenditure in the TTW (Tank-to-Wheel) system, but also CO_2 emissions to the environment. Based on the experimental data, the curves of total energy consumption per kilometer of the road section traveled were determined, showing a close correlation with the actual operating conditions. Obtained values were compared with homologation data from the WLTP test of the tested passenger car, where the average value of energy demand is 1.1 MJ/km and the CO_2 emission is 23 g/km.

Key words: *energy consumption, hybrid vehicle, road tests, energy consumption analysis*

1. Introduction

The global economy growth, and hence the development of society and its mobility, forces to introduce innovation to broadly understood means of transport, such as road and off-road vehicles, water and air vehicles. However, regardless of the type of means of transport, the requirements for limiting the amount of harmful substances emitted by them in exhaust gases are increasing, as well as strict limits on CO_2 emissions. The current limits of carbon dioxide CO_2 emissions forces to look for various technical solutions to meet these requirements, for example, to drive unit hybridization or search for its new type. The drive unit in a hybrid car is a combination of a modern internal combustion engine (ICE) and an electric motor (EM), thanks to which the car is equipped with two independent energy storage. The issues of replacing the car power unit evoke a lot of emotions and are the subject of many analyzes by specialists on different continents. In this matter, the "game" is high, because the introduction of even stricter emission limits for the year 2030 forces manufacturers to spend significant amounts on production or new technologies development for powering internal combustion engines. The introduction of new technologies is connected with the need to accept the driver as a user of such a vehicle. It is about obtaining satisfactory results of using the car in relation to economy, ecology, dynamics, and operating costs. Hence, the search for such technological solutions that allow to obtain satisfactory results in each of the above-mentioned areas is extremely difficult. The importance of each area is significant factor in car swapping, as outlined in Arthur D Little's report, The Future of Automotive Mobility. The report presents the preferences of car users based on several most important factors taken into account when buying cars as shown in Table 1 [7].

Table 1. Car preferences of users taken into account when buying a car, in % response to factor

Country	The most important factors %			
	Purchase price	Environment	CO_2 emission	Economy – total cost of ownership (TCO)
China	32	51	48	40
European Union	43	32	35	28
USA	35	28	29	32

These preferences show large differences among car users for individual countries. For example, in the USA, priority is given to the purchase price and operating costs. In Europe, however, less attention is paid to operating costs, as opposed to China, where environmental and operating costs are the most important.

New technologies implemented on cars are considered in several areas where a thorough analysis should be carried out:

– ecology – new materials and technology require new raw materials for production. At the same time, the new technology requires other energy sources to power drive units. The cost of energy carriers is high – for example, when obtaining hydrogen.
– economy – not only the costs of implementing the technology or production are considered, but also those related to the total operating costs of a given car. Not only current operating costs in the form of fuel/energy, but also purchase or maintenance and repair costs are taken

into account here [8]. The issue of reselling a car on secondary market is not without significance here.
- social – related to the acceptance of new technology, such as the mobility of new cars, understood as the ability to cover longer routes, the availability of infrastructure that allows to replenish energy storage in a short time. Time is essential, especially in a society that is constantly lacking it.
- legal – related to approval regulations, emission limits of individual components in exhaust gases or presence of certain elements in automotive parts, the issue of carbon footprint or taxes. The matter of recycling materials is also important.
- technological – at present, the challenge is the easiest to meet, due to the theoretical lack of limitations.

Currently, it seems that the natural successor to changing car market is the transformation from powertrain ICEV (Internal Combustion Engine Vehicle) to BEV (Battery Electric Vehicle). The electric drive has limitations in terms of mobility, infrastructure and density of energy stored in batteries and their mass. For this reason full hybrid cars are a good bridge to the transition from ICEV to BEV systems. The article focuses on car energy consumption indicators with a powertrain PHEV at different times of the year over total distance of 12 500 km. The car was operated in real traffic conditions from new products, i.e. from zero mileage in 2021. Energy consumption in the propulsion system is analyzed in terms of TTW (Tank to Wheels), which is the sum of total energy expenditure obtained from the storage in relation to the distance covered. These results were compared with the WLTP (The Worldwide Harmonized Light Vehicles Test Procedure) homologation test data.

2. Motion energy consumption

Many authors have analyzed motion energy consumption, drive efficiency and other properties of various drive system configurations. Ahman et al. [1] conducted a comparison of the average efficiency of classic ICEV systems and alternative BEV, HEV, FCEV systems. The obtained primary efficiencies ranged from 19% for ICEV to 31% for BEV. In the case of using renewable energy, the primary efficiencies was estimated as 57% for BEV and 26% for FCEV. However, it was noted that there is a potential for further optimization of the discussed systems and obtaining maximum efficiencies of 45% for ICEV and up to 76% for other types of drives. Sharer et al. [22] analyzed the demand for energy and the efficiency of ICEV and HEV in selected driving cycles. As shown by the tests, the efficiency of the drive systems was determined in the range of 18–27% for ICEV and 34–37% for HEV, depending on the compared driving cycle.

Some researchers made the energy requirements of various drive systems dependent on the preferred driving style. On the other hand Thomas et al. [23] checked the energy demand for ICEV and HEV in driving cycles using a cycle intensity index in the range 0.8 to 1.1. The obtained results indicate that an aggressive driving style simulated by an increase in the cycle intensity index causes an increase in energy consumption by about 74% for ICEV and as much as 105% for HEV.

Pitanuwat and Sripakagorn [20] conducted similar studies, but carried out in real conditions, comparing the energy consumption for a statistically normal driving style to the energy consumption of very aggressive driving. The increase in consumption was achieved for an aggressive driving style in the range of 80–113.8% for ICEV to 102.5 – 220% for HEV. Orecchinii at al. [17] compared the fuel consumption of ICEV and HEV vehicles in real driving conditions, stating that HEVs maintain fuel consumption in the range of 3.5–5.5 dm^3/100 km at average driving speeds in the range of 20–100 km/h. In turn, ICEV systems generate the highest fuel consumption at low average driving speeds resulting from driving in the city with high traffic density, up to 13.5 dm^3/100 km. In the case of ICEV, you can also see a minimum fuel consumption of approx. 4 dm^3/100 km at average speeds of 70–80 km/h, and then an increase in fuel consumption to approx. 5.5 dm^3/100 km at average speeds of 100 km/h is observed. Wang et al. [24, 25] compared fuel and energy consumption in selected 7 driving cycles for ICEV, HEV and BEV. The fuel consumption was in the range of 6.37–14.85 dm^3/100 km for the ICEV, 4.51–5.84 dm^3/100 km for the HEV and electricity consumption of 16.43–20.12 kWh/100 km. The recorded fuel consumption was also compared for real traffic conditions in Beijing. Electricity consumption BEV was converted to the equivalent of the consumed fuel. The obtained values are respectively 12.5 dm^3/100 km for ICEV, 5.5 dm^3/100 km for HEV and 2.0 dm^3/100 km for BEV.

Wenwei et al. [11] compared well-to-wheel energy consumption for different drivetrains. At the counting, the equivalent of fossil energy consumptions was assumed, with values from 3.4 $MJ \cdot km^{-1}$ for ICEV to 2.0 $MJ \cdot km^{-1}$ PHEV. For HEV were characterized by slightly higher energy of about 2.2 $MJ \cdot km^{-1}$ and BEV of 2.5 $MJ \cdot km^{-1}$. The results of measurements for urban driving in real conditions were also presented, obtaining 9.1 dm^3/100 km for ICEV and 17 kWh/100 km for BEV at the same time. The quoted comparison of fuel consumption and electricity consumption are calculated in different units, therefore they should be expressed in MJ/km.

The car motion can be analyzed regarding consequences of specific energy changes taking place in its drive system. It should be noted that currently the dominant technical solution for most powertrain is combination of the ICE with the drive train, forming a monoblock, most often installed on car's front axle. In energy balance of the entire moving car, by following the set speed profile, energy produced from burned fuel E_T is spent on its drive, but also on additional devices' drive and losses resulting from energy conversion and drive transmission to vehicle wheels. Thus, according to equation (1), it is the sum of: the energy supplied to wheels by drive system and defined as the motion energy consumption (E_M) needed to overcome the resistance of vehicle motion, energy losses of drive unit (ΔE_E) and energy losses of drive train (ΔE_D), as well as losses of energy supplied to drive system without transmitting to drive wheels (ΔE_L), i.a. car standstill phase:

$$E_T = E_M + \Delta E_E + \Delta E_D + \Delta E_L \tag{1}$$

All components of car energy balance vary over time and depend on speed profile parameters, and environmental conditions. For a simple car speed profile consisting of four car phases (accelerated motion, steady motion – constant speed, deceleration, and stop), the energy expenditure is calculated from start to stop, and car kinetic energy at the beginning and end is zero. The basic values of speed profile parameters, expressed as average speed $\overline{V}$, path length L or average acceleration $\bar{a}$, depend on participation of individual profile phases on a given road section. In practice, the presence of a simple speed profile is not common. In fact, there are complex speed profiles, where the kinematic profile parameters (speed, acceleration) are the average of many components of simple profiles (simple modules). The average speed of complex profile can be calculated from the dependence:

$$\overline{V} = \frac{\sum_i L}{\sum_i \int_{t_s}^{t_e} \frac{dv}{a} + \sum_i \frac{L_C}{V_C} + \sum_i \int_{t_s}^{t_e} \frac{dv}{a_D} + \sum_i T_L} \qquad (2)$$

Standstill is an undesirable phase of movement, because at this time, during operation of internal combustion engine, energy is generated from burned fuel, which is not received by the drive train.

In the authors' own work [9], attention was paid to the differentiated fuel demand of a car moving in real traffic conditions resulting from different dynamics of its acceleration. In road tests, significant discrepancies in mileage fuel consumption were found, ranging from 12.44 to 31.8 dm^3/100 km, recorded over the distance of ¼ mile, depending on the acceleration dynamics and gear selection in the driveline. Choosing a gear ratio with lower values resulted in a reduction in fuel consumption, with average efficiency of drive system ranging from 19.38 to 24.6%. The values shown above are registered for an ICEV car with an internal combustion engine built according to the downsizing philosophy.

In own work, the authors [4] analyzed the impact of various drive transmission systems, paying attention to AT and MT transmissions, for which maximum efficiency points were established at a speed of 70 km/h, amounting to 24%. However, regardless of the study and analysis of the car's motion phases, the issue of fuel consumption is a key point from the car's economy point of view. An important issue is the possibility of reducing fuel consumption by recovering car kinetic energy in its retarded motion phase, where in most cases energy is dissipated by the braking system to the environment. Hence, the introduction of Hybrid Electric Vehicle (HEV), was aimed at reducing the loss of energy in the drive system through its energy recovery [16, 21, 26]. In such cars, there is an integrated hybrid drive system with two energy storages (fuel and electricity), as well as two independent drive units (combustion and electric), which drive the vehicle together.

3. Hybrid drive system of a passenger car

It is predicted that over the next 30 years, the number of new cars produced in the world will increase by nearly 30%, which will result in over 2 billion cars driving on the world's roads in several dozen years [3, 10]. New cars will be equipped with advanced powertrains and this is due to the introduction of new, increasingly stringent emission standards and carbon dioxide into the atmosphere. Many countries plan to ban the registration of new cars powered only by an ICE (Table 2).

Table 2. Planned restrictions on the possibility of registering new cars

Country	Scheduled year for banning the ICEV
Netherlands	2025
India	2030
France	2040
Germany	2040
Spain	2040
United Kingdom	2040

In 2025 in the European Union, the introduction of a new exhaust emission standard called Euro 7 is announced, but fulfilment of new emission limits based only on the internal combustion engine will be very difficult or even impossible, while maintaining high values of vehicle traction parameters related to dynamics and achieving average speed of travel [14]. From the driver's point of view, the use of different drive units is not significant in the light of the requirements for a car designed to transport people and goods in a sufficiently short time on a given road section. Hence, hybrid drive systems have been dominated by known drive units, most often connected in a parallel manner (Fig. 1).

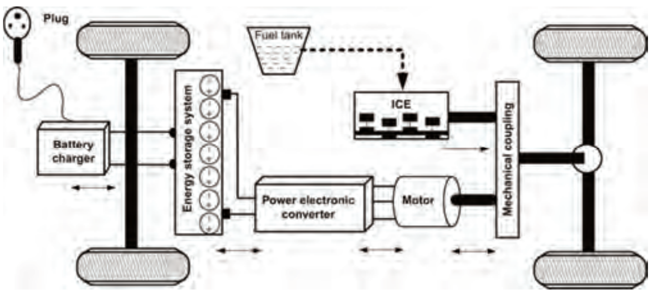

Fig. 1. Architecture of the parallel hybrid electric vehicle [7]

It results from the greater versatility of such a drive system solution in everyday use, both in urban and extra-urban traffic [2, 5, 18, 19]. Many authors conduct research on this type of hybrid drive systems in relation to the emission limits of harmful components [15, 16] as well as in terms of total energy consumption in normal operating conditions [12, 13, 20] or in relation only to the electric drive system [6, 19]. The real test that verifies such hybrid drive systems in terms of energy consumption is road measurements under real operating conditions. Therefore, as part of this study, the impact of road conditions on the car's mileage consumption was analyzed.

4. Methodology and course of own research

The difference in energy value of energy carriers stored in passenger cars with hybrid drive systems cause that a direct comparison of the mileage consumption for an internal combustion engine with the mileage consumption for an electric motor is not adequate in terms of units used. The use of converted mileage energy consumption in a standardized energy (SI system) measurement unit J per kilometer of distance traveled in relation to both drive units allows for increasing the possibility of comparing them as to their operation time within the drive system, total energy expenditure or the possibility of comparing the values obtained in operational tests to the values obtained in homologation test. Hence, the measurements were carried out with the car in real traffic conditions, at different times of the year, in relation to normal operating conditions resulting from everyday use of the car. It is not a reference to the RDE cycle where the driving cycle is divided into urban, extra-urban and motorway driving. However, the results of the measurements are related to the values recorded in the homologation of the Euro 6d car.

4.1. Mileage energy consumption

Mileage energy consumption is a measure of the energy expended from the storage of the car's propulsion units per kilometer of the distance traveled. Taking into account the internal combustion engine, the total energy (E_{Tf}) spent on driving a car depends on the product of amount of fuel consumed (VFC) and its calorific value (W_O),which can be presented by the equation:

$$E_{Tf} = W_o \cdot \int_{t_s}^{t_e} FC\, dt \quad (3)$$

where: VFC – vehicle fuel consumption, g/s, W_o – fuel calorific value, depending on its type (gasoline, diesel, etc.), J/kg, $t_{s,e}$ – start and end time of energy calculation, s.

For an electric drive unit, the total energy (E_{Te}) expended on the drive depends on the electric motor construction and the method of supplying with direct or alternating current and also the instantaneous power supplied from batteries to electric drive unit. For alternating current, the total energy can be calculated from equation (4):

$$E_{Te} = \int_{t_s}^{t_e} P\, dt \quad (4)$$

where: P – electric power, (W), for AC motors, the electric power is the product of P = U(t) I(t) cosφ(t), where U – electric voltage over time, I – electric current intensity over time, cosφ – ratio of active to apparent power over time, $t_{s,e}$ – start and end time of power consumption.

The total energy supplied to car's propulsion system is the sum of equations (3) and (4) and is equal to the energy drawn from various energy stores over time. In hybrid drive systems, it is possible to recover energy in delayed motion during coasting or braking, which, however, is not analyzed in terms of operation, because it replenishes the energy reservoir by recharging the batteries and thus increases the car's range.

The total energy consumed by a car, after conversion to the distance traveled, shows the mileage energy consumption of the car according to the equation (5):

$$Q_{PHEV} = \frac{E_T}{L} \quad (5)$$

The obtained values are varied and depend on used drive unit type and the parameters on a given road distance: average speed, time, and distance.

4.2. Course of research

The research concerned the analysis of mileage energy consumption in a passenger car equipped with a Plug-in Hybrid Electric Drive, taking into account:

1. The analysis of working time in the hybrid drive system of individual drive units.
2. The analysis of the car's mileage energy consumption during its operation.
3. The analysis of the ambient temperature influence on car's mileage energy consumption.

The monitoring of traction and energy parameters was carried out using the Mercedes-Benz software, which allowed for an ongoing overview of the following data:

– total range of the drive system,
– range divided by type of drive unit used,
– energy storage capacity,
– total distance traveled,
– distance divided by drive units,
– total travel time,
– travel time divided into drive units,
– average speed as well as energy expenditure as mileage fuel consumption and electricity consumption.

These data were systematically saved in a database and analyzed. The analysis of mileage energy consumption was carried out for the actual car's operating conditions resulting from daily runs on a specific road section. The driver was not subjected to any pressure in terms of driving style. The runs were characterized by free route choice with a length of about 50 km, as well as a random selection of drivers with the standard hybrid drive system control mode. The distance of the route for the test drives resulted from the range of the energy storage, so that the electric drive system was the dominant in the driving range. Before each of the runs, the electric reservoir was filled from the 230 V electric network using a factory charger up to the SOC indicator's value of 100%. In total, 67 runs were analyzed in detail.

4.3. Research object

The study of car's mileage energy consumption with a PHEV hybrid drive system in real operating conditions was carried out on a Mercedes-Benz A 250e vehicle (Table 3).

Table 3. Parameters of the tested vehicle [27, 28]

Producer	Mercedes-Benz
Type	A250e/V177
Internal combustion engine displacement	1332 cm^3
Internal combustion engine power	118 kW at 5500 rpm
Maximum torque of the internal combustion engine	210 Nm at 1750 rpm
Electric motor power	75 kW
Long – lasting electric motor power	55 kW
Maximum torque of the electric motor	450 Nm
Installation of the drive unit	At the front, transversely
Internal combustion engine supercharging	Turbocharger
Drive system type	PHEV
Drive train	Automatic – 8 gears
Vehicle mass	1817 kg
Emission standard	Euro 6 (AP)
Range on gasoline	450 km
Battery range	75 km
Average CO_2 emissions according to WLTP	23 g/km (1.0 dm^3/100 km)
Energy consumption for the EV system	209 Wh/km
Battery capacity (electricity storage)	15.6 kWh

It is a passenger car from 2021 with a parallel full hybrid drive system, where two drive units (electric and combustion) are installed on the front drive axle. The power units cooperate with an 8-speed 8 F-DCT (Front-Double Clutch Transmission) gearbox and a drive is transmitted to front wheels.

Table 3 shows the average energy consumption for electric drive train and the average CO_2 emissions according to the WLTP test, read from the approval certificate [27]. Attention should be paid to the increase in weight of the test car by nearly 300 kg in relation to the car with the ICEV internal combustion drive system due to the use of additional components of the EV electric drive system (storage tank, electric motor, inverter and control system).

5. Research results

In accordance with the adopted methodology, the car's mileage consumption analysis was carried out for its actual operating conditions in everyday driving for a distance of about 50 km. The test drives occurred in various weather and road conditions. Table 4 shows the traction and energy parameters for analyzed groups of runs, divided by season.

Table 4. Average values of drive system's operating parameters during runs made during the standard operating mode of hybrid drive

Group	L_T [km]	L_e [km]	t_T [min]	V [km/h]	Q_f [l/100 km]	Q_e [kWh/100 km]	Q_{Tf} [MJ]	Q_{Te} [MJ]	Q_{T_PHEV} [MJ]	Temp. [°C]
Winter (I)	48.7	46.9	54.2	55.0	0.21	19.12	3.58	33.49	37.07	5.1
Spring (II)	48.2	47.3	48.2	57.8	0.12	17.37	1.92	30.09	32.01	11.5
Summer (III)	49.7	49.0	47.4	59.5	0.08	13.70	1.27	23.33	24.60	24.0
Average	48.9	47.7	49.9	57.4	0.13	16.7	2.26	28.9	31.2	

In all groups of runs, the electric drive system of a car (BEV) is dominated, in which the combustion engine is turned on occasionally, which is reflected in mileage consumption of combustion engine. It should be noted that theoretically the range of tested car was 75 km on electric drive, hence the low mileage fuel consumption because most of the test drives were electric. However, the slight differences in the mileage consumption of fuel (Fig. 2a) do not correspond to the significant changes resulting from the mileage energy consumption (Fig. 2b).

The differences in mileage energy consumption are approximately 30% between the minimum and maximum values. It should be noted that the changes in average speed, distance and driving time have changed slightly. The difference between the average minimum and maximum speed was 4.5 km/h and is related to improved weather conditions on the road. The average temperature changed from 5.1°C (winter period) to 24.0°C (summer period). A significant change in temperature changed the total energy expenditure for a covering a distance of about 50 km (Fig. 3).

a)

b)

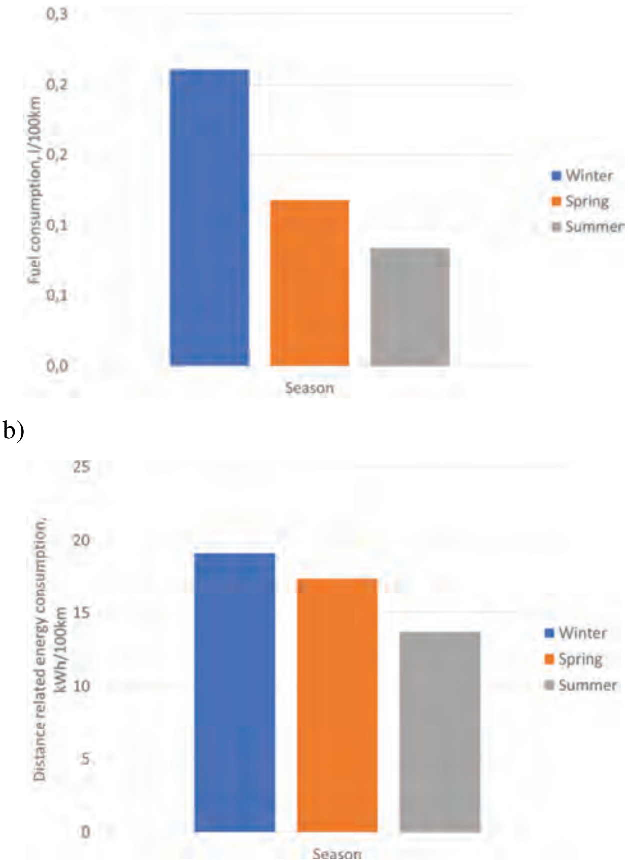

Fig. 2. The mileage consumption of energy carriers in relation to the season in which the measurements were carried out (for the distance traveled once)

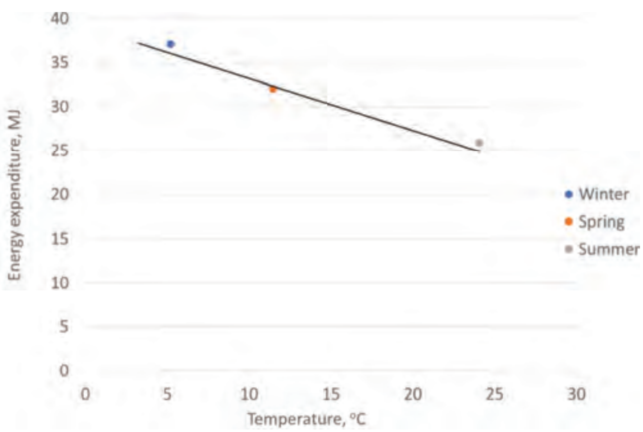

Fig. 3. Energy expenditure for a distance of 50 km in relation to the average temperature over a given season

Paying attention to values of energy expenditure, it can be stated that it depends on temperature, while the total cumulative energy expenditure of tested car over a distance of 12 500 km in a given quarter increases in a linear manner and is characterized by a high coefficient of determination R^2 (Fig. 4).

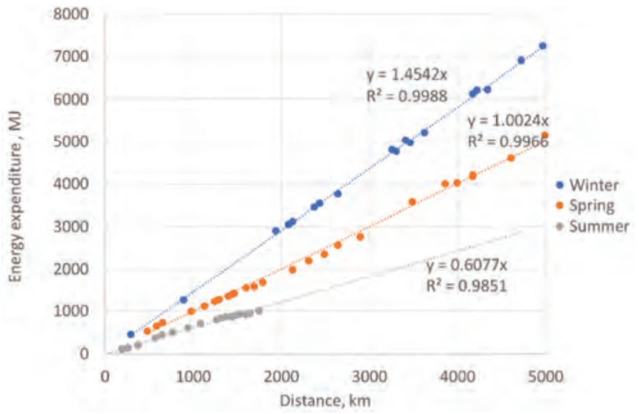

Fig. 4. The cumulative expenditure of converted energy (for a distance of approximately 50 km) in relation to the total vehicle mileage during the period considered

The diagram shows the energy expenditure for the entire Plug-in Hybrid Electric Drive, where the increase in its expenditure is proportional to the mileage (approximation in Fig. 4). The greater the energy expenditure MJ, the greater the range in km. For the course of these functions, the differential can be found and presented in the form of dependence (6):

$$\frac{\Delta E_T}{\Delta L} = tg\alpha = Q_{PHEV} \quad (6)$$

Thus, the slope of approximation line in Fig. 4 depends, on the one hand, on energy expenditure and on the other hand on road increment, which can be written directly as the quotient (6) describing the trigonometric function tgα, where the angle of this function is the angle of approximation line slope and presents the car's mileage energy consumption.

The mileage consumption of a car depends on distance traveled and its highest values are found in winter runs. The average instantaneous amount of energy expended in winter is 1.45 MJ/km, and in summer 0.60 MJ/km, and is more than twice as high. Moreover, in winter, after traveling a distance of 50 km, the range of an electric car was very often 0 km. In summer period, the range after driving 50 km is indicated about 22 to 25 km, which is consistent with the declared range of electric drive (Table 2).

At the same time, there are also significant discrepancies in relation to individual types of propulsion, taking into account the average values. From this point of view, (Fig. 5) shows the total energy consumption in relation to the distance traveled (50 km distance traveled at a time) and divided by usage of individual drive units to drive the vehicle.

The greatest differentiation in energy expenditure can be observed for combustion engine, where the energy expenditure per kilometer of road traveled varies from 0.14 MJ/km in summer to 0.93 MJ/km in winter (Fig. 5a). The fluctuations in energy expenditure for electric drive system are much smaller and range from 0.46 to 0.55 MJ/km and are much less dependent on temperature.

Referring to the mileage energy consumption of a car with the hybrid drive system in terms of the total vehicle mileage in each test, it is lower for mileage from groups II (spring) and III (summer) than that resulting from the WLTP approval tests, amounting to 1.09 MJ/km for the test car. In winter, the energy expenditure is 40% higher than the homologation cycle. The lowest values are for runs in group III (summer), where the value of mileage energy consumption was 0.60 MJ/km (Fig. 4).

a)

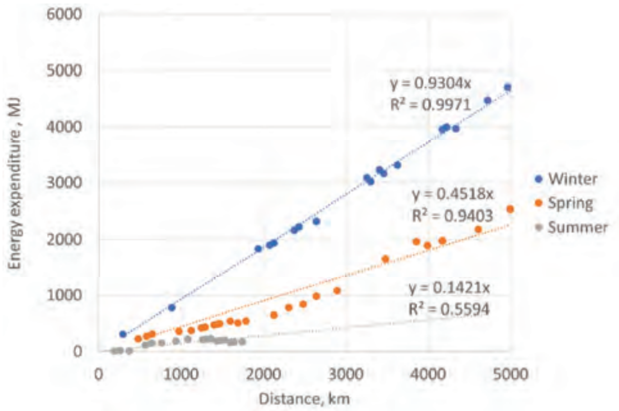

b)

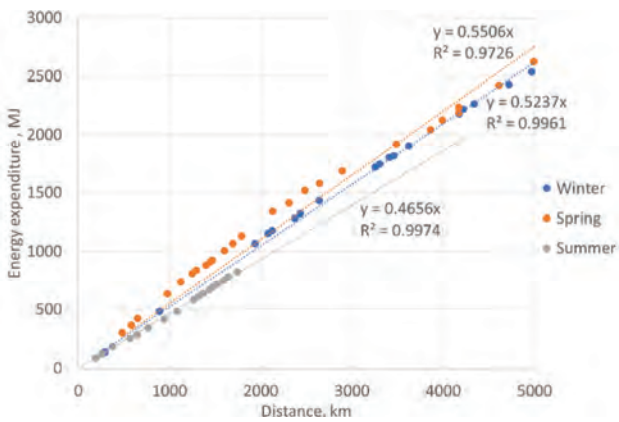

Fig. 5. Energy expenditure for distances of about 50 km in relation to the total mileage of the vehicle in the tested period, divided into individual drives: a) internal combustion engine, b) electric drive.

The presented values were related to results in the WLTP homologation cycle, however, it should be emphasized that only test drives performed at a distance close to the range resulting from the capacity of electric energy storage were analyzed. The implementation of longer test drives requires an increase in the capacity of electrical energy storage (batteries) to maintain the mileage consumption value below that obtained in the WLTP homologation tests.

During the research, attention was drawn to relation between the actual capacity of electric energy storage and ambient temperature. The problem of battery capacity reduction and the external temperature, described in the literature, was noticed, where at the temperature –15°C, the range of an electric car decreased to 21 km [9]. The range for electric drive declared in Table 2 allows for a distance of 75 km, but at a temperature higher than 18°C. After exceeding this distance, the driver has practically only the internal combustion engine (ICEV) with function of energy recovery in the deceleration process. For the test car, the average energy recovery is 25%.

6. Summary

The analysis of the car's mileage consumption for a Plug-in Hybrid Electric Drive in real operating conditions presented in the article shows a differentiated energy expenditure depending directly on the ambient temperature, but also on the type of drive system used. The presented calculations of energy expenditure based on unified data from real test drives in normal traffic conditions allow for the formulation of the following conclusions:

- the analysis of the car's mileage energy consumption in instantaneous and cumulative terms shows a significant increase in energy on the internal combustion engine side, which is structurally and mechanically complicated, but its advantage is the use of a simple energy storage device with high energy capacity. The electric drive unit is structurally and mechanically simple, while the electric energy reservoir is characterized by a complex structure, considerable weight, and limited capacity,
- the analysis of the car's mileage energy consumption, divided into individual drive units, shows an over 9-fold increase in its value depending on the temperature. For the electric drive unit in the TTW system, the changes are small,
- the analysis of ambient temperature influence on a passenger car range with a hybrid drive system causes a significant increase in the car's mileage energy consumption. And for test drives in the winter season with the ambient temperature –15°C, the real range of the during test car shortened to 21 km from the declared range of 75 km.

The various 67 runs presented in the article in the period from winter to summer, differing in terms of traffic conditions, but carried out on the same distance and route, can be compared with the values recorded in the WLTP test. Higher values of the car's mileage energy consumption were recorded for winter conditions, where the average temperature was 5.2°C. In the remaining periods, the average value of vehicle's mileage consumption is below the value obtained for the WLTP homologation test. At the same time, the converted value of carbon dioxide CO_2 emissions for these runs meets the requirements of the current (2021) Euro 6 (AP) emission standard of 95 g/km.

Nomenclature

$\bar{a}$	average acceleration [m/s^2]
AT	Automatic Transmission
BEV	Battery Electric Vehicle
E_M	motion energy consumption [J]
EM	Electric Motor
E_T	energy produced from burned fuel [J]
E_{Te}	total energy for electric drive unit [J]
E_{Tf}	total energy for combustion engine drive unit [J]
EV	Electric Vehicle
VFC	Vehicle Fuel Consumption [kg/s]
F-DCT	Front-Double Clutch Transmission
HEV	Hybrid Electric Vehicle
ICE	Internal Combustion Engine
ICEV	Internal Combustion Engine Vehicle
L	road length [m]
MT	Manual Transmission
P	electrical power [W]
PHEV	Plug-in Hybrid Electric Vehicle
Q_{PHEV}	mileage energy consumption [Wh/km]
Q_f	mileage fuel consumption [dm^3/100 km]
Q_e	mileage electric energy consumption [kWh/100 km]
Q_{Tf}	energy consumption as energy contained in the fuel [MJ]
Q_{Te}	energy consumptions of the electric drive unit [MJ]
Q_{T_PHEV}	energy consumption of PHEV [MJ]
SOC	State of Charge
$t_{s,e}$	start and end time of energy calculation [s]
TTW	Tank to Wheels
$\bar{V}$	average speed [m/s]
WLTP	The Worldwide Harmonized Light Vehicles Test Procedure
W_O	calorific fuel value [J/kg]
ΔE_D	energy losses of internal combustion engine [J]
ΔE_E	energy losses of electric drive unit [J]
ΔE_L	loss of energy supplied to the drive system without being transferred to the drive wheels [J]

Bibliography

[1] ÅHMAN, M. Primary energy efficiency of alternative powertrains in vehicles. Energy. 2001, **26**(11), 973-989. https://doi.org/10.1016/S0360-5442(01)00049-4

[2] BARTH, M., BORIBOONSOMSIN, K. Energy and emissions impacts of a freeway-based dynamic eco-driving system. *Transportation Research Part D: Transport and Environment*. 2009, **14**(6), 400-410. https://doi.org/10.1016/j.trd.2009.01.004

[3] BECKER, T., SIDHU, I., TENDERICH, B. Electric vehicles in the United States: a new model with forecasts to 2030. Technical Brief. University of California. *Center for Entrepreneurship and Technology*. Berkeley 2009.

[4] BIENIEK, A., GRABA, M., HENNEK, K. et al. Analysis of fuel consumption of a spark ignition engine in the conditions of a variable load. *MATEC Web of Conferences*. 2017, **118**. https://doi.org/10.1051/matecconf/201711800036

[5] BOKARE, P.S., MAURYA, A.K. Acceleration-deceleration behaviour of various vehicle types. *Transportation Research Procedia.* 2017, **25***,* 4733-4749. https://doi.org/10.1016/j.trpro.2017.05.486

[6] CHŁOPEK, Z. Research on energy consumption by an electrically driven automotive vehicle in simulated urban conditions. *Eksploatacja i Niezawodnosc – Maintenance and Reliability*. 2013, **15**(1), 75-82.

[7] ARENA, F., SPERA, D., LAGUARDIA F. What's in the future for fuel cell vehicles? 2017. https://www.adlittle.com/en/insights/viewpoints/what%E2%80%99s-future-fuel-cell-vehicles

[8] DELLOITLE. Fuelling the future mobility – hydrogen and fuel cell solutions for transportation. 2019. https://www2.deloitte.com/content/dam/Deloitte/cn/Documents/finance/deloitte-cn-fueling-the-future-of-mobility-en-200101.pdf

[9] GRABA, M., MAMALA, J., BIENIEK, A. et al. Impact of the acceleration intensity of a passenger car in a road test on energy consumption. *Energy*. 2021, **226**, 120429. https://doi.org/10.1016/j.energy.2021.120429

[10] International Energy Agency. Energy Technology Perspectives 2017 – Executive Summary. 2017. https://doi.org/10.1787/energy_tech-2014-en

[11] KE, W., ZHANG, S., HE, X. et al. Well-to-wheels energy consumption and emissions of electric vehicles: Mid-term implications from real-world features and air pollution control progress. *Applied Energy*. 2017, **188**, 367-377. https://doi.org/10.1016/j.apenergy.2016.12.011

[12] KROPIWNICKI, J., FURMANEK, M. Analysis of the regenerative braking process for the urban traffic conditions. *Combustion Engines*. 2019, **178**(3), 203-207. https://doi.org/10.19206/CE-2019-335

[13] KROPIWNICKI, J. A unified approach to the analysis of electric energy and fuel consumption of cars in city traffic. *Energy*. 2019, **182**, 1045-1057. https://doi.org/10.1016/j.energy.2019.06.114

[14] LIMBLICI, C. Investigation of engine concepts with regard to their potential to meet the Euro 7 emission standard using 1D-CFD software. Politecnico di Torino. *Master Thesis*. 2020. https://webthesis.biblio.polito.it/16275/

[15] MAMALA, J., GRABA, M., PRAŻNOWSKI, K. et al. Control of the effective pressure in the cylinder of a spark-ignition engine by electromagnetic valve actuator. *SAE Technical Papers* 2019-01-1201. 2019. https://doi.org/10.4271/2019-01-1201

[16] MAMALA, J., ŚMIEJA, M., PRAŻNOWSKI, K. Analysis of the total unit energy consumption of a car with a hybrid drive system in real operating conditions. *Energies*. 2021, **14**(13), 3966. https://doi.org/10.3390/en14133966

[17] ORECCHINI, F., SANTIANGELI, A., ZUCCARI, F. et al. Energy consumption of a last generation full hybrid vehicle compared with a conventional vehicle in real drive conditions. *Energy Procedia*. 2018, **148**, 289-296. https://doi.org/10.1016/j.egypro.2018.08.080

[18] PIELECHA, I., CIEŚLIK, W., SZAŁEK, A. Operation of electric hybrid drive systems in varied driving conditions. *Eksploatacja i Niezawodnosc – Maintenance and Reliability*. 2018, **20**(1), 16-23. https://doi.org/10.17531/ein.2018.1.3

[19] PIELECHA, I., PIELECHA, J. Simulation analysis of electric vehicles energy consumption in driving tests. *Eksploatacja i Niezawodnosc – Maintenance and Reliability*. 2020, **22**(1), 130-137. https://doi.org/10.17531/ein.2020.1.15

[20] PITANUWAT, S., SRIPAKAGORN, A. An investigation of fuel economy potential of hybrid vehicles under real-world driving conditions in Bangkok. *Energy Procedia*. 2015, **79**, 1046-1053. https://doi.org/10.1016/j.egypro.2015.11.607

[21] QIU, S., QIU, L., QIAN, L. et al. Hierarchical energy management control strategies for connected hybrid electric vehicles considering efficiencies feedback. *Simulation Modelling Practice and Theory*. 2019, **90**, 1-15. https://doi.org/10.1016/j.simpat.2018.10.008

[22] SHARER, P., LEYDIER, R., ROUSSEAU, A. Impact of drive cycle aggressiveness and speed on HEVs fuel consumption sensitivity. *SAE Technical Papers* 2007-01-0281. 2007. https://doi.org/10.4271/2007-01-0281

[23] THOMAS, J., HUFF, S., WEST, B. et al. Fuel consumption sensitivity of conventional and hybrid electric light-duty gasoline vehicles to driving style. *SAE International Journal of Fuels and Lubricants*. 2017, **10**(3). https://doi.org/10.4271/2017-01-9379

[24] WANG, H., ZHANG, X., OUYANG, M. Energy consumption of electric vehicles based on real-world driving patterns: A case study of Beijing. *Applied Energy*. 2015, **157**, 710-719. https://doi.org/10.1016/j.apenergy.2015.05.057

[25] WANG, Z., ZHAO, Z., WANG, D. et al. Impact of pilot diesel ignition mode on combustion and emissions characteristics of a diesel/natural gas dual fuel heavy-duty engine. *Fuel*. 2016, **167**, 248-256. https://doi.org/10.1016/j.fuel.2015.11.077

[26] YEO, H., HWANG, S., KIM, H. Regenerative braking algorithm for a hybrid electric vehicle with CVT ratio control. *Proceedings of the Institution of Mechanical Engineers, Part D: Journal of Automobile Engineering*. 2006, **220**(11), 1589-1600. https://doi.org/10.1243/09544070JAUTO304

[27] Mercedes-Benz A250e homologation certificate. 2020.

[28] Mercedes me media. https://www.mercedes-benz.pl/pasengercars mercedes-benz-cars/mercedes-me

Andrzej Bieniek, DEng. – Faculty of Mechanical Engineering, Opole University of Technology.
e-mail: *a.bieniek@po.edu.pl*

Prof. Jarosław Mamala, DSc., DEng. – Faculty of Mechanical Engineering, Opole University of Technology.
e-mail: *j.mamala@po.edu.pl*

Mariusz Graba, DEng. – Faculty of Mechanical Engineering, Opole University of Technology.
e-mail: *m.graba@po.edu.pl*

Krzysztof Prażnowski, DEng.– Faculty of Mechanical Engineering, Opole University of Technology.
e-mail: *k.praznowski@po.edu.pl*

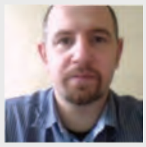

Krystian Hennek, MEng. – PhD student in the Faculty of Mechanical Engineering, Opole University of Technology.
e-mail: *k.hennek@po.edu.pl*

Article citation info:
RACZYŃSKI, R., SIADKOWSKA, K., ŚCISŁOWSKI, K. et al. An assessment of the transient effect on helicopter main rotor stability and power demand. *Combustion Engines*. 2022, **191**(4), 23-28. https://doi.org/10.19206/CE-146695

Radosław RACZYŃSKI
Ksenia SIADKOWSKA
Karol ŚCISŁOWSKI
Mirosław WENDEKER

Combustion Engines
Polish Scientific Society of Combustion Engines

An assessment of the transient effect on helicopter main rotor stability and power demand

ARTICLE INFO

Received: 6 December 2021
Revised: 5 January 2021
Accepted: 14 February 2022
Available online: 5 March 2022

The researched object is a helicopter main rotor with blades of variable geometric twist characteristics. Variable torsion refers to systems of actuators made of shape memory alloys. The presented numerical analyses allow for evaluating both the dynamics of the rotor in transient states, i.e. in the zone between the static phase and the full activation phase and the impact of the change on the pulsation of the amplitude of the necessary power generated by the rotor corresponding the flight state, and thus covering the demand by the disposable power generated by the engine. This study follows a methodology of numerical analyses based on Multi Body Dynamics and the Finite Element Method and uses fluid mechanics elements and algorithms to analyze lift generation, compiled in a single computational environment referring to the same period of time.

Key words: *propulsion, rotor, power demand, helicopter, transient effect*

1. Introduction

The problem of high exhaust emissions [9, 10] and energy requirements in aviation [13, 19] have been recently globally studied by researchers. Propulsion systems of light rotorcraft are usually internal combustion engines or electric motors [9, 21, 22]. The application of piston internal combustion engines for aircraft propulsion is associated with the problem of decreasing engine power as a result of increasing flight altitude [4]. The engine powering the aircraft must provide sufficient power supply to allow for flight and operation of on-board instrumentation. There are many ways to reduce power consumption [1]. These include the use of alternative fuels [3, 15] or another type of propulsion [5]. Safety considerations play a critical role. Most of essential systems in aircraft are redundant in nature [7].

As new technology and materials are developed, opportunities to reduce power requirements in certain flight states and to increase aircraft range and performance are emerging. Hybrid solutions combining beneficial features of different types of aircraft are known. An example of such objects are gyrocopters which, by combining the phenomenon of auto-rotation with the electric power supply of multi-rotorcraft, enable the optimization of the use of the power in flight [6]. There are also known modifications that give aircraft the possibility of vertical take-off and landing [17]. An interesting issue is also the use of modern construction materials, and more specifically intelligent materials such as shape memory alloys. They make it possible to change geometrical properties of the aircraft. As this is a relatively new issue, it requires a number of studies in aviation.

Shape memory alloys allow interaction with the shape of the aircraft during flight [2, 13], but also give the possibility to control the geometry of the main rotor blade [8, 12]. The application of shape memory materials to aircraft is itself already a complicated task. It is mainly related to the difficulty of controlling the parameters of material phase transitions and the low repeatability of their operation. Therefore, numerous investigations are carried out in order to better understand the phenomena occurring in smart materials and their influence on the aircraft [18, 20]. The use of any elements that change the geometry of the blade of the main rotor during its operation leads to the occurrence of a transient state. This situation affects the stability of rotor operation. The power required by the aircraft also changes. The purpose of such modifications is to optimize the operation of the main rotor by minimizing drag and generating the maximum lifting force in the various phases of flight [23].

The application of systems that change the geometry of the aircraft or main rotor blades influences the propulsion unit as well. By reducing the power requirement, it is possible to use an engine with less power and weight, which affects the payload capacity of the aircraft. The energy cost resulting from the use of shape memory materials is the need to power them. This is done by applying voltage or temperature changes [14, 24]. The aim of research is obviously to apply the technology in such a way that energy consumption in flight is reduced and performance is improved, which will have a positive effect on fuel consumption.

This paper discusses an evaluation of the influence of the transient state on the stability of the rotor operation. Numerical analyses of the phenomena that occur between the static phase and the full activation phase of the shape memory alloy actuator applied to the main rotor blade of a helicopter with a maximum take-off mass of 150 kg have been performed and described.

2. Methodology

Here, a methodology involving numerical analyses based on Multi Body Dynamics and the Finite Element Method was applied. The adopted methodology is based on the strategy of composite analyses using integrated MBD + FEM models as well as analyses related to typical fluid mechanics including algorithms of the blade element method and vortex theory. The application of such a combination of algorithms in analysis will allow a realistic assessment of the stability of the rotor in the form of structural dynamics and will also make it possible to assess its impact on the values of rotor thrust force T, side forces S as well as power demand and its harmonic components. The methodology to specify aerodynamic loads is based on algorithms of the Blade Element Method (Fig. 1), while inertial loads are specified from a coupled Multi Body Dynamic model (Fig. 2) in which rigid elements are replaced by susceptible ones in such a way as to reproduce the hub center motion and thus to take into account dynamic features of the rotor.

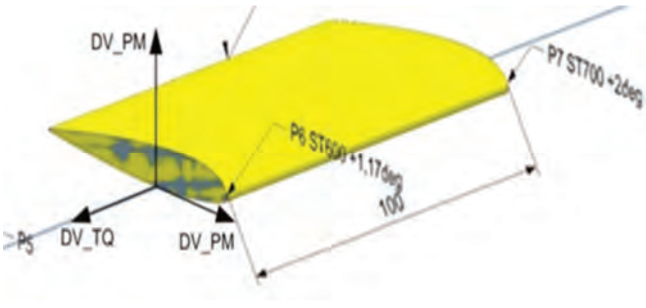

Fig. 1. Profile section intended for the determination of aerodynamic loads

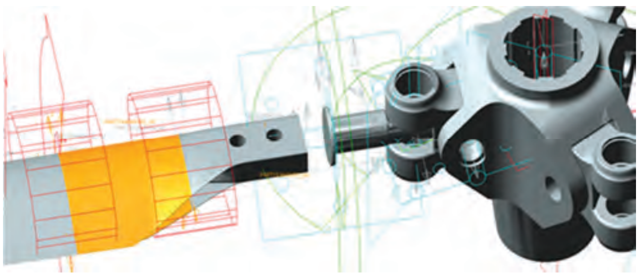

Fig. 2. The inertial system of the MBD model

The integrating element of the calculation process is the MATLAB/ Simulink software environment which controls the process and time step of the calculation (Fig. 3).

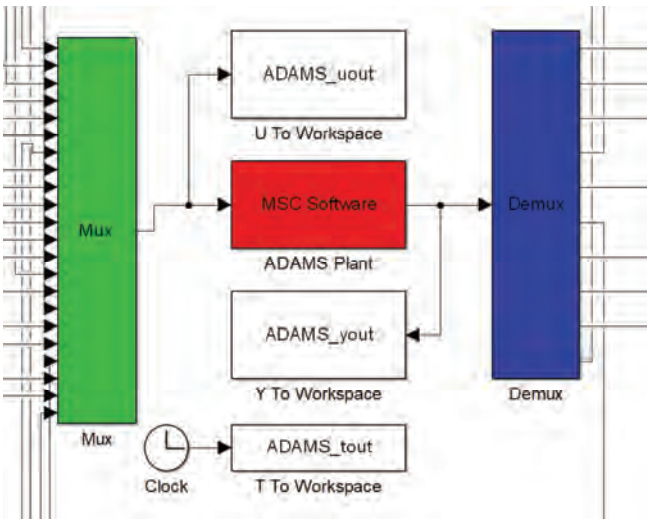

Fig. 3. Matlab/Symulink software integrator diagram

3. Research object

The researched object is a helicopter main rotor equipped with blades of variable geometric twist characteristics. The idea of variable twist is based on actuator systems made of shape memory alloys. The blade geometrical twist line is changed by deforming (twisting) the blade on its certain section to obtain a two-phase characteristic of the rotor, characterized by different performance properties that are more optimal for different flight conditions. An important research issue of such a system is the response of the rotor in transition states between the static phase in which the blade retains its original shape and the phase that results from the deformation of the geometric twist line due to the torsional moment load. The calculation model enables the evaluation of selected load components such as torque Q, rotor thrust force T and side force S.

The characteristic feature of the adopted system of SMA actuators is the dynamics of the process and the rate of shape change which assumes the 10–15 second process of changing the geometry. Compared to actuators based on piezoelectric systems, this period is many times longer, but the cost of adaptation of the actuator is much lower.

The transition time is crucial for rotor stability and thus safety. The expected time of the transition phase depends on the mechanical properties of alloys themselves, the adopted philosophy of providing the required thermal energy and thermal losses associated with this process.

The basis of this methodology is the assessment of rotor efficiency for particular configurations:

- a reference blade, i.e. a blade not activated SMA actuators,
- a blade with a theoretical linear geometric twist,
- a blade with a real twist with non-linear characteristics resulting from activation of the operating elements.
- Figure 4 shows a visualization of the geometric blade twist curves which will be numerically analyzed.

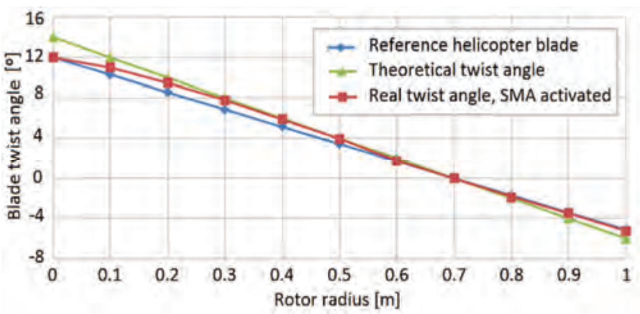

Fig. 4. Geometric blade twist angle

The rotor thrust was analysed for the reference and steady-state twist curves for which the SMA actuators were activated (Fig. 5).

The environment that integrates the analyses and controls the common computational time base is MATLAB/ Simulink using the MBD model integration function. Figure 6 shows a visualization of the base model which undergoes complex analysis.

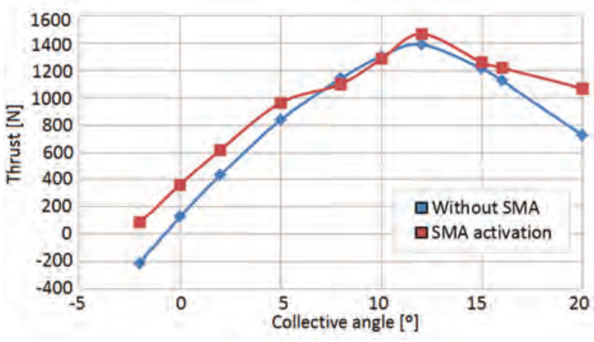

Fig. 5. Rotor thrust

Fig. 6. Visualisation of the MBD main rotor base model

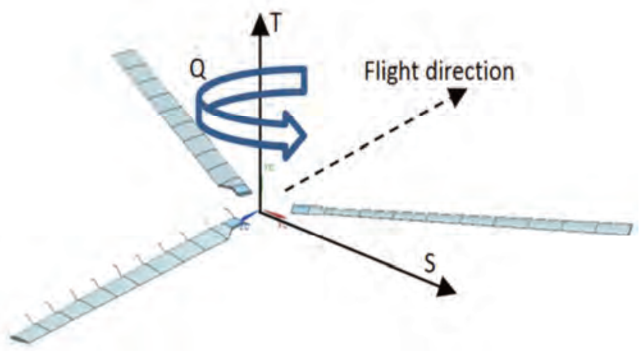

Fig. 7. Visualisation of the load distribution, T – thrust force, Q – propulsion torque, S – side force

The computational model assumes the simplification of rotor blade representation by dividing it into 10 computational sections (Fig. 8), connected by elastic elements with well-defined mass-rigidity properties and well-defined position of the center of gravity in relation to the twist axis. Aerodynamic and inertial loads are applied to the center of gravity of each section, which means that the aerodynamic centers of each section lie on the blade's twist axis.

Fig. 8. Blade division into calculation sections

According to the adopted concept, the actuators are activated between sections 8 and 7, and the actuators are an integral part of the blade and located as near as possible the twist axis. The course of the total twist angle change in the steady state during flight is shown in Fig. 9.

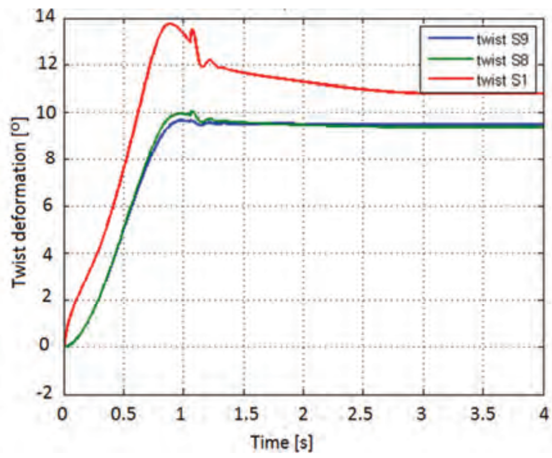

Fig. 9. SMA actuator activation time course

Besides the inertial forces loading the rotor, the main component of forces and moments are aerodynamic loads, determined by CFD analyses both for the individual sections (Fig. 10) and for the whole rotor disc (Fig. 11).

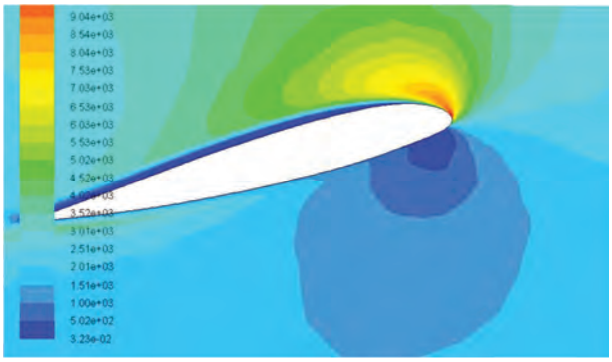

Fig. 10. Results of the CFD analysis of the blade profile section

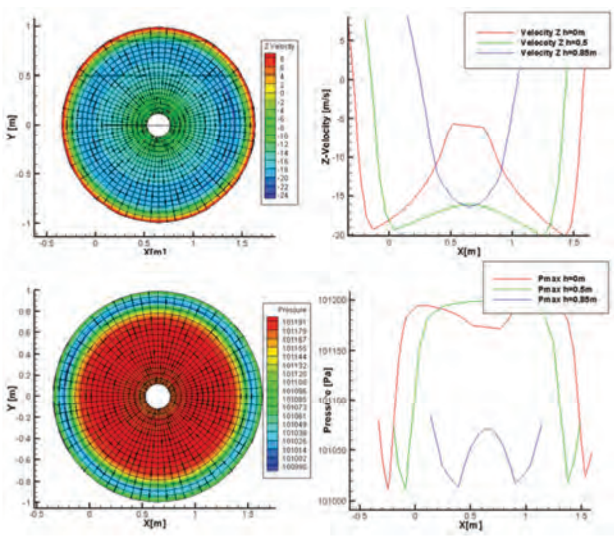

Fig. 11. Rotor disc loads

3.1. Analysis

The analysis covers the assembly of the main rotor loaded with aerodynamic and inertial forces in the steady state, i.e. hovering, and in the transient state when the SMA systems are activated. The analysis consists in comparing the rotational speed pulsations and the power demand necessary during take-off and transition to hovering before and during activation of the actuators. Figure 12 shows a visualization of the rotor start-up and transition to the hovering state.

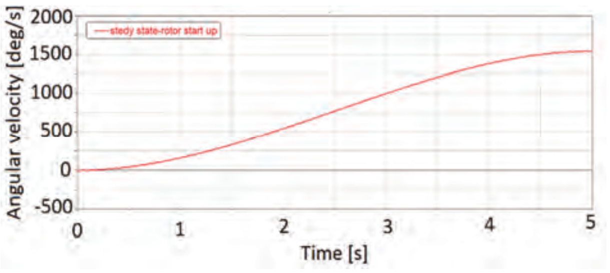

Fig. 12. Rotor speed course during start-up

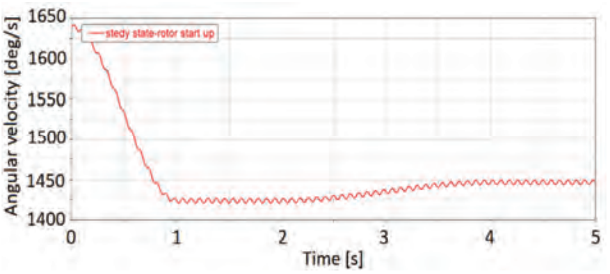

Fig. 13. Rotor lock and hover

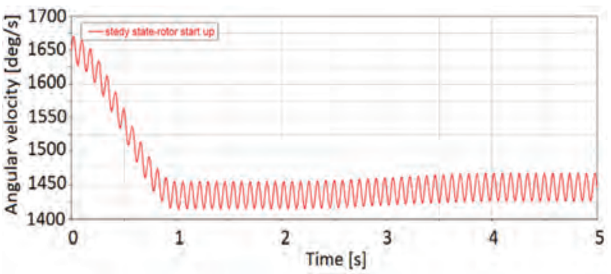

Fig. 14. Rotor lock and hover with SMA activation

The numerical analyses are limited to the transient states of the rotor start-up and transition to hovering. The comparison of the computational cases is limited to the states the SMA actuators are not activated and the case they are fully activated. All analyses were based on standard conditions, i.e. barometric operational altitude hb = 0 m, ambient temperature compatible with the standard atmosphere OAT = 15ºC.

4. Results

The aim of the analyses was to determine the conditions of power demand in states defined as non-stationary. The research enabled us to specify the main components of the power required by the rotor as well as the values of the lateral forces perpendicular to the longitudinal axis of the pylon system of the rotor assembly, bending the shaft at the moment of lock and the transition of the rotor to hovering (Fig. 15–20). The values and harmonics of the transverse forces determine the stability of the rotor precession axis, while the values of power pulsations are responsible for the assessment of the aerodynamic efficiency of the rotor.

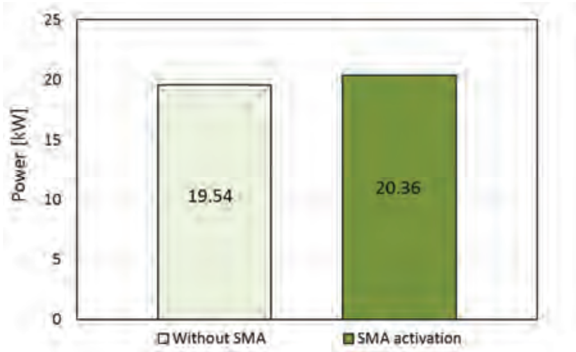

Fig. 15. Average power required for hovering

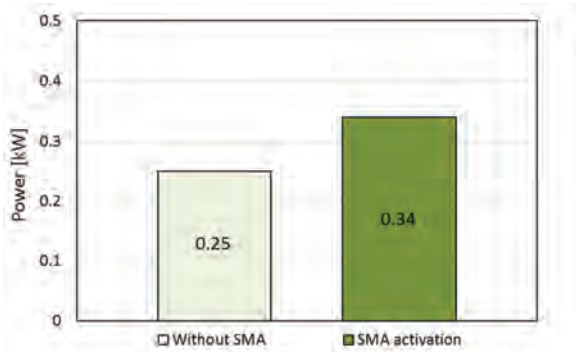

Fig. 16. Harmonics of the power required for hovering – I h power pulsation

Fig. 17. Harmonics of the power required for hovering – II h power pulsation

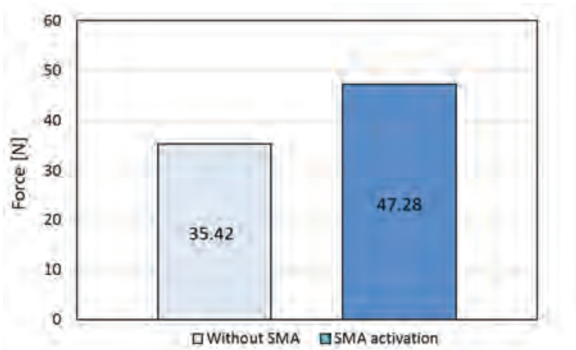

Fig. 18. Average force pulsation – side forces

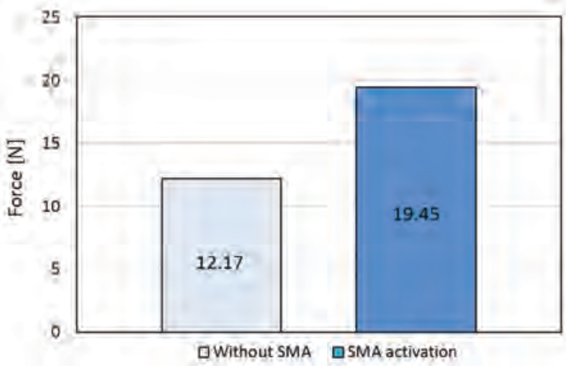

Fig. 19. Harmonics of the side forces – I h force pulsation

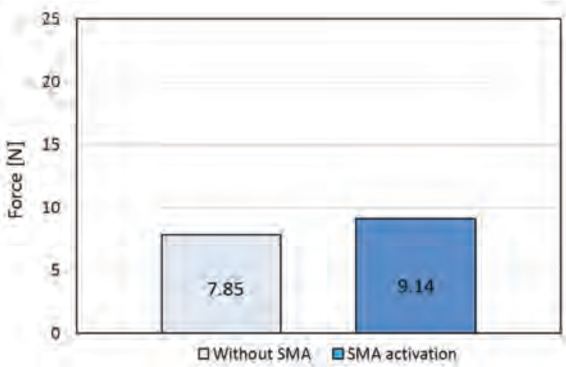

Fig. 20. Harmonics of the side forces – II h force pulsation

The key parameter affecting the safety of the structure is the time of the non-stationary state i.e. the time when the blade (rotor) changes its geometric features. The use of shape memory materials enables a geometric twist to be changed in a relatively long time compared to other active materials. The assumed full cycle of change defined as 10 s when the rotor was in a transient state showed no danger of losing stability but an increase in the harmonic components of the side force and propulsion torque values.

The correct selection of the main rotor construction parameters such as joint spacing, oscillation compensator, oscillation and deflection coefficients and Lock's number ensures structural stability and stops the uncontrolled growth of particularly non-harmonic loads which indicate a loss of stability and may lead to the occurrence of flatter and divergence phenomena. The phenomenon of instability itself, i.e. flatter and divergence was not analyzed. An example of incorrectly selected rotor design features is shown in the dynamic angle diagram below (Fig. 21).

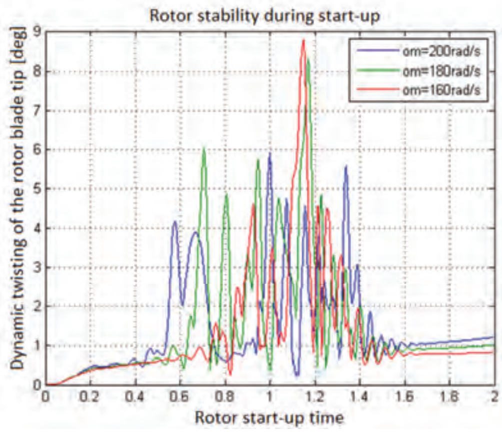

Fig. 21. Dynamic twist angle for the case of a rotor stability loss

5. Conclusions

The obtained results show that the application of active control systems of geometric features of the rotor does not significantly affect the stability of the rotor in transient states, i.e. between the state in which the actuators were not activated and the state of their full activation.

The parameters affecting the evaluation and selection of the propulsion unit were also analyzed to ensure a smooth regulation of the fuel flow to stabilize the fluctuations of the power required. The above results indicate that the selection of the drive unit, apart from a constant value, must take into account the pulsation values for both I h of rotation (25Hz) and III h (75Hz) while maintaining the torsional stability of the drive system.

Acknowledgements

This work has been financed by the National Centre for Research and Development under the LIDER program. Grant Agreement No. LIDER/45/0177/L-9/17/NCBR/2018.

Nomenclature

AoA	angle of atack	OAT	outside air temperature in Celsius degrees
FEM	finite element method	PCA	pitch control axis
MBD	multi body dynamics	SMA	shape memory alloys

Bibliography

[1] ALQAHTANI, A., SHOKROLLAHIHASSANBAROUGH, F., WYSZYNSKI, M.L. Thermodynamic simulation comparison of AVL BOOST and Ricardo WAVE for HCCI and SI engines optimisation. *Combustion Engines*. 2015, **161**(2), 68-72. https://doi.org/10.19206/CE-116893

[2] AMEDURI, S., CONCILIO, A. Morphing wings review: aims, challenges, and current open issues of a technology. *Proceedings of the Institution of Mechanical Engineers, Part C: Journal of Mechanical Engineering Science*. 2020. https://doi.org/10.1177/0954406220944423

[3] BAYRAMOĞLU, K., YILMAZ, S. Emission and performance estimation in hydrogen injection strategies on diesel engines. *International Journal of Hydrogen Energy*. 2021, **46**(57), 29732-29744. https://doi.org/10.1016/j.ijhydene.2020.08.135

[4] CARLUCCI, A.P., FICARELLA, A., LAFORGIA, D. et al. Supercharging system behavior for high altitude operation of an aircraft 2-stroke Diesel engine. *Energy Conversion and Management*. 2015, **101**, 470-480. https://doi.org/10.1016/j.enconman.2015.06.009

[5] CARLUCCI, A.P., FICARELLA, A., TRULLO, G. Performance optimization of a two-stroke supercharged diesel engine for aircraft propulsion. *Energy Conversion and Management*. 2016, **122**, 279-289. https://doi.org/10.1016/j.enconman.2016.05.077

[6] CZYŻ, Z., SIADKOWSKA, K. Measurement of air flow velocity around the unmanned rotorcraft. *2020 IEEE 7th International Workshop on Metrology for AeroSpace (MetroAeroSpace),* Pisa. 2020, 625-629. https://doi.org/10.1109/MetroAeroSpace48742.2020.9160062

[7] DOPONA, M., FOXHALL, N., DUTZLER, C. 912iS fuel injected aircraft engine. *SAE Technical Paper* 2012-32-0049. 2012. https://doi.org/10.4271/2012-32-0049

[8] FORTINI, A., SUMAN, A., MERLIN, M. et al. Morphing blades with embedded SMA strips: an experimental investigation. *Materials and Design*. 2015, **85**, 785-795. https://doi.org/10.1016/j.matdes.2015.07.175

[9] KALWARA, M., KUŹNIAR, M., ORKISZ, M. A rotating piston engine with electric generator in serial hybrid propulsion system for use in light aircraft. *Combustion Engines*. 2021, **187**(4), 42-45. https://doi:10.19206/CE-141353

[10] KARDACH, M., GALANT, M., FUĆ, P. Analysis of the ecological effectiveness of passenger transport by jets of various sizes. *Combustion Engines*. 2019, **178**(3), 252-256. https://doi:10.19206/CE-2019-344

[11] KOZAK, M., MERKISZ, J., BIELACZYC, P. The effect of fuel properties on exhaust emissions from diesel passenger car. *Silniki Spalinowe*. 2005, **1**(120), 19-30. https://doi.org/10.19206/CE-117408

[12] LACHENAL, X., DAYNES, S., WEAVER, P.M. Review of morphing concepts and materials for wind turbine blade applications. *Wind Energy*. 2013, **16**, 283-307. https://doi.org/10.1002/we.531

[13] ORKISZ, M., KUŹNIAR, M. 3E – a new paradigm for the development of civil aviation. *Combustion Engines*. 2020, **181**(2), 3-10. https://doi:10.19206/CE-2020-201

[14] PANKONIEN, A.M. Smart material wing morphing for unmanned aerial vehicles. University of Michigan. 2015. https://deepblue.lib.umich.edu/handle/2027.42/111533

[15] PRAJIT, R., SRIVATSAN, S., SATHWIK, V. Smart materials – a view towards SMA. *SAE Technical Paper* 2014-28-0045. 2014. https://doi.org/10.4271/2014-28-0045

[16] ROY, M.M., TOMITA, E., KAWAHARA, N. et al. An experimental investigation on engine performance and emissions of a supercharged H2-diesel dual-fuel engine. *International Journal of Hydrogen Energy*. 2010, **35**, 844-853. https://doi.org/10.1016/j.ijhydene.2009.11.009

[17] SAEED, A.S., YOUNES, A.B., ISLAM, S. et al. A review on the platform design, dynamic modeling and control of hybrid UAVs. *International Conference on Unmanned Aircraft Systems.* ICUAS, 2015, 806-815. https://doi.org/10.1109/ICUAS.2015.7152365

[18] SARKAR, P., RACZYNSKI, R. Gurney flap force calculations. In: Doerffer, P., Barako,s G.N., Luczak M.M. (Eds.) *Recent Progress in Flow Control for Practical Flows*. Springer. 2017, 126-135. https://doi.org/10.1007/978-3-319-50568-8

[19] SEHRA, A.K., WHITLOW, W. Propulsion and power for 21st century aviation. *Progress in Aerospace Sciences*. 2004, **40**(4-5), 199-235. https://doi.org/10.1016/j.paerosci.2004.06.003

[20] SIADKOWSKA, K. Aerodynamic measurement of the rotor blade for aviation application. *2020 IEEE 7th International Workshop on Metrology for AeroSpace (MetroAeroSpace).* Pisa, 2020, 610-614. https://doi.org/10.1109/MetroAeroSpace48742.2020.9160131

[21] SIADKOWSKA, K., CZAJKA, B., ŚCISŁOWSKI, K. et al. Analysis of propulsion units dedicated to test stands for aviation systems. *Combustion Engines*. 2021, **185**(2), 39-43. https://doi.org/10.19206/CE-139405

[22] SIADKOWSKA, K., MAJCZAK, A., BARAŃSKI, G. Studying a construction of pistons for the aircraft CI engine. *Combustion Engines*. 2017, **168**(1), 161-167. https://doi.org/10.19206/CE-2017-126

[23] SIADKOWSKA, K., RACZYNSKI, R., WENDEKER, M. Numerical analysis of the rotor in the co-simulation methodology. *IOP Conference Series: Materials Science and Engineering.* 2019, **710**(012009). https://doi.org/10.1088/1757-899X/710/1/012009

[24] SOFLA, A.Y.N., MEGUID, S.A., TAN, K.T. et al. Shape morphing of aircraft wing: status and challenges. *Materials and Design*. 2009, **31**, 1284-1292. https://doi.org/10.1016/j.matdes.2009.09.011

Radosław Raczyński, MEng. – Faculty of Mechanical Engineering, Lublin University of Technology.
e-mail: *raczynski_r@wp.pl*

Ksenia Siadkowska, MEng. – Faculty of Mechanical Engineering, Lublin University of Technology.
e-mail: *k.siadkowska@pollub.pl*

Karol Ścisłowski, MEng. – Faculty of Mechanical Engineering, Lublin University of Technology.
e-mail: *k.scislowski@pollub.pl*

Prof. Mirosław Wendeker, DSc., DEng. – Faculty of Mechanical Engineering, Lublin University of Technology.
e-mail: *m.wendeker@pollub.pl*

Article citation info:
MARSZALEK. N., LIS, T. The future of sustainable aviation fuels. *Combustion Engines*. 2022, **191**(4), 29-40.
https://doi.org/10.19206/CE-146696

Natalia MARSZALEK
Tomasz LIS

Combustion Engines
Polish Scientific Society of Combustion Engines

The future of sustainable aviation fuels

ARTICLE INFO

Received: 24 November 2021
Revised: 20 January 2022
Accepted: 14 February 2022
Available online: 13 March 2022

Presented work has an overview character and is focused on perspectives of sustainable aviation fuels application in civil aviation sector. The mean role of SAF application is to ensure reduction of greenhouse gas emissions and aviation footprint on environment. Paper describe the combustion proces of hydrocarbon fuels and problem related to the emission of carbon dioxide to the atmosphere. Fuel consumption, CO_2 emission and SAF production data was presented on the graphs. The sustainalbe aviation fuel has been characterized. Certified conversion technologies with potential feedstock used for SAF production was described. Literature studies indicate that sustainable aviation fuel is successfully used in air transport.

Key words: *sustainable aviation fuel, kerosene, emissions, carbon dioxide, renewable feedstock*

1. Introduction

Civil aviation is a dynamically developing sector, that is responsible for approximately 2.5% of global greenhouse gas emissions and before pandemic, their amount were constantly grow. Modern aircrafts used nowadays, emit about 80% less carbon dioxide per seat kilometer than they did 50 years ago [6]. Over the years, significant development took place in most areas of aviation sector. New lighter materials were implemented in aircraft and engine construction, aircraft aerodynamics was significantly improved, as well as attention has been paid on optimization of flight routes. More fuel-efficient turbofan or turboprop engines were introduced to the aviation fleet [42]. All taken activities lead to the one main goal – to reduction of anthropogenic CO_2 emissions [20]. Despite numerous actions, the main feature that still remain unchangeable is aviation fuel based on fossil feedstock. Generated by the aircraft engines emissions are directly related to the fuel burn process [42]. From this reason the type of applied fuel exert a direct impact on emissions level. The amount of fuel burned in aircraft engines is another important factor, because each kilogram of fuel that is not used, allow to reduce the emission of carbon dioxide by 3.16 kilograms [42].

An entire aircraft participation in CO_2 emission is about 2% in comparison to total global emissions [61]. This numbers indicate for relatively small contribution to global anthropogenic CO_2 emissions, however in case of aviation it should be taken into account that this emissions took place in upper layers of atmosphere (troposphere and lower stratosphere).

Aviation decarbonization is an unavoidable procedure that lead to development and implementation of new type of fuel, that ensure sustainability. For aviation industry, alternative fuels present opportunity to minimalize harmful emissions. A good near-term options are sustainable aviation fuels (SAF), which are non-fossil fuels, produced from variable feedstock [17]. Sustainability means that raw material used for SAF production cannot compete with food production or water resources and cannot degrade the natural environment [26].

The main properties of sustainable aviation fuel are ability to reduction of greenhouse gas emissions, compatibility with conventional aviation fuel, sustainability, clean burning process and renewable resources [23]. The amount of carbon dioxide absorbed by plants during photosynthesis is roughly equivalent to the amount of CO_2 produced by fuel burning in combustion engine. This feature allow SAF to be specified as carbon neutral over the life cycle [31].

The SAF production process (Fig.1) is also a source of contamination, therefore researches are carried out on development new conversion technologies, allowing for the CO_2 reduction at the production level and to meet the costs targets. Properties of SAF caused that it has the ability to significantly reduction of CO_2 emissions over the whole fuel life cycle. Application of such kind of fuel enable the reduction of carbon dioxide emission by 80% (over the fuel life cycle) compared to kerosene [2, 31].

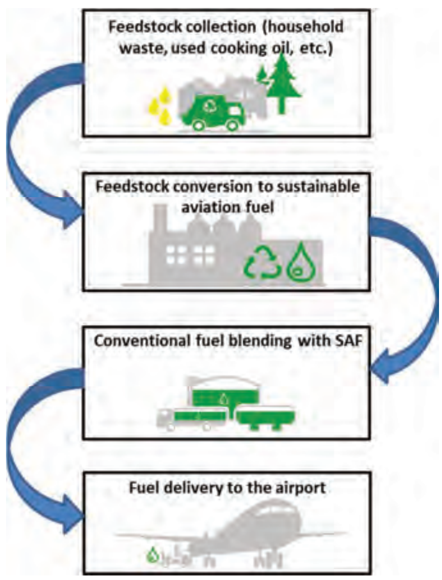

Fig. 1. Sustainable fuel production process [15]

The other advantage of sustainable aviation fuel is the low aromatic content which cause the reduction of soot formation and aerosol emission by 50 to 70% [24]. Taking into account that airlines industry and other transport sectors are dependent on the fossil fuels sources and changing prices of crude oil, SAF production would contribute to increasing the world-wide energy security.

In a recent years a lot of attention has been paid to reduction of carbon dioxide emission, due to its harmful effect on environment, local air quality and human health. Due to the fact that aviation industry work towards the systematical reduction of CO_2 emissions, two key goals have been formulated to achieve [7]:

– carbon-neutral growth: from 2020 net carbon emission, what means that the grow of flights will don't cause the grow in greenhouse gas emissions,
– 50% reduction in CO_2 emissions up to 2050 year from the level in 2005 year. In accordance with this target, 915 million tons of CO_2 emitted in 2019 year (Fig. 3) should be reduced to 325 million tons in 2050.

Commercial aircrafts release about 750 million tons of pollutants every year [9].

Presented on Fig. 2 statistical data [29] show the continuous growth of fuel consumption by commercial airlines. In 2019 the fuel consumption reach the level of 436 billion liters. Forecast for 2020 year expected further growth of fuel consumption however due to the COVID-19 pandemic, the fuel consumption drastically dropped to 236 billion liters due to the suspension of significant number of flights. Forecast for 2021 show a slight increase in fuel consumption compared to the previous year.

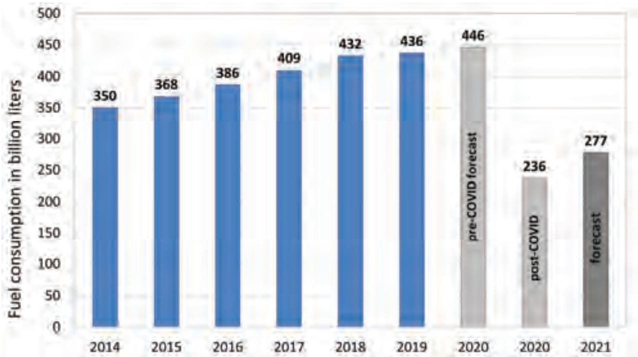

Fig. 2. Total fuel consumption of global commercial airlines [29, 57]

An increase in fuel consumption is accompanied by an increase in CO_2 emission, which is presented on Fig. 2. For 2019 the CO_2 emission reach the value of 915 million tones. The prediction made for 2020 year indicate the grow of emission up to 936 million tones, however the suspension of flights significantly reduce this value to 495 million tones.

Covid-19 pandemic drastically reduce the number of flights and at the same time emission of carbon dioxide (see Fig. 3). It is estimated that fuel consumption and CO_2 emissions will increase in coming decades as the demand for air transport. This trend will not be stopped by the decline in CO_2 per revenue passenger kilometer (RPK), caused by technological improvement [36].

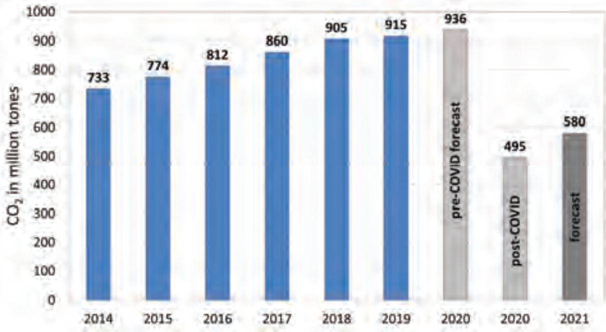

Fig. 3. CO_2 emission generated by the global commercial airlines [29, 56]

2. Combustion of hydrocarbon fuels and emission problem

A typical civil aviation fuel, used globally in turbines engines, is a JetA-1 (also called JP-1A) fuel, based on kerosene for which the mean C/H ratio is $C_{12}H_{23}$ [38]. At 20°C and under the pressure 1013 hPa, the JetA-1 appearance in liquid state, is transparent and characterized by low-viscosity. The flash point of JetA-1 is higher than 38°C and the freezing point below –47°C [50].

Aviation fuel is blended with a small amount of additives. Additives pay a different role, for example are used to prevent fuel igniting in uncontrolled manner or prevent fuel freezing. Jet fuels are subject to demanding international quality standards [50].

2.1. Hydrocarbon fuels burning process

Complete combustion of hydrocarbon fuel require sufficient amount of air to convert the fuel completely to carbon dioxide (CO_2) and water vapor (H_2O). The stoichiometric air-fuel-ratio can be calculated from the reaction equation (1) which for general hydrocarbon fuel of average molecular composition C_aH_b, takes the form [19]:

$$C_aH_b + \left(a + \frac{b}{4}\right)(O_2 + 3.773N_2) = aCO_2 + \frac{b}{2}H_2O + \\ +3.773\left(a + \frac{b}{4}\right)N_2 \quad (1)$$

The stoichiometric air-fuel-ratio [19]:

$$AFR = \frac{\left(a+\frac{b}{4}\right)(O_2+3.773N_2)}{C_aH_b} \quad (2)$$

The aviation fuel is a mixture of hydrocarbons. For Jet A-1 fuel based on kerosene, the number of carbon range between 8 to 16 [40]. For kerosene described by $C_{12}H_{23}$ chemical formula [39], relation (1) takes forms:

$$C_{12}H_{23} + 17.75\ O_2 + 66.97\ N_2 = \\ = 12\ CO_2 + 11.5\ H_2O + 66.97\ N_2 \quad (3)$$

The stoichiometric air fuel ratio (AFR) depends on the fuel composition [19] and for analyzed case, based on the equation (2) is 14.63. For each type of fuel the AFR will have a different value.

In modern turbine engines, during the combustion of 1 kg of aviation kerosene in 3.4 kg of oxygen are generated compounds such as [58]:

– 3.16 kg of CO_2,
– 1.29 kg of H_2O,
– less than 0.6 g of CO,

– less than 15 g of NO_x,
– less than 0.8 g of SO_2,
– less than 0.01 g of UHC,
– 0.01 to 0.03 g of soot.

The amount of carbon dioxide in exhaust gases can be calculated from stoichiometric relationship (3). The combustion reaction can be write as follows:

$$167 \text{ kg } C_{12}H_{23} + 568 \text{ kg } O_2 + 1875.16 \text{ kg } N_2 = \\ = 528 \text{ kg } CO_2 + 207 \text{ kg } H_2O + 1875.16 \text{ kg } N_2 \quad (4)$$

Assuming that 167 kg of $C_{12}H_{23}$ fuel produces 528 kg of CO_2, it can be written that:

$$1 \text{ kg } C_{12}H_{23} = 528/167 \text{ kg } CO_2 \quad (5)$$

Summarizing the above calculations, 1 kg of burned fuel produces about 3.16 kg of carbon dioxide.

Stoichiometric mixture contain sufficient amount of oxygen for complete combustion but the combustion process can also take place when there is excess (fuel rich) or deficiency of the oxygen (fuel lean). The deficiency of the oxygen result in incomplete combustion because there is insufficient amount of oxygen to fully oxidize the fuel ingredients carbon (C) and hydrogen (H) to CO_2 and H_2O. During incomplete combustion are formed such components as carbon monoxide (CO) and unburned hydrocarbons (UHC) [53]. In general the combustion process in gas turbines continues with the excess of air, thus the exhaust gases consist primarily of such combustion product as CO_2, H_2O, O_2 and N_2 [52].

The content of carbon dioxide in the exhaust gases generated by the aircraft engines comprises about 70% while the water vapor about 30%. Less than 1% of exhaust fumes consist of nitrogen oxides (NO_x), oxides of sulfur oxide (SO_x), carbon monoxide (CO), partially burned or unburned hydrocarbons (UHC), particulate matter (PM) generally called soot and other trace compounds. The source of 'aviation emissions' are not only aircrafts but also ground support equipment (GSE), auxiliary power units (APU) and other included in the airport service [20].

Emissions from aircraft engines exert the impact on the climate and local air quality, which in turn translates into people's health. The main emitted greenhouse gases (GHG) are CO_2 and H_2O.

The soot is an aerosol whereas SO_x, NO_x and hydrocarbons contributes to aerosol production after emission. Emission of water vapor in connection with aerosol lead to condensation trail formation [36].

NO_x from turbine engines operate like a catalyst in the oxidation process of CO, CH_4 and other hydrocarbon compounds. NO_x is not classified as a greenhouse gas but it change the concentration of two main GHG's, ozone (O_3) and methane (CH_4), through complex photochemical processes. Ozone increase at cruise altitude conduct to a positive Radiative Forcing (RF). Nitrogen oxide cause also increase of hydroxyl radical (OH), which react with CH_4 and in this way reduce its concentration and result in negative RF [36].

Carbon dioxide is long-lived greenhouse gas. Its atmospheric residence time is about 100 years [16]. The value of emission index (EI) for CO_2 is defined as 3160 ±60 g of CO_2 per 1 kg of jet fuel for complete combustion [38]. The residence time for N_2O is about 114 years while for H_2O about 9 days [16].

3. Sustainable aviation fuel

The SAF term describe the nonconventional aviation fuel [16]. Its chemical and physical properties are similar to the properties of conventional jet fuel (fossil fuel) used in turbine engines. This type of fuel can be directly added to regular jet fuel and safely mixed with them to varying proportions (Table 1). Application of such kind of non-conventional fuel do not require engines or airport infrastructure modification. Fuels with such properties are also named drop-in fuels. This feature of drop-in-fuel is very important for aviation industry, because do not require new infrastructure implementation which is associated with additional costs. In addition new fuel implementation require developing new safety and operational procedures [31].

3.1. Feedstock

Sustainable aviation fuel can be produce from a wide range of available feedstocks.

As the most common and cheapest feedstock for SAF production are considered waste oils (used cooking oil, animal fats, other fatty acids) [49]. Based on this feedstock the sustainable fuel is produced through the HEFA conversion process and can be blend with traditional aviation fuel up to 50% by volume (Table 1). Neste company is able to process about approximately 1 million tonnes of waste oils per year.

The production cost for HEFA fuel was set at €0.88 per liter, which is twice the cost of production of conventional aviation fuel based on kerosene [49].

Used cooking oil (UCO) can be received from commercial sources like restaurants and some households. In the European Union (EU) almost all recovered UCO is used for biofuel production [49]. Actually, 62% of UCO used for biofuel production in EU is imported. Three quarters of imported feedstock come from Asia. It has been estimated that collection of UCO from household would contribute to increase the availability to this raw material by 11% [49].

The animals fats (beef tallow, pork lard, chicken fat) are obtained from rendering plants and have application in food product, animal feed and soap processing. Costs of this feedstock are lower than for vegetable oil. Due to the fact that animals fats are used outside the biofuels sector, there is not expected the significant increase in demand of this raw material for SAF production within a decade [49].

The other example of raw material for sustainable fuel production are forestry residues, which with the excess wood can be processed into synthetic fuel through the Fischer-Tropsch process [49]. This feedstock can be also converted into renewable isobutanol and next through the ATJ process to jet fuel [49, 59].

Due to the large supply the municipal solid waste from households and industries can be used as sustainable feedstock for fuel production. This would reduce the emission of carbon dioxide and other gases that are released into atmosphere by municipal waste collected in landfills [10]. As examples can be mentioned products packing, food scraps, paper from newspapers or other articles, cardboard, bottles as well as clothing and furniture [10, 49]. Municipal waste of organic origin generate methane as a results of anaerobic decomposition [49].

Another group as an potential feedstock for SAF production are energy crops, like camelina, jatropha, algae and halophytes.

Camelina belongs to the group of non-food energy crops and is characterized by high lipid oil content (Fig. 4). The average oil content is about 30–40%. Camelina can grow on the infertile soil and is less susceptible to disease as other plants and can be cultivated as rotational crop for wheat and cereals [23]. After oil extraction remains the meal which can be used as animal feed. Energy crops used for sustainable fuel production should not compete with food production. They also should not have a negative impact on the environment and do not contribute to deforestation [23].

Fig. 4. Camelina [10]

The another example of energy crops is Jatropha (Fig. 5), which is inedible plant. This plant that can grow in marginal land which cause that is not compete with food production. Jatropha is characterized by rapid growth even in unfavorable conditions, is resistant to drought and pests. With a small amount of moisture the plant can yield for 40 years [23]. The meal left after oil extraction process is toxic, but due to the fact that contain nitrogen (N), potassium (K) and phosphorus (P), it can be used as organic fertilizer [23].

Fig. 5. Jatropha [10]

Algae (Fig. 6) are attractive raw material for SAF production due to several positive attributes. Algae are characterized by high lipid content, capacity to high absorption of CO_2 and quick growth. Algae do not require soil and water to growth, therefore do not affect the food cultivation [23]. Algae have ability to product large amount of lipids and carbohydrate by using sunlight, waste water and CO_2. The residue of the algae oil extraction is biomass, that can be used as animal feed, for bio-plastic preparing or further processed for energy production (dry biomass). Algae can produce 30 times more harvests per acre than other energy crops [23].

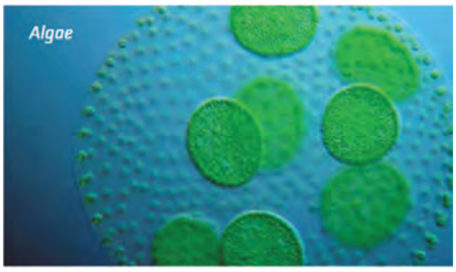

Fig. 6. Algae [10]

Halophytes (Fig. 7) are species of grasses that grow in salty water. Can grow in marshes, lakes, seashores, desert areas and in the sea. Due to the possibility of cultivation in difficult conditions, halophytes will not compete with food production [23].

Fig. 7. Halophytes [10]

3.2. SAF production

The diagram with SAF production data was presented on Fig. 8. The graph present information about SAF production from 2011 to 2019 as well as forecast for 2020 and 2021 year [25]. In present year, the production of SAF should achieve about 80 million litres. The estimated upper limit of production, that indicate the full production possibilities, get approximately 120 million of litres.

The forecast for 2025 year [25] indicate that SAF production will be on the level 3 billion of litres, however it is estimated that the upper production limit may reach approximately 4.5 billion litres [25].

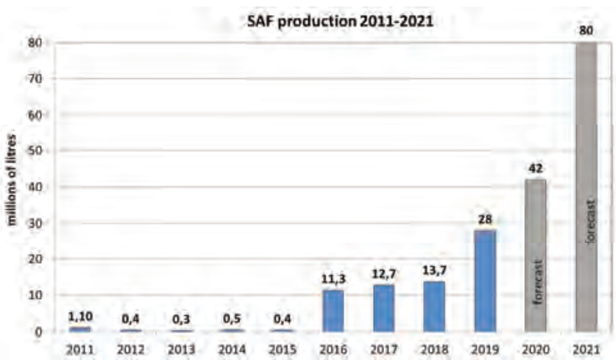

Fig. 8. SAF production data [25]

The quantity of sustainable fuel used by commercial aircraft increase by 65% between 2019 and 2020, despite of the financial losses suffered by the airlines caused by pandemic. The another increase in SAF consumption by 70% is expected in 2021 [8].

Actually there are eight certified SAF conversion technologies [18, 34,41]:

- Fischer-Tropsch hydroprocessed synthesized paraffinic kerosene (FT),
- Synthesized paraffinic kerosene from hydroprocessed esters and fatty acids (HEFA),
- Synthesized iso-paraffins from hydroprocessed fermented sugars (SIP),
- Synthesized kerosene with aromatics derived by alkylation of light aromatic from nonpetroleum sources (FT-SKA),
- Alcohol to jet synthetic paraffinic kerosene (ATJ-SPK),
- Catalytic hydrothermolysis jet fuel (CHJ),
- Synthesized paraffinic kerosene from hydrocarbon-hydroprocessed esters and fatty acids (HC-HEFA-SPK),
- Co-processing Synthetic Crude Oil in Petroleum Refinery.

In progress are three other conversion technologies such as [51]:

- High Freeze Point Hydroprocessed Esters and Fatty Acids Synthetic Kerosene (HFP HEFA-SK or HEFA+),
- Hydro-Deoxidation Synthetic Aromatic Kerosene (HDO-SAK),
- Alcohol-to-Jet Synthetic Kerosene with Aromatics (ATJ-SKA).

The information about the blending ratio (based on the technology pathway) and potential feedstock that can be used in a particular conversion process are listed in the Table 1.

Table 1. SAF conversion processes [34]

Reference documentation	Technology	Blending ratio	Feedstock
ASTM D7566 Annex 1	FT	50%	coal, natural gas, biomass
ASTM D7566 Annex 2	HEFA	50%	bio-oils, animal fat, recycled oils
ASTM D7566 Annex 3	SIP	10%	biomass used for sugar production
ASTM D7566 Annex 4	FT-SKA	50%	coal, natural gas, sawdust, biomass
ASTM D7566 Annex 5	ATJ-SPK	50%	biomass from ethanol or isobutanol production
ASTM D7566 Annex 6	CHJ	50%	triglicerydes such as soybean oil, jatropha oil, camelina oil, carinata oil, tung oil
ASTM D7566 Annex 7	HC-HEFA-SPK	10%	algae
ASTM D1655	Co-processing	5%	fats, oils, greases from petroleum refining

Coal and natural gas presented in Table 1 as a possible feedstock for FT and FT-SKA process, are non-renewable sources of raw material, therefore are not suitable for sustainable fuel production [35].

Fischer-Tropsch Synthetic Paraffinic Kerosene (FT-SPK) process was approved by ASTM in 2009 [52]. The FT conversion technology consists of steps such as biomass gasification, cleaning and conditioning of the produced synthesis gas. The synthesis gas is catalytically converted by the FT process into hydrocarbons such as jet fuel or diesel [18, 35]. Gasification is partial oxidation process that take place at high temperature (700–1500°C). During this process biomass and gasifying medium such as air, oxygen or steam is converted into synthesis gas, primarily consisting of CO, CH_4 and H_2 (hydrogen). After gasification syngas is prepared for catalytic conversion by cleaning and conditioning. Syngas consist also of CO_2, a range of higher hydrocarbon chains (tars) and other pollutants as hydrogen sulfide (H_2S) and particulate matter. The main objective of syngas cleaning is removal of tar, particular matter and chemical element such as S (sulfur), N (nitrogen), Cl (chlorine) [18].

The gas conditioning process is carried out to optimize gas quality before the catalytic synthesis of the syngas, which lead to the desired final product. In FT synthesis process, the CO and H_2 gases react in the attendance of the catalyst to create liquid hydrocarbons [18].

The fuels produced through the Fischer Tropsch pathway, named FT fuels, are characterized by non-toxicity, lack of nitrogen oxide emission, high cetane number which characterized the fuel ability to self-ignition of compressed fuel-air mixture. The other advantages of Fischer Tropsch fuels are low sulfur and aromatic content, reduced particulate matter emission and fuel combustion of such compounds as carbon dioxide and hydrocarbons [23]. In accordance with [23], the efficiency of FT conversion process ranges from 25 to 50%.

The fuels obtained by this production process are similar to Jet A-1 fuel. They are composed of hydrocarbons which amount and length may differ in comparison to conventional jet fuel. Also the number of H/C ratio may be different [16].

Hydroprocessed Esters and Fatty Acids (HEFA) process was approved in 2011. The HEFA pathway consist of catalytic reactions of various mechanism in hydrogen attendance. The first step in this conversion process is the hydrogenation, which consist in saturation of double bonds of the lipid chain by the catalytic addition of hydrogen. Hydrogen addition allow to remove the carbonyl group after hydrogenation and to brake the glycerol compound creating propane and chains of free fatty acid (FFA). The carboxyl group attached to the FFA can be removed to form straight paraffin chains by three ways: hydro-deoxygenation (HDO), decarboxylation (DCOX) or decarbonylation (DCO). To improve biofuel properties other processes are required: isomerization, cracking or cyclization [18]. The properties of final product are influenced by such factor as feedstock type and operating conditions (used catalyst, reaction pressure and temperature) [18].

Synthesized iso-paraffins (SIP) process was approved in 2014. This method is a biochemical conversion technology which allow for sustainable fuel production through the sugar fermentation [18]. As a feedstock can be used sugar cane or other sugar plants, for example sugar beets, sweet sorghum, cellulosic sugars or halophytes [18]. Direct sugar to hydrocarbon process (DHSC) include hydrolysis of biomass, carbohydrate fermentation, purification and hydroprocessing.

Alcohol-to-Jet Synthetic Paraffinic Kerosene (ATJ-SPK) technology was approved in 2016 [52]. This is biochemical conversion process for SAF production from alcohols such as methanol, ethanol, butanol and long-chain fatty alcohols [59]. First step in this technology pathway is biomass pretreatment and conditioning. After this activity alcohol can be produced through fermentation process. Further process of alcohol conversion to jet fuel include alcohol dehydration, oligomerization and hydrogenation [18].

Catalytic hydrothermolysis jet fuel (CHJ) receive certification in 2020 [37]. CHJ process consist of a reaction such as cracking, hydrolysis, decarboxylation, isomerization and cyclization. During the production pathway the triglycerides are change into the composition of straight chain, branched and cyclic hydrocarbons [59]. The reaction progress at presence of water and with/without a catalyst. The reaction process takes place at temperature 450–475°C and pressure of 210 bar [59]. The reaction products are processed to decarboxylation and hydrotreating for saturation and oxygen removal. The final step is fractionation for separation to naphtha, jet fuel and diesel [59].

Synthesized paraffinic kerosene from hydrocarbon-hydroprocessed esters and fatty acids (HC-HEFA-SPK) certified in 2020 [37]. In this process, the processed hydrocarbons are of biological origin. Their comes from oils found in *botryococcus braunii* algae [27].

Co-processing is the last approved SAF conversion pathway that contain co-processing of fats, oils and greases in conventional petroleum refinery, for supplying petroleum refining process [18]. This process was approved in 2018 and was include as an update (Annex A1) to ASTM D-1655 documentation [52].

The selected properties of neat fuels obtained by FT-SPK, HEFA, SIP and ATJ-SPK conversion technologies in relation to Jet A-1 fuel are presented in Table 2.

Table 2. Properties of selected fuels [32, 41, 43, 55, 60, 63, 64]

	Limits ASTM D1655 and D7566	Jet A-1	FT-SPK	HEFA	SIP	ATJ-SPK
Density 15°C kg/m^3	775–840	803.30	744.50	756.70	773.10	757.10
Kinematic Viscosity −20°C mm^2/s	max. 8.0	4.04	3.80	4.80	14.13	4.80
Heat of combustion MJ/kg	min. 42.80	43.25	44.10	44.15	44.10	43.20
Freezing point °C	–47	–49.60	–42.90	–54.40	< –80	< –80
Flash point °C	min. 38	40.50	51.50	42.00	107.50	47.50

3.3. SAF certification and quality control

Like all fuels used in aviation, sustainable aviation fuels need meets technical and certification requirements, allowing to use in commercial aircraft.

The standard specification for Jet A (commonly used in US) and Jet A-1 fuel (commonly used of the rest of the world) is ASTM 1655 'Standard Specification for Aviation Turbine Fuels'[28]. The other commonly used quality standard, confirmed by United Kingdom Ministry of Defence, is UK Defence Standard 91-91'Turbine Fuel, Aviation Kerosene Type, Jet A-1' (Def Stan 91-91) [41]. The differences between these two specifications are related to test limits for acidity level and naphthalene content [41].

The technical certification of SAF is regulated by the ASTM D7566 'Standard Specification for Aviation Turbine Fuel Containing Synthesized Hydrocarbons'[41]. This is the first specification that SAF need to meet. After that it can be blended with traditional fuel up to the allowable certified limit outlined in D7566. After blending process prepared fuel mixture is certified with ASTM D1655 [28].

Specifications allow to control the physical and chemical properties of fuel as well as allow for periodic checking for compliance. The deviations from standards included in the specifications are not permitted [28].

In many cases fuel have to travel many kilometers from the production facility to the direct recipient by various means of transport. From this reason the supply chain also require quality control. In situation when tested fuel does not meet the standards presented in ASTM (at the refinery or along the supply chain), the batch must be separate from other fuel and retested [41].

To the most common examples of quality documentations related to the sustainable aviation fuel are:
- Refinery Certificate of Quality (RCQ),
- Certificate of Analysis (COA),
- Recertification Test Certificate (RTC).

RCQ is the final document, created in the refinery for each part of product, that describe the quality of the product. It contains the results of measurements made in laboratory as well as information about the type and amount of additives that can be implemented to the fuel. This document contain also information about refinery name, batch number, date, as well as information that fuel meets ASTM D1655 [41].

COA can be issued by laboratories or by certified inspectors. This documentation include information about refinery name, batch number, date, information that fuel meets ASTM D1655 or D7655 [41]. COA does not contain detailed information about additives added previously but usually contain the results from ATA Specification 103: Standard for Jet Fuel Quality Control at Airports [41]. The Refinery Certificate of Quality and Certificate of Analysis are similar documents [41].

RTC confirms that recertification tests has been carried out. This process is implemented to check whether the fuel quality has not changed and meets specification requirements after transportation. Recertification is also necessary while the aviation product (fuel) is transfer to installation under conditions which may result in contamination, for example when fuel travel by the multiproduct pipeline [28, 41].

Quality process for conventional fuel begins with creation of RCQ in accordance to proper specification (ASTM D1655 or Def Stan 91-91). After leaving refinery, fuel start the transportation process to its destination, by variable means of transport (tanks, pipelines, trucks, etc.). At each transition point the fuel is re-inspected and COA certificate is issued. For neat SAF this process is similar but some additional steps occurred. In this case in refinery will be create RCQ in accordance with ASTM D7566 [28].

Blending process may occur directly at the refinery or at the suitable point along the supply chain (storage facility, airport). The choice of blending point depends on the access to conventional fuel [28]. Another important point is the fact, that conventional fuel composition is not constant and may vary within the range indicated by the specification. As an example can be used the density and aromatic content which are the key parameters for blending process, therefore at firs the composition of fuel should be known, to make sure that the final product meet the ASTM D7566 [28].

3.4. SAF producers

Actually, there are two main SAF producers: World Energy and Neste. World Energy (Fig. 9) start production in 2016 in their facility located in Paramount in California. Initially they supply United Airlines and later their expanded collaboration to KLM. Besides the SAF, the company also has in their offer biodiesel, renewable diesel, RINs and glycerin and fatty acids [62].

Fig. 9. World Energy in Paramount [14]

Neste (Fig. 10) is the world's largest SAF and renewable diesel producer. Their deliver SAF to San Francisco International Airport from refinery plant located in Rotterdam (Netherlands) by using existing multi-product pipeline infrastructure. Neste MY Renewable Jet Fuel ^{TM}, the brand name of produced SAF, is made from renewable waste and residue materials, like used cooking oil or animal fats [46].

Fig.10. Neste refinery plant in Rotterdam [47]

They manufacture renewable products in Finland, Netherlands and Singapore. The company plan increase its renewable annual production capacity from actual 3.2 to 4.5 million tons in the first quarter of 2023. 1.3 million tons will be provided by Singapore facility. The facility located in Rotterdam and Singapore are the biggest and the most advanced renewable fuels refineries in the world [45].

There are also other companies interested in SAF production. Fulcrum Bioenergy, is produce the low-carbon and low-cost transportation fuel from household garbage [21]. In this year the company finish the construction of the Sierra BioFuels factory located east of Reno in Nevada. They plan to convert 175 thousand tons of municipal solid waste into approximately 11 million gallons of synthetic crude [21].

Received product will be then upgraded to transportation fuels like sustainable aviation fuel, renewable diesel and renewable gasoline (Fulcrum FuelTM). The fuel production will begin during at fourth quarter of 2021 year. Fulcrum strategic partners include BP, United Airlines, Cathay Pacific, Japan Airlines and World Fuel Servicesand Marubeni [21].

Another example of company interested in SAF production is Red Rock Biofuels, which used a waste woody biomass as a feedstock. This company plans to convert 136 thousand tons of wood waste into 15 million gallons of SAF and renewable diesel [41].

The number of airports that distributing sustainable aviation fuel in the continuously manner or in batch is gradually increasing. Detailed information are contain in Table 3.

3.5. SAF application

Sustainable aviation fuels are an alternative option to conventional fuels and they properties may help to achieve the goals of aviation sector decarbonisation. Airbus, considered as a pioneer in SAF introduction, willingly supports all initiatives that contribute to sustainable fuel development and application in commercial flights. Today sustainable fuel can be applied in amount up to 50% without any modification of engine fuel system. Researches are carried out on the possibility of using larger amounts of alternative fuels. This will allow in the future for complete kerosene replacement by SAF.

On 29th June 2011, took place the first commercial Air-France KLM flight on sustainable jet fuel, using Boeing 737-800 [54]. Aircraft engines were operated on conventional jet fuel blended in 50% with sustainable fuel. The flight numbered KL1233 took place between Amsterdam Schiphol Airport and Paris Charles de Gaulle Airport carrying 171 passengers [54].

In 2012 took place the first flight of Air Canada (AC991), from Toronto to Mexico City, on airbus A319 aircraft powered by 50% blend of sustainable alternative fuel. Applied sustainable aviation fuel was produced from used cooking oil provided by SkyNRG. This flight was named "Perfect Flight" due to the fact that the routs and altitude were optimized, which finally help to decrease fuel consumption and reduce the noise generated by the aircraft [3].

Table 3. List of airports distributing SAF [33]

Date	Airport	State	Status	Fuel producer
06.10.2021	Toronto-Pearson Airport	Canada	Ongoing deliveres (offtake agreement)	Canada's Biojet Supply Chain Initiative (CBSCI)
14.09.2021	Boeing Field/King County Intl Airport	USA		–
23.08.2021	Le Bourget Airport	France		TotalEnergies
13.08.2021	Melbourne Orlando International Airport	Australia		Neste
14.07.2021	Farnborough Airport	United Kingdom		Neste
12.07.2021	Zurich Airport	Switzerland		Neste
28.06.2021	Cologne Airport	Germany		Neste
06.05.2021	Munich Airport	Germany		N/A
26.04.2021	Aspen Airport	USA		Neste
26.04.2021	Clemont-Ferrand Airport France	France		Air BP
06.04.2021	Biggin Hill Airport, London	United Kingdom		Air BP
23.03.2021	Van Nuys Airport	USA		World Energy
23.03.2021	John Wayne Orange County Airport	USA		World Energy
04.03.2021	Piedmont triad international airport	USA	Batch delivery	Neste
01.03.2021	Bristol Airport	United Kingdom	Batch delivery	BP
26.02.2021	Monterey Regional Airport	USA	Ongoing deliveres (offtake agreement)	Neste
26.02.2021	Oakland International Airport	USA		Neste
12.02.2021	Camarillo Airport	USA		N/A
08.12.2020	London Luton Airport	United Kingdom		Neste
03.02.2020	Fort Lauderdale Executive Airport	USA	Batch delivery	Gevo
07.09.2019	Bob Hope Burbank airport	USA	Ongoing deliveres (offtake agreement)	Neste
23.08.2019	Jackson Hole Airport	USA	Batch delivery	Gevo
01.06.2019	Umeå Airport	Sweden	Batch delivery	Air BP
01.06.2019	Malmö Airport	Sweden	Batch delivery	Air BP
02.05.2019	New York's Republic Airport	USA	Batch delivery	Gevo
17.01.2019	Van Nuys Airport	USA	Batch delivery	Gevo
19.12.2018	Stockholm Bromma Airport	Sweden	Ongoing deliveres (offtake agreement)	Air BP
19.12.2018	Åre Östersund Airport	Sweden	Batch delivery	World Energy
19.12.2018	Göteborg Landvetter Airport	Sweden	Batch delivery	World Energy
19.12.2018	Visby Airport	Sweden	Batch delivery	World Energy
19.12.2018	Luleå Airport	Sweden	Batch delivery	World Energy
06.12.2018	San Francisco Airport	USA	Ongoing deliveres (offtake agreement)	World Energy
12.11.2018	Kalmar Öland Airport	Sweden		World Energy
14.05.2018	Vaxjo Smaland Airport	Sweden		World Energy
19.04.2018	Toronto-Pearson Airport	Canada	Batch delivery	Canada's Biojet Supply Chain Initiative (CBSCI)
08.11.2017	Chicago O'Hare Airport	USA	Batch delivery	Gevo
03.10.2017	Brisbane Airport	Australia	Batch delivery	Gevo
21.08.2017	Bergen Airport	Norway	Ongoing deliveres (offtake agreement)	World Energy
26.07.2017	Halmstad City Airport	Sweden		World Energy
05.01.2017	Stockholm Arlanda Airport	Sweden		World Energy
24.05.2016	Montreal Trudeau Airport	Canada	Batch delivery	Canada's Biojet Supply Chain Initiative (CBSCI)
01.03.2016	Los Angeles Airport	USA	Ongoing deliveres (offtake agreement)	World Energy
22.01.2016	Oslo Airport	Norway		World Energy
26.01.2014	Karlstad Airport	Sweden	Batch delivery	Statoil

Between 2011 and 2015, 22 airlines accomplish over 2500 passenger flights on fuel containing up to 50% of bio-jet fuel. The bio-jet feedstock included used cooking oil, camelina, jatropha, algae and sugarcane [30].

On 18th of March 2021 took place the first test flight of Airbus A350 (Fig. 11) supplied by 100% Sustainable Aviation Fuel. Tests were conducted on Blagnac airport located in Toulouse, in France [2].

Nowadays all Airbus aircrafts are certified to fly on jet fuel blended with SAF up to 50%. An Airbus-led project named 'Emission and Climate Impact of Alternative Fuel' (ECLIF3) in collaboration with Rolls Royce, DLR (German Aerospace Research Center) and Neste (SAF producent) [2, 44]. The goal of the project is looking into the effect of 100% SAF application on engine emission and performance. Test are conducted on Airbus A350-900 powered by Trent XWB – three-shaft turbofan engine [2].

Fig.11. Airbus A350 flight on 100% SAF (2021) [2]

The emissions generated by 100% SAF fuel, measured during ground and flight tests were used for comparison with emissions emitted during kerosene burning and kerosene with low sulfur content [2]. Conducted researches will also include the control of particulate-matter emissions [2]. The first flight of aircraft fueled by 100% SAF went well, without noticeable difference in engine behavior.

On 18th of May 2021 at 15:40 took place the first long-haul flight on the aircraft supplied by SAF produced entirely in France. Air France Flight 342 was from Paris-Charles de Gaulle Airport (CDG) to Montreal in Canada. Fuel was made from waste and residue source that come from the circular economy. It was produced from used cooking oil by Total company in La Mede bio-refinery and Qudalle factory. Developed sustainable fuel received ISCC-EU certification from International Sustainability & Carbon Certification System. Prepared fuel mixture contained 16% of SAF and allow for CO_2 emission reduction by 20 tonnes. The Air France KLM conducted their first flight on SAF in 2009 year. Between 2014 and 2016 they made 78 flights on aircrafts powered by fuel with 10% of SAF blend [1].

On 17th June 2021 took place first commercial flight of Japan Airlines (JAL), numbered JL515, using two types domestically produced SAF, blend with the jet fuel. The flight on Airbus 350 aircraft, was from Tokyo Haneda to Sapporo (Chin-Chitose) [13]. The 3,132 liters of SAF was blended with conventional jet fuel at 9.1% blending ratio. The first type of used SAF was produced from wood chips by Mitsubishi Power, Toyo Engineering and JERA and the second from algae by IHI Corporation. The JAL Group plan permanently introduce 10% of SAF to conventional aviation fuel by 2030 [12, 13, 22].

Fig. 12. First Beluga flight with SAF [5]

The other example of SAF application is Airbus Beluga first flight in December 2019 (Fig. 12). Beluga aircrafts named also Super Transporter are used for transportation huge loads such as fuselage fragments or wings. Beluga fleet operating from Broughton in Wales, will be supply by 35% blend of non-fossil derived fuel. The sustainable feedstock is used to produce the SAF for Beluga fleet, such as cooking oil. The fuel is supplied to Airbus in Broughton and Hamburg by Air bp [4].

Since first passenger flight on SAF blend fuel in 2011 year until now, there was more than 375 thousand of commercial flights operated on this kind of fuel [11].

In previous year, the SAF production was about 190 thousand tones, which is less than 0.1% of the total fuel consumption. The main reason of such low production is SAF prices, which are two up to three times higher in accordance to fossil fuels [6].

It is worth to mentioned that Swiss International Air Lines (SWISS) create the first complex logistic chain for importing Neste MY Sustainable Aviation Fuel™ to Switzerland in collaboration with different business partners [51]. At the same time it does makes SWISS the first airline which use the SAF in its regular operation from Switzerland. In addition Swiss airlines collaborate with Lufthansa Group on SAF researches and adoption.

Lufthansa Group conducted in 2011 the first long-term test of biofuels in their scheduled flight operations in cooperation with Neste [48].

3.6. Infrastructure

Commercial airports have an extensive airport infrastructure for fuel management – fuel receive, storage and transmition to the fuel tanks located on the aircraft. Fuel infrastructure consist of fuel tanks, pipelines, fuel pumps, flow meters to control the flow of the fuel, filters to remove contaminants, safety system to detect and prevent fuel leakage. Fuel is delivered to the fuel tanks located in the aircraft wings by hydrant systems or fuel truck [41]. There are several means of transport used for fuel transition from manufacturer to the destination place. Commonly used in aviation Jet-A fuel is mostly transfer by pipes [41]. SAF can be transport by pipelines only in case when it is co-processing in refinery and meet ASTM standards. For example Neste company transport SAF to the West Coast where is blended with conventional jet fuel. Prepared fuel is delivered by pipes to the San Francisco International Airport [41].

The World Energy use different delivery schedule. The Jet-A fuel is delivered to the production facility by trucks and there blended with SAF. Then sustainable fuel is delivered to Los Angeles International Airport by truck. The delivery schedule depends on many factors. In case of methods used by World Energy decided mostly the neighborhood of airport, availability of Jet-A fuel nearby and low fuel volumes [41]. Different delivered methods will be used for low volume SAF production and for higher volumes.

There are two options of SAF blending in the terminal:

– In the first case (Fig. 13) both SAF and Jet-A are storage in separate tank. Individual tank is used to blending process. If the sample of blended fuel meet the requirements from ASTM D7655, is denote as ASTM D1655 and is ready to delivery,

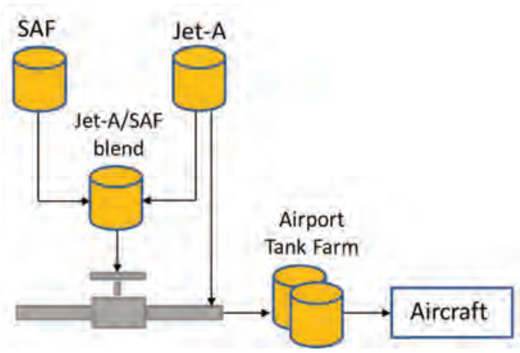

Fig. 13. First option of Jet-A and SAF blending at the terminal [41]

– In the second option (Fig. 14) SAF is deliver to the tank with Jet-A fuel. This option will require carefully control to identify the amount of added SAF.

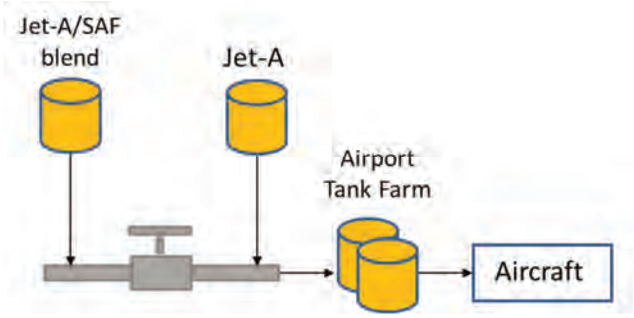

Fig. 14. Second option of Jet-A and SAF blending at the terminal [41]

Due to the fact that SAF meet the same standards as conventional jet fuel, specified by ASTM, therefore the problems with compatibility are not excepted [41].

4. Conclusions

Zero emission aircrafts are actually not available. SAF application don't require aircraft, engines, storage and distribution infrastructure modification. This feature of alternative fuel is very important and facilitate the introduction of alternative fuel to the aviation. Due to the fact that aviation sector has no near-term alternative to liquid hydrocarbon fuels, the SAF produced from variable renewable feedstock seems to be the best option for modern aviation fleet. The gradual SAF introduction in aircraft sector should result in reduction of CO_2 emission. The results of conducted literature studies indicate that the use of sustainable aviation fuels is of great interest. The number of flights on sustainable fuel increase very quickly, which also indicate high operational safety and reliable operation of turbine engines. New, more efficient SAF conversion technologies are still develop. The fuels obtained through different processes are characterized by different properties. For this reason, the blending process is a key stage in the production pathway that allows to obtain the final products with desired properties and compliant with the required standards.

Nomenclature

APU	auxiliary power unit
ASTM	American Society for testing and Materials
GHG	greenhouse gas
GSE	ground support equipment
IATA	International Air Transport Association
ICAO	International Civil Aviation Organization
IRENA	International Renewable Energy Agency
SAF	sustainable aviation fuel

Bibliography

[1] AIR FRANCE KLM GROUP. Air France-KLM, Total, Groupe ADP and Airbus Join Forces to Decarbonize Air Transportation and Carry Out The First Long-Haul Flight Powered By Sustainable Aviation Fuel Produced in France. https://www.airfranceklm.com/en/air-france-klm-total-groupe-adp-and-airbus-join-forces-decarbonize-air-transportation-and-carry-out

[2] AIRBUS. Aviation leaders launch first in-flight 100% sustainable aviation fuel emissions study on commercial passenger jet. https://www.airbus.com/en/newsroom/press-releases/2021-03-aviation-leaders-launch-first-in-flight-100-sustainable-aviation

[3] AIRBUS. Airbus and Air Canada make North America's first ever "Perfect Flight". http://www.airbus.com

[4] AIRBUS. Airbus further reduces its Beluga fleet's environmental impact. https://www.airbus.com/en/newsroom/press-releases/2021-04-airbus-further-reduces-its-beluga-fleets-environmental-impact

[5] AIRBUS. First Beluga Flight with Sustainable Aviation Fuel. http://www.twitter.com/airbus/status/1206628727494467589

[6] AIRBUS. Sustainable aviation fuel: A recipe for cleaner flight. https://www.airbus.com/en/newsroom/stories/2021-04-sustainable-aviation-fuel-a-recipe-for-cleaner-flight

[7] AIRBUS. Uniting & safeguarding for a more sustainable world. http://www.airbus.com/company/sustainability/environment/climate-change/decarbonisation.html

[8] AIRLINESS, IATA. Realizing the potential of sustainable aviation fuel. http://www.airlines.iata.org/analysis/realizing-the-potential-of-sustainable-aviation-fuel

[9] ANTOINE, N.E. Aircraft optimization for minimal environmental impact. *Journal of Aircraft*. 2004, **41**(4). https://doi.org/10.2514/1.71

[10] ATAG, Beginner's Guide to Sustainable Aviation Fuel, Edition 3, 2017. https://aviationbenefits.org/media/16-6152-/beginners-guide-to-saf_web.pdf

[11] AVIATION BENEFITS BEYOND BORDERS. Sustainable aviation fuel. http://www.aviationbenefits.org/envi-ronmental-efficiency/climate-action/sustainable-aviation-fuel

[12] AVIATION WEEK. Japan Airlines flies first SAF flight. http://www.aviationweek.com/special-topics/sustainabi-lity/gallery-saf-fuel-sustainability-initiatives

[13] BIOENERGY INTERNATIONAL. JAL conducts first flight with two domestically produced SAF types. http://www.bioenergyinternational.com/storage-logistics/jal-conducts-first-flight-with-two-domestically-produced-saf-types

[14] BIOMASS MAGAZINE. World Energy invests $350M to expand Paramount biofuel production. http://www.biomassmagazine.com/articles/15699/world-ener-gy-invests-350m-to-expand-paramount-biofuel-production

[15] BP. What is sustainable aviation fuel (SAF)? http://www.bp.com/en/global/air-bp/news-and-views/views/what-is-sustainable-aviation-fuel-saf-and-why-is-it-important.html

[16] BRAUN-UNKHOFF, M., RIEDEL, U., WAHL, C. About the emissions of alternative jet fuels. *CEAS Aeronautical Journal*. 2017, **8**, 167-180. https://doi.org/10.1007/s13272-016-0230-3

[17] CHIARAMONTI, D. Sustainable aviation fuels: the challenge of decarbonization. *Energy Procedia*. 2019, **158**, 1202-1207. https://doi.org/10.1016/j.egypro.2019.01.308

[18] CORSIA, Eligible Fuels Life Cycle Assessment Methodology. 2019. https://www.icao.int/environmental-protection/CORSIA/Documents/CORSIA_Supporting_Document_CORSIA%20Eligible%20Fuels_LCA_Methodology_V3.pdf

[19] EL-SAYED, A.F. Aircraft propulsion and gas turbine engines. *CRC Press*. 2017.

[20] FEDERAL AVIATION ADMINISTRATION. Aviation Emissions, Impacts & Mitigation: A Primer, FAA Office of Environment and Energy, January 2015. https://www.faa.gov/regulations_policies/policy_guidance/envir_policy/media/primer_jan2015.pdf

[21] FULCRUM BIOENERGY. Fulcrum BioEnergy completes construction of the Sierra BioFuels Plant. http://www.fulcrum-bioenergy.com/wp-content/uploads/2021/07/2021-07-06-Sierra-Construction-Completion-Press-Release-FINAL.pdf

[22] GREEN CAR CONGRESS. Japan Airlines conducts first flight with blend of two different types of SAF. http://www.greencarcongress.com/2021/06/20210621-saf.html

[23] HARI, T.K., YAAKOB, Z., BINITHA, N.N. Aviation biofuel from renewable sources: Routes, opportunities and challenges, *Renewable and Sustainable Energy Reviews*. 2015, **42**, 1234-1244. https://doi.org/10.1016/j.rser.2014.10.095

[24] HUO, X., HEYNE, J.S., UNOCIC, K. et al. Toward net-zero sustainable aviation fuel with wet waste-derived volatile fatty acids. *PNAS*. 2021, **118**(13). https://doi.org/10.1073/pnas.2023008118

[25] IATA. Annual review 2020. https://www.iata.org/contentassets/c81222d96c9a4e0bb4ff6ced0126f0bb/iata-annual-review-2020.pdf

[26] IATA. Climate Change fact Sheet. https://www.iata.org/contentassets/d13875e9ed784f75bac90f000760e998/fact_sheet_on_climate_change.pdf

[27] IATA. Fact sheet 2. Sustainable Aviation Fuel Technical Certification. https://www.iata.org/contentassets/d13875e9ed784f75bac90f000760e998/saf-technical-certifications.pdf

[28] IATA. IATA Guidance Material for Sustainable Aviation Fuel Management. 2015. https://www.iata.org/contentassets/d13875e9ed784f75bac90f000760e998/iata20guidance20material20for20saf.pdf

[29] IATA. Industry Statistics Fact Sheet. December 2019. https://www.iata.org/en/iata-repository/pressroom/fact-sheets/industry-statistics/

[30] IATA. Sustainable Aviation Fuels Fact sheet. 2019. https://www.iata.org/contentassets/d13875e9ed784f75bac90f000760e998/saf-fact-sheet-2019.pdf

[31] IATA. What is SAF? https://www.iata.org/contentassets/d13875e9ed784f75bac90f000760e998/saf-what-is-saf.pdf

[32] ICAO Environment. Alcohol to Jet-Isobutanol. ICAO Seminar on Alternative Fuels. 2017. https://www.icao.int/Meetings/altfuels17/Documents/Glenn%20Johnston%20-%20Gevo.pdf

[33] ICAO ENVIRONMENT. Airports. http://www.icao.int/environmental-protection/GFAAF/Pages/Airports.aspx

[34] ICAO ENVIRONMENT. Conversion processes. http://www.icao.int/environmental-protection/GFAAF/Pages/Conversion-processes.aspx

[35] ICAO. Conference on Aviation and Alternative Fuels. 2017. https://www.icao.int/Meetings/CAAF2/Documents/CAAF.2.WP.007.1.en.pdf

[36] ICAO. White paper on climate change. Aviation impacts on climate: state of the science. https://www.icao.int/environmental-protection/Documents/ScientificUnderstanding/EnvReport2016-WhitePaper-ClimateChange.pdf

[37] IRENA, Reaching zero with renewables biojet fuels. 2021. https://www.irena.org//media/Files/IRENA/Agency/Publication/2021/Jul/IRENA_Reaching_Zero_Biojet_Fuels_2021.pdf

[38] LEE, D.S. Aviation and climate change: the science. January 2009. https://doi.org/10.4324/9781849770774

[39] LEFEBVRE, A.H., BALLAL, D.R. Gas turbine combustion-alternative fuels and emissions, 3rd edition. *CRC Press*, 2010.

[40] MASIOL, M., HARRISON, R.,M. Aircraft engine exhaust emissions and other airport-related contributions to ambient air pollution: a review. *Atmospheric Environment.* 2014, **95**, 409-455. https://doi.org/10.1016/j.atmosenv.2014.05.070

[41] MORIARTY, K., KVIEN, A. U.S. Airport infrastructure and sustainable aviation fuel. *National Renewable Energy Laboratory NREL*/TP-5400-78368. 2021. https://www.nrel.gov/docs/fy21osti/78368.pdf

[42] MRAZOVA, M. Sustainable development – the key for green aviation. *INCAS BULLETIN*. 2014, **6**(1), 109-122. https://doi.org/10.13111/2066-8201.2014.6.1.10

[43] MÜLLER-LANGER, F., DOGNITZ, N., MARQUARDT, C. et al. Multiblend JET A-1 in practice: results of an R&D project on synthetic paraffinic kerosenes. *Chemical Engineering Technology*. 2020, **43**, 1514-1521. https://doi.org/10.1002/ceat.202000024

[44] NESTE. Aviation leaders launch first in-flight 100% sustainable aviation fuel emissions study on commercial passenger jet. http://www.neste.com/releases-and-news/aviation/aviation-leaders-launch-first-flight-100-sustainable-aviation-fuel-emissions-study-commercial

[45] NESTE. Business. http://www.neste.com/about-neste/who-we-are/business#52-713477

[46] NESTE. Neste delivers sustainable aviation fuel to San Francisco International Airport – first company to deliver it via pipeline. http://www.neste.com/releases-and-news/aviation/neste-delivers-sustainable-aviation-fuel-san-francisco-international-airport-first-company-deliver

[47] NESTE. Neste's acquisition of Bunge's refinery plant in Rotterdam completed. http://www.neste.com/releases-and-news/circular-economy/nestes-acquisition-bunges-refinery-plant-rotterdam-completed

[48] NESTE. SWISS becomes the first commercial airline to fly from Switzerland with Neste MY Sustainable Aviation Fuel. http://www.neste.com/releases-and-news/aviation/swiss-becomes-first-commercial-airline-fly-switzerland-neste-my-sustainable-aviation-fuel

[49] O'MALLEY, J., PAVLENKO, N., SEARLE, S. Estimating sustainable aviation fuel feedstock availability to meet growing European Union demand. Working Paper 2021-13, ICCT 2021. https://theicct.org/sites/default/files/publications/Sustainable-aviation-fuel-feedstock-eu-mar2021.pdf

[50] ORLEN. Paliwo JET A-1, Karta charakterystyki. https://www.orlen.pl/content/dam/internet/orlen/pl/pl/dla-biznesu/produkty/paliwa-lotnicze/jet-a-1/dokumenty/karta_charaktarystyki_jet_a1.pdf

[51] PAVLENKO, N., SEARLE, S. Fueling flight: assessing the sustainability implications of alternative aviation fuels. Working Paper 2021-11, International Council On Clean Transportation, 2021. https://theicct.org/sites/default/files/publications/Alternative-aviation-fuel-sustainability-mar2021.pdf

[52] PRUSSI, M., O'CONNELL, A., LONZA, L. Analysis of current aviation biofuel technical production potential in EU28. *Biomass and Bioenergy*. 2019, **130**, 105371. https://doi.org/10.1016/j.biombioe.2019.105371

[53] SARAVANAMUTTO, H., ROGERS, G., COHEN, H. et al. Gas turbine theory. *PEARSON Prentice Hall*, England 2009.

[54] SkyNRG. 2011, June 29th – First commercial flight KLM on sustainable jet fuel in the world. http://www.skynrg.com/track-records/june-29th-2011-first-commercial-flight-on-sustainable-jet-fuel-in-the-world-with-klm/

[55] STARCK, L., PIDOL, L., JEULAND, N. et al. Production of hydroprocessed esters and fatty acids (HEFA)-optimisation of process yield. *Oil&Gas Science and Technology – Revue d'IFP Energies nouvelles*. Institut Français du Pétrole, 2016, **71**(1). https://doi.org/10.2516/ogst/2014007

[56] Statista. Carbon dioxide emissions from commercial aviation worldwide from 2004 to 2022. http://www.statista.com/statistics/1186820/co2-emissionscommercial-aviation-worldwide

[57] Statista. Total fuel consumption of commercial airlines worldwide between 2005 and 2022. http://www.statista.com/statistics/655057/fuel-consumption-of-airlines-worldwide/

[58] SZUMAN, B., LIPKA., P., REKLEWSKI, T. Emisja spalin z silników lotniczych. ULC, Departament Techniki Lotniczej, Wydział Ochrony Środowiska, 2013. https://www.ulc.gov.pl/_download/informacje/emisja_spalin_z_silnikw_lotn.pdf

[59] WANG, W-C., TAO, L., MARKHAM, J. et al. Review of biojet fuel conversion technologies. *National Renewable Energy Laboratory*, NREL/TP-5100-66291, 2016. http://www.nrel.gov/publications

[60] WEISSER, K.L., TURGEON, R.T. 90/10 JP5-/Synthesized ISO-paraffin specification and fit-for-purpose test results. Naval Fuels&Lubricants Cross Functional Team. Report 441/14-010. https://apps.dtic.mil/sti/pdfs/ADA618841.pdf

[61] WINTHER, M., RYPDAL, K. EMEP/EEA air pollutant emission inventory guidebook 2019, 1.A.3.a, 1.A.5.b Aviation, 2019. https://www.eea.europa.eu/publications/emep-eea-guidebook-2019/part-b-sectoral-guidance-chapters/1-energy/1-a-combustion/1-a-3-a-aviation/view

[62] WORLD ENERGY. http://www.worldenergy.net/products/glycerin-fatty-acids/

[63] YANG, J., XIN, Z., HE, Q.S. et al. An overview on performance characteristics of bio-jet fuels. *Fuel*. 2019, **237**, 916-936. https://doi.org/10.1016/J.FUEL.2018.10.079

[64] ZSCHOCKE, A., SCHEUERMANN, S., ORTNER, J. High biofuel blends in aviation (HBBA). ENER/C2/2012/420-1, Final Report. https://ec.europa.eu/energy/sites/ener/files/documents/final_report_for_publication.pdf

Natalia Marszałek, MEng. – Faculty of Mechanical Engineering and Aeronautics, Rzeszow University of Technology.

e-mail: *n.marszalek@prz.edu.pl*

Tomasz Lis, DEng. – Faculty of Mechanical Engineering and Aeronautics, Rzeszow University of Technology.

e-mail: *list@prz.edu.pl*

Article citation info:
JANICKA, A., ZAWIŚLAK, M., GŁOGOZA, A. et al. Optimization of the electric bus radiator design in terms of noise emissions and energy consumption by computational fluid dynamics. *Combustion Engines*. 2022, **191**(4), 41-50. https://doi.org/10.19206/CE-147256

Anna JANICKA
Maciej ZAWIŚLAK
Artur GŁOGOZA
Radosław WŁOSTOWSKI

Combustion Engines
Polish Scientific Society of Combustion Engines

Optimization of the electric bus radiator design in terms of noise emissions and energy consumption by computational fluid dynamics

ARTICLE INFO

Received: 19 January 2022
Revised: 7 March 2022
Accepted: 9 March 2022
Available online: 13 March 2022

The paper presents the numerical optimization of an innovative radiator for use in electric buses in terms of energy consumption and noise emission. Computational fluid dynamics simulations were performed. The flow of the cooling medium was modeled using the RANS method. The two-equation k-ε turbulence model, the heat transfer model and the acoustic model were used. According to the research results, the separation of the air stream in individual fan sections contributes to the improvement of energy efficiency and reduces noise emissions. As a result of the simulation, it was found that the best solution in terms of noise emission as well as the occurring flow phenomena caused about a 2 dB decrease of maximum values of the noise level and allowed the equalization of the cooling medium velocity (prevailing velocity range between 4 and 9 m/s). The results of the simulations were verified under laboratory and field conditions, showing a very good convergence of the model with the results of the experiments (i.e. the maximum noise level was estimated at 57 dB, under measurement conditions for the same operating point at 59 dB) while maintaining the baseline energy demand, which indicates a new approach in the method of shaping internal elements of electric vehicle coolers.

Key words: *automotive engineering, electric bus, CFD, noise, ecodesign*

1. Introduction

The dynamic development of electromobility poses challenges to designers regarding not only the efficiency of energy transformation but also the battery life, which is influenced by the stability of its operating temperature. Sustainable design of cooling systems requires optimization of energy management taking into account other important environmental parameters. The multifaceted ecodesign of motor vehicles concerns not only reduction and optimization of energy and material consumption as well as pollutant emissions, but also aspects related to vibration and noise protection for both vehicle users and the external environment. The structure of the motor vehicle market is changing dynamically. In addition to the challenges common to all types of vehicle, such as aerodynamics and body morphology, ecodesign varies greatly depending on the type of drive used.

In the case of conventional vehicles equipped with internal combustion engines (ICE), designing in accordance with the principles of sustainable development currently focuses mainly on rightsizing trends [5], improving the efficiency of fuel combustion and its composition, as well as the efficiency of exhaust gas treatment systems [23, 24]. An interesting approach to improving ICE efficiency is demonstrated in the work of Sroka and Sadlak [18], where the authors present study results showing that the use of an active combustion chamber (based on thermal barriers) can improve the effective efficiency of the engine from 10 to 20%.

However, the dynamic development of electromobility observed in the last decade poses further challenges for designers. In addition to the issue of energy transformation efficiency, lifetime, capacity and recycling of batteries, there are also areas of concern identical to the vehicles equipped with a classic drive, such as noise emission. In this case, nevertheless, it does not apply to the drive unit itself, i.e. the electric motor, but to the coexisting systems. The use of an electric motor both as a stand-alone drive and in a hybrid system requires the use of new solutions in the field of cooling systems, whose task is to maintain the vehicle's batteries in appropriate thermal conditions.

The thermoregulation systems of batteries for use in electric vehicles are currently the subject of numerous studies related to energy optimization, the type and composition of the coolant, their effectiveness, noise emission and control. Shashank [15], in his literature review, emphasized the importance of thermal management in electric vehicles and its impact on the life of lithium-ion batteries, which are significantly sensitive to temperature. A year later, a similar review paper was published by Kim [11], demonstrating the advantages and disadvantages of various battery thermal management system (BTMS) solutions and presenting his own solution in this area. The dynamic development of technology and the ever-growing interest in battery cooling are also indicated in a paper published the following year. Mengyao et al. [12] demonstrated advances in research on electric vehicle cooling technology aimed at eliminating temperature peaks and large temperature gradients. He presented an overview of existing battery thermal management systems and the advantages and disadvantages of cooling systems based on both air and liquid cooling. He defined the trends in their development, such as miniaturization or reduction of relatively high energy demand. The paper also indicated that minimizing the impact on user comfort (mainly in relation to the noise generated by the airflow through the fan and enclosure) is an important research issue.

The problem of research on BTMS was also highlighted by Akinlabi and Solyali [1], who identified the incorrect temperature distribution in the battery pack (primarily in the significant temperature difference) as the cause of the main problems related to the battery operation. Jing et al. [25] stressed the importance of environmental aspects in the design of vehicle cooling systems and presented the results of a research study aimed at a detailed analysis of the operating medium in terms of environmental aspects. Shen and Gao [16] focused on the properties of the cooling medium in liquid-cooled battery systems and their impact on cooling efficiency. Another team of researchers has published interesting papers on the possibility of using heat pumps to cool car batteries. Dong et al. [7] and Wang et al [22] have shown in their experimental studies that such solutions have a high application potential in motor vehicles. Chen et al. [6] confirmed their conclusions by proposing a carbon dioxide-based heat pump to cool electric vehicle batteries. However, the researchers Qiu and Shi [14], presenting their theoretical analysis results, lean toward thermoelectric cooling.

The system control method is also an important direction of BTMS development. The future in this area may be the process proposed by Miranda et al. [13]. The authors of the paper, to face the future challenge of energy management of electric vehicles, propose a fuzzy logic control (FLC) strategy. The solution is applied to perform the power split among the electric motors to improve vehicle energy efficiency and dynamic performance under real driving conditions [13].

The problem of EV energy management in real drive conditions, especially in urban area, was also analyzed by Sun et al. [20]. The presented study proposed to simulate energy consumption of electric vehicles using real-world driving cycle (RWDC) data in urban area and developed method for formulating energy optimization schemes for electrical commercial vehicles.

Considering the problems of EV batteries cooling, it is necessary to take into account the physical phenomena occurring in the system, primarily the phenomena of heat transfer and phenomena occurring during the flow of cooling agents. Observation and analysis of flow and temperature distribution is crucial for the design of flow systems, which are certainly cooling systems. Only advanced numerical tools of fluid mechanics, which enable multicriterial visualization and then flow observation, allow to design highlyeffective solutions characterized by desired parameters.

The dynamic progress in the field of technical sciences in recent decades has made it necessary to develop mathematical and numerical tools to help solve many scientific concerns (not only current but also predicted [2, 8–10, 28]) and engineering problems in the design, improvement of efficiency and performance parameters of machines and devices [28]. Computational fluid mechanics (computational fluid dynamics), is a separate area of fluid mechanics in which numerical methods are used to solve problems with the description of fluids.

Discretization and numerical solution of partial differential equations describing the behavior of the fluid make it possible to approximate the distribution of physical quantities, such as velocity, pressure, temperature, and other flow parameters.

Modern CFD programs solve: flows taking into account the variability of viscosity and compressibility, multiphase flows, flows in which chemical reactions or combustion processes occur, flows through porous structures and flows in which the medium is a Newtonian or non-Newtonian fluid. Therefore, CFD simulations are now used to solve problems in many areas of science and industry (i.e., [2, 8–10, 19, 28]).

Numerical fluid mechanics, which is a research tool enabling the modeling of the effects of flow phenomena both for the purposes of analysis and diagnostics of systems, as well as their multicriteria optimization, has been used since the 1990s as a research method for vehicle design, and in recent years in electric vehicles, in particular in solving problems of aerodynamics, energy management, and noise modeling. In Zawiślak's paper [28], a review of the research conducted so far was made and then a method for designing flow machines and systems using CFD methods on the micro and macro flow scale was proposed and described. Three years later, Ruiqing et al. [17], reviewing the applications of CFD methods in the last decade (2010-2020), conclude that it is not only a tool for the diagnosis and design of flow devices and systems, but also a tool for a better understanding of the physical phenomena occurring in the flow system, indicating numerous possibilities for the use in the latest solutions in nonconventional vehicles (including electric vehicles).

Haowen et al.'s [26] paper presents the problem of noise distribution in the electric vehicle cabin, taking into account multiple sources. The authors indicate that the use of three-dimensional CFD calculations on the basis of a two-equation k-ε turbulence model allows for very good consistency of the calculation results with the measurement results. Zhang et al. [29] applied numerical fluid mechanics to optimize the vehicle cooling system taking into account the geometry of the entire vehicle under operational conditions. The researchers' interest was focused on optimizing the radiator and the cooling drag. Due to the use of CFD methods, design recommendations for efficient vehicle cooling have been specified.

Recently, there has been a significant increase of the numericians' interest in the cooling of electric vehicle batteries. Hamidreza et al. [3], using CFD methods, performed a comparative analysis of different hybrid vehicle battery cooling techniques and methods to assess thermal management efficiency. Also Benabdelaziz et al. [4] successfully use CFD tools to test battery cooling efficiency with the developed solution in various geometric variants. The result of the execution of their work is an improvement in the operation of the cooling system based on proprietary solutions (including heatpipe [29]), understood as a reduction of the temperature gradient on the battery pack. Yuan et al. [27] identify numerical and co-numerical modeling of flows based on the latest available computational fluid mechanics tools as the right direction for the design of cooling systems for vehicle components.

2. Research subject and purpose

The object of the research were radiators with an air distribution system in the housing, intended for use in cooling a pack of lithium-ion batteries / fuel cells. The developed solution can be applied in buses with an electric drive, including those with an optional braking resistor and in vehicles with a hydrogen drive. The cooling systems have been designed using the best available technologies in terms of material selection, type and shape of the core cross-section and verified using CFD methods.

The modules were equipped with a set of fans, liquid and air temperature sensors, a wire harness adapted to communication via the CAN 2.0B bus, with a transmission speed of 250 Kbps. Dedicated control systems with proprietary software that enable autonomous operation with the lowest possible demand for electricity have been developed and manufactured. The view of the research object – the object of numerical analysis – is shown in Fig. 1.

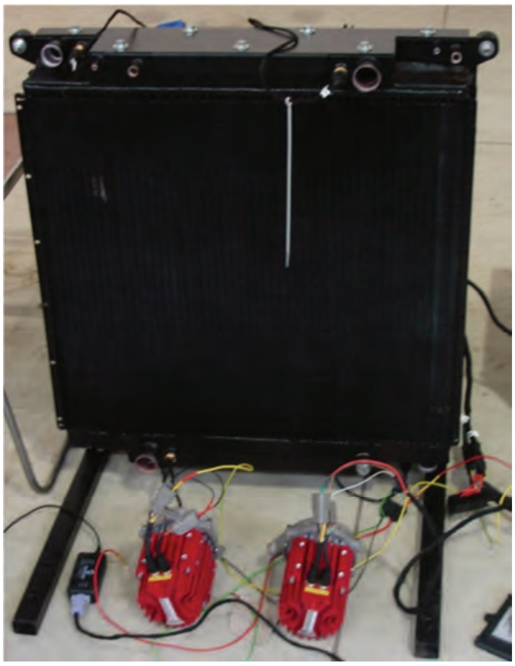

Fig. 1. The research object – radiator with an air distribution system, equipped with a set of fans, liquid and air temperature sensors, a wire harness adapted to communication via the CAN 2.0B bus, with a transmission speed of 250 Kbps

The aim of the research was numerical optimization of the device for minimizing noise emissions (improving the comfort of bus users) while maintaining the desired high efficiency of cooling the battery pack.

3. The research methods

For optimization of the electric bus radiator design in terms of noise emissions and energy consumption, the Zawiślak's method was applied [13]. The method is presented graphically in Fig. 2.

Numerical (simulation) tests were performed using the finite volume method (FVM), with the application of numerical fluid mechanics methods. ANSYS-FLUENT software was used. The flow of the cooling medium (air) was modeled using the RANS method. The two-equation k-ε turbulence model, the heat transfer model and the acoustic model were used. In order to determine the flow velocity boundary conditions, the available characteristics of the fan intended for use in the designed radiator were used. The assumed air temperature was 298 K and the assumed fluid temperature in the radiator was 373 K.

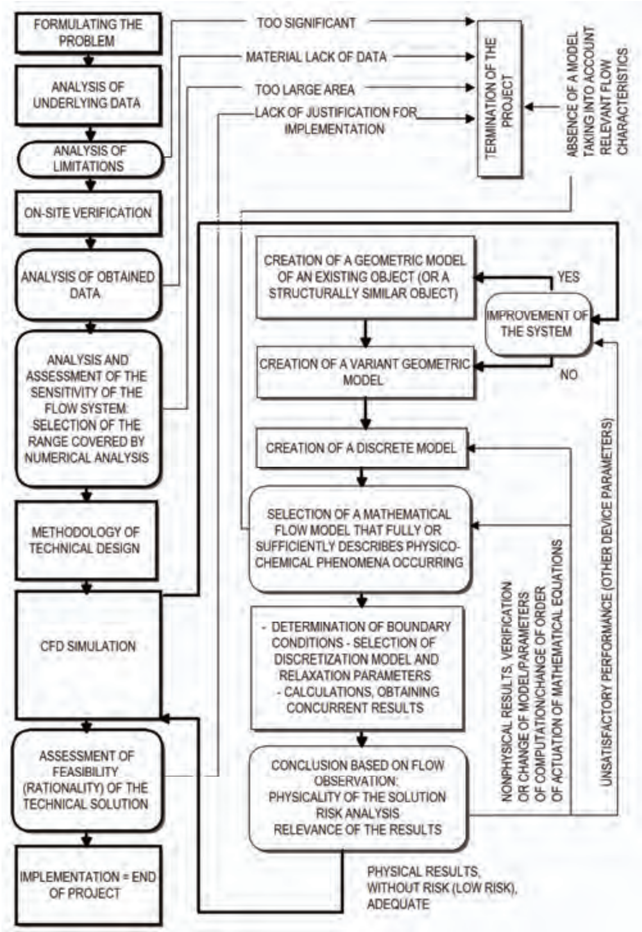

Fig. 2. Scheme of Zawiślak's method 'Design and modernisation of machines and flow systems using CFD software' [13]

Based on the results of numerical simulation, a prototype was created. In the next steps, the prototype was tested under laboratory and field conditions in order to perform a two-stage validation of the results of CFD calculations. The research methodology scheme is shown in Fig. 3.

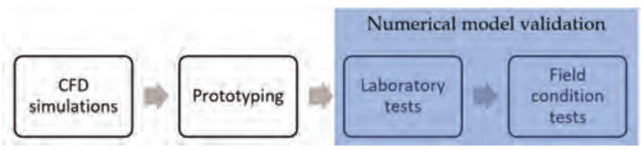

Fig. 3. Scheme of the research methodology

Measurements in laboratory conditions were carried out at the Division of Automotive Engineering of Wrocław University of Science and Technology. A test stand was built, on which the supplied system was installed, consisting of a radiator with connecting wires, a circulating pump mounted between the buffer tank and the radiator (the coolant is sucked from the buffer tank and then pumped into the radiator), a flow meter mounted on the return wire from the radiator (in front of the buffer tank). A diagram of the stand is shown in Fig. 4.

The buffer tank filled with coolant (water and glycol mixture, 5% vol. glycol), with a total volume of 65 dm^3, was equipped with three heating units with thermostatic systems with 18 kW of electric power. The system has 4 temperature sensors (PT-100); 2 sensors measuring the temperature of the coolant (coolant inlet and outlet from the radiator) and 2 sensors measuring the air temperature (air in front of the radiator and air behind the radiator at a distance of 1 m from the radiator. Electrical value measurements were made using a voltmeter, a current clump and an oscilloscope with recording software. Due to the type of control system, the current was measured by measuring the battery charging current.

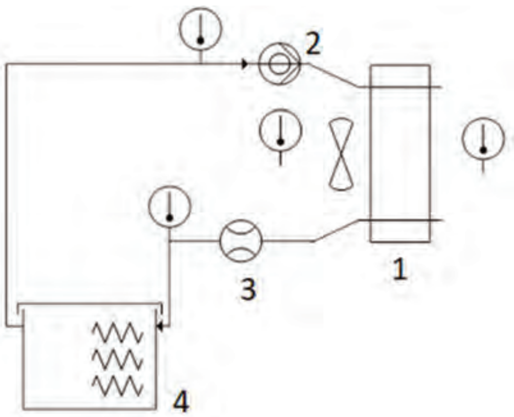

Fig. 4. A schematic diagram of the test stand: 1 – radiator, 2 – pump, 3 – flow meter, 4 – buffer tank

The characteristics of the coolant flow were determined depending on the load, expressed as a percentage of the load defined by the software. In addition, the characteristics of the current consumption of the circulation pump and cooling fans were determined, depending on the load defined as above. Additionally, oscilloscope waveforms of the current values at the device start-up were recorded. The maximum instantaneous values of current during start-up (at a nominal voltage of 27.1 V) did not exceed the nominal values of the devices.

Measurements in real (field) conditions were made at the Military Institute of Armoured and Automotive Technology on specially constructed measuring stands, according to a specially developed method (test certificate 41/LPE/2020) using a digital multimeter with instrumentation and a set of power batteries (device power) and a type 2250 sound level meter (noise level).

4. Results

Before starting the CFD simulations, numerical meshes were established based on the geometry of the bus and the radiator. The numerical mesh of the bus geometry was 1.2 million cells and 900,000 cells for the radiator. The tetra cells were applied in accordance with modeling principles [13] as suitable for modeling complex geometries.

Figure 5 shows a discrete model (a numerical mesh based on tetra cells) of the vehicle in which the analyzed radiator is planned to be installed.

A simulation of airflow around the vehicle was performed to determine whether there are no adverse flow phenomena at the cooling system attachment point (shown in Fig. 5).

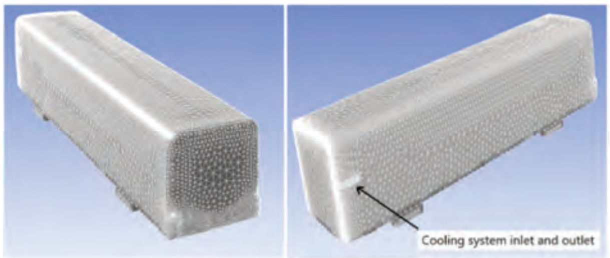

Fig. 5. A discrete model of an electric vehicle (bus)

Figure 6 presents the results of calculations showing the behavior of the streamlines during the flow under the given speed conditions (90 km/h).

Streamlines – radiator inlet grilles and streamlines with operating fans are shown in Fig. 7.

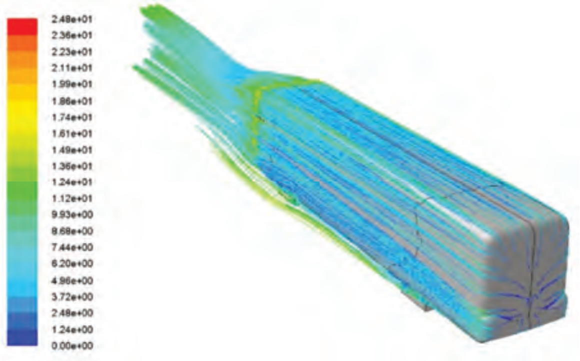

Fig. 6. Streamlines based on velocity [m/s] – view of the bus from the front of the vehicle on the side of radiator mounting

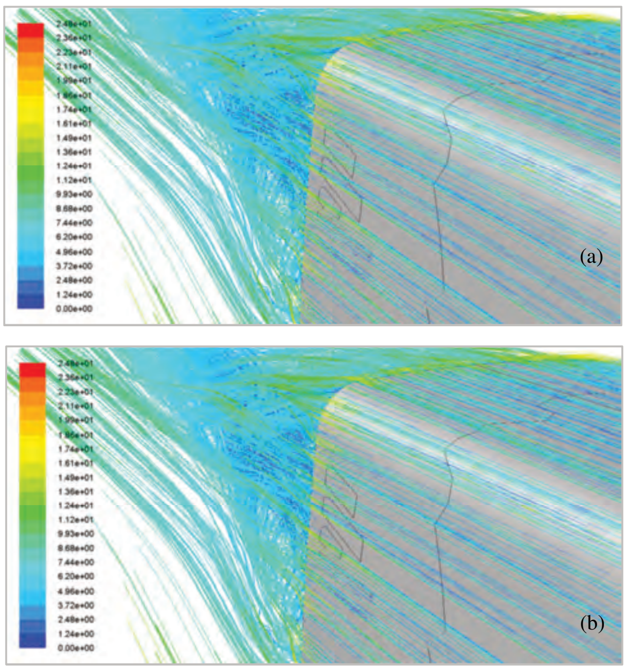

Fig. 7. Streamlines based on velocity [m/s] – radiator inlet grilles and streamlines with operating fans: view of the inlet grilles: a) when the vehicle is moving without the cooling system on, b) when the vehicle is moving with the cooling system on

Despite the correct air flow around the vehicle (Fig. 4), it was found that when the radiator fans were switched on, the flow into and out of the radiator box has swirl zones and dead-zones of the flow. To improve the flow condition (air inlet and outlet from the system), an analysis of the flow inside the radiator attachment point with operating fans (inside the radiator housing) was performed. The results of the calculation are presented in Fig. 8.

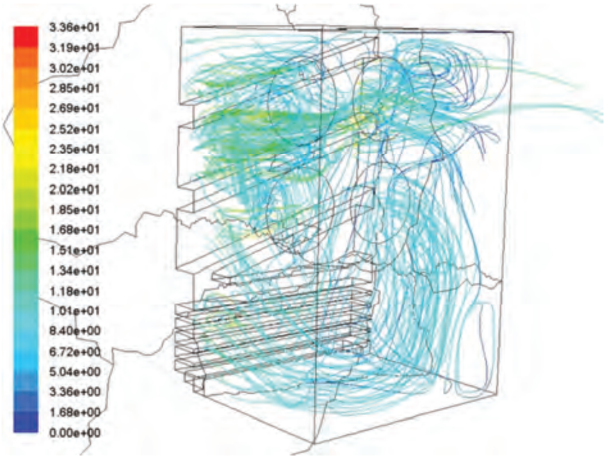

Fig. 8. Streamlines based on velocity [m/s] inside the radiator box

Observation of the streamlines indicates the need for precise direction the stream flow through the use of guide vanes.

The simulation results showed dead-fields of the flow, i.e. a decrease in the efficiency of the radiators and noise levels above 72 dB. Additionally, the position of the fans was found to be correct (no stream detachment and no flow swirl). However, flow dead-zones were observed during the operation of the fans. It was decided to redesign the fan-housing box. Four geometric models were selected for analysis (Fig. 9). They were modeled at the operating point corresponding to 50% of the fan load in the following geometry variants: (a) without a guide vane, (b) with one guide vane, (c) with two guide vanes, (d) with stream separation.

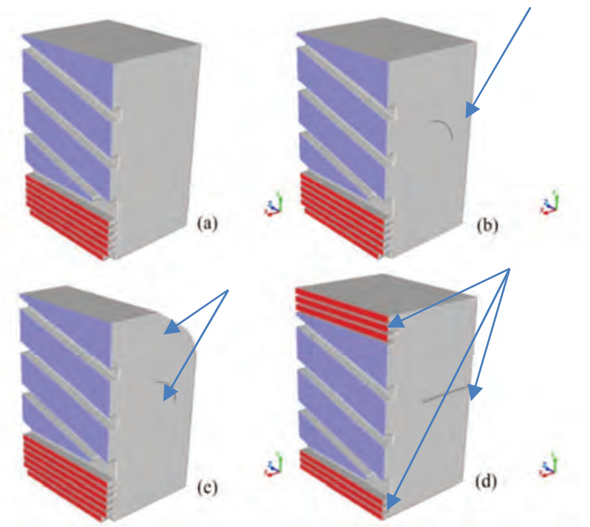

Fig. 9. Geometric models: (a) without guide vanes, (b) with one stream guide vane, (c) with two stream guide vanes, (d) with stream separation. The changes in geometry are indicated by arrows

Figure 10 shows the simulation results in the form of a determined distribution of acoustic pressure fields.

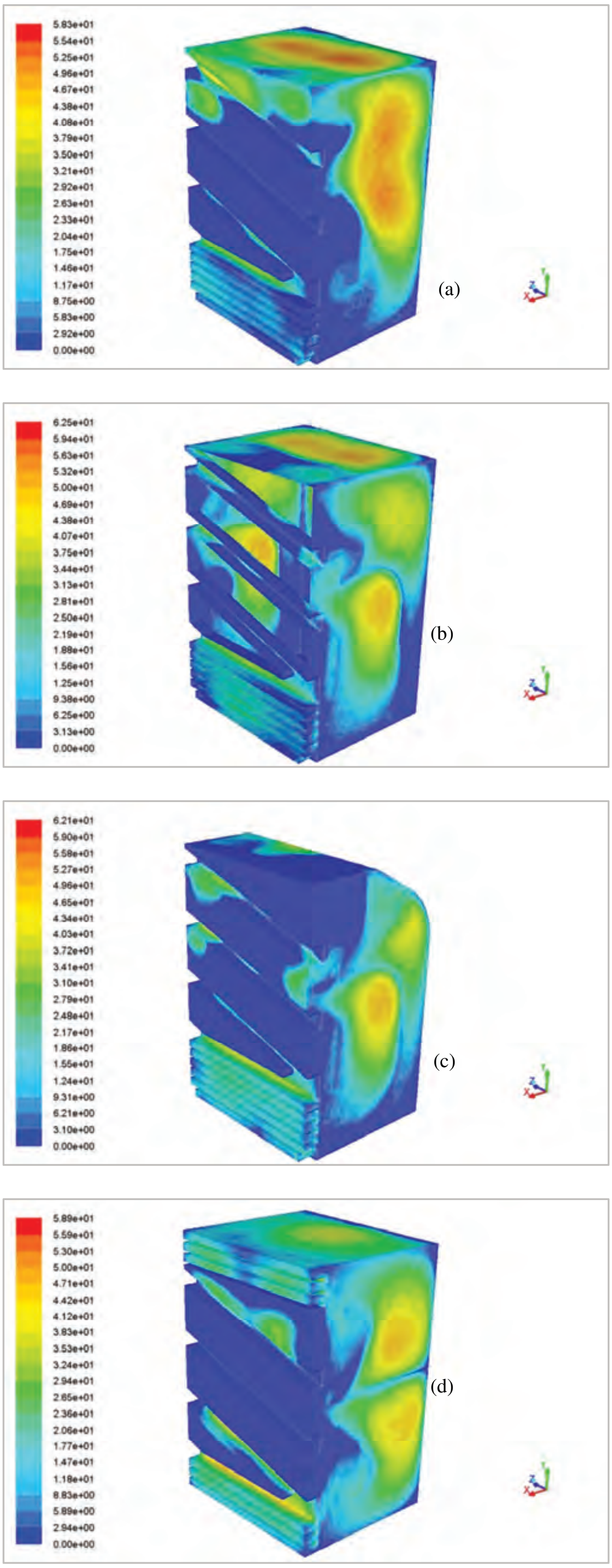

Fig. 10. Acoustic pressure fields [dB]: (a) without guide vanes, (b) with one stream guide vane, (c) with two stream guide vanes, (d) with stream separation

Velocity vector fields are shown in Fig. 11, while inlet and outlet velocity vector fields are presented in Fig. 12.

As a result of the simulation, it was found that the best solution in terms of noise emission as well as the flow phenomena that occur was obtained for variant d) – the variant ant d), no disadvantageous flow phenomena were observed (as opposed to other variants) like presence of dead-zones in the area of the inlet and outlet of the cooling medium and

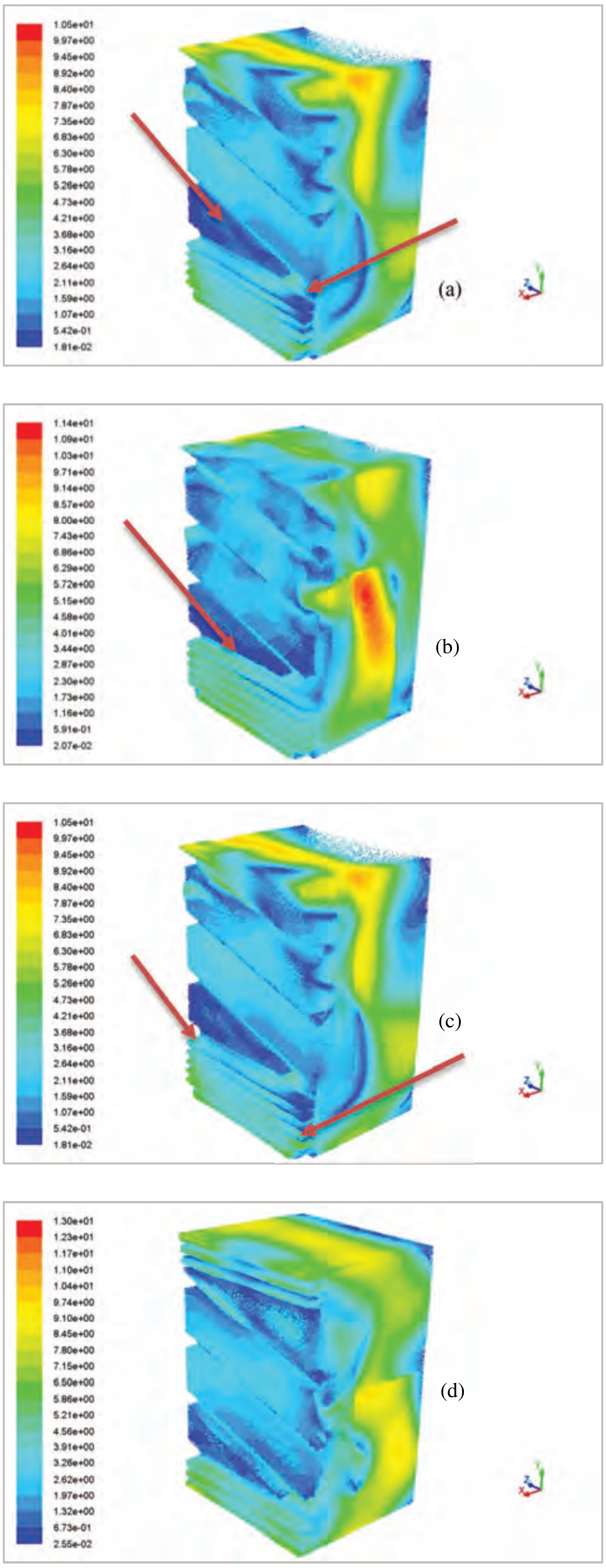

Fig.11. Velocity vector fields [m/s] (a) without guide vanes, (b) with one stream guide vane, (c) with two stream guide vanes, (d) with stream separation. The dead-zones and adverse flow events are indicated by red arrows

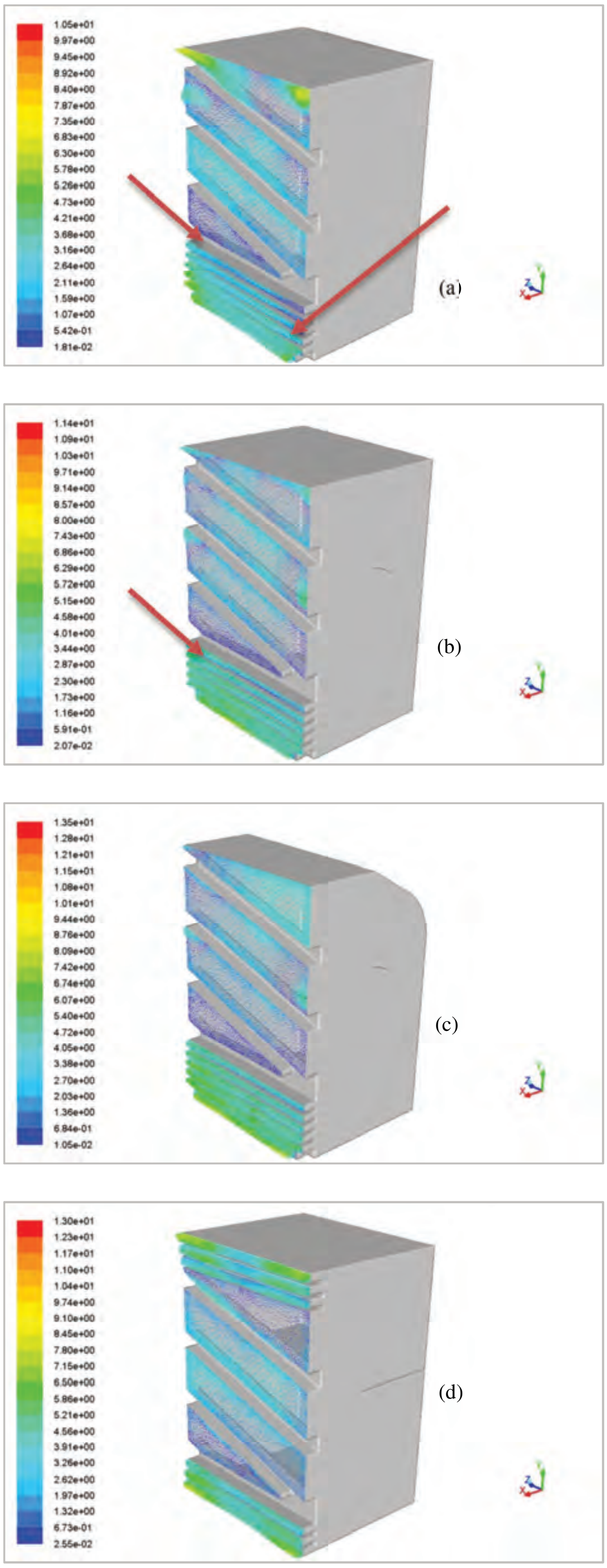

Fig. 12. Inlet and outlet velocity vector fields [m/s] (a) without guide vanes, (b) with one stream guide vane, (c) with two stream guide vanes, (d) with stream separation. The dead-zones and adverse flow events are indicated by red arrows

with the stream separation. The maximum values of the noise level for this variant were estimated at 57 dB. In vari return flow. The separation of the air stream improved the distribution of the velocity field, the pressure field and the acoustic field. A more even distribution of the velocity fields results in improved cooling efficiency while maintaining the same surface area of the cooling elements. Obtaining an even flow through the radiators also allows for the best cooling performance (energy efficiency).

The geometry of the system according to the d) variant is shown in Fig. 13.

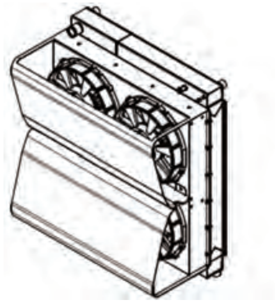

Fig. 13. Selected radiator geometry

In the next stage, empirical verification of the numerical model was conducted. A prototype device was made according to the geometric model selected as a result of simulation tests. The experimental tests were conducted under field conditions at the Military Institute of Armoured and Automotive Technology. Figure 14 shows the view of the test stand during the study implementation.

Comparative tests of the base solution (Fig. 1) and the solution resulting from the numerical tests (Fig. 13) were performed. The results of noise level measurements – comparison of the base and prototype versions (developed on the basis of numerical analysis) are shown in Fig. 15.

The accuracy of the calculation model was found to be very good – under simulation conditions, the maximum noise level was estimated at 57 dB, under measurement conditions for the same operating point (50% of fan power) at 59 dB.

The measurements were then carried out to determine the prototype power requirement in laboratory and field conditions according to the measurement methods described in Chapter 3.

Figure 16 shows the results of laboratory tests, while Fig. 17 shows the results of field tests.

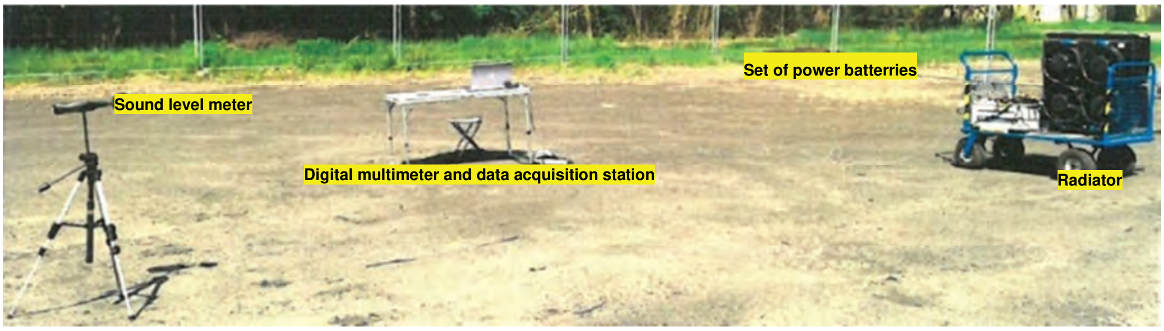

Fig. 14. The view of the test stand during the performance of acoustic pressure tests of the radiator in the field conditions at the Military Institute of Armoured and Automotive Technology (test certificate 41/LPE/2020)

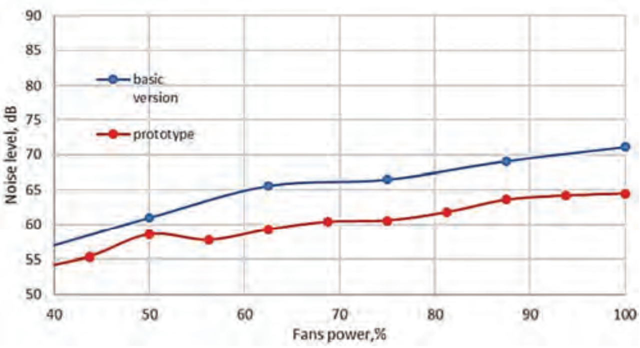

Fig. 15. Results of noise level measurements – comparison of the base and prototype versions (developed on the basis of numerical analysis)

It was found that the determined characteristics were convergent and that there were no changes in the electrical power requirement of the device after the optimization performed.

Based on the results of the power measurement in field conditions tests the model revealing the dependency of power requirement and fan power was developed. Figure 17 shows the curve fitted to the observations. The RMSE of the model is 219.9 and $R^2 = 0.9958$. The power of the model is determined by comparing the residuals to the Gaussian distribution.

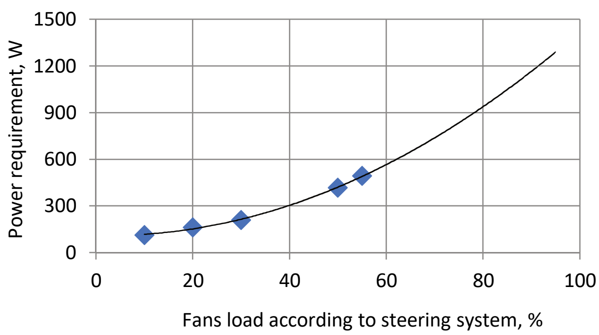

Fig. 16. Cooling fan power consumption depending on the % of the load defined by the control system in laboratory conditions

The verification was done by hypothesis testing and with the aid of the Shapiro-Wilk Kolmogorov Smirnov test. In this case the p = 0.3504. Therefore, there is no reason to

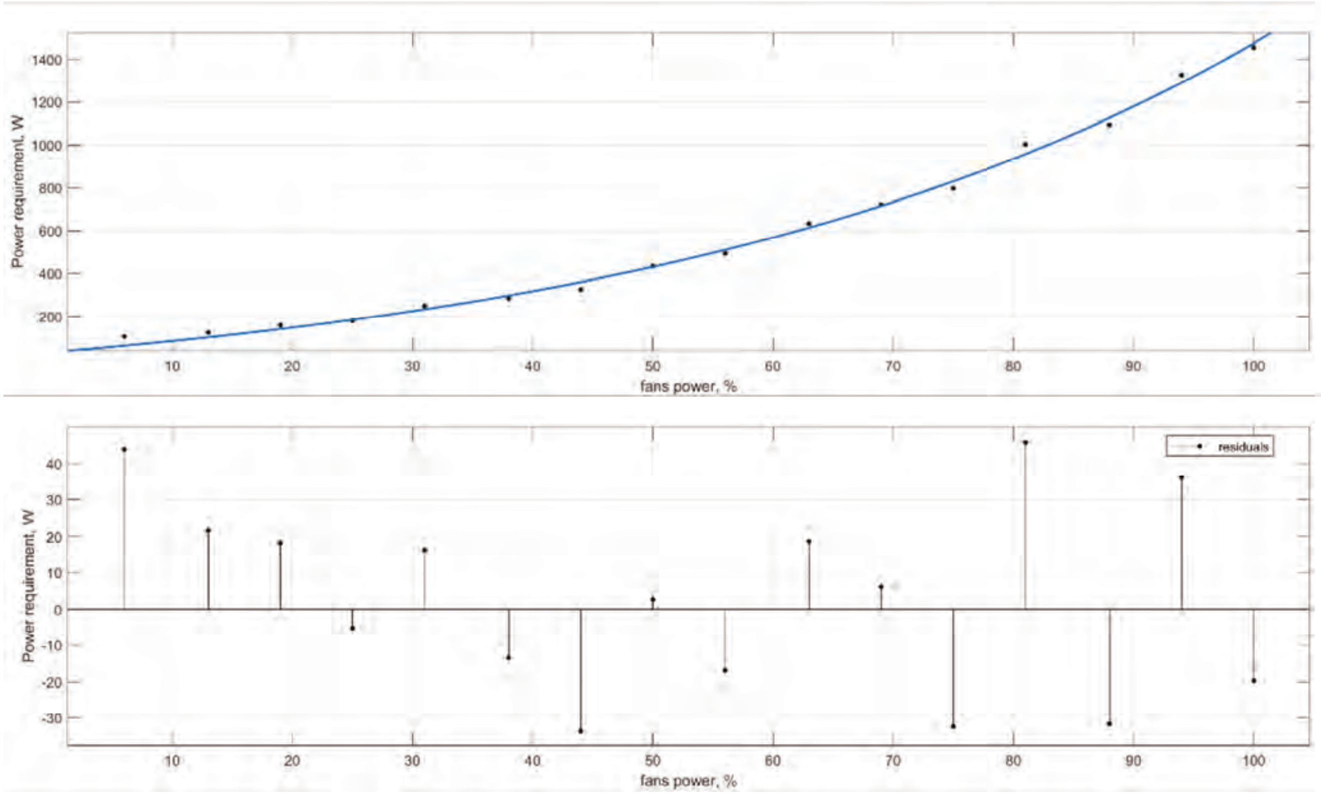

Fig. 17. Observed parameters of power requirement, W, with respect to fan load, %, in field conditions

reject the null hypothesis that constitutes the Gaussian distribution of the residuals. The relatively high value of the p coefficient proves that the model is accurate and reliable.

Based on the results it was found that the determined characteristics were convergent and that there were no changes in the electric power requirement of the device after the performed optimization

5. Conclusions

1. The application of the CFD RANS method of the two-equation k-ε turbulence model with the heat transfer and the acoustic model as a tool to optimize the vehicle's cooling system in terms of noise emission is an adequate instrument for the intended purpose. The model was validated in two stages under laboratory and field conditions. The consistency of the simulation results and test results of the real object was demonstrated, i.e., 57 dB as a result of the simulation and 59 dB on the basis of field tests.
2. As a result of the work, the design of the cooler for the electric bus battery pack was optimized. Based on the observation and flow analysis, it was decided to make a geometrical change involving the separation of the cooling medium stream, which improved the distribution of the velocity field, the pressure field and the acoustic field. During the numerical analysis of the selected geometry variant, no adverse flow phenomena were observed, such as the presence of dead-zones in the area of the inlet and outlet of the cooling medium and return flow.
3. The separation of the air stream flowing through the cooler resulted in the reduction of the maximum velocity values, which had a direct impact on the reduction of the flow resistance.
4. Reducing the pressure level and obtaining an even flow through the radiators allowed for a higher cooling efficiency while maintaining a comparable level of electric power.
5. The presented results indicate a new approach to the method of shaping internal elements of electric vehicle coolers for improving energy efficiency, which translates directly into economic indicators (also resulting from battery life) and reduces noise emissions.
6. The good convergence of the model with the results of the experiments points to the possibility of developing generalized guidelines for designers of electric vehicles, which, however, requires further research based on CFD analysis with the proposed method of calculating other design solutions for different battery powers and their location in the vehicle.
7. The results of the research indicate the necessity to change the priorities in the process of designing cooling systems in vehicles, taking into account the flow phenomena in the first place (currently these are mainly visual aspects).

Acknowledgements

The research was conducted as part of a project co-financed by the National Centre for Research and Development entitled: "Innovative generation of ultra-light cooling modules with minimized noise emission, electricity demand, through the implemented new system of ongoing monitoring of operating parameters, intended for new electric vehicles, including those powered by hydrogen cells", project no: POIR.01.01.01-00-0147/17.

Bibliography

[1] AKINLABI, H.A.A., SOLYALI, D. Configuration, design, and optimization of air-cooled battery thermal management system for electric vehicles: A review. *Renewable and Sustainable Energy Reviews*. 2020, **125**, 109815. https://doi.org/10.1016/j.rser.2020.109815

[2] BAN. L., DUB. W., JIN. T. et al. A roughness parameter considering joint material properties and peak shear strength model for rock joints. *International Journal of Mining Science and Technology*. 2021, **31**, 413-420. https://doi.org/10.1016/j.ijmst.2021.03.007

[3] BEHIA, H., KARIMIA, D., BEHIC, M. et al. A new concept of thermal management system in Li-ion battery using air cooling and heat pipe for electric vehicles. *Applied Thermal Engineering*. 2020, **174**, 115280. https://doi.org/10.1016/j.applthermaleng.2020.115280

[4] BENABDELAZIZ, K., LEBROUHI, B., MAFTAH, A. et al. Novel external cooling solution for electric vehicle battery pack. *Energy Reports*. 2020, **6**, 262-272. https://doi.org/10.1016/j.egyr.2019.10.043

[5] BIAŁY, M., PIETRYKOWSKI, K., TULWIN, T. et al. CFD numerical simulation of the indirect cooling system of an internal combustion engine. *Combustion Engines*. 2017, **170**(3), 8-18. https://doi.org/10.19206/CE-2017-302

[6] CHEN, Y., ZOU, H., DONG, J. et al. Experimental investigation on the heating performance of a CO_2 heat pump system with intermediate cooling for electric vehicles. *Applied Thermal Engineering*. 2021, **182**, 116039. https://doi.org/10.1016/j.applthermaleng.2020.116039

[7] DONG, J., WANG, Y., SHIWEI, J. et al. Experimental study of R744 heat pump system for electric vehicle application. *Applied Thermal Engineering*. 2020, **183**(1), 116191. https://doi.org/10.1016/j.applthermaleng.2020.116191

[8] HU, J., XU, G., SHIA, Y. et al. A numerical simulation investigation of the influence of rotor wake on sediment particles by computational fluid dynamics coupling discrete element method. *Aerospace Science and Technology*. 2020, **105**, 106046. https://doi.org/10.1016/j.ast.2020.106046

[9] ISHIHARA, T., QIAN, G.-W., QI, Y.-H. Numerical study of turbulent flow fields in urban areas using modified k-ε model and large eddy simulation. *Journal of Wind Engineering & Industrial Aerodynamics*. 2020, **206**, 104333. https://doi.org/10.1016/j.jweia.2020.104333

[10] JOUVET, G., HUSS, M., BLATTER, H. et al. Numerical simulation of Rhonegletscher from 1874 to 2100. *Journal of Computational Physics*. 2009, **228**, 6426-6439. https://doi.org/10.1016/j.jcp.2009.05.033

[11] KIM, J., OH, J., LEE, H. Review on battery thermal management system for electric vehicles. *Applied Thermal Engineering*. 2019. **149**, 192-212. https://doi.org/10.1016/j.applthermaleng.2018.12.020

[12] LU, M., ZHANG, X., JI, J. et al. Research progress on power battery cooling technology for electric vehicles. *Journal of Energy Storage*. 2020, **27**, 101155. https://doi.org/10.1016/j.est.2019.101155

[13] MIRANDA, M.H.R., SILVA, F.L., LOURENÇO, M.A.M. et al. Electric vehicle powertrain and fuzzy controller optimization using a planar dynamics simulation based on a real-world driving cycle. *Energy*. 2022, **238**, 121979. https://doi.org/10.1016/j.energy.2021.121979

[14] QIU, C., SHI, W. Comprehensive modeling for optimized design of a thermoelectric cooler with non-constant cross-section: Theoretical considerations. *Applied Thermal Engineering*. 2020, **176**, 115384. https://doi.org/10.1016/j.applthermaleng.2020.115384

[15] SHASHANK, A. Selection of thermal management system for modular battery packs of electric vehicles: A review of existing and emerging technologies. *Journal of Power Sources*. 2018, **400**, 621-640. https://doi.org/10.1016/j.jpowsour.2018.08.020

[16] SHEN, M., GAO, G. Structure design and effect analysis on refrigerant cooling enhancement of battery thermal management system for electric vehicles. *Journal of Energy Storage*. 2020, **32**, 101940. https://doi.org/10.1016/j.est.2020.101940

[17] SHEN, R., JIAO, Z., PARKER, T. et al. Recent application of computational fluid dynamics (CFD) in process safety and loss prevention: A review. *Journal of Loss Prevention in the Process Industries*. 2020, **67**, 104252. https://doi.org/10.1016/j.jlp.2020.104252

[18] SROKA, Z.J., SADLAK, Z. Thermal activation of the combustion chamber of a reciprocating internal combustion engine. *Journal of Thermal Science*. 2018, **27**(5), 449-455. https://doi.org/10.1007/s11630-018-1039-7

[19] SUN, D., SHI, X., ZHANG, Y. et al. Spatiotemporal distribution of traffic emission based on wind tunnel experiment and computational fluid dynamics (CFD) simulation. *Journal of Cleaner Production*. 2021, **282**, 124495. https://doi.org/10.1016/j.jclepro.2020.124495

[20] SUN, D., ZHENG, Y., DUAN, R. Energy consumption simulation and economic benefit analysis for urban electric commercial-vehicles. *Transportation Research Part D: Transport and Environment*. 2021, **101**, 103083. https://doi.org/10.1016/j.trd.2021.103083

[21] UÇAR, S., UÇAR, E., ÖZDEMIR, N. et al. Mathematical analysis and numerical simulation for a smoking model with Atangana–Baleanu derivative. *Chaos, Solitons and Fractals*. 2019, **118**, 300-306. https://doi.org/10.1016/j.chaos.2018.12.003

[22] WANG, Y., DONG, J., SHIWEI, J. et al. Experimental Comparison of R744 and R134a heat pump systems for electric vehicle application. *International, Journal of Refrigeration*. 2020, **121**, 10-22. https://doi.org/10.1016/j.ijrefrig.2020.10.026

[23] WORSZTYNOWICZ, B. Experimental verification of design calculations of the internal combustion engine cooling system. *Combustion Engines*. 2019, **179**(4), 132-135. https://doi.org/10.19206/CE-2019-421

[24] WORSZTYNOWICZ, B. Influence of the method of implementing the forced air flow through the cooling system on the temperature of the coolant in heavy-duty engines. *Combustion Engines*. 2017, **171**(4), 51-55. https://doi.org/10.19206/CE-2017-409

[25] WU, J., ZHOU, G., WANG, M. A comprehensive assessment of refrigerants for cabin heating and cooling on electric vehicles. *Applied Thermal Engineering*. 2020, **174**, 115258. https://doi.org/10.1016/j.applthermaleng.2020.115258

[26] YUAN, H., SU, H., WANG, L. et al. Numerical analysis on airflow and thermal field in quiet power vehicle compartment. *Procedia Engineering*. 2017, **174**, 571-578. https://doi.org/10.1016/j.proeng.2017.01.189

[27] YUAN, R., FLETCHER, T., AHMEDOV, A. et al. Modelling and co-simulation of hybrid vehicles: a thermal management perspective. *Applied Thermal Engineering*. 2020, **180**, 115883. https://doi.org/10.1016/j.applthermaleng.2020.115883

[28] ZAWIŚLAK, M. Method of designing and modernising machines and flow systems using Computational Fluid Mechanics. *Poznan Publishing House*, Poznan 2017.

[29] ZHANG, C., UDDIN, M., ROBINSON, A.C. et al. Full vehicle CFD investigations on the influence of front-end configuration on radiator performance and cooling drag. *Applied Thermal Engineering*. 2018, **130**, 1328-1340. https://doi.org/10.1016/j.applthermaleng.2017.11.086

Prof. Anna Janicka, DSc., DEng. – Mechanical Faculty, Wroclaw University of Science and Technology.
e-mail: *anna.janicka@pwr.edu.pl*

Artur Głogoza – OE INDUSTRY, Poland.
e-mail: *a.glogoza@oeindustry.com*

Maciej Zawiślak, DSc., DEng. – Mechanical Faculty, Wroclaw University of Science and Technology.
e-mail: *macej.zawislak@pwr.edu.pl*

Radoslaw Włostowski, MEng. – Mechanical Faculty, Wroclaw University of Science Technology.
e-mail: *radoslw.wlostowski@pwr.edu.pl*

Article citation info:
KAWALEC, M., PERKOWSKI, W., ŁUKASIK, B. et al. Applications of the continuously rotating detonation to combustion engines at the Łukasiewicz – Institute of Aviation. *Combustion Engines*. 2022, **191**(4), 51-57. https://doi.org/10.19206/CE-145409

Michał KAWALEC
Witold PERKOWSKI
Borys ŁUKASIK
Adam BILAR
Piotr WOLAŃSKI

Combustion Engines
Polish Scientific Society of Combustion Engines

Applications of the continuously rotating detonation to combustion engines at the Łukasiewicz – Institute of Aviation

ARTICLE INFO

Received: 10 November 2021
Revised: 20 December 2021
Accepted: 29 December 2021
Available online: 2 January 2022

In the paper short information about advantages of introduction of detonation combustion to propulsion systems is briefly discussed and then research conducted at the Łukasiewicz – Institute of Aviation on development of the rotating detonation engines (RDE) is presented. Special attention is focused on continuously rotating detonation (CRD), since it offers significant advantages over pulsed detonation (PD). Basic aspects of initiation and stability of the CRD are discussed. Examples of applications of the CRD to gas turbine and rocket engines are presented and a combine cycle engine utilizing CRD are also evaluated. The world's first rocket flight powered by liquid propellant detonation engine is also described.

Key words: *detonation, detonation engines, RDE, experimental rocket*

1. Introduction

The first idea concerning possibility of increasing efficiency of engines due to applications of detonative combustion came from Zeldovich [1], but at that time no one was interested in this idea. At the end of fifties and beginning of sixties of the last century continuously rotating spinning detonation was discovered in Institute of Hydrodynamics of the Soviet Academy of Sciences in Novosibirsk and was described in a few publications [2–4]. At the same time at the University of Michigan Nicholls et al. [5] was tested laboratory model of the Pulsed Detonation Engine (PDE) and a few years later research were undertaken on applications of CRD to rocket engines, but unfortunately at that time they been unable to succeed. Adamson et al. was only able to perform theoretical analysis of CRD structure in combustion chamber of rocket engines [6, 7]. Since that time research on application of the CRD to propulsion system was abounded for many years. Research on application of detonation to the PDE were reinitiated at the end of the last century by Edelman et al.[8, 9], and dominated the research on the applications of detonation to propulsion system up to beginning of twenty first century. More information about such research could be also find on survey paper devoted to the PDE [10–12]. Only at the end of last century and the beginning of this one research on the possible application of the CRD to propulsion system was nearly simultaneously reinitiated in Russia, France, Poland and Japan then exponential interest on such system was significantly increased [13–15]. Since that time many initiatives were undertaken to better understand nature of detonative propulsion and to develop engines based on detonation. The rate of increase publications devoted to RDE at the beginning of XXI century is shown in Fig. 1.

The aim of the article is to discuss the latest works related to the issue of rotating detonation carried out at Łukasiewicz – Institute Aviation.

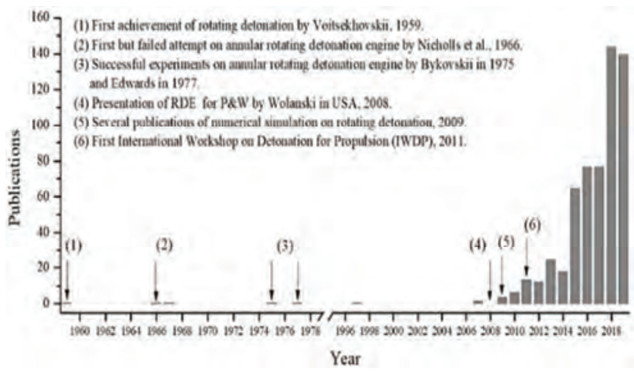

Fig. 1. Graphical illustration of numbers of publication related to RDE research from time of first experimental obtainment of the continuously rotating detonation up to recent time (2019) (Courtesy of Bing Wang) [16]

2. Detonation versus deflagration

It is well known that combustion of gaseous mixtures can happen at two different modes: deflagration and detonation. During deflagration, combustion is usually slow and flame velocity is always subsonic, while for detonative mode flame propagate with supersonic velocity. For deflagrative combustion pressure at the end of combustion always decrease, while for detonative combustion is always increased. Typically for detonation of fuel air mixtures pressure can be increased about 15 times, while detonation of fuels with gaseous oxygen can increase more than 30 times. Details of the detonative combustion of gaseous mixtures can be found in many publications [14–17]. Because combustion of the same mixture can result in very different parameters depending on the deflagrative or detonative mode, application of different modes of combustion to a propulsion system can also result in different performance of the propulsion system. It was shown already in many publications that application of detonative combustion to engines can result in significant increase of engine efficiency. For example, if detonative combustion is applied to the turbojet engine, theoretical engine efficiency could be even increased more than 30% [14], but even if in reality this efficiency will be increased only by 10%, the fuel saving for one year will result in many billions of dollars, as well as significant reduction of CO_2 emission.

3. Detonative engines

Detonative combustion could be applied in three different configurations of engines: Standing Detonation Engines, Pulsed Detonation Engines (PDE) and Rotating Detonation Engines (RDE). Application of detonation combustion for Standing Detonation Engines was already proposed in fifties of the last century [5, 25, 26], but beside theoretical analyses they have been extensively tested, since for a such engine operation speed is limited to the velocity close to the theoretical detonation velocity. Such engine could only operate in flight velocity higher than theoretical detonation velocity, but not too much higher, since then external drag of the engine could overcome thrust produced by the engine. Only realistic applications of the detonation to propulsion system are PDE and RDE engines configurations.

3.1. Research on the PDE

Principles of operation of the PDE is very simple. Long tube is filled with gaseous fuel (hydrogen) and air. When mixture is form, combustion is initiated by electrical spark. Composition of the mixture and dimension of the tube should allow fast transition into detonation. During detonative combustion of the mixture, very high pressure is generated and thrust is produced. Then after completion of detonation high pressure combustion products leaves tube and produce low pressure, due to expansion, and pressure in the tube drops below the surrounding pressure. This initiates flow of air into the tube and mix it with injected fuel. After mixture is created, ignition is again initiated and the new cycle begins. Detailed descriptions of such cycle can be found in [14, 15]. First pulsed detonation engine was build and successfully tested at the University of Michigan (Fig. 2) [5], but at that time there were no interests in development of such propulsion system, so research on PDE were abandoned and reinitiated at the end of XX century [8–10]. Many PDE were developed in different laboratory [11–21], mostly in USA, Russia and China, and at the beginning of XXI century even experimental aircraft powered by PDE was built and tested by a team from the US Air Force Research Laboratory [12].

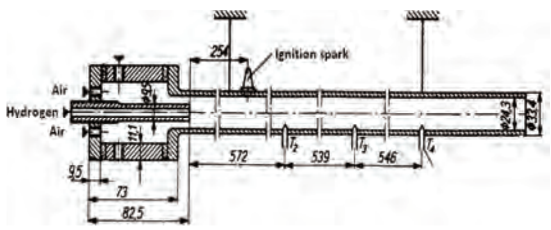

Fig. 2. Schematic diagram of the first PDE developed at the University of Michigan [5, 14]

The engine for this aircraft (Fig. 3) consisted of four tubes producing pulse detonations at a frequency of 80 Hz, creating thrust of 890 newton. Only one test of such aircraft was conducted during which the PDE operated only for 10 s at the altitude of 30 m. Due to a very high noise (195–200 dB) and very high vibration, produced by the PDE, test of such propulsion system were terminated and this aircraft is now in Air Force Museum at Wright-Patterson Air Force Base – Fig. 3.

Fig. 3. The first and only flight of aircraft powered by PDE on 31st of January 2008 at the US Air Force Mojave Air and Space Port [23]

Similar thing happened to a gas turbine with pulsed detonation combustion chamber which has been developing by GE [22]. Even the system was working at the laboratory conditions, pulsating character of detonation chamber created to many problems which have to be solved before application of such system to practical use. Termination of this project was also effected by rapid development of application of continuously rotating detonation to propulsion systems.

3.2. Research of the RDE

Continuously rotating detonation, which was first discovered nearly 60 years ago by Russian scientists in Novosibirsk [2, 3], is now commonly used in developing of the RDE as well as in chambers of gas turbine, not only in aircraft engines but it also could be used in stationary power system installations. Typical scheme of annular detonation chamber is shown in Fig.4.

Air or oxidizer is supply trough narrow entry slit and fuel is injected trough many tiny holes which are located around one wall of the detonation chamber.

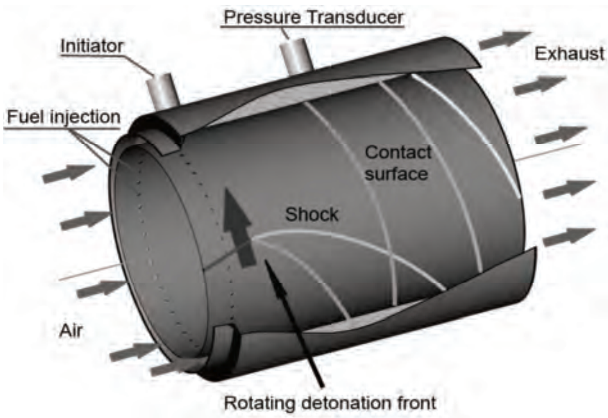

Fig. 4. Schematic diagram of annular detonation chamber [14]

Such way of oxidizer and fuel supply is necessary to ensure quick mixing of both components to form nearly uniform mixture which can support detonation. In the chamber also initiator is installed to initiate detonation as well as ports for measurement of detonation parameters. The height of the annulus channel should be also larger than critical dimension, which will allow detonation to propagate. So for each mixture critical dimensions, which allow detonation to propagate depends on mixture parameters, such as mixture composition, initial pressure in the chamber and rate of mixture supply to the chamber [29–31]. If all necessary conditions of mixture supply are fulfilled and sufficient energy of initiation is released, then in a short time a stable continuously rotating detonation in the chamber will be achieved. Pressure record of stable detonation in the annular chamber is shown in Fig.5. and numerically calculated structure of stable detonation is shown in Fig.6. In this case two detonation waves are propagating in the same direction, but generally many different conditions of waves propagation in detonation chambers are observed.

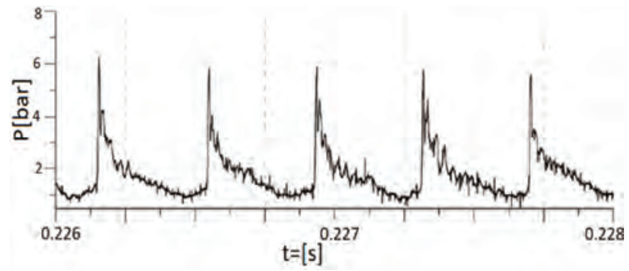

Fig. 5. Pressure variations of stable detonation in the annular chamber [14]

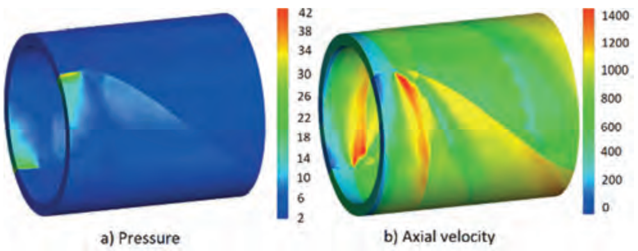

Fig. 6. Numerically calculated 3-D flowfield of the two waves stable rotating detonation structure in annular detonation chamber [32]

Stabilization of direction of rotating detonation wave was studied by Kawalec et al. [33], which show that direction of rotation could be controlled by small eccentricity synchronized with selected initiation place.

CRD could be initiated also in different shape of the chambers, such as presented by Bykovskii et al. – Fig. 7. [34], but also con-shaped and successfully tested by Kawalec et al. [33]. There are also other geometries already tested, such as cylindrical chamber with short insert and hollow chamber and disk-shaped connected to the nozzle and other [24–27, 35–41].

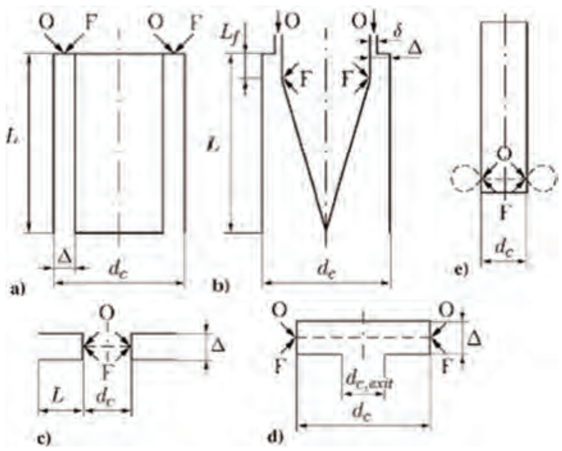

Fig. 7. Geometries of detonation chambers tested by Bykovskii et al. a) annular chamber, b) partially annular with inner cone, c) open space inner disc, d) disc chamber, e) open space external disc [34]

4. Research on application of the CRD to propulsion systems at the Łukasiewicz – Institute of Aviation

Research on the application of the CRD to propulsion system is carried out at the Institute of Aviation for more than 10 years. During that time a few systems with CRD were developed, such as GTD-350 with detonation chamber, special system of mixture preparation which guarantee stable operation in annular/cylindrical chambers working on liquid fuels, control of directions of rotating of detonation wave in the annular chamber, development of disk and con shaped detonation chambers working on liquid propellants with regenerative cooling and designing and launching of first in the world rocket powered by disk-shaped detonation liquid rocket engine. We will briefly mention first two systems, which are already described in the publications [27, 42–43], but more details will be presented on the development of rocket and rocket-ramjet engine as well as a very successful flight of experimental rocket powered by disk-shaped liquid rocket engine utilizing CRD.

4.1. Research on applications of the CRD to the air-breathing propulsion

During 2010–2015 development of gas turbine engine with detonation combustion chamber was carried out at our Institute under the project UDA-POIG.01.03.01-14-071 “Gas turbine with detonative combustion chamber” supported by EU and Ministry of Regional Development of Poland. During this project many problems were studied, such as: mixture formation, development of proper geometry of detonation chamber, detonation initiation as well as the operation of this engine with detonation chamber. Engine was tested on the following fuels: Jet-A, Jet-A with additions of gaseous hydrogen and on gaseous hydrogen only. It was found that engine operating on gaseous hydrogen demonstrated increased thermal efficiency by 5–7%, as compared to the based engine operating on conventional fuel with the classical combustion chamber. Details of this research can be found in [27, 42, 43]. It must be also added that recent initiatives of the Airbus company to develop aircraft powered by hydrogen fuel will also open a way for the introduction of turbojet engine with detonative combustion chamber, since it was already proved, much higher efficiency can be achieved with applications of the turbojet engines utilizing CRD in engine’s combustion chamber [44, 45].

Another research which was continued, after the above project was completed, was focused on development of the new system of preparation of liquid jet fuels for combustion in annular detonation chamber. Development of such system for air-breathing engines utilizing CRD will improving engine efficiency and thus results in fuel saving. This research concerns development of system which could allow preparation of liquid fuel-air mixture which can support stable CRD in annular chamber [24]. Schematic diagram of such system is presented in Fig. 8a and typical recorded pressure signals of detonation in Fig. 8b.

a)

b)

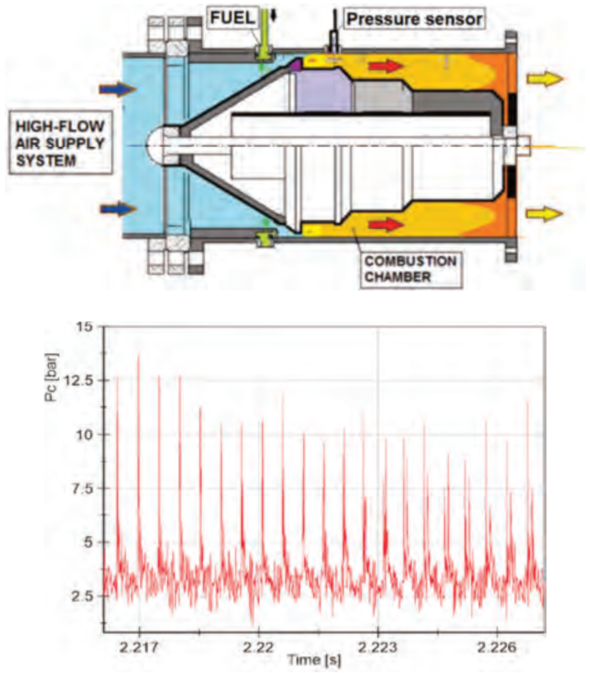

Fig. 8. Schematic diagram of the annular detonation chamber (a) and recorded pressure of the CRD for Jat-A – air mixture (b)

4.2. Research on applications of the CRD to rocket engines

For the last few years in the Institute research on application of the CRD to rockets engines were initiated. Initiation of those research came from US Air Force Research Laboratory with granted the project related to development of the methods of wave direction control in rocket engine. The main goal of this research was to find effective way of control direction of wave rotation in detonation engine. Tests were carried out for gaseous mixtures such as hydrogen-air and methane-oxygen. A few different methods were tested to control direction of wave motion, but it was found that applying small eccentricity such control could be achieved (see Fig. 9).

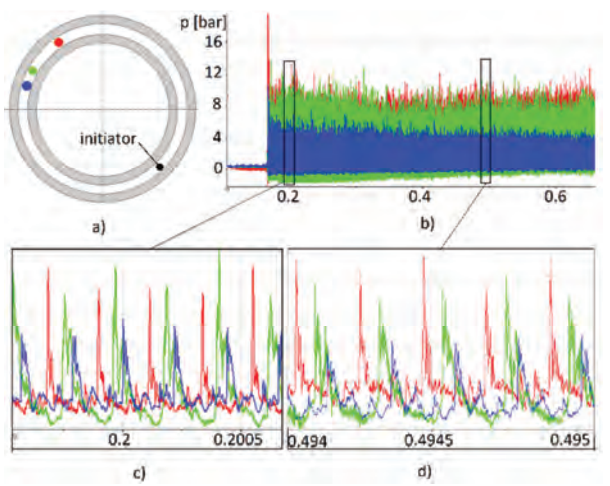

Fig. 9. The example of an experiment with the use of the initiator close to the small eccentricity, a) schematic of the cross section of the annular detonation chamber with colored points of located pressure transducers and indication of the position of the initiator, b) recorded pressure by the three transducers, c, d) enlarged randomly selected pressure records. More detailed description of this research can be found in [33]

Another research was directed in development of the liquid propellant rocket engine which utilize CRD. As a propellants liquid propane (C_3H_8) and liquid nitrous oxide (N_2O) were used. The tests were carried out in an engines with an annular, a disc-shaped and a cone-shaped detonation chambers. Pictures of the tested engines can be seen in Fig. 10. The specific impulse obtained of the disk-shaped engine was equal to 1600 m/s, about 80% of theoretical value. For con-shaped engine with regenerative cooling, the specific impulse increased to 2005 m/s.

a)

b)

c)

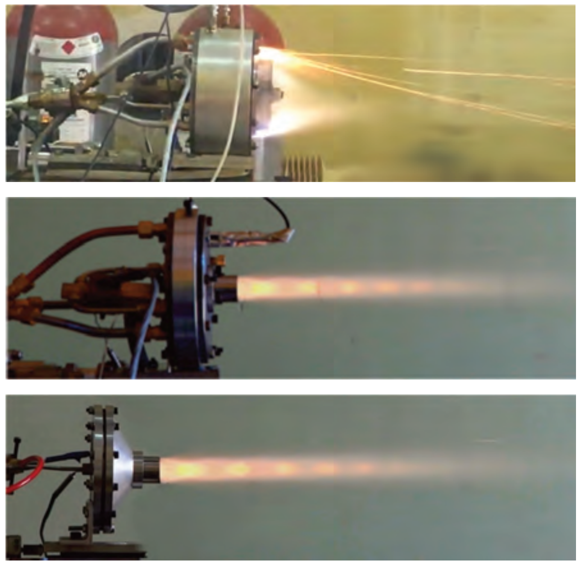

Fig. 10. Rocket RDE: with annular cylindrical detonation chamber (a), with disc-shaped detonation chamber (b) and with con-shaped detonation chamber (c) [21]

Also the first research on possibility of using combined cycle rotating detonation in rocket-ramjet engine was conducted. For this case rocket engine was operating on fuel rich conditions. This allow afterburning of hot, not completely reacted products from the rocket engine, which was burning with air passing through ramjets subsonic combustion chamber and generate extra trust. It was shown that such combined cycle Rocket-Ramjet can, in optimum operating condition exhibit 25% increase of efficiency as compare to rocket itself operating in similar conditions. Picture of the rocket-ramjet engine during test at the experimental stand at our Institute is shown in Fig. 11.

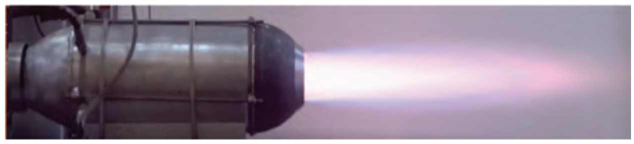

Fig. 11. Test of the rocket-ramjet engine at the experimental test stand at Łukasiewicz – Institute of Aviation [33]

4.3. Development of experimental rocket powered by liquid fueled rocket engine utilizing CRD

Since the liquid rocket engines utilizing CRD were developed at our Institute, the next logical step was to apply one of the engine to propel the experimental rocket. The cone-shaped engine was chosen as the propulsion system for the rocket. Before installing it on the rocket, special validation tests were carried out in the laboratory. As it was already mentioned, as propellants liquid Propane and liquid Nitrous Oxide were used. To ensure a few seconds work, engine was design in such a way that both liquid components were used for cooling engine's walls. Engine was first tested at the research stand in horizontal conditions, but after completion of such tests engine was integrated with the rocket and was also tested in vertical condition and with supply of both propellants from the rocket tanks. Both propellant tanks were pressurized before experiment by gaseous helium. This guaranteed nearly constant rate of feeding of engine with both propellants. Only after such successful static tests of the engine integrated with the rocket, the experiments was conducted at the military test range outside Warsaw at WITU in Zielonka On September 15, 2021 at 9:29 rocket was successfully launched and reached the altitude of 450 m.

Fig.12. Launch of the experimental rocket power by liquid fueled RDE which utilize CRD at the military test range in WITU, Zielonka

Picture of the liftoff of the rocket is shown in Fig.12. The rocket engine, according to the plan, worked for 3.2 s, accelerating the rocket to a speed of 93 m/s, which allowed the rocket to reach an altitude of 450 m. It was the world's first attempt to use a detonation engine powered by liquid propellants (liquid propane and liquid nitrous oxide) to propel a rocket. It was also world's first detonation engine that achieved flight under its own power.

5. Conclusions

Łukasiewicz – Institute of Aviation is engaged in research on application of CRD for different propulsion system for more the 10 years. The most important achievements in this field are:

1. Development of the detonation combustion chamber for GTD-350 engine, which working on gaseous hydrogen fuel shows improvements of engines efficiency by 5–7% as compare to base engine supply by Jet-A fuel.
2. Development of effective mixture preparation system which allow to achieve stable sustainable operation of CRD in the annular detonation chamber for the Jet-A – air mixture.
3. Development of effective way of control of detonation wave rotation in the model of rocket engine combustion chamber.
4. Development of the liquid propellant disc-shaped and cone-shaped rocket engines with regenerative cooling by liquid propellants.
5. Development the combine cycle rocket-ramjet engine working on liquid propellants.
6. Development of the experimental rocket which utilized RDE cooled by liquid propellants and perform its successful flight test. It's the world's first detonation engine that achieved flight under its own power.

Due to this activities and achievements Institute will be more engaged in further development of this very promising research and hopefully will widen international cooperation in this field.

Acknowledgments

Authors would like to thank Direction of the Łukasiewicz – Institute of Aviation for the continuous support of the research of application of the CRD to propulsion systems. Also authors thanks WITU in Zielonka for providing test range for rocket launch.

Bibliography

[1] ZELDOVICH, Y.B. On the use of detonative combustion in power engineering. *Journal of Technical Physics*. 1940, **10**, 1453-1461.

[2] VOITSEKOVSKII, B.B. et al. Work of the Siberian Division of the Academy of Sciences of SSSR, 1958, **9**.

[3] VOITSEKHOVSKII, B.V., MITROFANOV, V.V., TOPCHIYAN, M.E. Structure of the detonation front in gases. *Izdatielstvo SO AN SSSR*. Novosibirsk 1963 (in Russian).

[4] SOLOUKHIN, R.I. Shock waves and detonations in gases. *Mono Book Corp*. Baltimore 1966.

[5] NICHOLLS, J.A., WILKINSON, H.R., MORRISON, R.B. Intermittent detonation as a thrust-producing mechanism. *Jet Propulsion*. May 1957.

[6] ADAMSON, T.C., OLSSON, G.R. Performance analysis of a rotating detonation wave rocket engine. *Acta Astronautica*. 1967, **13**, 405-415.

[7] SHEN, P.I.-W., ADAMSON, T.C. Theoretical analysis of a rotating two-phase detonation in liquid rocket motors. *Acta Astronautica*. 1972, **17**, 715-728.

[8] EIDELMAN, S., GROSSMANN, W., LOTTATI, I. Review of propulsion applications and numerical simulations of the pulsed detonation engine concept. *Journal of Propulsion and Power*. 1991, **7**(6), 857-865. https://doi.org/10.2514/3.23402

[9] EIDELMAN, S., GROSSMANN, W. Pulsed detonation engine: experimental and theoretical review. *American Institute of Aeronautics and Astronautics Paper*. 1992. https://doi.org/10.2514/6.1992-3168

[10] KAILASANATH, K. Review of propulsion application of detonation waves. *American Institute of Aeronautics and Astronautics Journal*. 2000, **38**(9), 1698-1708. https://doi.org/10.2514/2.1156

[11] HINKEY, J.B., WILLIAMS, J.T., HENDERSON, S.E. et al. Rotary-valved, multiple-cycle, pulse detonation engine experimental demonstration. *American Institute of Aeronautics and Astronautics Paper*. 1997. https://doi.org/10.2514/6.1997-2746

[12] GUSTAVSSON, J., NORI, V., SEGAL, C. Inlet/engine interactions in an axisymmetric pulse detonation engine system. *Journal of Propulsion and Power*. 2003, **19**(2), 282-286. https://doi.org/10.2514/2.6109

[13] RASHEED, A., GLASER, A., DUNTON, R.A. et al. Experimental and numerical investigation of a valved multi-tube PDE. *46th AIAA Aerospace Sciences Meeting and Exhibit*. Reno 2008. https://doi.org/10.2514/6.2008-110

[14] MATSUOKA, K., ESUMI, M., KASAHARA, J. et al. Study on valve systems for pulse detonation engines. *46th AIAA/ASME/SAE/ASEE Joint Propulsion Conference & Exhibit*. Nashville 2010. https://doi.org/10.2514/6.2010-6672

[15] SHIMO, M., HEISTER, S.D. Multicyclic-detonation-initiation studies in valveless pulsed detonation combustors. *Journal of Propulsion and Power*. 2008, **24**(2), 336-344. https://doi.org/10.2514/1.29546

[16] PENG, C., FAN, W., ZHENG, L. et al. Experimental investigation on valves air-breathing dual-tube pulse detonation engines. *Applied Thermal Engineering*. 2012, **51**(1-2), 1116-1123. https://doi.org/10.1016/j.applthermaleng.2012.10.026

[17] LU, J., ZHENG, L., WANG, Z. et al. Operating characteristics and propagation of back-pressure waves in a multi-tube two-phase valveless air-breathing pulse detonation combustor. *Experimental Thermal and Fluid Science*. 2015, **61**, 12-23. https://doi.org/10.1016/j.expthermflusci.2014.10.010

[18] LU, J. Investigations on key technologies of the pulse detonation turbine engine. *Northwestern Polytechnical University*.

[19] RASHEED, A., TANGIRALA, V.E., VANDERVORT, C.L. et al. Interactions of a pulsed detonation engine with a 2D blade cascade. *42nd AIAA Aerospace Sciences Meeting and Exhibit*. Reno 2004. https://doi.org/10.2514/6.2004-1207

[20] FROLOV, S.M. (ed.) Pulsed Detonation Engines. *Torus Press*. Moscow 2006.

[21] FROLOV, S.M., AKSENOV, V., IVANOV, V. et al. Catapult launching tests of an unmanned aerial vehicle with a ramjet pulsed detonation engine. *European Conference for Aeronautics and Space Sciences*. 2008. https://doi.org/10.13009/EUCASS2019-178

[22] DEAN, A.J., RASHEED, A., TANGIRALA, V.E. et al. Operation and noise transmission of an axial turbine driven by a pulse detonation combustor. *Proceedings of International Gas Turbine Institute*. ASME Turbo Expo 2005, **6**, 1275-1284. https://doi.org/10.1115/GT2005-69141

[23] NORRIS, G. Pulse power: pulse detonation engine-powered flight demonstration marks milestone in Mojave. *Aviation Week & Space Technology*. 2008, **168**(7), 60.

[24] WOLAŃSKI, P. Detonation engines. *Journal of KONES*. 2011, **18**(3), 515-521.

[25] WOLAŃSKI, P. Detonative propulsion. *Proceedings of the Combustion Institute*. 2013, **34**(1), 125-158. https://doi.org/10.1016/j.proci.2012.10.005

[26] XIE, Q., JIA, Z., WENA, H. et al. Review on the rotating detonation engine and typical problems. *Transaction on Aerospace Research*. 2020, **4**(261), 107-163. https://doi.org/10.2478/tar-2020-0024

[27] WOLAŃSKI, P. (ed.) Research on detonative propulsion in Poland. *Wydawnictwa Naukowe Sieci Badawczej Łukasiewicz – Instytutu Lotnictwa*. Warsaw 2021.

[28] NETTLETON, M.A. Gaseous Detonations: Their Nature, Effects and Control. *Butterworths*. London 1987.

[29] WOLAŃSKI, P. Rotating detonation wave stability. *23rd International Colloquium on the Dynamics of Explosions and Reactive Systems*. Irvine 2011. http://www.icders.org/ICDERS2011/abstracts/ICDERS2011-0211.pdf

[30] XIE, Q., WEN, H., LI, W. et al. Analysis of operating diagram for H2/air rotating detonation combustors under lean fuel condition. *Energy*. 2018, **151**, 408-419. https://doi.org/10.1016/j.energy.2018.03.062

[31] SUCHOCKI, J., YU, S.T., HOKE, J. et al. Rotating detonation engine operation. *50th AIAA Aerospace Sciences Meeting including the New Horizons Forum and Aerospace Exposition*. Nashville 2012. https://doi.org/10.2514/6.2012-119

[32] YI, T-H., JING, L., TURANGAN, C. et al. Numerical study of detonation processes in rotating detonation engine and its propulsive performance. *Transaction on Aerospace Research*. 2020, **3**(260), 30-48. https://doi.org/10.2478/tar-2020-0015

[33] KAWALEC, M., PERKOWSKI, W., WOLANSKI, P. Development of rocket engines with detonation combustion chamber. [In] Wolański, P. (ed.): Research on detonative propulsion in Poland. *Wydawnictwa Naukowe Sieci Badawczej Łukasiewicz – Instytutu Lotnictwa*. Warsaw 2021.

[34] BYKOVSKII, F.A., ZHDAN, S.A., VEDERNIKOV, E.F. Continuous spin detonations. *Journal of Propulsion and Power*. 2006, **22**(6), 1204-1216. https://doi.org/10.2514/1.17656

[35] ANAND, V., GEORGE, A.S., DRISCOLL, R. et al. Characterization of instabilities in a rotating detonation combustor. *International Journal of Hydrogen Energy*. 2015, **40**(46), 16649-16659. https://doi.org/10.1016/j.ijhydene.2015.09.046

[36] TANG, X.M., WANG, J.P., SHAO, Y.T. Three-dimensional numerical investigations of the rotating detonation engine with a hollow combustor. *Combustion and Flame*. 2015, **162**(4), 997-1008. https://doi.org/10.1016/j.combustflame.2014.09.023

[37] FOTIA, M. Update on air breathing detonation driven propulsion research. *International Workshop on Detonation for Propulsion*. 2015.

[38] FOTIA, M., HOKE, J., SCHAUER, F. Experimental performance scaling of rotating detonation engines operated on gaseous fuels. *Journal of Propulsion and Power*. 2017, **33**(5), 1-10. https://doi.org/10.2514/1.B36213

[39] HEISTER, S., SLABAUGH, C. et al. Advancing pressure gain combustion in terrestrial turbine systems. *University Turbine Systems Research Workshop*. 1004. 2016. https://www.netl.doe.gov/sites/default/files/2017-11/utsr-25343-kickoff-presentation.pdf

[40] EUDE, Y., DAVIDENKO, D., FALEMPIN, F. et al. Use of the adaptive mesh refinement for 3D simulations of a CDWRE (continuous detonation wave rocket engine). *17th AIAA International Space Planes and Hypersonic Systems and Technologies Conference*. San Francisco 2011. https://doi.org/10.2514/6.2011-2236

[41] DAVIDENKO, D., EUDE, Y., FALEMPIN, F. Numerical study on the annular nozzle optimization for rocket application. *16th AIAA/DLR/DGLR International Space Planes and Hypersonic Systems and Technologies Conference*. Bremen 2009. https://doi.org/10.2514/6.2009-7390

[42] WOLAŃSKI, P., KALINA, P., BALICKI, W. et al. Development of Gasturbine with Detonation Chamber. Detonation Control for Propulsion, Pulse Detonation and Rotating Detonation Engines. *Springer*, Cham 2018. https://doi.org/10.1007/978-3-319-68906-7_2

[43] WOLAŃSKI, P., BALICKI, W., PERKOWSKI, W. et al. Experimental research of liquid-fueled continuously rotating detonation chamber. *Shock Waves*. 2021, **31**, 807-812. https://doi.org/10.1007/s00193-021-01014-w

[44] FLOTTAU, J., DUBOIS, T. Airbus places big bet on hydrogen propulsion as aviation's future. *Aviation Week and Space Technology*. 2020, 25 September. https://aviationweek.com/aerospace/program-management/airbus-places-big-bet-hydrogen-propulsion-aviations-future

[45] WARWICK, G., NORRIS, G., DUBOIS, T. Drive to decarbonize aviation raises green hydrogen challenges. *Aviation Week and Space Technology*. 2020, 8 October. https://aviationweek.com/special-topics/sustainability/drive-decarbonize-aviation-raises-green-hydrogen-challenges

Michał Kawalec, DEng. – Aircraft Propulsion System Department, Łukasiewicz Research Network – Institute of Aviation.
e-mail: *michal.kawalec@ilot.lukasiewicz.gov.pl*

Borys Łukasik, DEng. – Aircraft Propulsion System Department, Łukasiewicz Research Network – Institute of Aviation.
e-mail: *borys.lukasik@ilot.lukasiewicz.gov.pl*

Witold Perkowski, DEng. – Aircraft Propulsion System Department, Łukasiewicz Research Network – Institute of Aviation.
e-mail: *witold.perkowski@ilot.lukasiewicz.gov.pl*

Adam Bilar, MEng – Aircraft Propulsion System Department, Łukasiewicz Research Network – Institute of Aviation.
e-mail: *adam.bilar@ilot.lukasiewicz.gov.pl*

Prof. Piotr Wolański, DSc., DEng. – Łukasiewicz Research Network – Institute of Aviation.
e-mail: *piotr.wolanski@ilot.lukasiewicz.gov.pl*

Article citation info:
ANDRYCH-ZALEWSKA, M., CHŁOPEK, Z., MERKISZ, J. et al. Determination of characteristics of pollutant emission from a vehicle engine under traffic conditions in the engine. *Combustion Engines*. 2022, **191**(4), 58-65. https://doi.org/10.19206/CE-147327

Monika ANDRYCH-ZALEWSKA
Zdzisław CHŁOPEK
Jerzy MERKISZ
Jacek PIELECHA

Combustion Engines
Polish Scientific Society of Combustion Engines

Determination of characteristics of pollutant emission from a vehicle engine under traffic conditions in the engine test

ARTICLE INFO

Received: 8 February 2022
Revised: 6 March 2022
Accepted: 13 March 2022
Available online: 13 March 2022

The paper describes the method of determination of exhaust emission characteristics from a vehicle engine based on the results obtained in a driving test simulated on an engine dynamometer. These characteristics are the relations between the specific distance emissions and the zero-dimensional characteristics of the process of vehicle velocity: the average velocity value and the average value of the absolute value of the product of vehicle velocity and acceleration. The exhaust emission characteristics are used to simulate the emissions from vehicles operating in different types of traffic conditions. The engine operating states in the engine dynamometer tests were determined by the operating conditions of the vehicle during the test. The authors applied the Monte Carlo method in order to determine the characteristics of different values of the zero-dimensional characteristics of the vehicle velocity process. This enabled the determination of the characteristics based on the test results from a single realization of the process of vehicle velocity. Additionally, the developed method allowed a replacement of the empirical research on the chassis dynamometer with the one performed on the engine dynamometer. The obtained exhaust emission characteristics are in line with the characteristics obtained on the chassis dynamometer in multiple tests.

Key words: *combustion engine, pollutant emission, driving test, engine test, characteristics of pollutant emission, the Monte Carlo method*

1. Introduction

Engineers need to know the motor vehicle exhaust emission characteristics that allow a simulation of the specific distance exhaust emissions, particularly if changes in the traffic organization or the structure of the vehicles in use occur [3, 7, 9–11, 15, 16]. There exists a serious problem with the development of a method of assessment of the driving properties of motor vehicles that characterize their environmental impact. The simplest and most frequently applied quantity characterizing the vehicles in motion is the average vehicle velocity [3, 7–11]. It is, therefore, necessary to know the exhaust emissions for the categories of individual motor vehicles under different traffic conditions [3, 7, 9–11, 21].

Category (from Greek: κατηγορείν – to assert), in philosophy is a term introducing a structure: a class of objects possessing certain characteristics related with one another.

Vehicle categories are divided in terms of their different criteria, particularly [3, 7, 9–11]:
– designation,
– conventional size of the vehicles and their engines,
– properties of motor vehicles and their engines in terms of their engine cycle and detailed technological solutions as well as their usable properties (exhaust emissions in particular),
– engine fuels,
– technical level of advancement of the vehicles and their engines.

The elementary category of motor vehicles [7] are the ones of the same criteria-related characteristic features such as passenger vehicles fitted with diesel engines of the displacement not exceeding 2 dm^3 of the Euro 6 emission standard, fueled with diesel fuel.

The accumulated category of motor vehicles [7] are vehicles not having the same criteria-related characteristic features such as passenger vehicles fitted with spark ignition engines.

The most accumulated vehicle category of motor vehicles is all motor vehicles.

In order to determine the exhaust emission characteristics of vehicles from individual categories, it is necessary to carry out empirical research in driving tests corresponding to the actual operating conditions of the tested object [1, 2, 4, 5, 12, 13, 20, 22]. Information on such properties is contained in a variety of databases such as INFRAS AG [11] or COPERT [9]. Figure 1 presents the example relation between the average specific distance emission of carbon monoxide and the average vehicle velocity for passenger vehicles fitted with spark ignition engines of the displacement range 1.4–2 dm^3 and the emission category of Euro 5 according to INFAS AG [11].

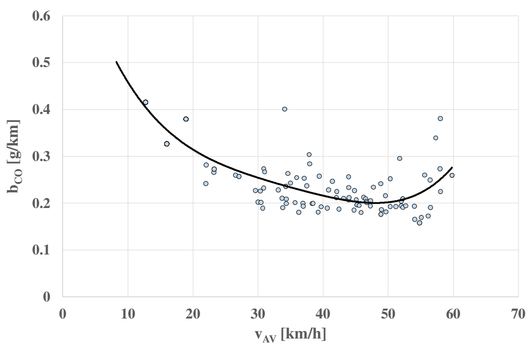

Fig. 1. Example characteristics of exhaust emissions – relation between the average specific distance emission of carbon monoxide and the average vehicle velocity

One can observe specific properties of the characteristics: high average emission of carbon monoxide for low average vehicle velocity, typical of non-stable vehicle motion and an increasing average emission of carbon monoxide for high vehicle load and increasing average velocity.

It is, however, difficult to validate these characteristics. In such a case, it is necessary to carry out time-consuming empirical research in laboratories that are generally hardly accessible. These are laboratories equipped with chassis dynamometers and laboratory equipment for exhaust emission analysis. It is, therefore, purposeful to develop simpler methods of determination of the exhaust emission characteristics for motor vehicles under different conditions of their operation.

Literature does not provide many examples regarding alternative methods of determination of exhaust emission characteristics from motor vehicles. Conventional methods are described in detail in [3, 10].

Much more materials one can find in literature as regards the results of research carried out in driving tests. In [2, 4, 5, 7, 12, 13] the authors describe the influence of the dynamic properties on the exhaust emissions from motor vehicles. Majority of the works treats on the exhaust emission results from driving tests [1, 2, 5, 7, 12, 13], including actual traffic conditions.

In [6] the application of the Monte Carlo method used for the determination of the exhaust emission characteristics under quasi-random conditions was first described. The Monte Carlo method was also used in the synthesis of the driving tests to investigate the properties of motor vehicles operated in quasi-random conditions [8].

In this paper, the authors present the results that are a validation of the developed methodology of determination of exhaust emission characteristics from motor vehicles based on the results of empirical research performed on a combustion engine on an engine dynamometer in a test simulating the engine operating states in a driving test.

2. Research aim, object, program and equipment

The aim of the investigations was the development of the method of determination of exhaust emission characteristics corresponding to the varied conditions of operation of a motor vehicle based on the tests performed on an engine dynamometer in a single dynamic test without the necessity of performing multiple tests on a chassis dynamometer.

For the determination of the exhaust emission characteristics, the authors used the results of empirical research described in detail in [1, 2].

The object of the research was a Fiat 1.3 JTD MultiJet diesel engine fitted in Fiat Idea. This is a four-cylinder, straight, turbocharged engine of the displacement of 1300 cm^3. The engine fueling system uses a common rail solution with a direct injection of the maximum injection pressure of 140 MPa. The engine power output is 51 kW at 4100 min^{-1}. The engine's mean effective pressure under nominal conditions is 1.15 MPa, therefore the engine does not have a high power/displacement ratio even though it is a turbocharged one. Under the conditions of maximum torque (180 N·m at 1750 min^{-1}) the mean effective pressure amounts to 1.74 MPa.

The engine exhaust system is fitted with an oxidation catalyst but it does not have a diesel particulate filter. The investigated vehicle falls in the emission category of Euro 4.

The program of the research included a performance of an engine dynamometer test developed based on the engine parameters recorded in a separate driving test.

To this end, the authors used a special test designed at Poznan University of Technology and carried out in the streets of Poznan in actual traffic. The test was named 'The Malta test' referring to Lake Malta, around which the test route extended. The test route (Fig. 2) was selected in such a way as to make the vehicle driving conditions as close to the NEDC (New European Driving Cycle) test conditions as possible. The route profile was varied in terms of elevation above the sea level and the maximum difference was 25.2 m.

Fig. 2. The Malta test route

During the test drive the following were recorded: the vehicle velocity (Fig. 3) and the engine speed and load.

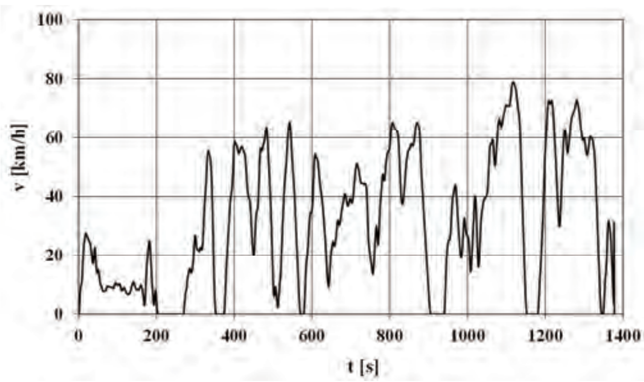

Fig. 3. The process of vehicle velocity in the Malta test

During the Fig. 4 and 5 present the engine speed and relative torque.

The engine relative torque was defined as:

$$M_{er}(n) = \frac{M_e(n)}{M_{e\,ext}(n)} \tag{1}$$

where: n – engine speed, M_e – engine torque, $M_{e\,ext}$ – engine torque at full throttle.

Figure 6 presents the collective engine operating states in the Malta test in the following coordinates: engine speed–relative engine torque. In the graph, the following points were marked: average engine speed (AV[n]) and average value of the relative torque (AV[M_{er}]). As we can see, the average engine load is not high – approx. 20% at a moderate engine speed of approx. 1500 min^{-1}.

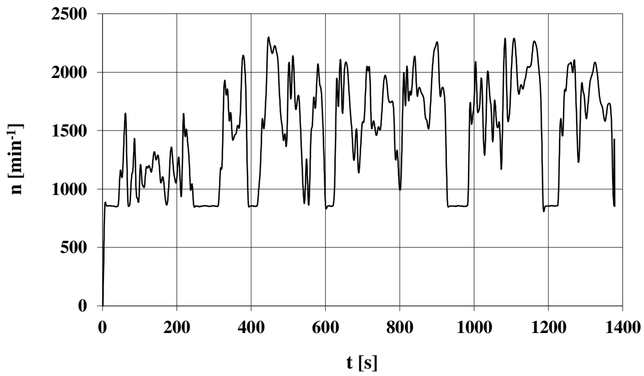

Fig. 4. The process of engine speed in the Malta test

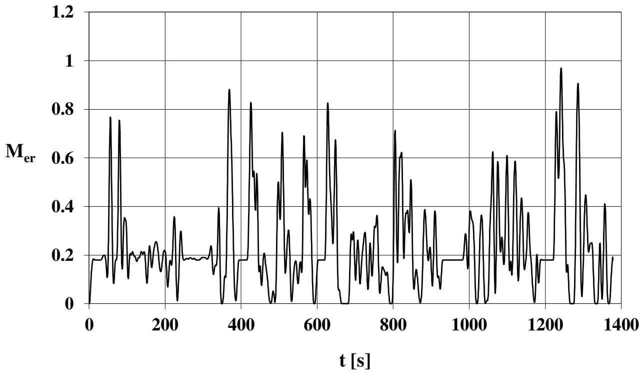

Fig. 5. The process of relative engine torque in the Malta test

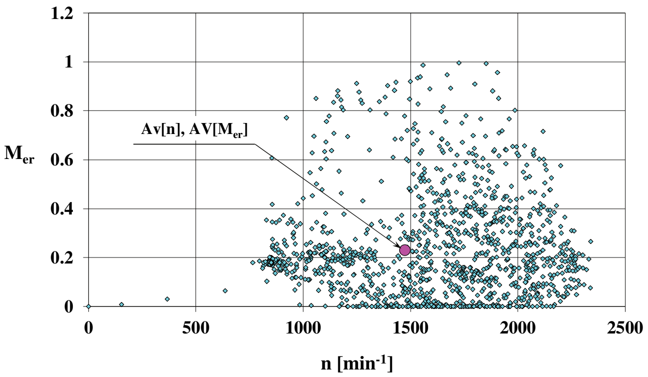

Fig. 6. Set of engine operating states in the Malta test

The engine tests in the Malta test performed on an engine dynamometer were carried out for a thermally stabilized engine.

The tests were carried out on Dynoroad 120 kW by AVL that enables the recording of parameters in a wide range of measurement resolutions while maintaining the high sampling quality (10 Hz).

For the testing of the exhaust emissions under dynamic engine states, the Semtech DS analyzer was applied with the following modules [18]:

- Flame Ionization Detector (FID) determining the concentration of hydrocarbons,
- Non-Dispersive Ultraviolet (NDUV) module utilizing ultraviolet radiation for the measurement of nitrogen monoxide and nitrogen dioxide,
- Non-Dispersive Infrared (NDIR) module utilizing infrared radiation for the measurement of the concentration of carbon monoxide and carbon dioxide,
- an electrochemical analyzer for the determination of the concentration of oxygen,
- an exhaust flow measurement module.

For the measurement of the particle number, the TSI 3090 EPSS™ (Engine Exhaust Particle Sizer™ Spectrometer) was applied [19]. The TSI 3090 EPSS™ analyzer measures the particle size distribution in the diameter range of 5.6 nm to 560 nm.

The measurement quantities in the dynamic conditions were recorded with the frequency of 10 Hz and then filtered using the second order Savitzky-Golay filter to reduce the share of noise in the high frequency signals [17].

3. Methodology

The subject of the research presented in this paper was the exhaust emission characteristics under the conditions corresponding to actual engine operation in a vehicle.

As the values characterizing the exhaust emissions, the specific distance exhaust emissions and the specific distance particle number were adopted.

The specific distance exhaust emissions (b) are a derivative of the exhaust emissions against the distance covered by the vehicle [7]:

$$\hat{b}_i = \frac{m_i}{ds} \tag{2}$$

where: m_i – emission of an exhaust component, s – distance covered by the vehicle, i = CO (carbon monoxide), i = HC (hydrocarbons), i = NO_x (nitrogen oxides), i = CO_2 (carbon dioxide).

The specific distance particle number (b_{PN}) is a derivative of the particle number (PN) against the distance covered by the vehicle:

$$\hat{b}_{PN} = \frac{PN}{ds} \tag{3}$$

The following independent variables of the exhaust emission characteristics were adopted:

- average vehicle velocity

$$v_{AV} = AV[v(t)] = \frac{1}{t_2-t_1}\int_{t_1}^{t_2} v(t)\,dt \tag{4}$$

where: AV – average value operator, v – vehicle velocity, t – time, t_1 – start time of averaging, t_2 – end time of averaging; $t_2 > t_1$,

- average value of the absolute value of the product of vehicle velocity and acceleration

$$A = AV\big[Abs[v(t) \cdot a(t)]\big] = \frac{1}{t_2-t_1}\int_{t_1}^{t_2} |v(t) \cdot a(t)|\,dt \tag{5}$$

where: Abs – absolute value operator, a – vehicle acceleration.

The interpretation of the average vehicle velocity as the characteristics of the process of vehicle velocity is obvious. This quantity characterizes the vehicle engine load [3, 7, 10]. The interpretation of the average value of the absolute value of the product of vehicle velocity and acceleration characterizes the engine load under dynamic states [3, 7].

For the determination of the average specific distance exhaust emissions and the average specific distance particle number, the recorded tracings of the following were used:

- exhaust emission intensity (carbon monoxide – E_{CO}, hydrocarbons – E_{HC}, nitrogen oxides – E_{NOx}, carbon dioxide – E_{CO2}),
- intensity of particle number (E_{PN}).

The average specific distance exhaust emissions and the average specific distance particle number was determined from the formulas:

$$b_i = AV[\hat{b}_i] = \frac{1}{s(t_1,t_2)} \cdot \frac{1}{t_2-t_1}\int_{t_1}^{t_2} E_i(t) \qquad (6)$$

where: $s(t_1, t_2)$ – distance covered by the vehicle in time between t_1 and t_2.

$$s(t_1,t_2) = \int_{t_1}^{t_2} v(t)\,dt \qquad (7)$$

For the determination of the exhaust emission characteristics, the authors applied the Monte Carlo method [14] generating the realization of the processes of vehicle velocity and acceleration as well as the exhaust emission intensities and the particle number intensities as fragments of tracings recorded in the empirical research of random values of the start and end time. If, in formulas (3)–(6), we assume the value of time t_1 and t_2 as quasi-random values, we obtain the average values of specific distance emissions of pollutants and the average value of specific distance particle number as quasi-random. Similarly, the independent variables of the characteristics are also quasi-random ones.

The values of time t1 and t2 are obtained as:

$$t_1 = rnd \cdot t_{max} \qquad (8)$$

$$t_2 = rnd \cdot t_{max} \qquad (9)$$

where: t_{max} – test duration, rnd – quasi-random number from the 0, 1 interval of even distribution.

Thanks to the application of the Monte Carlo method in determination of the exhaust emission characteristics it is possible to determine these characteristics based on the results from a single test rather than multiple tests with varied average velocities, as applied in conventional empirical research.

4. Research results and discussion

Figures 7–11 present the exhaust emission intensities and the intensities of particle emissions.

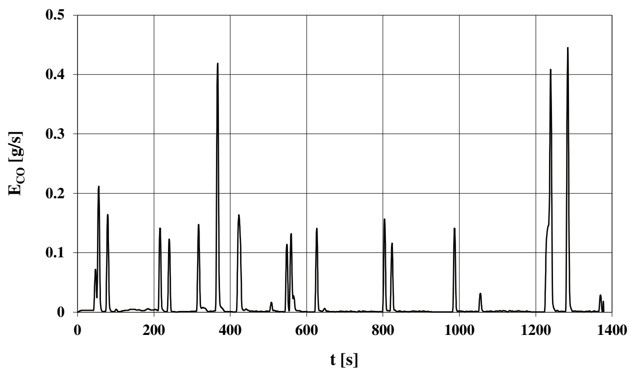

Fig. 7. The process of carbon monoxide emission intensity in the Malta test

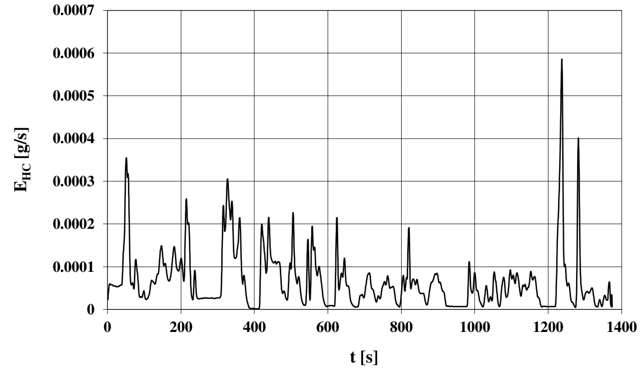

Fig. 8. The process of hydrocarbons emission intensity in the Malta test

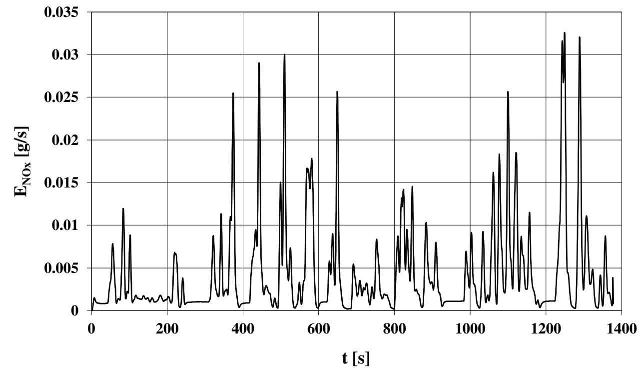

Fig. 9. The process of nitrogen oxides emission intensity in the Malta test

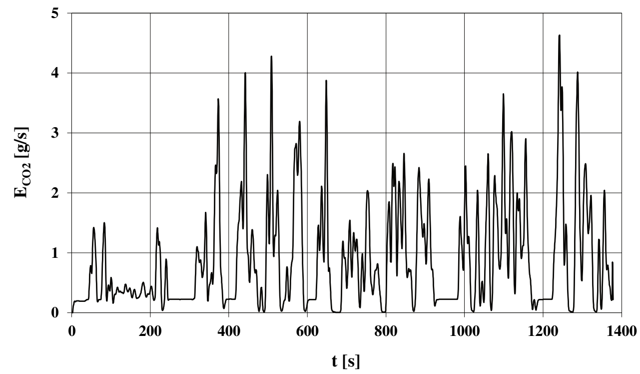

Fig. 10. The process of carbon dioxide emission intensity in the Malta test

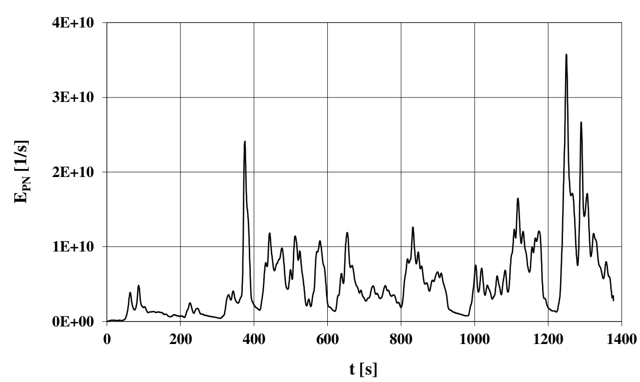

Fig. 11. The process of particle number intensity in the Malta test

Figure 12 presents the example realizations of the process of vehicle velocity in the portions of the Malta test used to determine the exhaust emission characteristics.

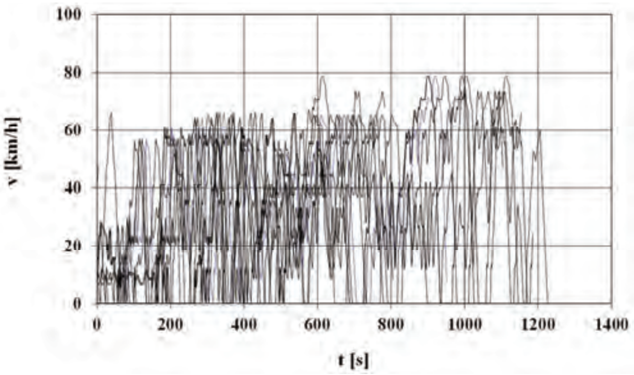

Fig. 12. Examples of vehicle velocity processes in fragments of the Malta test

Figures 13–17 present the exhaust emission characteristics in the form of a dependence of the average specific distance exhaust emissions and the average specific distance particle number on the average vehicle velocity in the Malta test.

The obtained characteristics were approximated with polynomial functions of the maximum degree lower than 7.

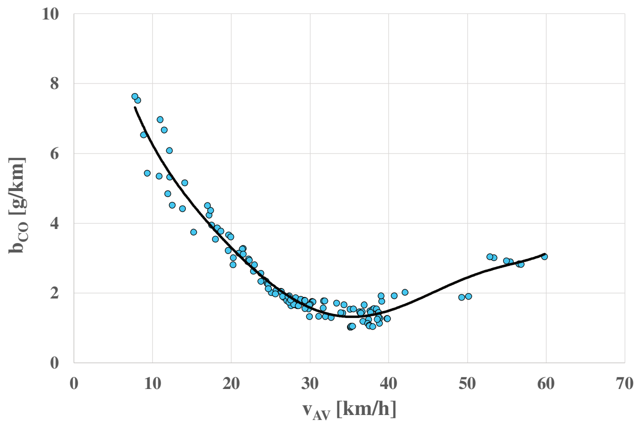

Fig. 13. Dependence of the average specific distance emission of carbon monoxide on the average vehicle velocity in the Malta tes

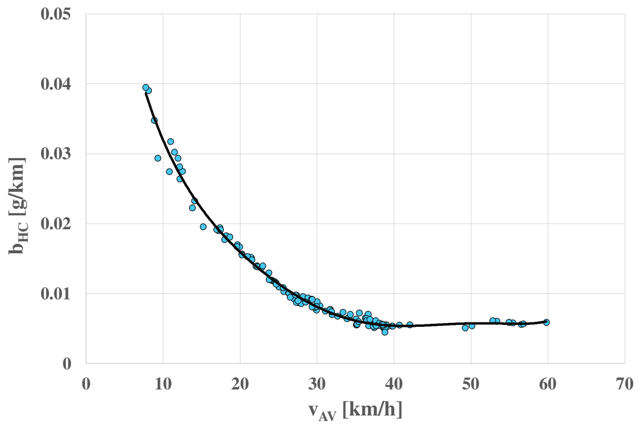

Fig. 14. Dependence of the average specific distance emission of hydro carbons on the average vehicle velocity in the Malta test

The quality of the approximation is characterized by the coefficient of determination. In the case of the determined characteristics, the highest value had the coefficient of determination for the characteristics of the emission of hydrocarbons (0.9897). For the outstanding exhaust components, the value of the coefficient of determination was also high – the lowest occurred for the nitrogen oxides (0.8793). The spread of the determined points for the characteristics of the particle number was much higher – the coefficient of determination was only 0.3742.

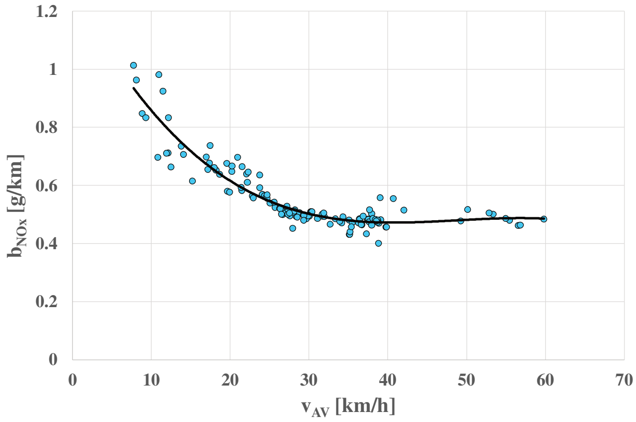

Fig. 15. Dependence of the average specific distance emission of nitrogen oxides on the average vehicle velocity in the Malta test

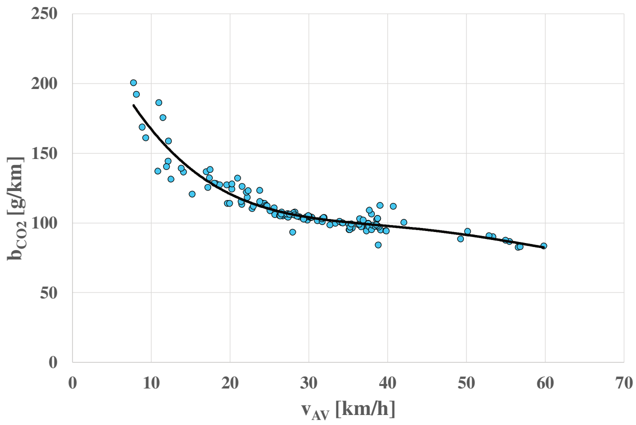

Fig. 16. Dependence of the average specific distance emission of carbon dioxide on the average vehicle velocity in the Malta test

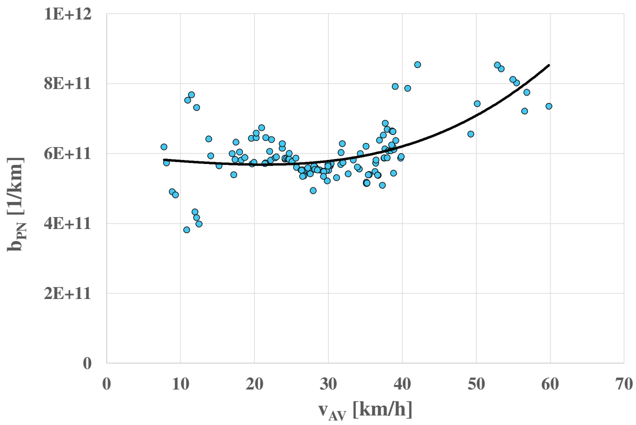

Fig. 17. Dependence of the average specific distance particle number on the average vehicle velocity in the Malta test

The obtained characteristics indicate a high level of regularity and compliance with the experiments [3, 6, 7, 9–11].

Figures 18–22 present the exhaust emission characteristics in the form of dependence of the average specific distance exhaust emissions and the average specific distance particle number on the average value of the absolute value of the product of velocity and acceleration of the vehicle in the Malta test.

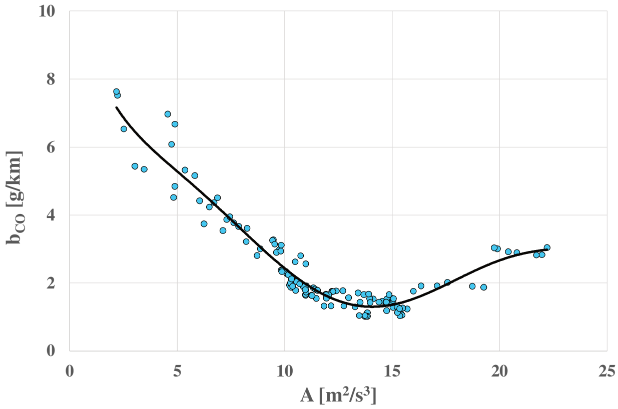

Fig. 18. Dependence of the average specific distance emission of carbon monoxide on the average value of the absolute value of the product of vehicle velocity and acceleration in the Malta test

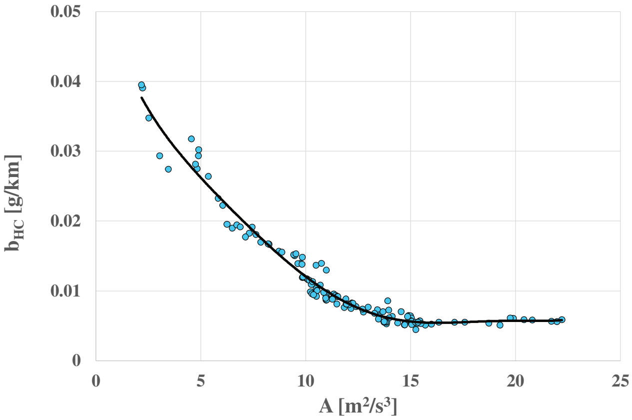

Fig. 19. Dependence of the average specific distance emission of hydrocarbons on the average value of the absolute value of the product of vehicle velocity and acceleration in the Malta test

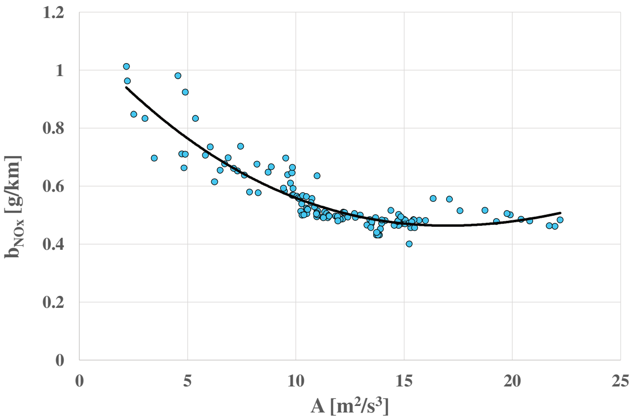

Fig. 20. Dependence of the average specific distance emission of nitrogen oxides on the average value of the absolute value of the product of vehicle velocity and acceleration in the Malta test

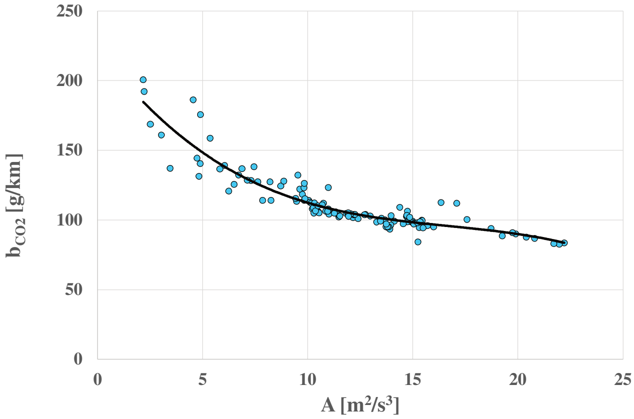

Fig. 21. Dependence of the average specific distance emissions of carbon dioxide on the average value of the absolute value of the product of vehicle velocity and acceleration in the Malta test

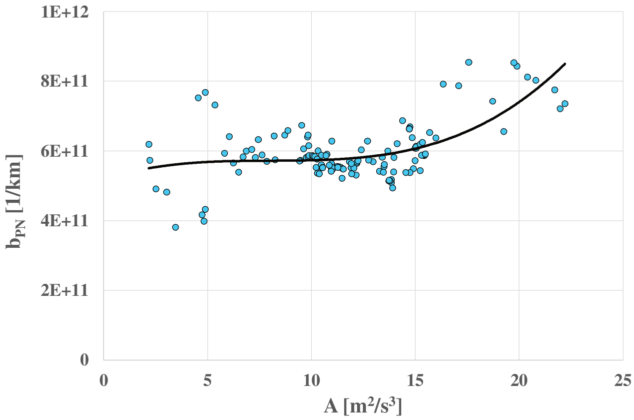

Fig. 22. Dependence of the average specific distance particle number on the average value of the absolute value of the product of vehicle velocity and acceleration in the Malta test

The obtained characteristics were approximated with polynomial functions of the maximum degree lower than 7.

The quality of the approximation of the determined characteristics was similar in nature to the characteristics in the domain of average values. The best matching quality of the approximating function occurred for the characteristics of hydrocarbons – the coefficient of determination was 0.9725. For the outstanding exhaust components, the coefficient of determination was greater than 0.82 (the lowest value occurred for nitrogen oxides – 0.8242).

Similarly to the characteristics in the domain of average values of velocity, the greatest spread occurred for the characteristics of particle number – the coefficient of determination was 0.3888.

The obtained characteristics show a significant regularity and compliance with the experiments [3, 7].

Therefore, one can assess that the expectation was met that it is possible to practically use the obtained characteristics to simulate the exhaust emissions under different vehicle operating conditions.

5. Conclusions

The paper As a result of the performed investigations the following conclusions can be drawn:

1. The possibility of the application of the Monte Carlo method for the determination of the exhaust emission char-

acteristics based on the results of empirical research carried out in a single test is hereby confirmed. This is an obvious benefit since, in conventional methods, multiple tests of different properties have to be carried out and these are tests that are costly, time-consuming and difficult to complete.

2. The authors have confirmed the possibility of application of the results of the engine tests on an engine dynamometer (rather than on the chassis dynamometer) for the determination of the exhaust emission characteristics. This is an important feature of the proposed method because we know that tests on chassis dynamometers are much more difficult to carry out and less cost-efficient compared to the tests performed on an engine dynamometer. Besides, ensuring greater accuracy and repeatability is simpler to obtain on an engine dynamometer compared to a chassis dynamometer. Another advantage is the fact that in the tests simulated on the engine dynamometer, engineers can investigate heavy-duty vehicle engines: heavy-duty trucks and buses as well as heavy machinery. The performance of tests of heavy-duty vehicles on chassis dynamometers is extremely limited by the access to such laboratories. For example, in Europe there are only a few laboratories having such equipment designed for scientific research of heavy-duty trucks. Obviously, for heavy non-road machinery, load simulation on chassis dynamometers is impossible.

3. The obtained characteristics are congruent with the current state of knowledge, which confirms the possibility of their practical application.

The investigations presented in this paper can be continued. It is possible to consider the two-dimensional exhaust emission characteristics in the domain of vehicle average velocity and the average value of the absolute value of the product of vehicle velocity and acceleration as well as multidimensional characteristics in the domain of other zero-dimensional characteristics of the vehicle velocity process [3, 7].

Nomenclature

A	average value of the absolute value of the product of vehicle velocity and acceleration
a	vehicle acceleration
Abs	absolute value operator
AV	average value
b_i	specific distance emission of the i-th pollutant
CO	carbon monoxide
CO_2	carbon dioxide
E_i	emission intensity of the i-th pollutant
E_{PN}	emission intensity of particle number
EPSS™	Engine Exhaust Particle Sizer™ Spectrometer
FID	flame ionization detector
HC	hydrocarbons
$M_{e\ ext}$	engine torque at maximum engine throttle position
M_e	engine torque
M_{er}	relative engine torque
n	engine speed
NDUV	non-dispersive ultraviolet
NIDR	non-dispersive infrared
NO_x	nitrogen oxides
PEMS	portable emissions measurement system
PN	particle number
t	time
t_1	start time of averaging
t_2	end time of averaging
v	vehicle velocity
v_{AV}	average vehicle velocity

Bibliography

[1] ANDRYCH-ZALEWSKA, M., CHŁOPEK, Z., MERKISZ, J. et al. Assessment of the internal catalyst efficiency in a diesel engine of a vehicle under the conditions simulating real driving. *Energies*. 2020, **13**(24), 6569. https://doi.org/10.3390/en13246569

[2] ANDRYCH-ZALEWSKA, M., CHŁOPEK, Z., MERKISZ, J. et al. Exhaust emission from a vehicle engine operating in dynamic states and conditions corresponding to real driving. *Combustion Engines*. 2019, **178**(3), 99-105. https://doi.org/10.19206/CE-2019-317

[3] BUWAL (Bundesamt für Umwelt, Wald und Landschaft), INFRAS AG (Infrastruktur-, Umwelt- und Wirtschaftsberatung). Luftschadstoffemissionen des Strassenverkehrs 1950-2010, *BUWAL-Bericht*. 1995; 255.

[4] CHŁOPEK, Z., BIEDRZYCKI, J., LASOCKI, J. et al. Modelling of motor vehicle operation for the evaluation of pollutant emission and fuel consumption. *Combustion Engines*. 2017, **171**(4), 156-163. https://doi.org/10.19206/CE-2017-426

[5] CHŁOPEK, Z., BIEDRZYCKI, J., LASOCKI, J. et al. Assessment of the impact of dynamic states of an internal combustion engine on its operational properties. *Eksploatacja i Niezawodnosc – Maintenance and Reliability*. 2015, **17**(1), 35-41.

[6] CHŁOPEK, Z., LASKOWSKI, P. Pollutant emission characteristics determined using the Monte Carlo Method. *Eksploatacja i Niezawodnosc – Maintenance and Reliability.* 2009, **2**(42), 42-51.

[7] CHŁOPEK, Z. Modelowanie procesów emisji spalin w warunkach eksploatacji trakcyjnej silników spalinowych. Prace Naukowe. Seria „Mechanika”, **173**. *Oficyna Wydawnicza Politechniki Warszawskiej*. Warszawa 1999 (Habilitation dissertation – in Polish).

[8] CHŁOPEK, Z. Synthesis of driving cycles in accordance with the criterion of similarity of frequency characteristics. *Eksploatacja i Niezawodnosc – Maintenance and Reliability.* 2016, **18**, 572-577. https://doi.org/10.17531/ein.2016.4.12

[9] COPERT 5 – *Manual.* https://copert.emisia.com/manual/ (accessed on 2019.12.01).

[10] EEA/EMEP *Emission Inventory Guidebook.* **13**, 2019. https://www.eea.europa.eu/publications/emep-eea-guidebook-2019

[11] INFRAS, AG. Handbook emission factors for road transport 4.1. Quick reference. Version 4.1. Bern, 2019. https://www.hbefa.net/e/help/HBEFA41_help_en.pdf

[12] KURTYKA, K., PIELECHA, J. The evaluation of exhaust emission in RDE tests including dynamic driving conditions. *Transportation Research Procedia*. 2019, **40**, 338-345; https://doi.org/10.1016/j.trpro.2019.07.050

[13] MERKISZ, J., PIELECHA, J. Comparison of real driving emissions tests. *IOP Confferences Series: Materials Science and Engineering*. 2018, **421**. https://doi.org/10.1088/1757-899X/421/4/042055

[14] METROPOLIS, N, ULAM, S. The Monte Carlo method. *Journal of the American Statistical Association*. 1949, **247**(44), 335-341. https://doi.org/ 10.1080/01621459.1949.10483310

[15] Poland's informative inventory report 2019. Submission under the UN ECE Convention on Long-range Transboundary Air Pollution and the Directive (EU) 2016/2284. *Institute of Environmental Protection – National Research Institute*. National Centre for Emission Management (KOBiZE), Warszawa 2019.

[16] Poland's National Inventory report 2019. Greenhouse gas inventory for 1988-2017. Submission under the UN Framework Convention on Climate Change and its Kyoto Protocol. *Institute of Environmental Protection – National Research Institute.* National Centre for Emission Management (KOBiZE), Warszawa 2019.

[17] SAVITZKY, A., GOLAY, M.J.E. Smoothing and differentiation of data by simplified least squares procedures. *Analytical Chemistry*. 1964, **36**(8), 1627-1639. https://doi.org/10.1021/ac60214a047

[18] Semtech-DS On Board Vehicle Emissions Analyzer. *User Manual*. Document: 9510-086, Revision: 2.01. October 2010.

[19] TSI 3090 EEPS™ (Engine Exhaust Particle Sizer™), *User Manual*, 2008.

[20] Worldwide emission standards. Passenger cars and light duty vehicles. Delphi. *Innovation for the real world*, 2020/2021. https://www.delphi.com/innovations

[21] ANDRYCH-ZALEWSKA, M., CHŁOPEK, Z., MERKISZ, J. et al. Static internal combustion engine operating states in vehicle driving tests. *Combustion Engines*. 2019, **177**(2), 50-54. https://doi.org/10.19206/CE-2019-209

[22] ANDRYCH-ZALEWSKA, M., CHŁOPEK, Z., MERKISZ, J. et al. Evaluation of the test drive cycle conditions impact on exhaust emissions from an internal combustion engine. *Combustion Engines*. 2018, **175**(4), 3-9; https://doi.org/10.19206/CE-2018-401

Monika Andrych-Zalewska, DEng. – Faculty of Mechanical Engineering, Wroclaw University of Science and Technology.
e-mail: *monika.andrych@pwr.edu.pl*

Prof. Jerzy Merkisz, DSc., DEng. – Faculty of Civil and Transport Engineering, Poznan University of Technology.
e-mail: *jerzy.merkisz@put.poznan.pl*

Prof. Zdzisław Chłopek, DSc., DEng. – Faculty of Automotive and Construction Machinery Engineering, Warsaw University of Technology.
e-mail: *zdzislaw.chlopek@pw.edu.pl*

Prof. Jacek Pielecha, DSc., DEng. – Faculty of Civil and Transport Engineering, Poznan University of Technology.
e-mail: *jacek.pielecha@put.poznan.pl*

Article citation info:
WAKASUGI, T., TSURU, D., TASHIMA, H. Influences of the pre-chamber orifices on the combustion behavior in a constant volume chamber simulating pre-chamber type medium-speed gas engines. *Combustion Engines*. 2022, **191**(4), 66-76.
https://doi.org/10.19206/CE-148171

Takuya WAKASUGI
Daisuke TSURU
Hiroshi TASHIMA

Combustion Engines
Polish Scientific Society of Combustion Engines

Influences of the pre-chamber orifices on the combustion behavior in a constant volume chamber simulating pre-chamber type medium-speed gas engines

ARTICLE INFO

Received: 12 February 2022
Revised: 19 March 2022
Accepted: 8 April 2022
Available online: 17 April 2022

The study aims to clarify the influence of pre-chamber (PC) configurations on the combustion process in the main chamber (MC) of medium-speed spark-ignition gas engines equipped with an active PC. A constant volume combustion chamber was prepared to simulate the chamber configurations of the gas engines. A high-speed shadowgraph was applied to visualize the torch flame development and the combustion process in the MC. Experiments were done by changing the charged gas in the MC, the number, and the diameter of the PC orifices. Combustion was most accelerated when the PC orifice configuration was set appropriately so that the adjacent torch flames would combine with each other. It was also found that the unburned mixture in the PC, which ejected prior to the torch flame, supported the penetration of the torch flame.

Key words: *gas engine*, *pre-chamber, torch flame, combustion visualization, natural gas*

1. Introduction

In recent years, emission regulations on internal combustion engines have become stricter because of global environmental issues growing concern. Harmful emissions such as NO_x, SO_x, and PM have long been regulated due to their direct impact on human health, and GHG reduction is now an urgent issue. Then natural gas has become popular in marine and industrial applications because it emits less carbon dioxide, no sulfur, and much fewer PM [1]. Moreover, natural gas is so flexible that it can be used in both diffused combustion (gas diesel) and premixed combustion (gas engine). Except for extra-large propulsion applications, premixed gas engines are used regularly. In premixed combustion of natural gas, a lean combustion system reduces fuel consumption, reduces thermal NO_x, and improves thermal efficiency [2]. However, a leaner mixture has less ignitability and lower combustion speed [3], and it tends to result in methane slippage [4] and cycle to cycle variation [5, 6]. Hence, various high-energy ignition methods are necessary, such as plasma ignition [7–9], laser-induced ignition [10], and pre-chamber (PC) ignition [11].

A combustion chamber is separated into two different chambers in the PC ignition gas engines. One is the main chamber (MC), surrounded by a cylinder head, cylinder liner, and piston. Another is a pre-chamber with a small volume of around 2% of the MC and is connected to the MC through its multiple orifices. Firstly, a spark plug ignites the mixture in the PC, and then a hot flame propagates in the PC. Finally, flame jets eject through the orifices into the MC as enhanced ignition sources, sometimes called torch flames or turbulent jets. The PC ignition has been proved to improve the stability and reproducibility of the MC combustion and promote heat release by dispersing the ignition location and increasing ignition energy [12].

The PC ignition is divided into two types according to the method of filling the PC with the mixture: active type and passive type. The former has an independent fuel supply system, while the latter utilizes the mixture flowing from the MC during a compression stroke. The active PC requires the additional cost of a separate mixture delivery system. Still, it has significant advantages in increasing the ignition energy of the flame jets and in expanding the lean limit of the MC mixture [13, 14].

The PC combustion system, known as turbulent jet ignition (TJI) in the automotive field, has been comprehensively and thoroughly reviewed by Alvarez et al. [15], and more recently by Zhua et al. [16]. In order to investigate the detailed mechanism of PC combustion, optical visualization of combustion using rapid compression machines (RCM) and constant volume combustion chamber (CVCC), a numerical simulation based on CFD, and experimental studies using actual metal engines have been conducted. Validi et al. [17] performed numerical simulations of combustion in a rapid compression machine (RCM) using an LES/FMDF computational model. They suggested that there are three main combustion phases for turbulent jet ignition in the RCM: (i) cold fuel jet, (ii) turbulent hot product jet, and (iii) reverse fuel-air/product jet. Sadanandan et al. [18] studied the ignition behavior of unburned hydrogen/air mixtures by combining OH-LIF, fast sequences of Schlieren images, and simple numerical simulations. From their observations, ignition was found to occur near the tip of the jet but not at the sides of the jet due to the difference in mixing behavior. Biswas et al. [19] performed simultaneous measurements of fast Schlieren and OH⁄chemiluminescence methods for PC combustion of premixed CH_4/air and H_2/air to visualize the process of jet penetration and ignition. They clarified the existence of two ignition mechanisms: flame ignition (ignition by reacting jet) and jet ignition (ignition by reacted jet). They also note that as the orifice diameter of the PC increases, the ignition mechanism tends to switch from jet ignition to flame ignition, with flame ignition becoming more dominant as the pressure increases.

The geometric parameters of the PC are essential factors that determine the quench of the flame through the orifice, the velocity of the jet of combustion products, the dispersion of the ignition point in the MC, and the turbulent structure [20, 21]. Gentz et al. [22] investigated the effects of the number of orifices and the amount of auxiliary fuel on combustion by optical observation and pressure analysis using the RCM. They showed that changing the number of orifices caused differences in end-gas autoignition behavior. Zhou et al. [23] conducted optical observations of CVCC and tests on a single-cylinder engine and showed that the adoption of an appropriate multi-orifice PC leads to improved combustion and that a smaller orifice diameter leads to jet flame quenching. However, there are few examples of investigations of the effect of PC structure on combustion, simulating engines with large bores, such as marine engines and industrial generators [24].

In this study, optical observation and pressure analysis were conducted in a CVCC with a large bore to investigate the effects of the PC orifice diameter, the number of orifices, and the main chamber gas on the torch flame ejection and the main chamber combustion.

2. Experimental methods

2.1. Constant volume combustion chamber

All experimental testing was performed in an optically accessible Constant Volume Combustion Chamber (CVCC). The schematic view and main specifications of the tested CVCC are shown in Fig. 1 and Table 1 respectively.

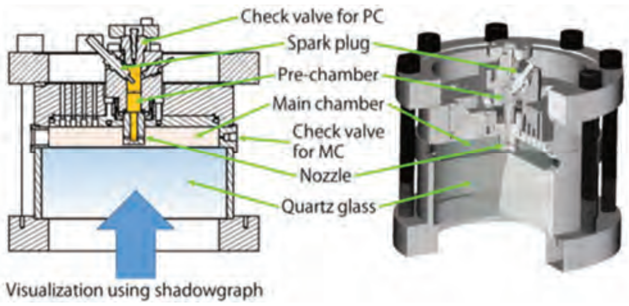

Fig. 1. Schematic of the constant volume combustion chamber (CVCC)

Table 1. Main specifications of the CVCC

Main chamber (D × H)	∅240 mm × 30 mm
Optical window (D × t)	Quartz, ∅260 mm × 100 mm
Max. pressure	10 MPa
Fuel gas in pre-chamber	CH_4/air premixture
Ambient gas in the main chamber	N_2, Air, CH_4/air premixture

The diameter (∅240 mm) and height (30 mm) of the tested combustion chamber correspond to the shape of the main combustion chamber at the top dead center of a typical medium-speed natural gas engine. The PC is installed above the MC, and the configurations of the PC, such as orifice diameter and the number of orifices, can be changed by exchanging the PC tip. The PC and MC have independent air/fuel mixture intake paths, and each can supply air/fuel mixture of different compositions. The bottom of the MC is made entirely of quartz glass, and the inner surface of the chamber top lid is mirror polished, allowing full optical access to in-cylinder combustion phenomena from the bottom. A pressure sensor, gas supply port for the MC, and an exhaust valve are installed on the side of the MC. A spark plug and another pressure sensor are inserted at an angle from the side of the PC. The gas supply port for the PC locates at the top of the PC.

2.2. PC tip configuration

The experiments of the study were done by exchanging PC tips and using the main body of the PC in common. Figure 2 and Table 2 show the cross-sectional view of the PC tip and the list of PC specifications. Five PC tips identified as #1~#5 were prepared to explore the effect of PC configuration on the combustion process. The PC orifices were drilled horizontally to measure the cone angle and penetration of the torch flame directly from the visualized combustion images through the bottom window of the CVCC. The reference configuration is tip number #1, where the orifice diameter; D_{ori} is 3.5 mm and the and the number of orifices; N_{ori} is eight. Tips #2 and #3 have N_{ori} values of 6 and 10, respectively, and their D_{ori} is determined so that the total area of orifices is almost the same as that of #1 tip. For tips #4 and #5, N_{ori} was set constant at 8 and D_{ori} was set to 2.5 mm and 5.0 mm, respectively.

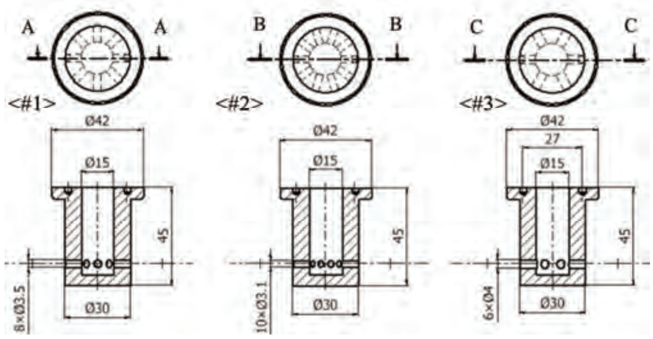

Fig. 2. Cross-sectional view of the PC tip #1~#3

2.3. Mixture preparation

As previously mentioned, the CVCC has independent gas supply systems. Figure 3 shows the schematic diagram of the gas supply systems. The supply system has a primary mixer that prepares the artificial air from O_2 and N_2, and a secondary one that prepares CH_4/Air mixture. Pressure regulators and solenoid valves are inserted in the pipeline, and the air/fuel ratio of the mixture is minutely determined by controlling the pulse duty ratio of the solenoid valves. This configuration assures the productivity of the experiments.

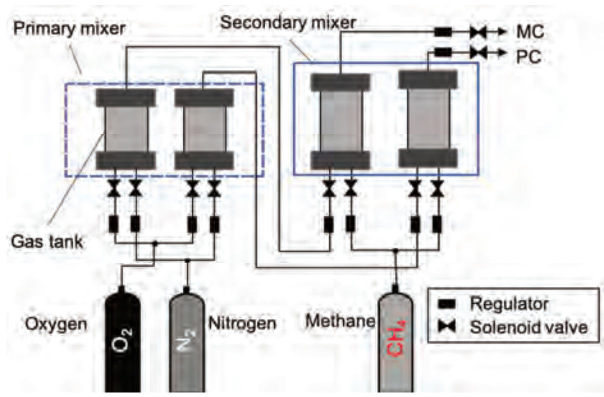

Fig. 3. Schematic of the gas supply system

Table 2. Main specifications of the pre-chamber tip #1~#5

PC tip ID	Orifice dia.: D_{ori} [mm]	Orifice length: L_{ori} [mm]	No. of orifices: N_{ori} [-]	Tip inner dia.: D_{itip} [mm]	V_{PC} ratio to V_{MC} [%]	L_{ori}/D_{ori} [-]	Area of orifices: A_{ori} [cm]	A_{ori} ratio to V_{PC} [cm^{-1}]
#1	∅3.5	7.5	8	∅15	2.3	2.14	0.770	0.0271
#2	∅4.0	7.5	6	∅15	2.3	1.86	0.754	0.0265
#3	∅3.1	7.5	10	∅15	2.3	2.42	0.755	0.0265
#4	∅2.5	7.5	8	∅15	2.3	3.00	0.393	0.0138
#5	∅5.0	7.5	8	∅15	2.3	1.50	1.571	0.0052

Table 3 summarizes the conditions of the charging gas in the MC and PC in the experiments. Three different gases were charged as atmospheric gas in the MC. The first one is nitrogen, in which the torch flame ejected from the PC cannot continue its combustion, and the pure behavior of a torch flame can be captured. The second is artificial air, in which the torch flame can sustain its combustion by entraining oxygen in the artificial air. The third one is the lean CH_4/Air mixture, in which an entire combustion process from the ignition of the lean mixture by torch flames to the growth of ignited flame in the MC can be observed. Hereafter, these ambient gas conditions are classified as "inert", "sustainable", or "combustible", respectively.

Table 3. Charging gas conditions in the main chamber and pre-chamber

Reaction in MC	**"Inert"**	**"Sustainable"**	**"Combustible"**
Gas in PC	CH_4/Air mixture (λ = 1.0)		
Gas in MC	Nitrogen	Artificial air	CH_4/Air (λ = 1.7)
Input heat in MC	39 kJ		
Input heat in PC	0.0 kJ	0.0 kJ	1.5 kJ
Initial pressure	1.0 MPa		
Initial temperature	290 K		

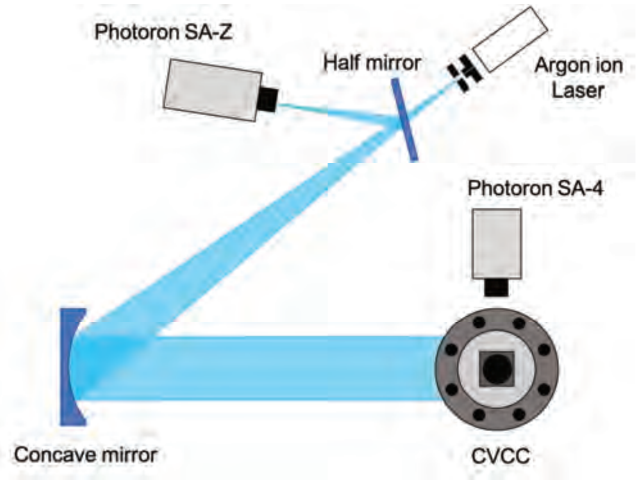

Fig. 4. Bird's eye view of the shadowgraph optical setup

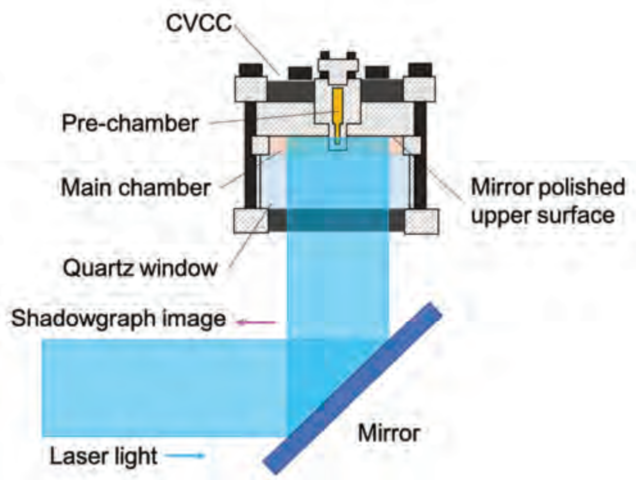

Fig. 5. Detailed view of the double path type shadowgraph optics and the bottom-up optical layout

2.4. High-speed shadowgraph imaging

Figure 4 and Fig. 5 show a schematic of the shadowgraph optical setup and a detailed view of the optical path of the bottom-up optics layout in this experiment. As known, the premixed flame in gas engines is difficult to visualize, especially under lean-mixture conditions in the gas engines. The shadowgraph optical system was applied in the study. A parallel light beam is irradiated perpendicularly to the measurement volume in the technique.

Since each ray passing through the volume refracts proportional to the quadratic spatial gradient of the density, the pattern of brighter and darker spots is acquired if the disturbance of the density field caused by premixed flame exists in the measurement volume. In the experiment, double path type shadowgraph optics was realized thanks to the mirror-polished chamber lid and bottom-up optics layout, and the half mirror between a shadowgraph light source and a high-speed camera. The high-speed CMOS camera (Photron Ltd., SA-Z) with Nikon Teleconverter TC200 2X and Nikon f 2.8 objective lenses were used to take shadowgraph images of torch flame and combustion process in the MC. The frame rate was set to 20,000 fps, and the shutter speed was set to 10.0 μs. The camera resolution was set to 1024 × 1024 pixels. An argon ion laser (Spectra-Physics, Inc., Stabilite 2017) was prepared as a light source. Another high-speed camera (Photron Ltd., SA4) was applied to determine the ignition timing of the spark plug in the PC.

3. Results and discussion

3.1. Effects of the main chamber atmosphere

As listed in Table 3, three different gases were charged as ambient gas in the MC. Figure 6 shows an example of torch flame observation in the MC. The figure also exemplifies the definition of penetration and cone angle. The former is the distance from the orifice exit to the tip of a torch flame. It should be noted that the penetration is determined based on a clear boundary formed by the flame front. The latter is quantified as the angle between two tangent lines descending from the center of the PC to the outer edge of the torch flame.

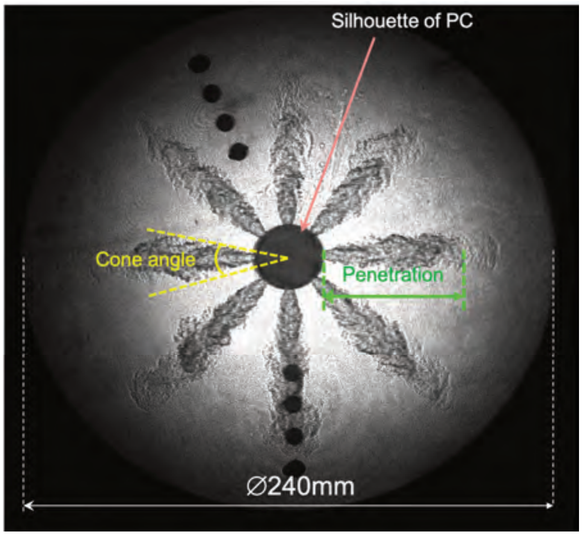

Fig. 6. Example of torch flame observation in the main-chamber

Figure 7 shows the time history of penetration and cone angle of the torch flames under the three different ambient gas conditions, and Fig. 8 shows the shadowgraph images of the torch flames corresponding to the above conditions. The elapsing time in Fig. 7 starts when the torch flames begin ejecting from the orifices of the PC. The experiments were conducted five times for all the conditions, and the penetration and the cone angle of the torch flame are obtained as the averages of the torch flames from all orifices, and furthermore, they are averaged over the five runs.

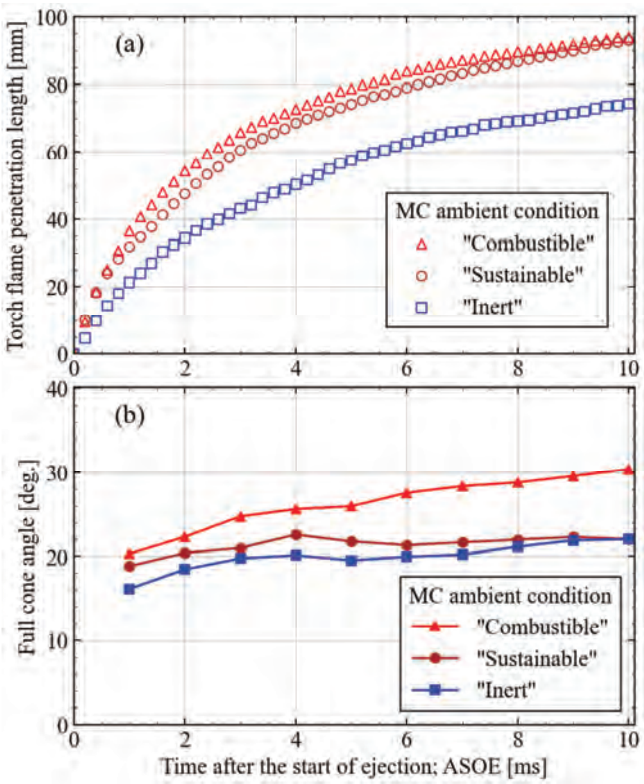

Fig. 7. Time history of (a) penetration, and (b) cone angle of torch flames under different main chamber gas conditions; "combustible" (lean CH_4/air mixture), "sustainable" (artificial air), and "inert" (N_2)

Validi et al. [9] pointed out that the unburned mixture in the PC was forced out into the MC ahead of the torch flame. This unburned mixture ejection significantly influences the torch flame behavior in the MC. The unburned mixture entrains the MC ambient gas along with the progression of the torch flame. When the unburned mixture on the tip of the torch flame is diluted by the nitrogen, the penetration becomes much shorter than in the other two ("sustainable", "combustible") cases.

The penetration in the "sustainable" case is almost equal to the "combustible" case at 10 ms ASOE (after the start of ejection) despite the slight shortness in the early stage of the ejection. In the "sustainable" case, the penetration comparable with the "combustible" case is hard to be expected since the torch flames barely maintain the thermal reactions. These findings could be explained as follows. The unburned tip keeps combustible by entraining fresh air, and it can contribute to maintaining the apparent flame length.

Contrarily, the cone angle of the torch flame varies significantly depending on the combustibility of the MC gas. In both the "inert" and "sustainable" cases, the cone angle remained at around 20 degrees during the entire development process of the torch flame. In contrast, that in the "combustible" case was consistently more extensive than the other two and increased monotonically with time, reaching about 30 degrees at 10 ms ASOE.

These results indicate that the flame propagation of the MC occurs mainly in the direction perpendicular to the torch flame axis, not parallel to the axis.

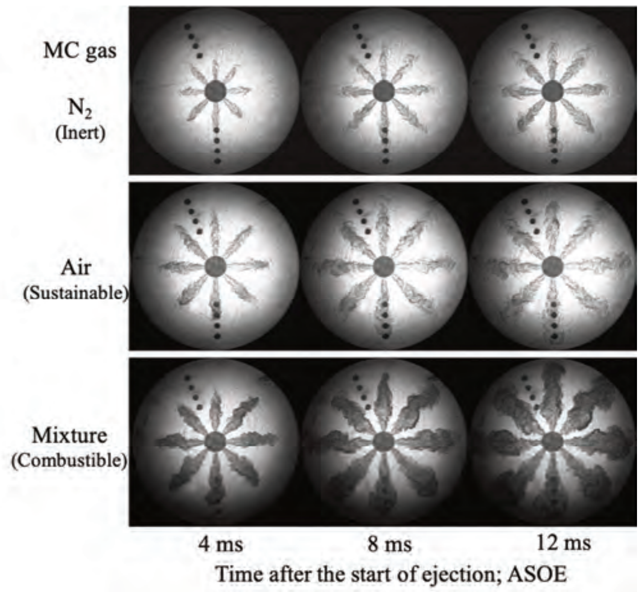

Fig. 8. Shadowgraphs of torch flames under different main chamber gas conditions; "combustible" (lean CH_4/air mixture), "sustainable" (artificial air), and "inert" (N_2)

3.2. Effects of the number of orifices

In this section, the effects of the number of orifices (N_{ori}) of the PC on torch flame and combustion are explored based on the visualization and pressure analysis. Similar to the number of nozzles in a compression ignition engine, the number of orifices in a PC-type gas engine is an important design factor that directly impacts the flame distribution and the contact area with the MC mixture. The number of orifices (N_{ori}) in the study was selected to be 6, 8, and 10 (tip ID #1, #2, and #3). The PC volume was constant regardless of the number of the orifices. The orifice diameters were 4.0 mm, 3.5 mm, and 3.1 mm for the 6, 8, and 10 orifices. These combinations of numbers and diameters aimed to keep the total cross-sectional area of orifices constant. The “inert” and the “combustible” conditions were chosen as MC atmosphere in this investigation.

Figure 9 shows the cone angle and the penetration under the "inert" condition with the three different numbers of orifices, and Fig. 10 exemplifies shadowgraph images corresponding to the condition.

Torch flame penetration showed little difference until about 2 ms ASOE in all cases, but the growth gradient for the 10-orifice case became slower around the timing, and the 6-orifice case showed a similar behavior at about 6 ms ASOE. The penetration becomes proportional to the square root of time after its growth becomes slower. This trend could be attributed to the difference in the momentum possessed by the individual torch flames. The larger the number of orifices is, the smaller the momentum of each torch flame is, and the earlier the penetration growth slows down. It suggests that the preceding unburned PC mixture could support the torch flame penetration according to the amount of the unburned mixture before slowing down claimed by Zhou et al. [23].

In contrast, the cone angle does not differ significantly depending on the number of orifices and increases slightly with the progress of the torch flame for any number of orifices. The boundary of the 6-orifice torch flame is more apparent than that of other torch flames. Whereas the boundaries of the 8 and 10-orifice cases are dimmer, especially around the tip of the torch flame. These may reflect the allocation of the energy possessed by the PC to each torch flame becomes larger for smaller orifice numbers.

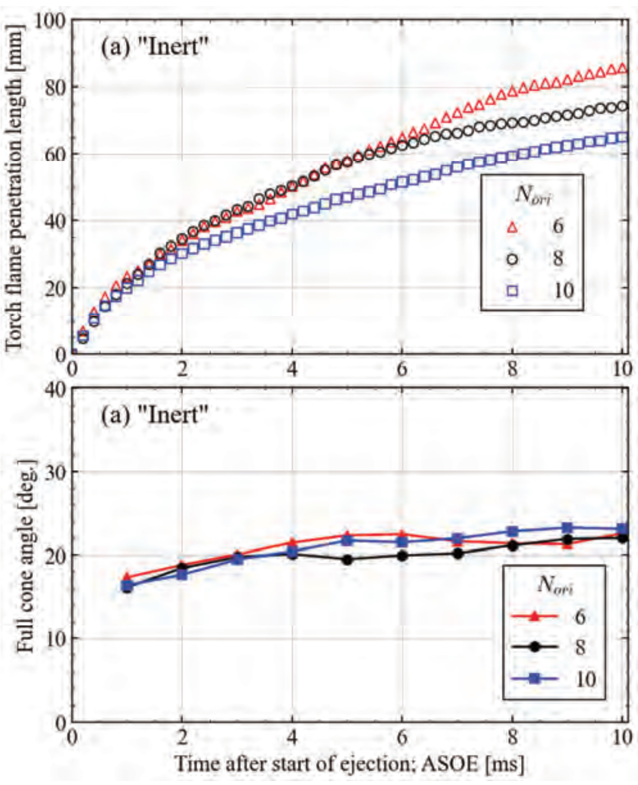

Fig. 9. Time history of (a) penetration, and (b) cone angle of the different number of orifices (N_{ori} = 6, 8, 10) under “inert” conditions

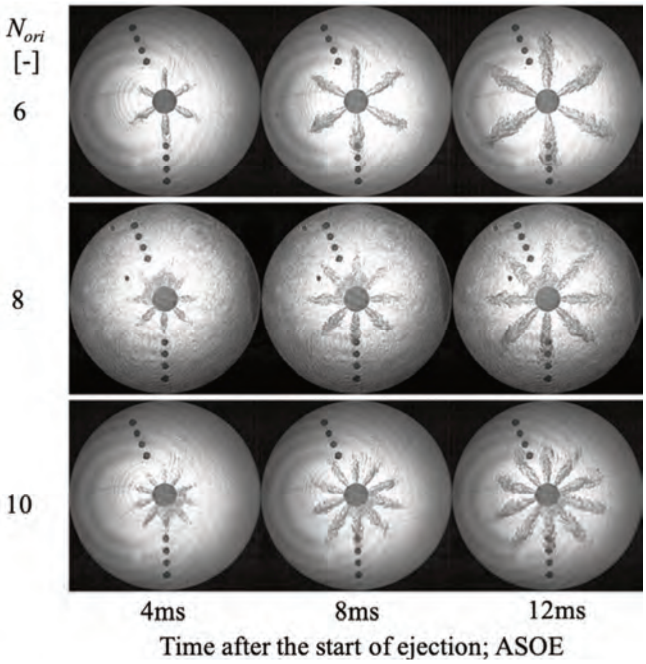

Fig. 10. Shadowgraphs of the different number of orifices (N_{ori} = 6, 8, 10) under “inert” condition

Figure 11 shows the effect of the number of orifices on the penetration and cone angle under “combustible” conditions.

Figure 12 shows the example images of torch flame ejection behavior under the corresponding conditions. The less the number of orifices is, the greater the amount of unburned air-fuel mixture ejected from each orifice is. This can promote the following MC combustion and results in a longer torch flame penetration and a wider cone angle of torch flame than those of the “inert” case. As mentioned before, in the "inert" case, the torch flames showed complicated behavior in the aspect of penetration due to the effects of the preceding unburned gas. However, in the "combustible" case, the preceding un-burned gas was quickly ignited by the torch flame, so the penetration changed according to the initial momentum of the torch flame. The torch flame in the 10-orifices case accelerates from the late stage of the penetration.

In contrast with the slight expansion of the cone angle over time in the “inert” conditions, the cone angle of torch flame under “combustible” conditions increases monotonically regardless of N_{ori}. This increase can be attributed to the combustion of the MC mixture. Especially when N_{ori} = 6, the torch flame expands more rapidly than the other two. Its slowest increase in cone angle can also explain the suppression of combustion in the case of N_{ori} = 8. From the observation results shown in Fig. 9, the torch flame has almost reached the combustion chamber wall by 15 ms ASOE regardless of the number of orifices. By the time of 10 ms ASOE shown in Fig. 9, some of the flame contours of N_{ori} = 6 and 10 became horseshoe-shaped because the flames grew large enough to touch the bottom surface of the combustion chamber.

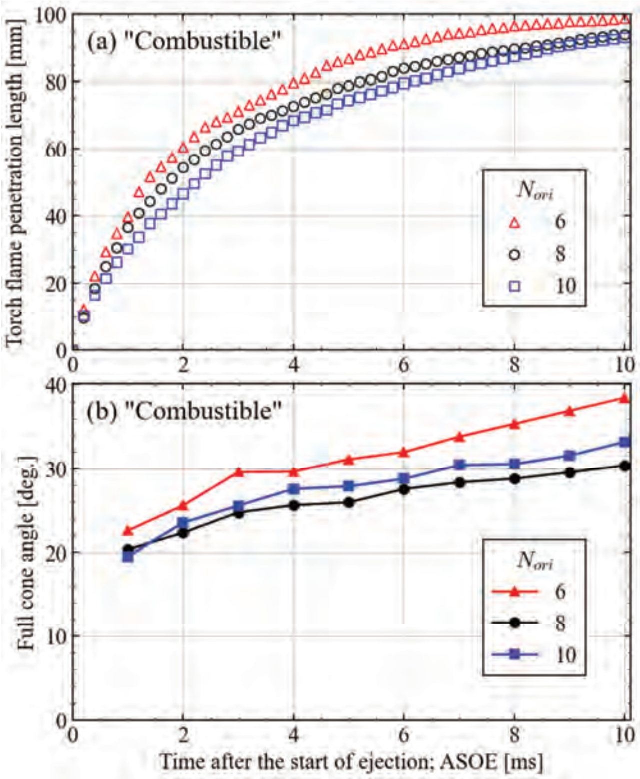

Fig. 11. Time history of (a) penetration, and (b) cone angle of the different number of orifices (N_{ori} = 6, 8, 10) under "combustible" conditions

In N_{ori} = 8, however, most of the torch flames were not flattened at 10 ms ASOE. This is consistent with the slowest growth of the cone angle of N_{ori} = 8 in Fig. 8. Thus, the heat releasing process after 15 ms ASOE is mainly influenced by the flame propagation perpendicular to the orifice axis, that is, into the unburned MC mixture between two adjacent torch flames.

In N_{ori} = 10 at 10 ms ASOE, the torch flames begin to connect with each other. By 20 ms ASOE, they formed a united flame front with an undulating surface corresponding to the number of orifices. Compared to the other two cases,

N_{ori} = 10 case seemed to burn the entire MC mixture including the vicinity around the PC thanks to the connection.

Figure 13 shows the time history of the rate of heat release (ROHR) and the total amount of heat release based on the MC pressure. The rate of heat release is calculated from the measured pressure in MC using eq. (1) where Q is apparent heat release (heat release from combustion minus heat losses) and V is the volume of MC. The specific heat ratio κ is calculated based on the averaged MC gas composition and bulk mean MC temperature.

$$\frac{dQ}{dt} = \frac{V}{\kappa-1}\frac{dP}{dt} \tag{1}$$

The time axis is ASOI (time after the start of ignition); for N_{ori} = 6 and N_{ori} = 10 cases, almost 12 ms ASOI, and for N_{ori} = 8 case, almost 14ms ASOI corresponds to 0 ms ASOE. As mentioned above, the torch flame reaches the MC wall at 15 ms ASOE. In N_{ori} = 6 and 10, around 15 ms ASOE corresponds to the time of the maximum heat release rate. In N_{ori} = 8, the timing was delayed. This is because N_{ori} = 8 case lags behind other N_{ori} cases in the development of combustion to the radial direction of the torch flame.

Here, we introduce an index named t_{40}. The t_{40} describes the time at which 40% of the heat from combustion has been released. The time base of t_{40} is also set to ASOI.

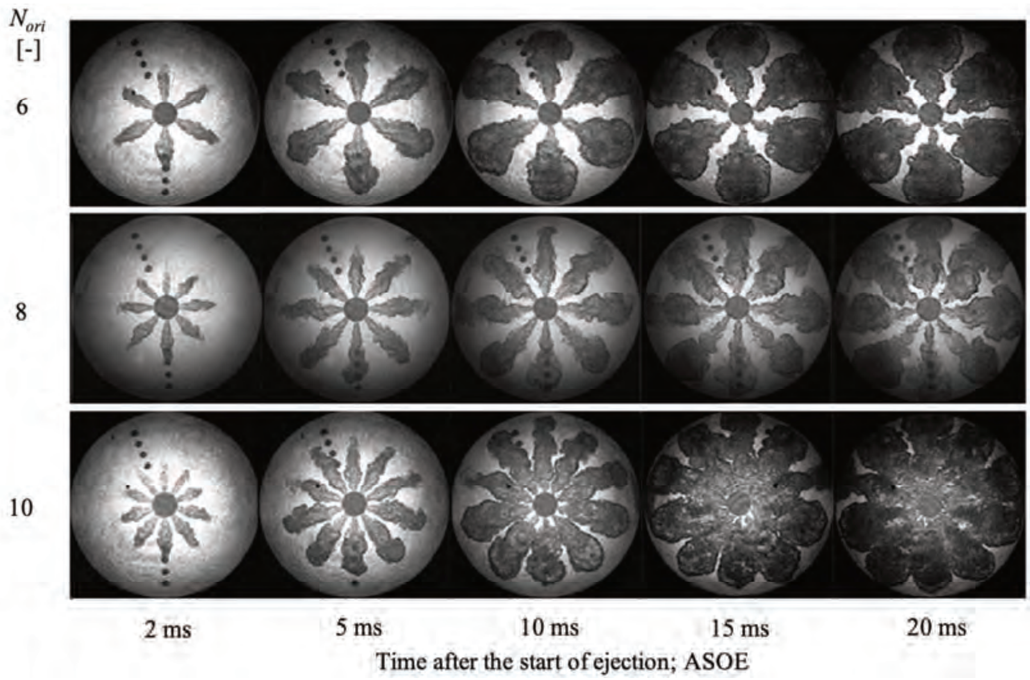

Fig. 12. Shadowgraph images of the different number of orifices (N_{ori} = 6, 8,10) under "combustible" conditions

The t_{40} indicates the timing of the combustion end since the heat loss to the cold chamber wall would be dominant in the case of the CVCC and 40% of input heat was a good measure to estimate the maximum of released heat. When N_{ori} is 6, 8, and 10, t_{40} is 131 ms, 88.3 ms, and 78.2 ms, respectively. The t_{40} shows that the case with N_{ori} = 10 has the shortest combustion duration.

The peak value of the heat release rate is the highest in N_{ori} = 10 case in which the torch flames merged. After the heat release rates peaked at around 30 ms ASOI, the combustion was completed at t_{40} = 78.2 ms in N_{ori} = 10. The peak of heat release rate in N_{ori} = 8 was the most delayed and gentle among the three N_{ori} cases. The heat release rate of N_{ori} = 6 case rose quickest to its peak, but the period until the t_{40} is significantly longer than the other cases.

Based on the results of combustion visualization and pressure analysis described above, the entire mixture in the MC tended to burn efficiently when the torch flames merged, as explained in N_{ori} = 10 case.

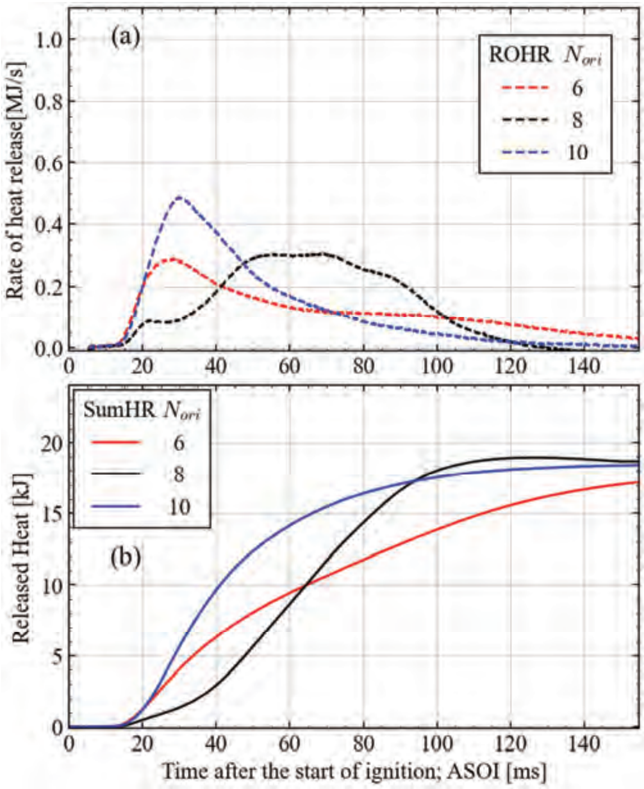

Fig. 13. Time history of (a) ROHR, and (b) of the different number of orifices (N_{ori} = 6, 8,10) under "combustible" conditions

3.2. Effects of the orifice diameter

This section investigates the effect of orifice diameter change in the PC on the torch flame and MC mixture combustion. Since the number of orifices was constant at eight and the orifice diameters (D_{ori}) were set to 2.5 mm, 3.5 mm, 5.0 mm (tip ID #4, #1, #5), the ratio of the total cross-sectional area of these orifices was about 1: 2: 4.

Figure 14 shows the elapsed time history of the torch flame's penetration length and cone angle when the MC was filled with "inert" ambient gas. Figure 15 shows the corresponding shadowgraph images of torch flames under the "inert" condition.

The penetration length increases with decreasing the orifice diameter, and this tendency has already appeared in the early stage of ejection. According to the momentum theory of a diesel spray [25], the penetration length of the spray varies in proportional to the square root of the orifice diameter.

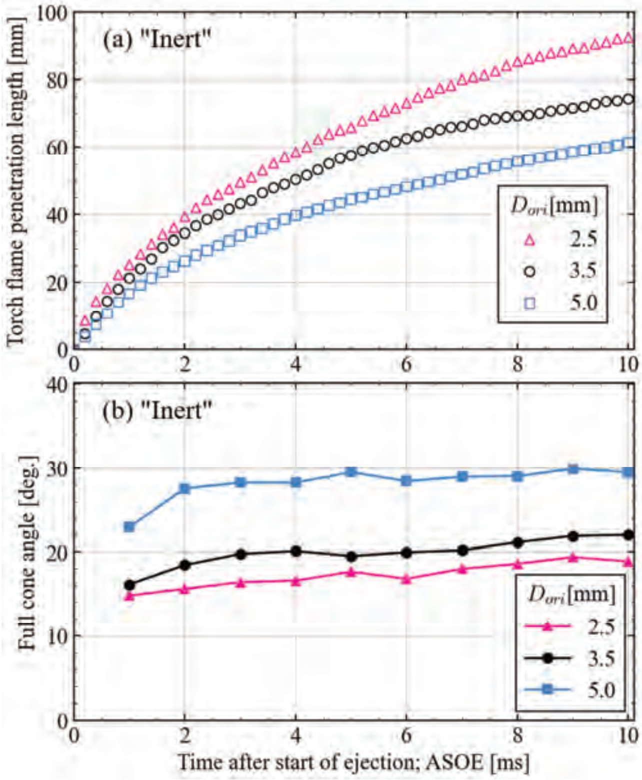

Fig. 14. Time history of (a) penetration, and (b) cone angle of different orifice diameter (D_{ori} = 2.5, 3.5, 5.0 mm) under "inert" condition

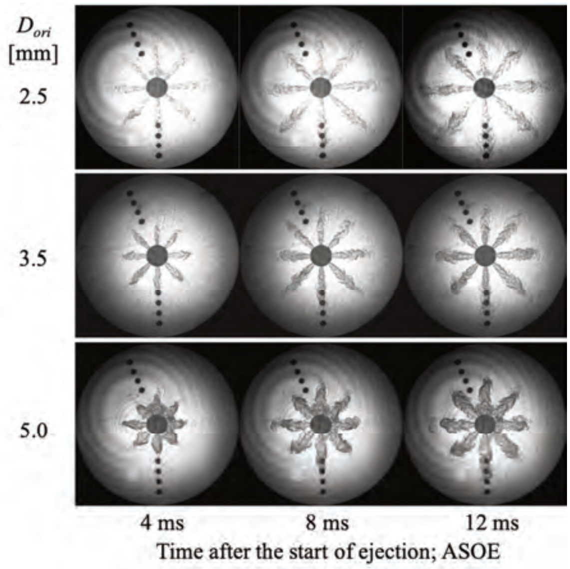

Fig. 15. Shadowgraphs of different orifice diameter (D_{ori} = 2.5, 3.5, 5.0 mm) under "inert" condition

The ratio of the square root of the orifice diameter is 1: 1.18: 1.41, and the ratio of the corresponding penetration length from the center of the PC is 76.6 mm (1): 89.4 mm

(1.17): 108.5 mm (1.42) at 15 ms ASOE, so the momentum theory seems to fit the torch flame as well. The cone angle is consistently larger for a larger orifice diameter.

For the smallest diameter case, D_{ori} = 2.5 mm, the torch flame boundary is unclear, and the flame tends to quench, especially near the exit of the PC orifice because the torch flames may be excessively stretched and cooled [19, 23] in the case of D_{ori} = 2.5 mm just after the ejection.

For D_{ori} = 3.5 mm, the unburned mixture can be observed to precede the tips of torch flames. The torch flame of D_{ori} = 5.0 mm clearly differs from the other orifices in the aspect of combustion, and the combustion continues even in the MC. For a D_{ori} = 5 mm, the cooling effect through the orifice would be reduced, and the torch flame would not be quenched. This implies that the orifice diameter greatly affects the ejection behavior of torch flames from the PC.

Figure 16 shows the effect of orifice diameter on the torch flame's penetration length and cone angle under "combustible" conditions. Figure 17 shows the corresponding shadowgraph images of torch flame ejection behavior under "combustible" conditions.

As explained, the penetration lengths in the "combustible" condition are longer than those in the "inert" condition. From the discussion in Section 3.1, this elongation of the penetration length can be attributed to the ignition of the unburned mixture volume attached to the torch flame tip and the combustion continuing in the MC mixture. The tendency for smaller orifice diameters to result in longer penetration length remains unchanged under combustible conditions.

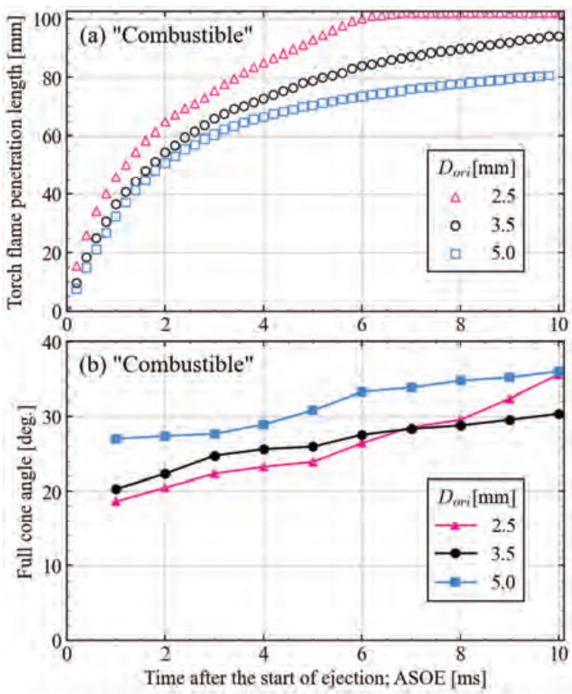

Fig. 16. Time history of (a) penetration, and (b) cone angle of different orifice diameter (D_{ori} = 2.5, 3.5, 5.0 mm) under "combustible" condition

In particular, the torch flame from D_{ori} = 2.5 mm impinged on the chamber wall at as early as 6 ms ASOE. Unlike the "inert" condition, the cone angle increased with time, and the increasing gradient was more evident in D_{ori} = 2.5 mm than in other orifice diameters. In D_{ori} = 2.5 mm case, the combustion process is inferred to be different from others.

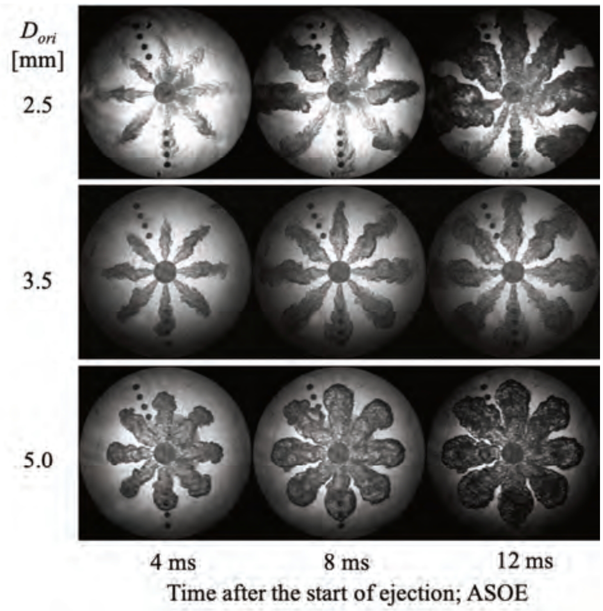

Fig. 17. Shadowgraphs of different orifice diameter (D_{ori} = 2.5, 3.5, 5.0 mm) under "combustible" condition

From the shadowgraph images in Fig. 17, the ignition process of MC mixture by the PC torch flames can be discussed in detail. In the case of D_{ori} = 2.5 mm at 4 ms ASOE, half of the torch flames could not ignite the MC mixture, and their ignition delay would be longer than 4 ms ASOE. At 8 ms ASOE, most of the torch flame ignited the MC mixture around the tip of the torch flames, but the torch jets still failed to ignite around their base. Finally, all the torch flames ignited the mixture at 12 ms ASOE, but the MC mixture flames could not go up to the orifice because of the excessive ejection velocity of the torch. Consequently, the combustion variation among the torch flames was evident when the orifice diameter was too small.

The torch flame of D_{ori} = 3.5 mm has already ignited the MC mixture at 4ms ASOE, but its tip is still thin at this timing. In the 12 ms ASOE, the tip of the torch flame expanded, but the MC mixture between two adjacent torch flames remained unburned.

In contrast, the torch flame of D_{ori} = 5.0 mm already ignited the MC mixture before 4 ms ASOE, and the tip of the torch flame is swelling like a snakehead. The torch flames merged in the vicinity of the PC and succeeded in consuming the mixture between the torch flames efficiently.

Figure 18 shows the difference in the history of the heat release rate and total heat release amount based on the MC pressure depending on the diameter of the orifice. The time axis is ASOI, and approximately 13 ms ASOI corresponds to ASOE for all orifice diameters.

The t_{40}, which is used as an index of the combustion end timing in the tested CVCC, was NA (combustion was too slow to reach 40% level), 88.3 ms, and 38.5 ms for D_{ori} = 2.5, 3.5, and 5.0 mm, respectively.

In D_{ori} = 2.5 mm, which showed a very non-uniform combustion pattern, the maximum value of heat release rate was the smallest, and the period of heat release was excessively extended as explained above. However, this D_{ori} = 2.5 mm case has the shortest period before the heat release rate reaches its maximum value. On the other hand, for D_{ori} = 5.0 mm, the maximum heat release rate is at least three times higher than in the other cases. The peak value was the highest among all the orifices used in this experiment. In addition, the heat release rate rose rapidly, and the heat release ended quickly after its peak.

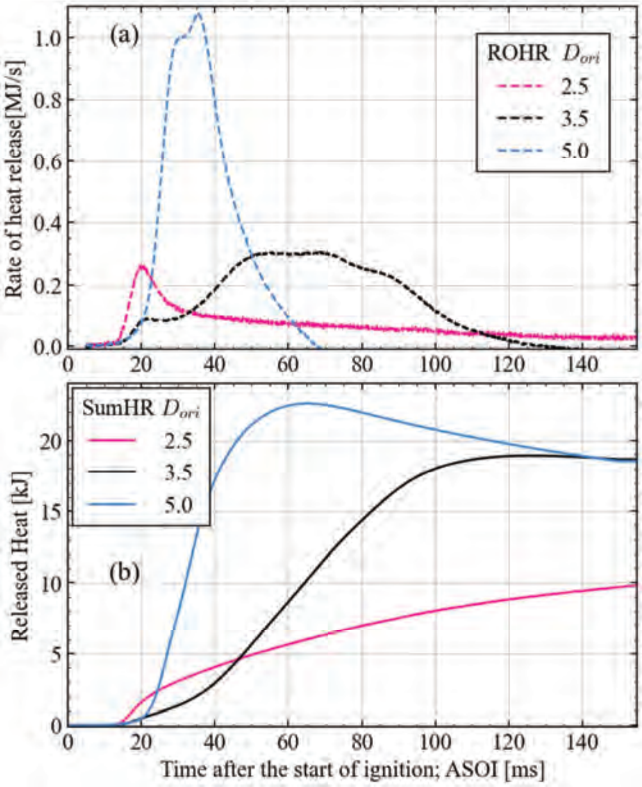

Fig. 18. Time history of (a) ROHR, and (b) of different orifice diameter (D_{ori} = 2.5, 3.5, 5.0 mm) under “combustible” condition

Thus, in the CVCC experiments under the initial condition at room temperature, it can be seen that the orifice diameter has significant effects both on the torch flame ejection behavior and the following MC combustion. Excessively small orifice diameter resulted in excessive ejection velocity and deterioration of ignition possibility of a torch flame. This result is in agreement with the experimental results of a PC-type small gas engine [26].

Contrariwise, larger orifice diameter resulted in slower torch ejection, but the combustion speed could be significantly accelerated when the torch flames were thick enough to merge near the exit of PC orifices. Therefore, it seems to be important for PC-type gas engines to promote combustion in the area between the torch flames by optimizing PC tip configuration.

4. Conclusions

This study investigates the effects of the PC configurations on torch flame propagation and MC combustion. The number and the diameter of the orifices were chosen as parameters to investigate. Combustion visualization and pressure analysis were performed using a constant volume combustion chamber, which simulates the combustion chamber of a medium-speed pre-chamber type gas engine used in marine and industrial applications. The results can be summarized as follows:

The potential of PC for ejecting effective torch flames was objectively examined by changing the MC ambient gas from nitrogen, and artificial air, to lean CH_4/air mixture. With nitrogen filled in MC, the “inert” case named in this paper, the pure momentum of torch flame ejected from PC can be evaluated, whereas the torch flame combustion can continue with the latter two MC ambient gases. The flame propagation from torch flames can be detected with the mixture ambient which is named the “combustible” case. The “inert” MC gas showed the shortest penetration because the unburned mixture on the tip of the torch flame is diluted by the nitrogen, but the other two ambient gases showed about the same penetration. This implies torch flame penetration is determined only by the sustainability of combustion reactions instead of the combustibility of the MC gas.

Contrarily, the cone angle of the torch flame varies significantly depending on the combustibility of the MC gas. In both the "inert" and the artificial air cases, the cone angle remained constant, but the cone angle in the "combustible" case was consistently more extensive and increased monotonically with time. Flame propagation of the MC mixture in a PC-type gas engine appears as radial growth perpendicular to the axis of the torch flame, rather than in the axial direction.

The effects of the number of orifices; N_{ori} were investigated by keeping the total opening area of orifices constant. In the “inert” cases, a small number of orifices was advantageous for getting longer penetration, but N_{ori} hardly affects the cone angle of the torch flame. As for the penetrating behavior of torch flame irrespective of N_{ori}, the initial penetration proceeds at a certain distance in proportion to time, and the penetration becomes proportional to the square root of time after the torch flame is fully developed. This behavior is similar to that of a steady gas jet.

Torch flame and MC combustion behavior were observed under "combustible" conditions in the MC. Penetration gets longer than the "inert" condition regardless of N_{ori}, and increases as N_{ori} decreases. However, the preceding unburned gas was quickly ignited by the torch flame, so the penetration changed according to the initial momentum of the torch flame. On the contrary, cone angle increases with flame growth. When N_{ori} is small, the initial growth of the torch flame is faster, but the premixed gases between the torch flames take a longer time to burn because of the wider spacing between the torch flames. Based on observations of heat release rates and visualization images, an important factor for PC-type premixed gas engines is to promote combustion of the premixed gas between the torch flames. With small N_{ori}, both penetration and cone angle increase due to the increased momentum of individual torch flames, but the combustion of the premixed air between torch flames is not necessarily promoted. When the optimum number of orifices is selected, the torch flames come into contact with each other in the early stage of combustion and grow toward the chamber wall as an apparently unified turbulent flame, resulting in faster combustion.

The effects of orifice diameter; D_{ori} were also investigated. Under "inert" conditions in the MC, the ratio of the square root of D_{ori} to the ratio of the penetration is in good agreement. Thus, the torch flame can be regarded as a steady gas jet, and the momentum theory of the spray can be applied to torch flames. The cone angle is consistently larger for larger D_{ori}. Excessively high jet velocity at small D_{ori} increases flame stretching and cooling losses at the orifice hole.

Under "combustible" conditions, the penetration is consistently larger than in the "inert" cases, but smaller D_{ori} results in longer penetration as well as in the "inert" case. The cone angle trend is related to the ignitability of the torch flame to the MC premixture. When the jetting velocity of the torch flame is excessive, the ignition delay is also elongated, and after ignition, it is rapidly expanded by the entrained MC premixture. For this reason, the smaller D_{ori}, the greater the rate of increase in cone angle. For a small D_{ori}, the rate of heat generation is faster at the onset and at the first peak, but the subsequent combustion is slower. When D_{ori} is large, the start-up is slightly slower, but the flame propagates into the premixed air between the torch flames, and the total heat generation increases. When D_{ori} increases to a certain degree and the torch flames come into contact in the early stage of combustion, faster combustion as described above is achieved.

Nomenclature

A_{ori}	total area of pre-chamber orifice
ASOE	after the start of ejection
ASOI	after the start of ignition
CFD	computational fluid dynamics
CH_4	methane
CVCC	constant volume combustion chamber
D	diameter
D_{itip}	inner diameter of pre-chamber tip
D_{ori}	diameter of pre-chamber orifice
FMDF	filtered mass density function
GHG	greenhouse gas
H	high
LES	large eddy simulation
LIF	laser-induced fluorescence
L_{ori}	length of pre-chamber orifice
MC	main chamber
N_{ori}	the number of pre-chamber orifice
NO_x	nitrogen oxide
N_2	nitrogen
O_2	oxygen
PC	pre-chamber
PM	particulate matter
RCM	rapid compression machine
SO_x	sulfur oxide emissions
t	thickness
TJI	turbulent jet ignition
V_{MC}	volume of main chamber
V_{PC}	volume of pre-chamber
λ	global air excess ratio

Bibliography

[1] AL-ENAZI, A., OKONKWO, E.C., BICER, Y. et al. A review of cleaner alternative fuels for maritime transportation. *Energy Reports*. 2021, **7**, 1962-1985. https://doi.org/10.1016/j.egyr.2021.03.036

[2] LIU, J., ULISHNEY, C.J., DUMITRESCU, C.E. Experimental investigation of a heavy-duty natural gas engine performance operated at stoichiometric and lean operations. *Energy Conversion and Management*. 2021, **243**, 114401. https://doi.org/10.1016/j.enconman.2021.114401

[3] KHAN, M.I., YASMIN, T., SHAKOOR, A. Technical overview of compressed natural gas (CNG) as a transportation fuel. *Renewable and Sustainable Energy Reviews*. 2015, **51**, 785-797. https://doi.org/10.1016/j.rser.2015.06.053

[4] CHO, H.M., HE, B.Q. Spark ignition natural gas engines – a review. *Energy Conversion and Management*. 2007, **48**(2), 608-618. https://doi.org/10.1016/j.enconman.2006.05.023

[5] EINEWALL, P., JOHANSSON, B. Cylinder to cylinder and cycle to cycle variations in a six cylinder lean burn natural gas engine. *SAE Technical Papers* 2000-01-1941. https://doi.org/10.4271/2000-01-1941

[6] DUAN, X., DENG, B., LIU, Y. et al. An experimental study the impact of the hydrogen enrichment on cycle-to-cycle variations of the large bore and lean burn natural gas spark-ignition engine. *Fuel*. 2020, **282**, 118868. https://doi.org/10.1016/j.fuel.2020.118868

[7] DALE, J.D., CHECKEL, M.D., SMY, P.R. Application of high energy ignition systems to engines. *Progress in Energy and Combustion Science*. 1997, **23**(5-6), 379-398. https://doi.org/10.1016/S0360-1285(97)00011-7

[8] STARIKOVSKIY, A., ALEKSANDROV, N. Plasma-assisted ignition and combustion. *Progress in Energy and Combustion Science*. 2013, **39**(1), 61-110. https://doi.org/10.1016/j.pecs.2012.05.003

[9] BAK, M.S., DO, H., MUNGAL, M.G. et al. Plasma-assisted stabilization of laminar premixed methane/air flames around the lean flammability limit. *Combustion and Flame*. 2012, **159**(10), 3128-3137. https://doi.org/10.1016/j.combustflame.2012.03.023

[10] WERMER, L., LEFKOWITZ, J.K., OMBRELLO, T. et al. Spark and flame kernel interaction with dual-pulse laser-induced spark ignition in a lean premixed methane–air flow. *Energy*. 2021, **215**, 119162. https://doi.org/10.1016/j.energy.2020.119162

[11] BUESCHKE, W., SZWAJCA, F., WISLOCKI, K. Experimental study on ignitability of lean cng/air mixture in the multi-stage cascade engine combustion system. *SAE Technical Papers* 2020-01-2084. 2020. https://doi.org/10.4271/2020-01-2084

[12] GHORBANI, A., STEINHILBER, G., MARKUS, D. et al. Ignition by transient hot turbulent jets: An investigation of ignition mechanisms by means of a PDF/REDIM method.

Proceedings of the Combustion Institute. 2015, **35**(2), 2191-2198. https://doi.org/10.1016/j.proci.2014.06.104

[13] ATTARD, W.P., FRASER, N., PARSONS, P. et al. A Turbulent Jet Ignition pre-chamber combustion system for large fuel economy improvements in a modern vehicle powertrain. *SAE International Journal of Engines.* 2010, **3**(2), 20-37. https://doi.org/10.4271/2010-01-1457

[14] ATTARD, W.P., KOHN, J., PARSONS, P. Ignition energy development for a spark initiated combustion system capable of high load, high efficiency and near zero NO_x emissions. *SAE International Journal of Engines*. 2010, **3**(2), 481-496. https://doi.org/10.4271/2010-32-0088

[15] ALVAREZ, C.E.C., COUTO, G.E., ROSO, V.R. et al. A review of prechamber ignition systems as lean combustion technology for SI engines. *Applied Thermal Engineering*. 2018, **128**, 107-120. https://doi.org/10.1016/j.applthermaleng.2017.08.118

[16] ZHU, S., AKEHURST, S., LEWIS, A. et al. A review of the pre-chamber ignition system applied on future low-carbon spark ignition engines. *Renewable and Sustainable Energy Reviews*. 2022, **154**, 111872. https://doi.org/10.1016/j.rser.2021.111872

[17] VALIDI, A.A., SCHOCK, H., JABERI, F. Turbulent jet ignition assisted combustion in a rapid compression machine. *Combustion and Flame*. 2017, **186**, 65-82. https://doi.org/10.1016/j.combustflame.2017.07.032

[18] SADANANDAN, R., MARKUS, D., SCHIEßL, R. et al. Detailed investigation of ignition by hot gas jets. *Proceedings of the Combustion Institute*. 2007, **31**(1), 719-726. https://doi.org/10.1016/j.proci.2006.08.027

[19] BISWAS, S., TANVIR, S., WANG, H. et al. On ignition mechanisms of premixed CH_4/air and H_2/air using a hot turbulent jet generated by pre-chamber combustion. *Applied Thermal Engineering*. 2016, **106**, 925-937. https://doi.org/10.1016/j.applthermaleng.2016.06.070

[20] BUESCHKE, W., SKOWRON, M., SZWAJCA, F. et al. Flame propagation velocity in 2-stage gas combustion system applied in SI engine. *IOP Conference Series: Materials Science and Engineering*. 2018, **421**(4). https://doi.org/10.1088/1757-899X/421/4/042009

[21] BUESCHKE, W., SKOWRON, M., WISŁOCKI, K. et al. Comparative study on combustion characteristics of lean premixed CH_4/air mixtures in RCM using spark ignition and turbulent jet ignition in terms of orifices angular position change. *Combustion Engines*. 2019, **176**(1), 36-41. https://doi.org/10.19206/CE-2019-105

[22] GENTZ, G., GHOLAMISHEERI, M., TOULSON, E. A study of a turbulent jet ignition system fueled with iso-octane: pressure trace analysis and combustion visualization. *Applied Energy*. 2017, **189**, 385-394. https://doi.org/10.1016/j.apenergy.2016.12.055

[23] ZHOU, L., SONG, Y., HUA, J. et al. Effects of different hole structures of pre-chamber with turbulent jet ignition on the flame propagation and lean combustion performance of a single-cylinder engine. *Fuel*. 2022, **308**, 121902. https://doi.org/10.1016/j.fuel.2021.121902

[24] PIELECHA, I., BUESCHKE, W., SKOWRON, M. et al. Prechamber optimal selection for a two stage turbulent jet ignition type combustion system in CNG-fuelled engine. *Combustion Engines*. 2019, **176**(1), 16-26. https://doi.org/10.19206/CE-2019-103

[25] WAKURI, Y., FUJII, M., AMITANI, T. et al. Studies on the penetration of fuel spray of diesel engine. *Transactions of the JSME*. 2015, **7**(11), 101-104. https://doi.org/10.1299/kikai1938.25.820

[26] NAKANO, H., KAYA, R., KOBAYASHI, S. et al. A study on the influence of the strength of ejected jet on combustion in a natural gas lean burn engine with a sub-chamber with direct injector inside. *COMODIA 2017 – 9th International Conference on Modeling and Diagnostics for Advanved Engine Systems*. 2017. https://doi.org/10.1299/jmsesdm.2017.9.c301

Takuya Wakasugi, BEng. – Interdisciplinary Graduate School of Engineering Sciences, Kyushu University, Japan.
e-mail: *wakasugi.takuya.875@s.kyushu-u.ac.jp*

Hiroshi Tashima, DEng. – Faculty of Engineering Sciences, Kyushu University, Japan.
e-mail: *tajima.hiroshi.539@m.kyushu-u.ac.jp*

Daisuke Tsuru, DEng. – Faculty of Engineering Sciences, Kyushu University, Japan.
e-mail: *dtsuru@ence.kyushu-u.ac.jp*

Article citation info:
MATLA, J. Possible applications of prechambers in hydrogen internal combustion engines. *Combustion Engines*. 2022, **191**(4), 77-82. https://doi.org/10.19206/CE-148170

Jędrzej MATLA

Combustion Engines
Polish Scientific Society of Combustion Engines

Possible applications of prechambers in hydrogen internal combustion engines

ARTICLE INFO

Received: 25 February 2022
Revised: 27 March 2022
Accepted: 8 April 2022
Available online: 24 April 2022

In order to ensure better control of the combustion process in a internal combustion engine powered by hydrogen, it has been proposed to use a split combustion chamber solution. Following paper contains a description of a hydrogen combustion system that includes an analysis of possible technical solutions. The considerations take into account the issues of the dual nature of hydrogen knocking and the problem of burning a stratified charge of a hydrogen-air mixture in a cylinder.

Key words: *hydrogen combustion, hydrogen knock, prechamber, H2ICE, combustion engine*

1. Introduction

In theory, internal combustion engines powered by hydrogen fuels, being less efficient than fuel cells, are an attractive alternative for them. The reasons for this state are mainly their high production potential and well-developed production technologies. The relatively simple structure and low cost of recycling compared to fuel cells allow to conclude with a high probability that hydrogen-powered combustion engines will be the main source of power in electricity and heat generation, as well as marine propulsion source in the near future [5, 15, 25]. The main advantage of using hydrogen as a fuel is its presence in most organic substances, which makes it an open source of power based on renewable technologies. Another advantage of hydrogen combustion in an internal combustion engine is almost complete elimination of carbon from the combustion process, which significantly improves the composition of the exhaust gases in terms of ecology. Complete elimination of carbon from the combustion process seems to be impossible at the moment due to technological limitations and its penetration through the piston rings gaps into the combustion chamber. Considering its negligible amount in relation to its content in commonly used fossil fuels, this issue is not considered in this paper. Aspects in favor of hydrogen fuels are also their high resistance to autoignition from compression and a higher auto-ignition temperature than in the case of petrol resulting from its high octane number (Table 1).

Table 1. Selected parameters of hydrogen and other fuels [16]

	Hydrogen	Methane	Methanol	Ethanol	Gasoline	Unit
Chemical formula	H_2	CH_4	CH_3OH	C_2H_5OH	C_4H_{12}	–
Molecular weight	2.02	16.04	32.04	46.07	100–105	u
Density	0.0838	0.668	791	789	751	kg/m^3
Air flammability range	4.0–75.0	5.0–15.0	6.7–36.0	4.3–19.0	1.4–7.6	vol%
Autoignition temperature	585	540	385	423	230–480	ºC
RON	> 130	120	109	109	88–108	–

Despite the aforementioned advantages of hydrogen fuels, their combustion in internal combustion engines is sometimes quite problematic, mainly because of the low ignition energy, which is lower by an order of magnitude compared to gasoline. The low value of the ignition energy of hydrogen makes it easier to start a cold engine significantly, but it also causes a high sensitivity to the formation of spontaneous self-ignition regions resulting in knocking combustion of the air-fuel mixture. Hydrogen knock is a highly undesirable phenomenon, mainly due to the durability aspect. Knocking combustion that generates pressure pulsations in the main combustion chamber leads to excessive wear of the crankshaft bearings and is an additional source of thermal loads. In addition to affecting durability, the phenomenon of hydrogen knock also contributes to a significant reduction in engine performance [29].

Following article presents the results of the considerations on the use of split combustion chambers in hydrogen-powered combustion engines. These considerations take into account aspects related to, inter alia, the dual nature of hydrogen combustion, the combustion of a stratified charge and their influence on the emissivity of harmful substances, with main focus on nitrogen oxides.

2. Hydrogen combustion

Hydrogen, as an alternative source of power for commonly used combustion engines, has many advantages, the most important of which is the absence of carbon-based compounds in the exhaust gases. Currently, mainly due to costs, the most popular form of hydrogen storage and transport in vehicle fuel systems is the gas form [14].

2.1. Hydrogen knock

According to the definition, knocking combustion of the air-fuel mixture in an internal combustion engine is a typical example of an incorrectly performed combustion process [6]. Self-ignition of the air-fuel mixture resulting from increased pressure and temperature in the combustion chamber is assumed to be the main cause of knocking in a spark ignition engine. Hot spots, which are the ignition point of the mixture, are also a factor contributing to knocking combustion. The pressure wave from uncontrolled ignition and the accompanying characteristic sound have an adverse effect on the engine for several reasons. Firstly, a rapid increase of pressure in the combustion chamber causes expeditious wear of the crank system bearings, secondly, this phenomenon significantly contributes to the increase in thermal loads, mainly in the area of the piston crown, and thirdly, overlapping pressure waves having different sources of formation cause significant lowering of the indicated pressure, which in turn contributes to a decrease in its overall efficiency.

In theory, hydrogen as a fuel is characterized by a high compression ignition resistance, which is indicated by the octane number (ON). It describes the resistance of the fuel to knocking combustion, and in the case of hydrogen, its research value (RON) is 130 [23]. On the other hand, practice shows that hydrogen combustion promotes the formation of pressure waves much higher than in the case of gasoline combustion with a research octane number close to 100 [26]. The index used in that case called the motorized octane number (MON) is at level of 60 [32]. Large discrepancies between the values of the RON and MON indexes indicate that they should not be used in relation to hydrogen. A better choice for the evaluation of knock resistance is the methane number (LM) proposed by Ryan et al. used to determine the parameters of gaseous fuels commonly used to express the probability of engine heavy run [20]. Methane number describes the percentage of methane in the reference mixture consisting of hydrogen and methane. Taking into account the methane number equal to 0 in the case of hydrogen, it can be concluded that it is the fuel with the most favorable properties for the occurrence of the knocking combustion phenomenon resulting from unstable course of combustion process.

Table 2. Methane number of selected gaseous fuels [11, 12]

Fuel	Hydrogen	Coal gas	Propane	Natural gas	Methane
Methane number	0	24–30	34	75–95	100

As research shows, the hydrogen knock phenomenon may have two mechanisms of formation, thus we are talking about its dual nature. The first cause, as in the case of a conventional gasoline-air mixture, is the spontaneous combustion of hydrogen as a result of the excessively elevated temperature and pressure at the end of the power stroke. This type of hydrogen knock is defined as heavy and causes a noticeable increase in pressure in the combustion chamber up to several MPa. Its formation also closely correlates with the engine compression ratio [31]. The second mechanism of hydrogen knock generation is the so called light knock, whose cause is claimed to be the unstable combustion process initiated by the spark plug. Although the limit of light knock cannot be clearly established, the pressure pulsations caused by this phenomenon are in the range of 20–100 kPa. It is not as harmful to the engine as heavy knock, but it is also an undesirable phenomenon, therefore it is justified to improve the control of the combustion process in the area of its occurrence.

An important factor influencing the occurrence of hydrogen knock is also the composition of the fuel-air mixture (Fig. 1). Due to the fact that the lean mixture contributes to a decrease in the speed of flame propagation, it reduces the risk of knocking. Research has shown that the intensity of hydrogen knock is the highest for a stoichiometric mixture [11, 12], and therefore it is aimed to deplete the mixture.

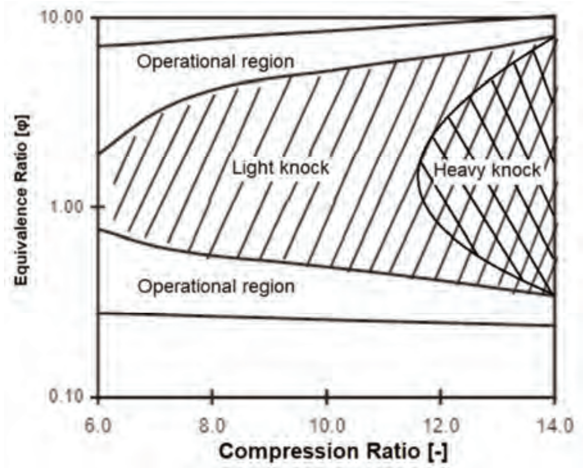

Fig. 1. Regions of hydrogen combustion in SI engines with the heavy knock distinction introduced by the author [11, 28]

Other solutions to impede the occurrence of knock are also changes in the engine operation cycle [33], water injection [3] or exhaust gas recirculation [27], although they usually decrease the overall efficiency of the engine. The location of the self-ignition occurrence is also important, therefore combustion chambers have been developed to prevent knocking through their geometrical features [34].

2.2. Compression ratio

The compression ratio is one of the most important parameters that describe an internal combustion engine mainly due to its direct impact on engine efficiency. According to the equation for ideal gas, an increase of the compression ratio is accompanied by the temperature elevation of the mixture in the combustion chamber. In the case of a mixture of hydrogen and air, this is not considered a disadvantage at first glance, because of its higher autoignition temperature than in the case of gasoline. However, an increase in the temperature of the mixture at the moment of ignition has a significant impact on shortening the delay of its self-ignition. As a result, the speed of the combustion process increases, which can be observed by rapid pressure pulsation. The generated high-amplitude pressure waves are, in turn, the main cause of the hydrogen knock phenomenon.

The second, but not less important, factor in the influence of the compression ratio on the occurrence of the knock phenomenon is the increase in the energy density of the charge in the combustion chamber resulting from the decreasing volume of the chamber during the compression stroke. A higher concentration of chemical compounds involved in the combustion reaction increases the amount of heat released in its course, which, in turn, increases the temperature of the entire process. The increased substrate concentration results in a consequent higher combustion rate, causing the pressure in the combustion chamber to rise rapidly. As research shows, an important factor influencing the formation of the combustion process is also the temperature stratification inside the combustion chamber, therefore it is reasonable to take into account the temperature inhomogeneities responsible for the formation of the so-called hot spots. The limit value indicated by the research teams is 30 K [21, 22]. When this value is exceeded, a high probability of knocking occurs.

It seems reasonable to say that an increase in pressure may cause a decrease in the speed of the combustion process [19], however due to the relatively small influence of this phenomenon compared to the increase in temperature, this was not taken into account in further considerations.

Influence of the compression ratio on the ignition of a mixture with the excess air coefficient λ = 1, investigated in details by Szwaja et al. [13, 24] and Karim et al. [14, 16], shows a clear increase in pressure pulsation intensity for compression ratio values greater than 11 (Fig. 2). After exceeding this value, the hydrogen combustion mechanism of the mixture was described as a heavy knock, resulting from self-ignition in the final phase of combustion process [8].

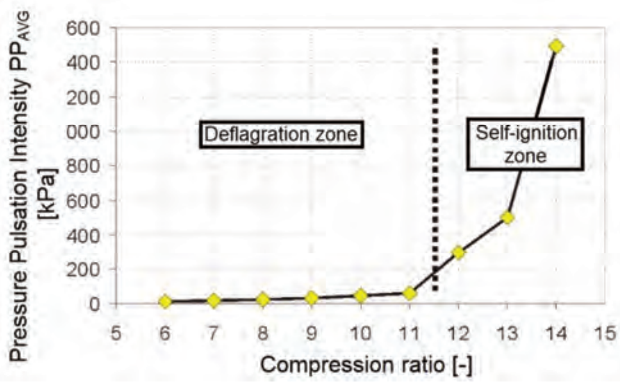

Fig. 2. Compression ratio influence on pressure pulsation intensity of CFR engine [28]

In the range of compression ratios 6–11, combustion of the mixture was described as deflagration with no signs of heavy knock. Deeper analysis showed pressure pulsations with a much smaller amplitude in the range from 20 kPa to 100 kPa caused by the unstable combustion process. This process, called light knock, is also an undesirable phenomenon, despite its less destructive effect on engine components than in the case of heavy knock. As a result of the vibrations of the piston rings, it can cause their accelerated wear, therefore it is reasonable to improve the combustion process in this area.

For compression ratio values below 7, the pressure pulsation amplitudes are so low that they do not have a significant effect on engine operation. It should be mentioned that all ranges for the occurrence of the hydrogen knock phenomenon for the stoichiometric mixture are arbitrary, therefore special attention should be paid to the interpretation of the results of tests carried out especially in the areas of these contractual limit values.

2.3. Lean combustion of hydrogen

The strategy of combustion of the mixture with excess air is a solution commonly used in internal combustion engines for many years. Its general purpose is to improve the economy by reducing fuel consumption and improving the emissivity of the engine.

Currently, lean mixture combustion in conventional spark ignition engines reduces pumping losses in the intake manifold by keeping the throttle valve open at low loads. Furthermore, the higher specific heat of the lean mixture increases the efficiency of the Otto cycle, thus increasing the overall efficiency of the engine [2]. The main factor that limits the excess air coefficient is the exhaust gas temperature, which decreases along with the depletion of the mixture. This phenomenon is important from the point of view of the efficiency of the three-way catalytic converter, which operation depends on the process temperature and the oxygen content in the exhaust gases. In the context of hydrogen combustion, the depletion of the air-fuel mixture slows down the combustion process. As noted by Szwaja, along with the increase of the excess air coefficient, the intensity of pulsation of the combustion pressure decreases linearly (Fig. 3). This phenomenon can be used to increase the efficiency of the engine by increasing its compression ratio.

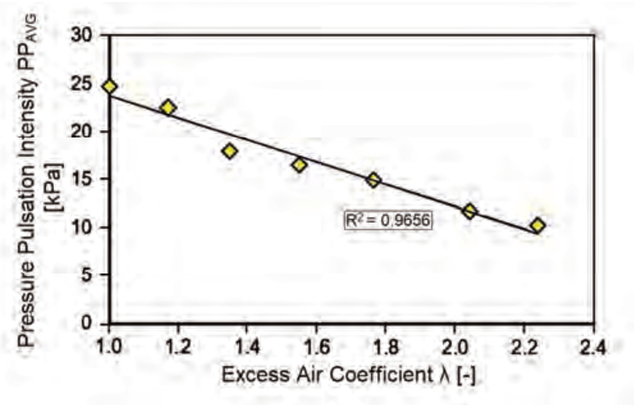

Fig. 3. Excess air influence on pressure pulsation intensity [25]

Lowering the temperature of the combustion process closely correlates with the self-ignition delay, which decreases with temperature deterioration (Fig. 4). Excessive shortening of the self-ignition delay increases the probability of self-ignition, which directly translates into the occurrence of the hydrogen knock phenomenon.

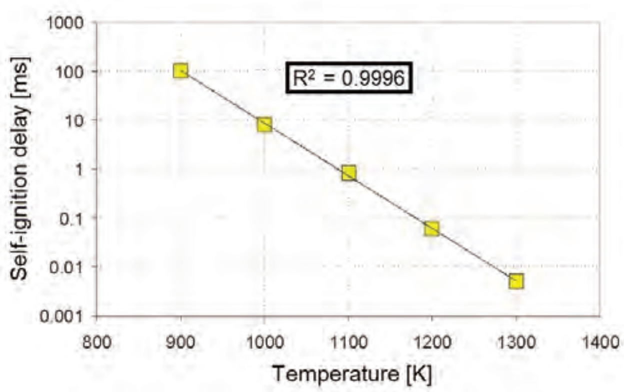

Fig. 4. Combustion process temperature influence on self-ignition delay for stoichiometric air-hydrogen mixture [29]

The results of the research indicate the optimal value of excess air coefficient (λ) at the level of 2.2 [24, 25], whose exceeded value does not have significant effects in terms of emissivity and efficiency. Research by Lee et al. [10] shows that the next step to increase the overall efficiency of a hydrogen-powered internal combustion engine is to burn a stratified charge. This strategy allows for the attainment of better stability of the combustion process by increasing the time of mixture formation and allows for its further depletion in order to increase engine overall efficiency.

3. Prechambers

One of the methods of increasing the control of mixture formation is the implementation of a split combustion chamber. It is a solution based on the concept of dividing the combustion chamber into the main and preliminary space, showing a different structure depending on the fuel used. In compression ignition engines (Fig. 5b), the prechamber is classified as active, which means that the fuel is injected directly into it and its volume is usually from 25% to 40% of of the main chamber volume [17]. The shape of the prechamber separated from the main chamber by a necking enables the creation of controlled conditions for the self-ignition of the mixture by generating a sufficiently high temperature in it and reducing the excess air coefficient. The swirl chambers (Fig. 5a) also allow for the creation of a turbulence that allows for better mixing of the load. In the next phase of the combustion process, the high-speed ignition of the rich mixture in the prechamber at its exit allows for quick mixing with the excessive air in the main space, creating a lean mixture, the combustion of which is initiated by the ignition of the rich mixture.

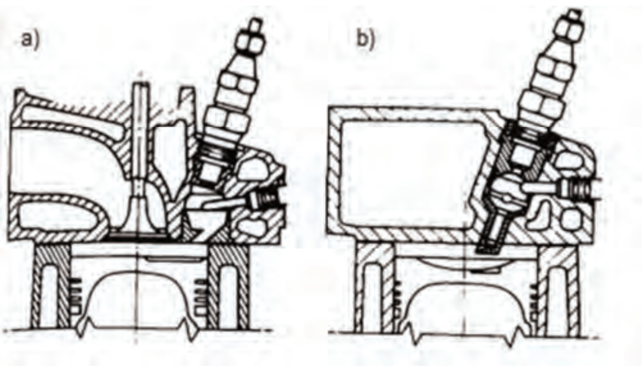

Fig. 5. Splitted chamber systems of CI engines: a) swirl chamber, b) prechamber [6]

In the case of spark ignition internal combustion engines, except some special cases, the prechambers are not a commonly used solution. The reasons for this state of matter can be found in the physicochemical properties of liquid fuels. Due to the smaller volume of the prechamber compared to compression ignition engines amounting only up to a few percent of the main chamber volume, phenomenon of fuel deposition on the walls of the chamber occurs, so that part of it does not participate in the combustion process, resulting in an increase in hydrocarbons emissions. The prechambers, on the other hand, exhibit promising results in the context of engines powered by gaseous fuels [31, 32]. As the research shows, the best results are obtained when an active chamber is used, which allows to obtain a stratified charge through an additional injector installed in it (Fig. 6b). This solution allows for the formation of an ultra-lean mixture with an excess air ratio above 3 in the main combustion chamber.

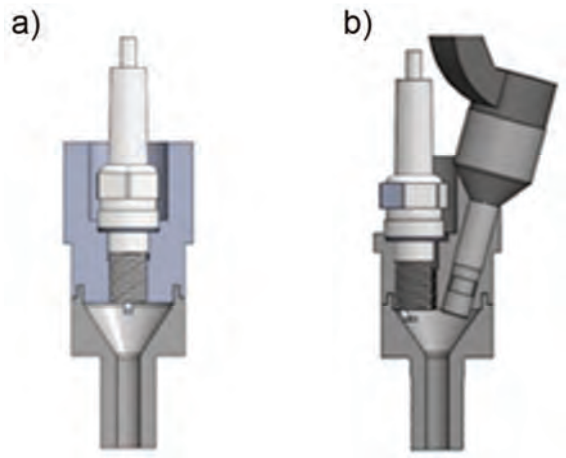

Fig. 6. Prechambers used in SI engines: a) passive prechamber; b) active prechamber [1]

4. Proposed system description

The preliminary function of a system proposed by the author is to improve the combustion parameters of the hydrogen-air mixture in the area of light knock. The use of an active prechamber integrated with the head should enable the use of a greater degree of mixture depletion than in the case of chambers screwed into the spark plug seating. This solution should ensure better heat transmission from the combustion process and allow for even flame propagation due to orifices installed in the prechamber necking area. The main advantage of the discussed system should be a higher compression ratio while maintaining pressure pulsation below the light knock limit.

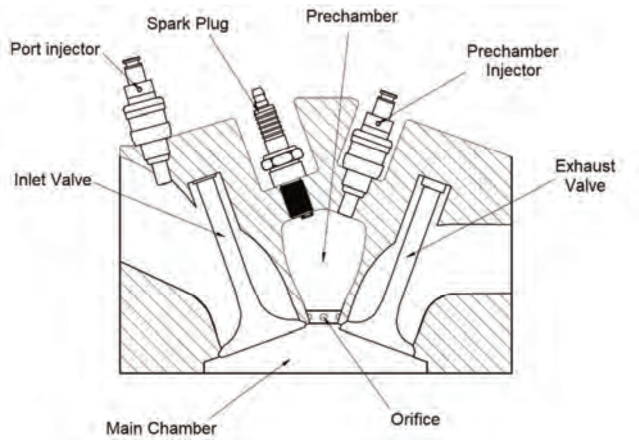

Fig. 7. Simplified scheme of hydrogen combustion prechamber system

The presented system (Fig. 7) assumes the formation of a lean or ultra-lean mixture in the space of the main combustion chamber by means of indirect hydrogen injection. It is also considered to apply direct injection system in the future as it gives better results in real conditions tests [4]. In the space of the preliminary chamber, the volume of which is assumed to be a few percent of the volume of the main chamber, integrated with the cylinder head, the ignition of the stoichiometric or lean mixture is initiated. The mixture then ignites in the main chamber, creating a stratified charge combustion mechanism. The geometry of the prechamber and the detailed parameters of the optimal excess air coefficients will be the subject of further research by the author.

5. Summary

Taking into account the factors mentioned in the previous chapters, it seems justified to conduct research aimed at examining the effect of using split combustion chambers in hydrogen powered combustion engines. Further research in this direction could contribute to the popularization of hydrogen as a fuel, and thus increase the share of fuels from renewable sources.

Combustion of hydrogen in internal combustion engines generates a number of problems, mainly due to the complicated mechanism of combustion. In the course of the analysis, it was found that the compression ratio and the degree of mixture depletion are the factors that have the greatest impact on the hydrogen combustion process. On the basis of the literature review, their impact on the generation of hydrogen knock was determined, which, depending on the intensity of pressure pulsation in the combustion chamber, can be divided into heavy knock, which is a highly undesirable phenomenon, and light knock, in the area of which, according to the author, it is possible to improve the combustion process.

Based on the analysis of the issues discussed in the following article, the author presents a preliminary proposal for a hydrogen combustion system in an internal combustion engine, the operation of which should be verified in further research. In principle, this system is to be characterized by efficiency higher than that of any previously known solution.

Nomenclature

CFR	cooperative fuel research
CI	compression ignition
CR	compression ratio
MN	methane number
MON	motorized octane number
ON	octane number
PP_{AVG}	average pressure pulsation intensity
RON	research octane number
SI	spark ignition
λ	excess air coefficient
φ	equivalence ratio ($1/\lambda$)

Bibliography

[1] ALVAREZ, C.E.C., COUTO, G.E., ROSO, V.R. et al. A review of prechamber ignition systems as lean combustion technology for SI engines. *Applied Thermal Engineering*. 2018, **128**, 107-120. https://doi.org/10.1016/j.applthermaleng.2017.08.118

[2] BONTORIN, A.C.B., DE OLIVEIRA CARVALHO, L. Investigation of the impact of lean mixtures on the performance of GDI engines. *SAE Technical Papers* 2016-36-0326. 2016. https://doi.org/10.4271/2016-36-0326

[3] BORETTI, A. Stoichiometric H2ICEs with water injection. *International Journal of Hydrogen Energy*. 2011, **36**(7), 4469-4473. https://doi.org/10.1016/J.IJHYDENE.2010.11.117

[4] BRZEŻAŃSKI, M., RODAK, Ł. Investigation of a new concept of hydrogen supply for a spark-ignition engine. *Combustion Engines*. 2019, **178**(3), 140-143. https://doi.org/10.19206/CE-2019-324

[5] GIS, M., GIS, W. The current state and prospects for hydrogenisation of motor transport in Northwestern Europe and Poland. *Combustion Engines*. https://doi.org/10.19206/CE-144560

[6] HEYWOOD, J.B. Internal combustion engines fundamental. *McGraw-Hill Inc*. New York 1988.

[7] KARIM, G.A. Hydrogen as a spark ignition engine fuel. *International Journal of Hydrogen Energy*. 2003, **28**(5), 569-577. https://doi.org/10.1016/S0360-3199(02)00150-7

[8] KAWAHARA, N., TOMITA, E. Visualization of autoignition and pressure wave during knocking in a hydrogen spark-ignition engine. *International Journal of Hydrogen Energy*. 2009, **34**(7), 3156-3163. https://doi.org/10.1016/J.IJHYDENE.2009.01.091

[9] KREBS, S., BIET, C. Predictive model of a premixed, lean hydrogen combustion for internal combustion engines. *Transportation Engineering*. 2021, **5**, 100086. https://doi.org/10.1016/j.treng.2021.100086

[10] LEE, S., KIM, G., BAE, C. Lean combustion of stratified hydrogen in a constant volume chamber. *Fuel*. 2021, **301**, 121045. https://doi.org/10.1016/j.fuel.2021.121045

[11] LI, H.K., KARIM, G.A. Knock in spark ignition hydrogen engines. *International Journal of Hydrogen Energy*. 2004, **29**(8), 859-865. https://doi.org/10.1016/j.ijhydene.2003.09.013

[12] LUO, Q., SUN, B. Inducing factors and frequency of combustion knock in hydrogen internal combustion engines. *International Journal of Hydrogen Energy*. 2016, **41**(36), 16296-16305. https://doi.org/10.1016/j.ijhydene.2016.05.257

[13] MALENSHEK, M., OLSEN, D.B. Methane number testing of alternative gaseous fuels. *Fuel*. 2009, **88**(4), 650-656. https://doi.org/10.1016/j.fuel.2008.08.020

[14] MAZLOOMI, K., GOMES, C. Hydrogen as an energy carrier: prospects and challenges. *Renewable and Sustainable Energy Reviews*. 2012, **16**(5), 3024-3033. https://doi.org/10.1016/j.rser.2012.02.028

[15] MENES, M. Program initiatives of public authorities in the field of hydrogenation of the economy in a global perspective, as of the end of 2020. *Combustion Engines*. 2022, **189**(2), 18-29. https://doi.org/10.19206/CE-142170

[16] PERRY, R.H. Perry's Chemical Engineers' Handbook. VII. *McGraw-Hill Inc*. New York 1997.

[17] PISCHINGER, S. The combustion process in diesel engines. Intern. Combust. Engines II Lect. Notes. *RWTH-Aachen University*, 2017; 171-177.

[18] PÖSCHL, M., SATTELMAYER, T. Influence of temperature inhomogeneities on knocking combustion. *Combustion and Flame*. 2008, **153**(4), 562-573. https://doi.org/10.1016/j.combustflame.2007.11.009

[19] REYES, M., TINAUT, F.V., CAMAÑO, A. Experimental study of premixed gasoline surrogates burning velocities in a spherical combustion bomb at engine like conditions. *Energies*. 2020, **13**(13), 3430. https://doi.org/10.3390/en13133430

[20] RYAN, T.W., CALLAHAN, T.J., KING, S.R. Engine knock rating of natural gases–methane number. *Journal of Engineering for Gas Turbines and Power*. 1993, **115**(4), 769-776. https://doi.org/10.1115/1.2906773

[21] SANTOS, N.D.S.A., ALVAREZ, C.E.C., ROSO, V.R. et al. Combustion analysis of a SI engine with stratified and homogeneous pre-chamber ignition system using ethanol and hydrogen. *Applied Thermal Engineering*. 2019, **160**, 113985. https://doi.org/10.1016/j.applthermaleng.2019.113985

[22] SANTOS, N.D.S.A., ALVAREZ, C.E.C., ROSO, V.R. et al. Lambda load control in spark ignition engines, a new application of prechamber ignition systems. *Energy Conversion and Management*. 2021, **236**, 114018. https://doi.org/10.1016/j.enconman.2021.114018

[23] SWAIN, M., FILOSO, P., SWAIN, M. Ignition of lean hydrogen–air mixtures. *International Journal of Hydrogen Energy*. 2005, **30**(13-14), 1447-1455. https://doi.org/10.1016/j.ijhydene.2004.10.017

[24] SZWAJA, S., BHANDARY, K.R., NABER, J.D. Comparisons of hydrogen and gasoline combustion knock in a spark ignition engine. *International Journal of Hydrogen Energy*. 2007, **32**(18), 5076-5087. https://doi.org/10.1016/j.ijhydene.2007.07.063

[25] SZWAJA, S. Wodór jako paliwo podstawowe i dodatkowe do tłokowego silnika spalinowego. *Wydawnictwo Politechniki Częstochowskiej*, Częstochowa 2019.

Jędrzej Matla, MEng. – PhD student, Wrocław University of Science and Technology.
e-mail: *jedrzej.matla@pwr.edu.pl*

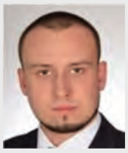

[26] SZWAJA, S. Origin of combustion pressure oscillations in both a gasoline – and a hydrogen-fueled internal combustion engine. *Archivum Combustionis*. 2010, **10**(1-2), 27-49.

[27] SZWAJA, S. Dilution of fresh charge for reducing combustion knock in the internal combustion engine fueled with hydrogen rich gases. *International Journal of Hydrogen Energy*. 2019, **44**(34), 19017-19025. https://doi.org/10.1016/j.ijhydene.2018.10.134

[28] SZWAJA, S. Studium pulsacji ciśnienia spalania w tłokowym silniku spalinowym zasilanym wodorem. *Wydawnictwo Politechniki Częstochowskiej*, Częstochowa 2010.

[29] SZWAJA, S. Hydrogen resistance to knock combustion in spark ignition internal combustion engines. *Combustion Engines*. 2011, **144**(1), 13-19. https://doi.org/10.19206/CE-117118

[30] SZWAJA, S., NABER, J.D. Impact of leaning hydrogen-air mixtures on engine combustion knock. *Journal of Kones*. 2008, **15**(2), 483–92.

[31] SZWAJA, S., NABER, J.D. Dual nature of hydrogen combustion knock. *International Journal of Hydrogen Energy*. 2013, **38**(28), 12489-12496. https://doi.org/10.1016/j.ijhydene.2013.07.036

[32] VERHELST, S., WALLNER, T. Hydrogen-fueled internal combustion engines. *Progress in Energy and Combustion Science*. 2009, **35**(6), 490-527. https://doi.org/10.1016/j.pecs.2009.08.001

[33] WEI, H., SHAO, A., HUA, J. et al. Effects of applying a Miller cycle with split injection on engine performance and knock resistance in a downsized gasoline engine. *Fuel*. 2018, **214**, 98-107. https://doi.org/10.1016/J.FUEL.2017.11.006

[34] XU, H., GAO, J., YAO, A. et al. The relief of energy convergence of shock waves by using the concave combustion chamber under severe knock. *Energy Conversion and Management*. 2018, **162**, 293-306. https://doi.org/10.1016/J.ENCONMAN.2018.02.024

Article citation info:
KLYUS, O., RAJEWSKI, P., LEBEDEVAS, S. et al. Determination of fuel atomization quality in compression ignition engines using acoustic emission signal. *Combustion Engines*. 2022, **191**(4), 83-91. https://doi.org/10.19206/CE-149370

Oleh KLYUS
Przemysław RAJEWSKI
Sergejus LEBEDEVAS
Sławomir OLSZOWSKI

Combustion Engines
Polish Scientific Society of Combustion Engines

Determination of fuel atomization quality in compression ignition engines using acoustic emission signal

ARTICLE INFO

Received: 15 July 2021
Revised: 6 August 2021
Accepted: 21 April 2022
Available online: 29 May 2022

The analysis of fuel injection processes in diesel engines showed the convergence of physical parameters affecting the mean diameter of the Sauter SMD (selected as a spray quality parameter) of the atomized fuel droplets and the parameters of the acoustic signal emission originating from the spring waves accompanying the atomization process. In experimental studies, the laser diffraction method was used to measure the atomization quality with the Malvern Spraytec device. For the acoustic signal recording and processing there was used the measurement set with a Fujicera 1045S sensor. The correlation between the values of the Sauter diameter and the energy of the acoustic signal has been obtained on the basis of which a method has been developed to assess the quality of fuel atomization in compression ignition engines by measuring the acoustic signal recorded during the fuel injection process.

Key words: *Diesel engines, fuel injection, atomization, Sauter mean diameter, acoustic emission*

1. Introduction

Basic requirements for the internal combustion engines primarily concern the limitation of toxic compound emissions in the exhaust gases and the reduction of fuel consumption. The achievement of these demands entails the application of various types of oxidizing and toxic compound reducing devices in the exhaust system and the organization of the work process in the combustion chamber. The areas of improvement of tested processes include: the preparation, injection and combustion of the fuel, which will enable a smaller amount of toxic compounds generated [11, 15] and can be reduced in the exhaust after-treatment system. In compression-ignition engines, such solutions concern inter alia using an injection equipment with the injected fuel of an increased pressure, which at present reach the value of 220–270 MPa e.g. Bosch injectors with the sensors: NCC and VCC EM (220 MPa) and piezo (250 MPa), heavy goods vehicles 270 MPa. There is also a research conducted on increasing that pressure to 300 MPa [11, 22, 33], regulating the course of fuel injection characteristic in storage systems of Common Rail type and optimizing the combustion chamber structure to the shape of injected fuel spouts [19, 21, 24, 36]. For each construction of diesel engine, there are specific optimal combinations of injection and atomization characteristics combined with the air charge and combustion chamber shape, which provide the best operation parameters of the diesel engine [31]. It should be emphasized that the occurring processes of fuel and air mixing make a decisive impact on physical phenomena (fragmentation and vaporization) and chemical phenomena (initial chemical reactions and oxidation), which have a decisive influence on self-ignition delay period, diffusive and kinetic combustion [12].

In this regard during examination of processes of creation, and combustion of flammable mixture in the diesel combustion chamber, what is essential are fuel drop diameters, which set among others evaluate the quality of the atomized fuel [15]. The laboratory tests of fuel atomization processes [5, 6] most frequently do not take into account the complex changes of flows and pressure inside the engine cylinder. Enhancing the computing capabilities made it possible to apply the numerical simulation methods in order to specify the shape of atomized fuel spout and the size of emerging drops. An example are the developed programs for the simulation of atomization process course [10, 18, 34] and liquid fuel drop evaporation [28, 30], where inter alia on the drop size depend the time of transition from the liquid to the gas phase, in which the fuel ignites and combusts.

Determining the size of atomized fuel drops entail the selection and application of the appropriate measurement method [1, 15, 16, 35] and specialized devices enabling the implementation of the selected method. Sometimes the complexity of the specialized equipment complicates the essential measurements. It needs to be emphasized that not every method of determining the quality of the atomized fuel is possible to be applied directly on a working diesel engine [10, 34].

On the other hand, processes occurring during the fuel flow and atomization are pulse in nature, during which the spring waves are formed emitting the acoustic signal at the same time [8, 9, 29]. Measurement of such a signal is simple enough, however the treatment and processing of that signal in order to gain diagnostics information concerning the work state of the specific engine element, is complex. First of all, it is related to recording all overlapping acoustic signals emitted by the elements of the working engine. Therefore, the energy level of the signal through the time-frequency decomposition of the signal enables the determination of the background noise which is characteristic in the designated frequency bands. The effective value of the signal is also the base value for determining the so-called "cut planes" in the result spectrum called the effect spectrum [25, 26]. The papers [4, 25, 26, 28] show the possibilities of using the acoustic emission (EA) to determine the technical condition of elements of injection equipment in compression-ignition engines, such as injection pump or injectors, but this information is usually of a nature comparative to the previously recorded model reference signal of injection equipment elements and does not have any features related to the quality of the processes taking place, including the quality of fuel atomization.

In the study source literature, there is lack of information on the topic of relation between fuel atomization quality and the emitted acoustic signal, which accompanies the atomization process. Therefore, the purpose of the conducted analytical and experimental studies is developing a method of determining the quality of fuel atomization in diesel engines in the form of droplet size and distribution in the injected fuel spout with the use of a non-invasive diagnostic method based on the analysis of the acoustic emission signal, emitted during fuel atomization.

2. Atomization quality and acoustic emission during fuel injection

2.1. Quality of the injected fuel atomization

For the fuel injection processes in compression ignition engines, it is important to know the mechanisms of the formation of an atomized spout. The issues and the history of the theory concerning the mechanism of the droplet formation are described, among others, in the works [2, 17, 20]. They concerned the disintegration of a cylindrical spout of non-viscous liquid in a vacuum, and the small disturbance method (Rayleigh mechanism) was used to analyse the instability and disintegration of the spout. In the next analyses, the viscosity of the liquid and its influence on the growth of disturbances, the influence of environmental forces on the spout, including those deflecting the axis of the spout and various parameters ranges of the phenomenon, and others were taken into account [17]. The complexity of the processes imposed the necessity to assume simplifications and limit ourselves to selected physical quantities influencing the atomizing phenomenon. The result of analytical tests based on differential equations and dimensional analysis are criterion equations and similarity numbers characterizing the course and effects of atomization. For compression ignition engines, due to the heat exchange processes, evaporation and droplet combustion, in the case of assessing the fuel spout in the combustion chamber, the criterion is the Sauter mean diameter (d_{32} or SMD – Sauter Mean Diameter), which expresses the equality of the volume ratio to the droplet surface (the amount of N_i drops of diameter D_i) in the spout real and theoretical: $D_{32} = \Sigma N_i \cdot D_i^3/\Sigma N_i D_i^2$. Data on a representative droplet diameter, crucial for the analysis of the processes of heating, evaporation and combustion of fuel droplets in the diesel engine chamber, may come from various sources – literature, based on previously published results of experiments in atomizing and burning a spout of fuel [20], calculations according to formulas formulated thanks to the theory of similarity, semi-empirical or empirical formulas, confirmed in experience with available methods of determining the microstructure of the spout, e.g. [2, 13, 14, 28, 32]. These dependencies include:

- Hiroyasu and Kadota equation:

$$D_{32} = 2362 d_0^{0.262} \rho_A^{0.121} \rho_F^{-0.0665} \Delta p_F^{-0.0695} \tag{1}$$

- Tanasawa and Toyoda equation:

$$D_{32} = 3.98 \cdot 10^7 d_0 w_F^{-1} \sigma^{0.25} \rho_A^{-0.25} g^{0.5} \cdot$$
$$\cdot [1 + 3.34 \cdot 10^{-2} \eta g^{0.5} (\sigma \rho_F d_0)^{-0.5}] \tag{2}$$

and other [17]. Despite the differences in the dependencies obtained by the Authors, caused by individual methods and the measuring equipment used, it can be concluded that the droplet diameter in jet atomizers is influenced by the following physical quantities: nozzle hole diameter d_0, relative initial velocity of fuel in the gas (outflow from the atomizer) w_F, surface tension σ, dynamic fuel viscosity η_F, dynamic air viscosity η_A, fuel density ρ_F, air density ρ_A:

$$D_{32} = f(d_0, w_F, \eta_F, \eta_A, \rho_F, \rho_A, \Delta p, \sigma) \tag{3}$$

2.2. Acoustic emission

Acoustic emission as a method of diagnosing the phenomena occurring in internal combustion piston engines has not found wide application. However, among the few works on determining the technical condition of these engines, one can mention attempts to diagnose the condition of fuel injectors, which is important for such systems as storage (Common Rail type) or timing systems [4, 27, 28]. The main reason for this is the rather difficult processing of acoustic emission signals along with their further interpretation, which should indicate the location of the damage or provide information about the technical condition of this element, which imitates an acoustic signal. It is important for such elements or phenomena which cannot be investigated with other diagnostic methods, such as storage injection systems.

The processes taking place in the injector during fuel atomization, among others, are related to disturbances caused by the components of flow velocities [17, 23], which can be presented in the form of the Schnerr-Sauer model, in which the transfer equation has the form [16, 17]:

$$\frac{\partial \alpha}{\partial t}(\alpha \rho_A) + \nabla(\alpha \rho_A w_A) = \frac{\rho_A \rho_F}{\rho} \frac{d\alpha}{dt} \tag{4}$$

where: α – volume steam concentration, ρ_A i ρ_F – gas and liquid phase density, ρ – density of the mixture ($\rho = \alpha\rho_A + (1 - \alpha)\rho_F$), w_A – gas phase velocity.

Relationship between mixture density and gas phase density is presented by the equation:

$$\frac{d\rho}{dt} = -(\rho_F - \rho_A) \frac{d\alpha}{dt} \tag{5}$$

In turn, the difference in phases density; gas and liquid during turbulent flow, which occurs in the process of fuel atomization in compression ignition engines, is presented in a differential-integral form, linking turbulent motion with the acoustic field resulting from such a flow [3, 7]:

$$\rho_F - \rho_A = \frac{1}{w_0^2} A - \frac{1}{w_0^2} \frac{\partial}{\partial x_i} B + \frac{1}{w_0^2} \frac{\partial^2}{\partial x_i \partial x_j} C \tag{6}$$

where: w_0 – velocity of density fluctuation, x_i and x_j acoustic wave coordinates, A, B and C – respectively, integrals describing the acoustic field, the local speed of pressure impulse (pulsation) change and volume deformation.

For example the acoustic field (A) generated by the velocity disturbance source is presented by the integral [3]:

$$A = \int_S \frac{\partial}{\partial t}[\rho_i w_i \bar{n}] \frac{dS(i,j)}{4\pi r} \tag{7}$$

local velocity of momentum change (B) from the pulse character of pressure change:

$$B = \int_S [(\rho_i w_i + p_{ij})\bar{n}_i] \frac{dS(y)}{4\pi r} \tag{8}$$

volume deformation (*C*) under the influence of applied forces:

$$C = \int_V \frac{\bar{T}_{ij}}{4\pi r} dV(y) \tag{9}$$

where: S – surface of the disturbance source, $\bar{n}$ – surface normal S, r – volume distance from the surface S to the disturbance source, p_{ij}, T_{ij} – tensors of tensions and density of disturbance impulse stream.

It should be emphasized that the A, B and C integral equations mainly include the phase density parameters; gas and liquid (ρ_A and ρ_F) and their velocities w, surface tension σ and pressure difference Δp of the mixture and the medium into which this mixture is injected.

Developing the problem presented this way in paper [3] it was shown that frequency and the intensity of sound disturbances as well as the change in energy flux density are determined by velocities w and the change in density ρ, while the rate of change in acoustic resistance in the form of acoustic energy Z over time τ can be written in the form:

$$\left(\frac{\partial Z}{\partial \tau}\right)_{i,j,k} = \int_{w_1}^{w_n}\int_{\rho_1}^{\rho_n} (\partial w\, \partial \rho)_{i,j,k} \tag{10}$$

where: i, j, k – acoustic wave move coordinates.

Analysing the problem of acoustic phenomena presented in this way, it can be concluded that the energy of the acoustic signal:

$$Z = f(w_F, \rho_F, \rho_A, \Delta p, \sigma) \tag{11}$$

depends on the same physical parameters involved in determining the quality of the sprayed fuel (SMD) – velocity w, density ρ, pressure Δp and surface tension σ, present in equation (3), so it provides the basis for linking the fuel injection processes and the accompanying acoustic phenomena to evaluation of the quality of fuel atomization in compression ignition engines.

2.3. Analytical study

The above-mentioned mathematical relationships concerning fuel atomization and acoustic emission were used in analytical tests. At the same time, the essential construction parameters of the atomiser as well as the physical parameters of the selected fuels were selected for further experimental research. Figure 1 shows the cross-section of the tip of the D1LMK 148/1 type atomizer used in compression ignition engines of type 359, while Table 1 shows the geometric parameters of the atomizing slots.

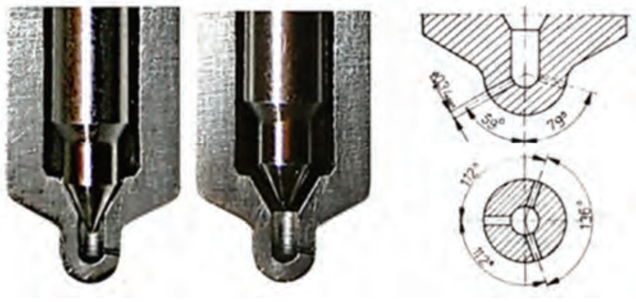

Fig. 1. Geometric parameters of D1LMK 148/1 atomizer used at the test stand

Table 1. Geometric parameters of slots of the atomizer D1LMK 148/1

No.	Parameter	Dimension
1.	Atomizer slot diameter do	0.34 mm
2.	Channel length Lo	1.2 mm
3.	Proportion Lo/do	3.5

The selection of this type of atomizer was not random and took into account the possibility of conducting further experimental tests on a laboratory stand. The same concerned the selected fuel – in the analytical tests there were used the physicochemical parameters of petroleum diesel fuel (DF) and its mixture with methyl esters of rapeseed oil (RME). Physical parameters of these fuels have been presented in Table 2.

Table 2. Physical parameters of the fuels selected for the analytical and experimental studies

Fuel	Kinematic viscosity	Density	Dynamic viscosity	Surface tension
	ν_F	ρ_F	η_F	σ
	10^6 m^2/s	10^{-3} kg/m^3	10^3 Pas	10^3 Nm
DF	4.49	0.8240	3.70	27.36
5%RME	4.57	0.8251	3.78	27.47
7%RME	4.63	0.8263	3.82	27.53
10%RME	4.65	0.8286	3.85	27.57
100%RME	5.39	0.8700	4.69	30.13

In the Figure 2 and 3 there are presented the results of analytical studies concerning determination of Sauter mean diameter of atomized fuels drops (SMD) on the basis of Hiroyasu and Kadota equations (equation 1) and acoustic resistance (Z) accompanying this atomization as a function of the pressure of selected fuels injection (equations 4–10).

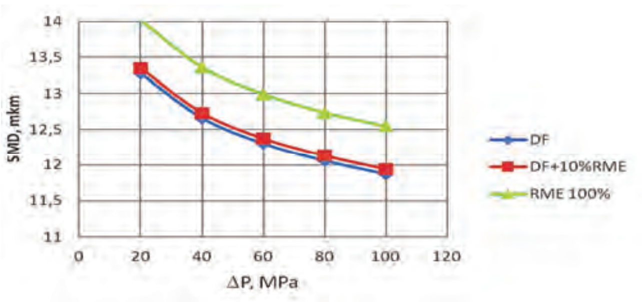

Fig. 2. Change of the average diameter of atomized fuel drop depending on the injected fuel pressure

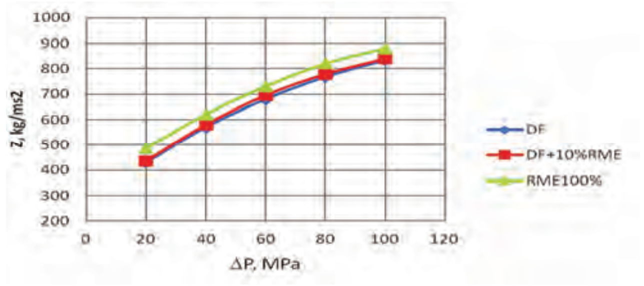

Fig. 3. Acoustic resistance change (*Z*) as a function of the pressure of selected fuels injection

The obtained results fully correspond to the physical phenomena of the fuel atomization process. Increasing the pressure of fuel injection causes the reduction of the droplet average diameter, and thereby the increase of acoustic emission of the atomization process. The same effect occurs also for the mixture of petroleum fuels with methyl esters of rapeseed oil (RME) – increase of density, viscosity and surface tension in the fuel mixture causes the SMD increase and the emitted acoustic signal increase.

3. Experimental studies

In addition to the previously discussed methods for determining the droplet diameter, coming from the source literature, based on previously published experimental results, calculations according to formulas based on the theory of similarity, semi-empirical or empirical formulas [26], the most reliable method for determining the representative value of the droplet diameter seems to be a direct analysis of the microstructure of the real atomized fuel spout using modern techniques of recording and processing signals [1, 19].

The Spraytec apparatus by Malvern (MAL 1057129), equipped with an optical system designed to measure the size of droplets in the range from 0.1 to 900 μm, was used to determine the structure of the fuel spout atomized in the atmospheric air. The instrument uses the laser diffraction technique, which measures the diffused light intensity distribution as it passes through the aerosol of a parallel laser beam. The beam with a wavelength of 632.8 nm emitted by the He-Ne laser is subject to collimation before entering the measuring zone of the instrument. The light diffused by the aerosol passes through an optical system that directs the radiation to a set of photodetectors. The results of the measurement of the diffused light intensity are subject to computer analysis in order to calculate the particle size distribution of the aerosol droplets which caused the specified distribution of the diffused light intensity.

The device uses software that allows to compare the effects of a laser beam diffusion while passing through a real set of droplets to the theoretical model of light diffusion proposed by L. Lorentz and G. Mie [18, 33]. The model results from solving Maxwell's equations for a beam of electromagnetic waves passing through a set of spherical particles using an infinite, convergent number series. The sampling frequency of the diffused light intensity distribution by the measuring module of the instrument can be up to 10 kHz. Thanks to the enclosed user software, it is possible to calculate and record the values of standard parameters (e.g., mean diameter D_{32}, volumetric concentration Cv), as well as other derivatives (e.g., arithmetic or geometric standard inflections of droplet distribution).

Laser light diffusion measurement signal, recorded by each device detector, consists of three components: an electronic background signal, an optical background signal and the actual laser light diffusion signal. The first two are distortions of the real image of the diffused light intensity. The software of the device automatically corrects the measurement signal by subtracting both noise components registered by individual detectors, just before starting the actual measurement. Both the corrected and uncorrected signals are recorded in the device memory, both for background control during the measurement and for further analyses.

During measurements, the correction option included in the application software was used for the results distorted by multiple light dispersions, caused by the high concentration of tested fuel aerosol. The algorithm for the multiple dispersion correction was a part of the measurement procedure, prepared and tested before the start of the measurement series [16]. It defined essential process parameters and device settings. They included, among others: injection character and optical properties of the liquid, the method of measurements triggering, alarm levels of the optical condition, the predicted shape and spatial position of the spout, the limit size of the droplets and the type of derivative parameters indicated in the analysis of the results. When designing the measurement procedure, the optimal distance of the spout from the optical system was established. It resulted from the assessment of the relative level of signals from different detectors. Too large a distance of the spout causes the loss of the measurement signal formed by the droplets with the smallest diameters (vignetting). Too short a distance causes accelerated contamination of the optics by the tested aerosol, despite the use of a pneumatic pollution reduction system. In addition, the measuring cross-section should be outside the zone of the compact fuel stream at the nozzle opening. At the same time, the considered measuring cross-section should be in the stabilized zone of the SMD. Since the measurement with the Spraytec device requires the prior determination of the spout flare angle α, the criterion for the distance of the measuring cross-section from the nozzle opening can be determined with the formula:

$$\frac{B}{D} = \frac{1}{2}\frac{\alpha}{2} \tag{12}$$

where: B – measuring cross-section distance to the atomizer slot, D – spout diameter in the measuring cross-section, α – spout flare angle, and the obtained parameters are entered into the Spraytec device dialog box (Fig. 4).

As mentioned earlier, the sources of acoustic emission are the moving parts of the engine, such as the piston-crank system, valves and others, as well as resonance effects that create background noise occurring in the low frequency range (< 1000 Hz) [25]. In the injection apparatus, the signal EA is created as a result of the propagation of the fuel pressure wave along the high-pressure lines as a result of slight changes in fuel pressure at the time of fuel injection and the emission resulting from the fuel phase change. The source of AE is also reflected waves due to the closing of the injectors, the closing and opening of the injection pump valves, not to mention the signals generated during the closing of the intake and exhaust valves. The determination of the fuel atomization EA signal is possible thanks to the use of the so-called event gate, which enables the analysis of the tested signal in the selected frequency band as opposed to the total acoustic emission band. It is not possible to record only the spectrum of the impulse emission emitted by the injectors, therefore it is necessary to use, in addition to the filter eliminating low frequencies, the highest possible sampling rates (separation of individual synchronous sources of acoustic emission in time) in the EA signal amplifier and the use of an event filter.

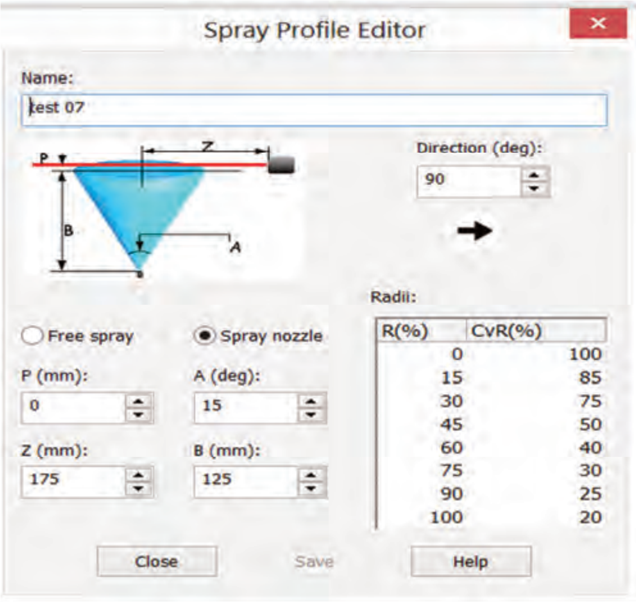

Fig. 4. Spout geometric parameters entry dialog box

The experimental tests were carried out on a special stand (Fig. 5), which included the above-mentioned Spraytec device (3), and the EPS 200 testing table by Bosch (4) for pumping fuel into the injector (1). One of the atomized fuel spouts is directed into the field of the laser beam, while after passing through this field, this spout, as well as the others, are directed to special traps (6) located in the fume cupboard (7). In turn, the acoustic signal is registered by the sensor (10) and is then amplified and processed in the tester (11). The stand is equipped with a set of thermocouples (8, 9), thus ensuring the uniformity of measurement conditions.

The module for acoustic signals registering made the measuring unit, consisting of acoustic emission sensor made by FUJICERA, type 1045S (Fig. 5, pos. 10) and tester-recorder of signal with the 24-bit analogue-to-digital converter and PC (Fig. 5, pos. 11 and 5). It needs to be emphasized that the sensor installation is not a technical problem and it can be located on the body parts of the injector at the laboratory stand as well as on a working diesel engine [4].

Atomization quality measurement method, basing on the SMD value criterion provides for entering to the Spraytec device menu certain structural parameters such as the atomizer distance to the laser beam, or the flare angle of the atomized fuel spout. Figure 6 shows an example of a screen shot of the measurement results for droplets distribution in the atomized fuel spout.

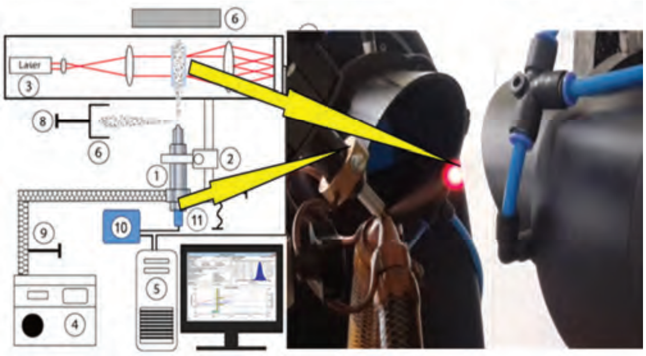

Fig. 5. Scheme of the experimental device for determining the quality of the atomized fuel and acoustic emission: 1 – nozzle, 2 – nozzle attachment point, 3 – Spraytec STP 5000 device, 4 – EPS 200 installation, 5 – personal computer, 6 – spray catchers, 7 – fume hood, 8, 9 – thermocouples, 10 – acoustic emission sensor, 11 – acoustic tester

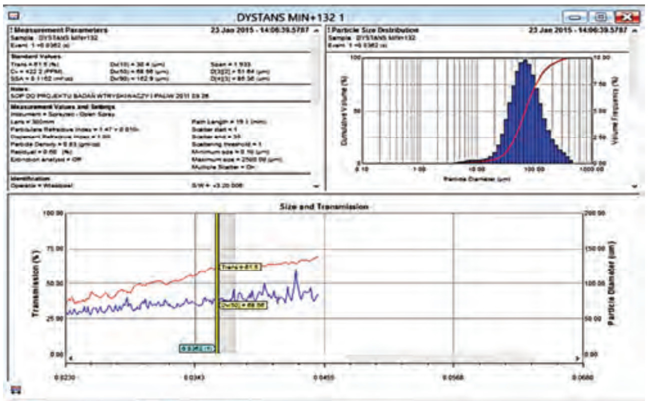

Fig. 6. Dialog box screen shot for differential and integral distribution of fuel atomization

In turn, the method of recording, processing and mathematical analysis of the acoustic signal [30] took into account the measurement of the source signal (Fig. 7a), determining the frequency band with the maximum signal (Fig. 7b) with the use of fast Fourier transform, and determining the maximum signal energy at a specific moment in time during the fuel injection process in the determined frequency band (Fig. 7c).

Such a presented algorithm of the procedure with the use of acoustic signal during the analysis process of fuel injection, is used, among others, for diagnosing the diesel engines injection device. For this purpose it is essential to determine the characteristic shape: signal energy – frequency band (Fig. 7c), which indicates the proper functioning of individual components of this device, such as high-pressure pump and the injector with its components. However, for the association of such phenomena as fuel atomization (and above all the quality of atomization) with the emitted acoustic signal of this process, the recording of the maximum value of signal energy in the determined frequency band is sufficient.

The method of EA measurement presented in this way was used in experimental tests with the use of a three-hole injector of the D1LMK 148 type (similarly to the analytical tests, Fig. 1), with only one spout being directed into the laser measurement field and the remaining ones directed to the spray catchers, which allows to eliminate disturbances caused by the superimposition of atomized fuel spouts. The value of the fuel injection start pressure changed in the range of 20.0–30.0 MPa. In these tests, as the reference fuel, there has been selected petroleum fuel (PN-EN 590 + A1: 2011 – analogous to analytical tests) used in compression ignition engines and its mixture with methyl ester of rapeseed oil (PN-EN 14214), the physical parameters of which are presented in Table 2.

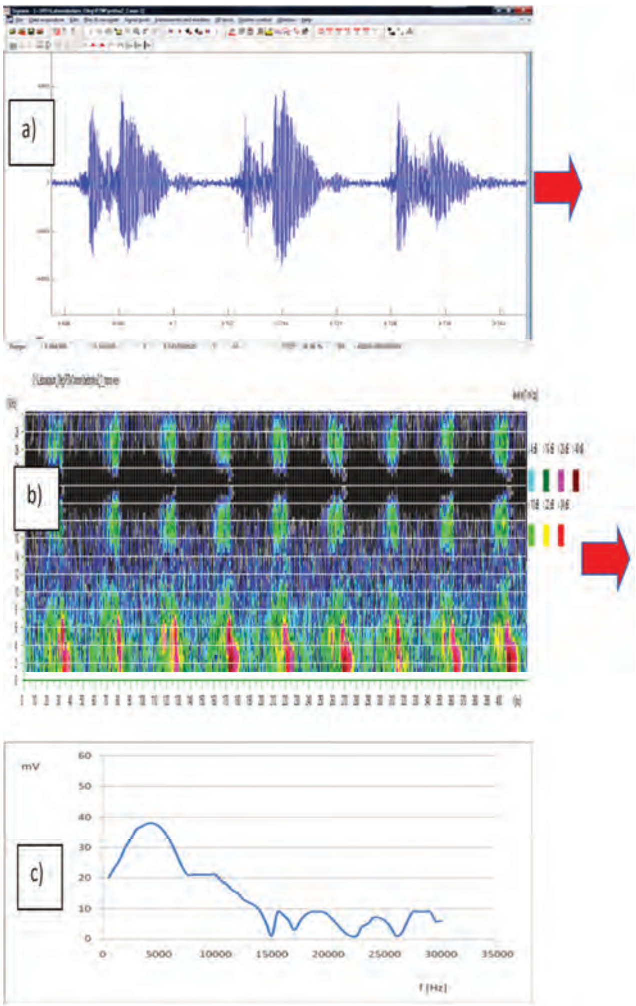

Fig. 7. Recorded source signal (a), transformation of source signal into time-frequency spectrogram and determination of the frequency band with the maximum signal (b), determination of acoustic emission signal energy in recorded frequency band at a specific moment in time (c)

Figure 8 and 9 show selected results of experimental tests concerning the registration of AE parameters and the distribution of droplets in the spout of the injected reference fuel at the change of the fuel injection start pressure.

The program for processing the recorded data of the Malvern device allows you to read the Sauter's average diameter for individual injections, which enables an unambiguous assessment of the atomization quality for selected measurement conditions – the selected fuel and the injection start pressure. In turn, the maximum signal energy in the 15 kHz frequency band was selected as a representative value of the EA signal.

Figure 10 shows the results of experimental tests on the determination of the atomization quality parameters of the reference fuel (SMD) and the acoustic emission signal level (EA) for the petroleum fuel (DF) and its mixture with the addition of 7% rapeseed oil methyl esters (RME) for the fuel injection start pressure 22.0 (Fig. 10a); 24.0 (Fig. 10b) and 26.0MPa (Fig. 10c).

The results of experimental tests presented in this way show a close relationship between the quality of fuel atomization, presented in the form of the average diameter of the atomized fuel drops (SMD), and the acoustic emission signal (EA) generated in the atomization process. The mathematical relationship of these results is described with high accuracy by polynomial equations (the coefficient of determination R^2 with a value above 0.98), while the direct relationship between the mean Sauter diameter and the energy value of the acoustic emission signal is fully described by the second-degree polynomial equation.

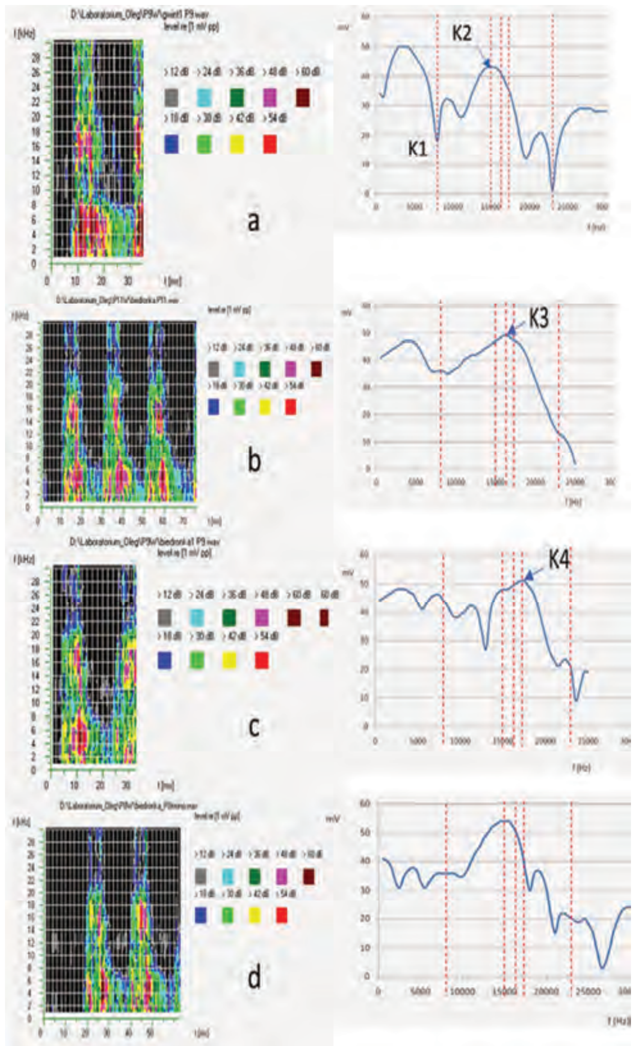

Fig. 8. Time-frequency spectrograms and energy of the EA signal in the recorded frequency band at a specific moment in time for the reference fuel: a, b, c and d – fuel injection start pressure, respectively 20.0; 22.0; 24.0 and 26.0 MPa; K1, K2, K3, K4 – reference points

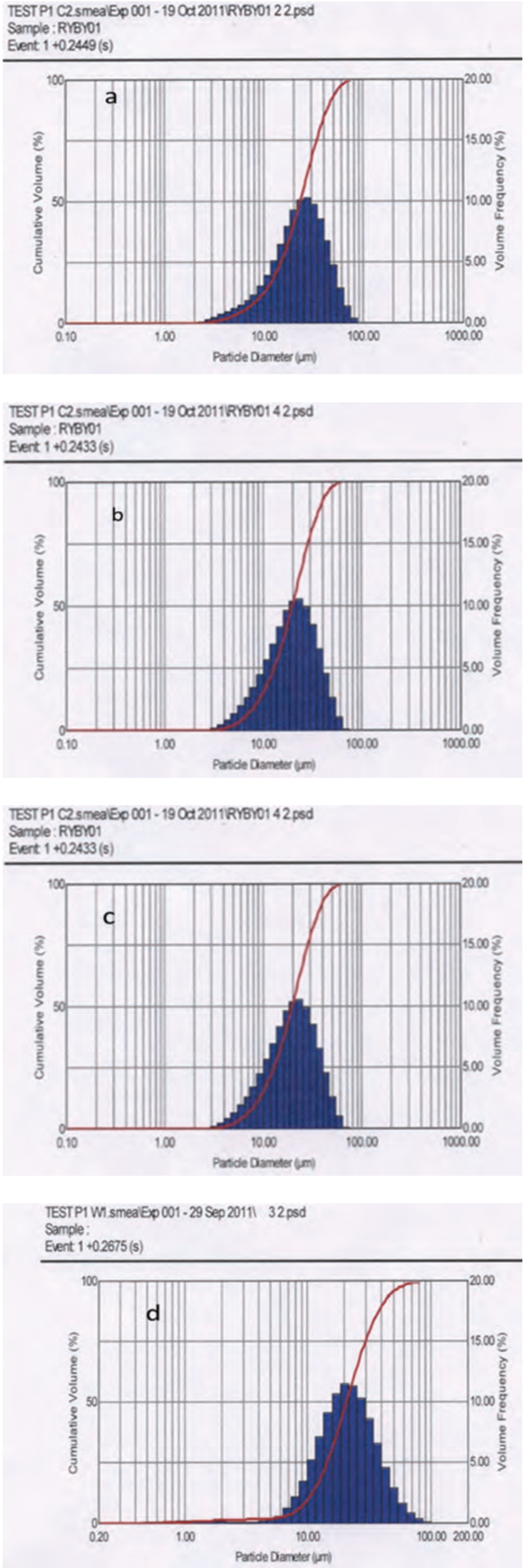

Fig. 9. Distribution of drops of the injected reference fuel: a, b, c and d – fuel injection start pressure, respectively 20.0; 22.0; 24.0 and 26.0 MPa

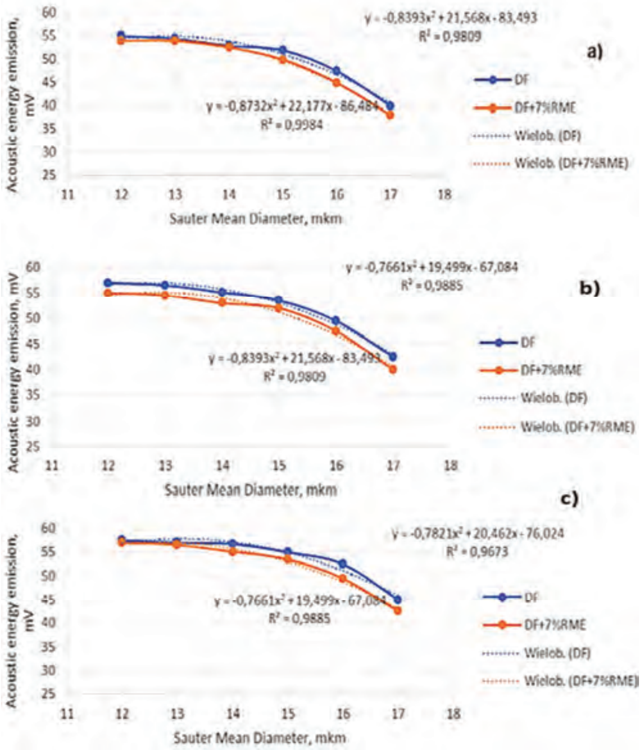

Fig. 10. Relationship between Sauter mean diameter of atomized fuel drop and level of the acoustic emission formed in the atomization process for the start fuel injection pressure: a – 22.0 MPa; b – 24.0 MPa; c – 26.0 MPa

According to the obtained results, the difference in the obtained relationships for petroleum diesel and its mixture with rapeseed oil methyl esters is 3%, which can be explained by the difference in the kinematic viscosity of these fuels (values of these parameters in Table 1 constitute 3%).

In turn, the method of determining the quality of fuel atomization used for diesel engines takes into account the measurement of the source signal emission level and determination of the signal energy in the registered frequency band. The obtained value of this energy is converted into the value of the mean Sauter diameter according to the second-degree polynomial equation. It is worth noting that this method enables the non-invasive assessment of the quality of fuel atomization directly on the running engine, thus enabling the diagnostics of the entire injection system of diesel engines.

4. Conclusions

The fuel atomization process is one of the main elements in the organization of the work process in compression-ignition engines. It has a decisive impact on obtaining the best economic and ecological parameters of their work. The qualitative determination of the fuel atomization process is directly related to the Sauter mean diameter parameter, the value of which is determined experimentally using complex test stands. The atomization itself takes place as a result of the hydrodynamic processes occurring in the fuel system elements, and one of the effects of this process is the formation of spring waves accompanied by the emission of an acoustic signal.

Based on the analysis of the state of knowledge and analytical tests, it was proved that in modelling the atomization and acoustic emission processes, the values of the same physical parameters of the fuel as density, viscosity and surface tension as well as the structure parameters of the atomizers, seem to be important, so it seems reasonable to combine these processes into a common model. For this purpose, experimental studies were carried out to determine the relationship of the quality parameters of the atomized fuel in the form of the Sauter's mean diameter, generated as a result of the acoustic signal atomization process. The measuring equipment used in the experimental tests – the measurement of the atomization quality using the laser diffraction method and the acoustic emission measuring set showed a high accuracy of the dependence of the discussed parameters. The second order polynomial equation can be successfully used to estimate the mean Sauter diameter of fuel drops using the value of the acoustic emission energy generated in the fuel atomization process. It should be emphasized that such tests can be carried out non-invasively on a working engine, which is a significant value in the field of research and operation of internal combustion engines.

On the basis of the presented method of determining the quality of fuel atomization using the acoustic emission signal, the direction of further research on the discussed issue is related to the development of universal mathematical relationships on the basis of second-degree polynomials during the statistical processing of the results of experimental tests when changing the physical parameters of fuels (density, viscosity, surface tension), structure of nozzles (diameter and length of spray slots) and fuel injection characteristics, including multiphase spraying occurring in Common Rail type injection equipment.

Acknowledgements

This research outcome has been achieved under the research project no. 00004-6520.13-OR1600001/19/20 "*Redukcja zużycia energii w aspekcie zmniejszenia negatywnego wpływu rybactwa śródlądowego i morskiego na środowisko*" financed from a subsidy of EU.

Bibliography

[1] ACHEBE, C.H., OGUNEDO, B.M.O., CHUKWUNEKE, J.L. et al. Analysis of diesel engine injector nozzle spray characteristics fueled with residual fuel oil. *Heliyon.* 2020, **6**(8), e04637. https://doi.org/10.1016/j.heliyon.2020.e04637

[2] ASHGRIZ, N. (ed.) Handbook of Atomization and Sprays. Theory and Applications. *Springer Science+Business Media.* LLC 2011. https://doi.org/10.1007/978-1-4419-7264-4

[3] BARSUKOV, S.I., KNAUB, L.V., RODKIN, T.A. Mixing and born out the fore-chambers of the diesel engine. *Conspal, Tadeusz Kosciuszko Military Academy*. 2002, 25-32.

[4] BEJGER, A. The application of acoustic emission signal to the investigation of diesel engine fuel injection systems. *Problemy Eksploatacji.* 2007, **3**, 17-23.

[5] BIANCHI, G.M., PELLONI, P. Modeling the diesel fuel spray break-up by using a hybrid model. *SAE Technical Paper*. 1999-01-0226. 1999. https://doi.org/10.4271/1999-01-0226

[6] BIANCHI, G.M., PELLONI, P., CORCIONE, F.E. et al. Modeling atomization and drop break-up of high-pressure diesel sprays. *ASME Journal of Engineering for Gas Turbine and Power*. 2001, **123**(2), 419-427. https://doi.org/10.1115/1.1361110

[7] CURLE, N. The influence of solid boundaries upon aerodynamic sound. *Proceedings of the Royal Society A*. 1955, **231**(1187), 505-514. https://doi.org/10.1098/rspa.1955.0191

[8] EL-GHAMRY, M., STEEL, J.A., REUBEN, R.L. et al. Indirect measurement of cylinder pressure from diesel engines using acoustic emission. *Mechanical Systems and Signal Processing*. 2005, **19**(4), 751-765. https://doi.org/10.1016/j.ymssp.2004.09.004

[9] FRANCES, A.K., GILL, J.D., REUBEN, R.L. et al. Investigation into identification of faults in small HSDI diesel engine using acoustic emission. *European Conference on Acoustic Emission Testing.* Berlin 2004, **30**, 311-320.

[10] HE, Z., XUAN, T., XUE, Y. et al. A numerical study of the effects on injection rate shape on combustion and emission of diesel engines, *Thermal Science.* 2014, **18**(1), 67-78. https://doi.org/10.2298/TSCI130810013H

[11] HE, Z., XUAN, T., JIANG, Z. et al. Study on effect of fuel injection strategy on combustion noise and exhaust emission of diesel engine, *Thermal Science*. 2013, **1**(17), 81-90. https://doi.org/10.2298/TSCI120603159H

[12] HEYWOOD, J.B., Internal Combustion Engines Fundamentals. *McGraw-Hill Inc*. 2018. https://www.accessengineeringlibrary.com/content/book/9781260116106

[13] HIROYASU, H. Diesel engine combustion and its modeling in diagnostics and modeling of combustion in reciprocating engines. COMODIA 85, *Proceedings of Symposium,* Tokyo 1985, 53-75.

[14] HIROYASU, H., KADOTA, T. Fuel droplet size distribution in diesel combustion chamber. *Japan Society of Mechanical Engineers.* 1976, **19**(135), 1064-1072. https://doi.org/10.1299/jsme1958.19.1064

[15] JANKOWSKI, A., SANDEL, A. Influence of fuel quality on mixture preparation and exhaust emissions from diesel engines with common rail system. *Journal of KONES Internal Combustion Engines*. 2003, **10**, 3-4.

[16] KRAUSE, P., KIDACKI, G., KLYUS, O. Variability of the diesel fuel spray microstructure during the injection into stagnant air by a typical diesel engine injector. *Journal of Machine Construction and Maintenance.* 2018, **109**, 101-107.

[17] LEFEBVRE, A.H., McDONELL, V.G. Atomization and sprays. Second edition. *Taylor & Francis, CRC Press.* 2017, 284.

[18] LEVIN, A.D., SADAGOV, Y.M., KOROLI, L.L. Determination of nanoparticle dimension colloidal solutions with elemental analysis in an electrothermal atomic-absorption spectrometer. *Measurement Techniques*. 2012, **54**, 1186-1190. https://doi.org/10.1007/s11018-012-9869-2

[19] LIMIN, G., YANJUAN, W., YUEYING, W. et al. Effect of the injection pressure and orifice diameter on the spray characteristics of biodiesel. *Journal of Traffic and Transportation Engineering (English Edition).* 2020, **7**(3), 331-339. https://doi.org/10.1016/j.jtte.2018.12.004

[20] LIU, H. Science and Engineering of Droplets. Fundamentals and Applications. *William Andrew Inc*. 2000.

[21] LIU, J., WANG, J., ZHAO, H. Optimization of the combustion chamber and fuel injection of a diesel/natural gas dual fuel engines. *Energy Procedia*. 2019, **158**, 1418-1424. https://doi.org/10.1016/j.egypro.2019.01.344

[22] MATSUMOTO, S., YAMADA, K., DATE, K. Concepts and evolution of injector for common rail system. *SAE Technical Paper* 2012-01-1753. 2012. https://doi.org/10.4271/2012-01-1753.

[23] MCCARTHY, P., RASUL, M.G., MOAZZEM, S. Analysis and comparison of performance and emissions of an internal combustion engine fuelled with petroleum diesel and different bio-diesels. *Fuel*. 2011, **90**, 2147-2157. https://doi.org/10.1016/j.fuel.2011.02.010

[24] NAUMOV, V.N., POGULYAEV, Y.D., BAYTIMEROV, R.M. et al. New diesel engine fuel supply system able to control pressure of pre- and post-main injections. *SAE Technical Paper* 2015-01-2805. 2015. https://doi.org/10.4271/2015-01-2805

[25] OLSZOWSKI, S., MARCZAK, M., OLSZOWSKI, T. Tworzenie bazy danych dla akustycznej metody diagnozowania stanu układu wtryskowego silników z systemem Common Rail. *Logistyka.* 2014, **6**, 9.

[26] OLSZOWSKI, S., MARCZAK, M. Acoustic emission as the best way in making diagnosis of the diesel engines. *Trans-Comp.* Zakopane 2007, 1-6.

[27] POGULYAEV, Y.D., BAITIMEROV, R.M., ROZHDESTVENSKIY, Y.V. Detailed dynamic modeling of common rail piezo injector. *Procedia Engineering*. 2015, **129**, 93-98. https://doi.org/10.1016/j.proeng.2015.12.014

[28] RAKOPOULOS, C.D., GIAKOUMIS, E.G. Diesel Engines Transient Operation. *Springer-Verlag*. London 2009. https://doi.org/10.1007/978-1-84882-375-4

[29] ROBERTSON, A.I.F., DOUGLAS, R.M., NIVESRANGSAN, P. et al. Source identification using acoustic emission on large bore cylinder liners. *European Conference on Acoustic Emission Testing.* Berlin 2004, **65**, 637-643.

[30] SAZHIN, S.S., AL QUBEISSI, M., KOLODNYTSKA, R. et al. Modelling of biodiesel fuel droplet heating and evaporation. *Fuel.* 2014, **115**, 559-572. https://doi.org/10.1016/j.fuel.2013.07.031

[31] SHATROV, G., MALCHUK, I., DUNIN, Y. A laboratory investigation into the fuel atomization process in a diesel engine for different configurations of the injector nozzles and flow conditions. *Fluid Dynamics & Materials Processing*. 2020, **16**(4), 747-760. https://doi.org/10.32604/fdmp.2020.08991

[32] TANASAWA, Y., TOYODA, S. On the atomization characteristics of injection for diesel engines. [*Tech. Rep*.]. Japan Tohoku University. 1956, **21**(1), 117-145.

[33] WANG, X., HUANG, Z., ZHANG, W. et al. Effect of ultra-high injection pressure and micro-hole nozzle on flame structure and soot formation of impinging diesel spray. *Applied Energy*. 2011, **88**, 1620-1628. https://doi.org/10.1016/j.apenergy.2010.11.035

[34] ZHANG, L., HE, Z., WANG, Q. et al. Effect of nozzle hole size coupling with exhaust gas re-circulation on the engine emission performance based on KH-ACT spray model. *Thermal Science*. 2015, **19**(6), 2003-2012. https://doi.org/10.2298/TSCI150417182Z

[35] YAN, Z. Numerical analysis about effect of multiple injections on diesel engine with the common rail injection system. *M.Sc. Thesis.* Jilin University, Jilin 2008.

[36] ZHU, W. Simulation of the influence of pilot injection and post injection on the combustion and emission of diesel engine. *M.Sc. Thesis*. BJTU, Beijing 2009.

Prof. Oleh Klyus, DSc., DEng. – Mechanical Faculty, Maritime University of Szczecin, Poland.
e-mail: *o.klyus@am.szczecin.pl*

Prof. Sergeus Lebedevas, DSc., DEng. – Marine Engineering Department, Klaipeda University, Lithuania.
e-mail: *l_sergeus@mail.ru*

Przemysław Rajewski, DSc., DEng. – Mechanical Faculty, Maritime University of Szczecin, Poland.
e-mail: *p.rajewski@am.szczecin.pl*

Sławomir Olszowski, DSc., DEng. – Faculty of Transport, Electrical Engineering and Informatics, Technological-Humanistic University of Radom, Poland.
e-mail: *s.olszowski@uthrad.pl*

Article citation info:
SZYDLOWSKI, T., SICZEK, K., GLOGOWSKI, M. The effect of machined valve springs application on dynamic properties of electro-hydraulically driven valve train. *Combustion Engines*. 2022, **191**(4), 92-104. https://doi.org/10.19206/CE-148172

Tomasz SZYDLOWSKI
Krzysztof SICZEK
Michal GLOGOWSKI

Combustion Engines
Polish Scientific Society of Combustion Engines

The effect of machined valve springs application on dynamic properties of electro-hydraulically driven valve train

ARTICLE INFO

Received: 1 February 2022
Revised: 31 March 2022
Accepted: 8 April 2022
Available online: 29 May 2022

Nowadays, the constant striving to reduce the emission and increase the overall efficiency over a wide range of speeds and loads of the internal combustion engine (CE) is observed. The different methods for improving the charge exchange in the engine, particularly ones based on the variable valve timing are sought. This variability can be achieved, among others by using the electrohydraulic valve drive. The goal of the present study is to compare the dynamic parameters of the engine valvetrain utilizing the unilateral electrohydraulic valve drive and various types of valve springs. The model of such a drive being developed by authors and experimentally verified was used for the analysis. Using the Finite Element Method, the models of springs made through the machining from single sleeves were developed. The effect of various geometrical parameters of the modernized springs on their stiffness and on the resulted valvetrain dynamics was examined.

Key words: *electro-hydraulic drive, valvetrain, machined valve spring, dynamics*

1. Introduction

Nowadays, many engines are equipped with camless valvetrain. One way to achieve camless valve operation is electrohydraulic valve control/actuation. Such valve drive converts fluid pressure into motion in response to a control signal. It could be realized as a one-side action drive or double-acting one. In the double-acting electrohydraulic drive (Fig. 1), the hydraulic oil causes the valve movement in both directions. The input for such a system is also current in the windings of the electromagnet. It generates the force exciting the movement of the distributor slider opening slits through which the operating fluid flows to and from the hydraulic cylinder. Upward movement of the slider (Fig. 2) causes the connection of space above the piston of the cylinder with a supply channel (of high pressure) and the simultaneous connection of space under the cylinder piston with return flow channel (of low pressure). The appearance of the different pressures on the sides of the piston leads to its movement – in this case, to open the valve. The return movement is also electrically excited. Changing the direction of current flow in the windings of the electromagnet leads to the generation of the force exciting movement of the distributor slider in the opposite direction. By moving down, the distributor slider first closes individual channels and then opens the connection between the supply channel and the space under the piston and the return channel and the space above the piston. The resulting pressure difference causes movement of the drive upwards. The movement ends with the closing of the valve. To prevent a situation in which the valve could remain unclosed, a spring holding the valve in the closed position can be used.

In this embodiment, the hydraulic oil causes movement of the valve in both directions. However, the valve is maintained in the upper position by a spring and not by the control system. This solution also eliminates the falling of the valves due to the pressure drop in the hydraulic system. This is important in the case of start-up when there is a possibility of valve collision with the bottom of the piston.

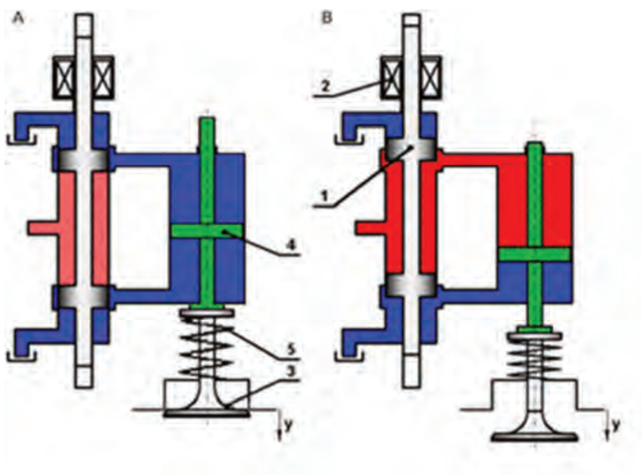

Fig. 1. Functional model of an electrohydraulic double-acting drive with spring outside the drive: 1 – slider of solenoid, 2 – electromagnetic coil; 3 – valve, 4 – cylinder piston, 5 – spring of cylinder piston (also valve spring)

Particularly, the spring position is outside the cylinder. The scheme of the drive valve system with the valve spring outside the cylinder is shown in Fig. 2. When the piston (Fig. 3, number 1) of the hydraulic drive (D) is in the upper position (UP) (Figure 2A) and operating oil pressure is not applied on its surface, the valve head (7) is pressed against its seat insert (8) by the valve spring (10). This pressure provides sealing of the valve.

With the start of oil flow at a predetermined pressure to the cylinder space, the piston (1) moves in the direction of the bottom position (BP) of the drive piston, causing compression of the spring (10) and opening the valve (V). This continues until the piston (1) meets the stop (5), limiting further movement of the piston (Fig. 2b). The piston moves in the section from UP to BP corresponding to piston stroke (S) equal to the stroke (H) of the valve (V). The drive operation is accompanied by the following impacts: one from the lower part of the piston (1) against the stop (5) and another one from the head (7) of the valve (V) against its seat insert (8) at the time of closing of the valve. This requires the introduction of appropriate modifications to the schema of construction and operation of a one-side action hydraulic drive involving the use of braking of the so-called run piston before it reaches the extreme positions of the BP and UP.

Braking of this run piston is the reduction of the piston speed to zero at the end stages of its stroke. Selection of the piston braking performance, specifically the choice of suitable counter-braking characteristics, can only occur after the determination of the basic parameters of the hydraulic valve drive, which include the pressure of oil supplied to the hydraulic drive and courses of the piston movement corresponding to the courses of valve lift.

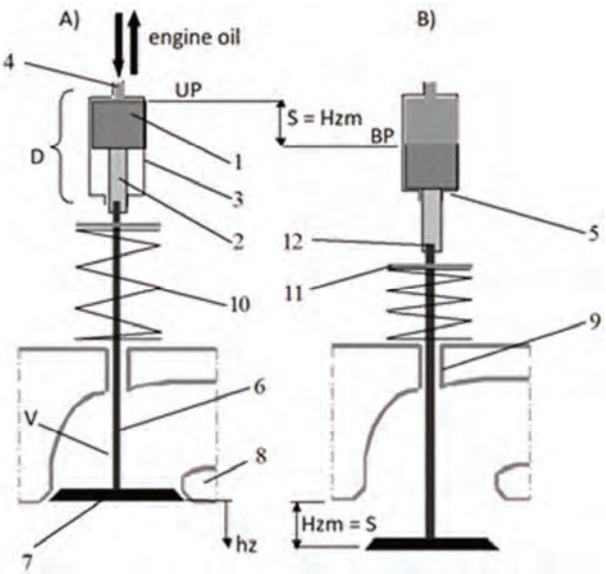

Fig. 2. Scheme of the electrohydraulic system: drive valve using a valve spring: (A) the drive (actuator) in a state corresponding to a closed valve, (B) the drive (actuator) in a state corresponding to an open valve; BP, bottom position of the drive piston; D, hydraulic drive (actuator); hz, valve lift; Hzm, valve stroke; S, stroke of drive piston; UP, the upper position of the drive piston, V – valve of engine: 1 – drive piston, 2 – piston rod, 3 – operating cylinder, 4 – inlet channel of operating (engine) oil, 5 – stop-limiting piston stroke, 6 – valve stem, 7 – valve head, 8 – seat insert, 9 – valve guide, 10 – valve spring, 11 – lock of the valve spring, 12 – connector between the valve and piston rod

There are many different realizations of electro hydraulically driven valvetrains applied both to combustion engines (CEs) and to the research stands used to investigation of variable valvetrains.

The correctness of operation of such systems is strongly affected by the features of engine oil used including degree of oxidation, degree of nitration, degree of sulfonation, water content, glycol content, total base number (TBN), total acid number (TAN) and kinematic viscosity at 40°C and 100°C, which varies during engine operation [21].

2. Realizations of electro hydraulically driven valvetrain

According to [19], many research groups have built at least a one-cylinder test engine for experimental tests, which increases the validity of the results.

The systems and studies of them are described in [1, 4-5, 10, 12-14, 16, 20, 22, 24-26, 34-38, 40-41, 47, 49, 50, 52, 55, 56, 61-64, 69, 76, 77, 79].

Commercially available research electrohydraulic variable valve actuation (VVA) systems are produced by Sturman Industries and Lotus Engineering [19]. Different mechanisms and solutions were developed and investigated in earlier research. Variable valve systems have often been designed to produce conventional or pure sinusoidal valve lift motion instead of optimized valve lift. In recent years, variable valve movement has been taken for granted, and research has concentrated on other areas, such as NO_x production, homogeneous charge compression ignition mixture control, and total controllability of the engine.

All VVA system publications have focused on small- and medium-bore engines (Ø120 mm bore), and gas exchange valve (GEV) strokes were mostly 6–10 mm (maximum, 12 mm), moving masses under 1 kg, and actuating forces a few hundred Newtons. Overall, no fully flexible valve actuation systems were found in the large-bore (Ø180 mm) engines, except in [1] and the two-stroke engine solutions of Wärtsilä and MAN B&W. All other large-bore-related systems were either "lost motion" or "hydraulic pushrod" types of systems in which the hydraulic pressure required by the GEV stroke is controlled by camshaft, which limits the operating range of the VVA system. On the other hand, two-stroke applications also have different requirements/boundary conditions due to moving masses, frequencies, and valve lifts. There is a lack of research on four-stroke large-bore systems.

Dresner and Barkan [16] provides a review and classification of variable valve timing mechanisms, in which 15 different VVA concepts are introduced. Large-bore two-stroke class engines have two commercial hydraulic actuated outlet valve systems: RT-Flex from Wärtsilä [8, 69, 74] and the MAN Diesel&Turbo (ME Intelligent engine) [68].

The sample realization of a double-acting system is the Ford concept given in [3]. It is the electrohydraulic system of variable control of timing, speed, and lift of the valves. The valves are opened and closed by hydraulic cylinders.

Another realization of the electrohydraulic system is the active double-action valve timing of Lotus (AVT) [54]. The system allows for individual control of valves and can perform a variety of valve lift profiles for different valves [39].

The system can open the valves more than once during the engine cycle [2, 54]. This system is used only for research purposes and is not suitable for mass-produced engines because the technology used is very expensive and fast servo valves do not allow control of the speed with sufficient accuracy at an engine speed greater than 4000 rpm [39]. Lotus and Eaton collaborated on the development of the AVT [72]. The AVT system was studied using a one-cylinder test engine [15].

In [27], the Jacobs VVT loss motion system called Evolve is presented. It can achieve degrees of early IVC, late IVC with partial lift, and early EVO. The system allows for a variable compression ratio to be obtained.

Sturman Industries elaborated the HVA system used in variable valve trains and in diesel injector technology [28, 71]. This system allows fine control of seating velocities and the ability to respond to viscosity changes in working fluids. Sturman's hydraulic valve actuation system was implemented in several test engines from passenger cars to heavy duty trucks and some demonstration vehicles. Also, a module was developed for research purposes.

Fiat developed the electrohydraulic MULTIAIR system used in the Fiat Punto Evo [6]. In addition to eliminating the throttle valve, the intake side does not have a mechanical camshaft, but on the exhaust side generated pressure controlled by an electronic valve in each case works on one inlet valve. With the MULTIAIR system, five different operating modes are possible [29].

Reference [30] reported on the full variable valve train used in the BMW K71 tester engine. The valves are driven by a piezoelectric actuator with a hydraulic stroke ratio. Valve control with a piezoelectric actuator and hydraulic fluid allows for full dynamic variable inlet and outlet phasing, lift, opening time, and lift function.

Pournazeri [51] discussed a VVA system for a single engine valve studied on the tester. The system includes two rotary spool valves, two differential phase shifters, and a single-acting spring-return hydraulic cylinder for the engine valve connected to the piston of the cylinder.

Brader and Rocheleau [9] reported an electrohydraulic valve train in which the solenoid actuators were replaced with piezoelectric stacks. The proposed system is capable of a maximum valve lift of 12.4 mm and bandwidth frequency of up to 500 Hz.

Electrohydraulic valve drive systems can allow fully variable valve control. However, disadvantages of such systems are that they are expensive to manufacture due to the need for high precision and they require excessive energy consumption. In addition, there are changes in features of the operating medium, caused by changes in temperature.

One of electrohydraulic valve drive applied to the research stand was realized in the authors' department in the Lodz University of Technology. The numerical model of such a drive was also developed [65], experimentally verified [66] and used for simulation studies on different configurations of the chosen electrohydraulic valvetrain. The goal of the present study was to compare the dynamic parameters of the engine valvetrain utilizing the unilateral electrohydraulic valve drive and various types of both valve springs and valve materials. Ultimately, it is planned to create a subassembly of the test stand using the head of the internal CE with an electro-hydraulic valve drive and various configurations of valve springs.

Lou et al. [38] reported the electrohydraulic VVA system allowing continuously variable timing and two discrete lifts. The lift control was provided via a lift control sleeve hydraulically switching between two mechanically set positions to provide accurate lifts.

Nam et al. [41] presented the design and dynamic simulation of an electro-hydraulic camless engine valve actuator (EH-CEVA) and the experimental verification conducted using lift position sensors.

Giardiello et al. [20] proposed the utilizing of a 0D/1D CFD model of the entire electrohydraulic valvetrain VVA module, coupled with 1D lumped mass representing the inlet valve, for simulating of that valve motion and the interactions between flow and mechanical systems of the solenoid hydro-mechanical valve.

di Gaeta et al. [14] presented the mathematical model of an Electro-Hydraulic Valve Actuator (EHVA) prototype and the use of such a model for the design of cycle-by-cycle Valve Lift Control(VLC).

Zsiga et al. [79] reported the FlexWork valve train allowing the full variability for inlet and outlet valves and the cylinder deactivation.

Sun and Kuo [61] presented the transient control of a laboratory electro-hydraulic fully flexible valve actuation system. Such a control comprised transients of lift, duration, phase, speed, and mode of valves.

3. Valve springs in valvetrains of CEs

Vasilyev et al. [73] stated that the valve spring has the lowest stiffness and exhibits the lowest natural frequency compared to other valve train components.

Labore [32] noticed that there are several spring designs available today including the most popular cylindrical one, conical ones and beehive ones allowing reduction of movable masses and the use of the lighter retainers. The beehive ones can posses ovate wires providing a multi-arc design distributing more material into the high-stress portion of the spring, thus spreading out the stress load. Ovate wires also allow for higher lifts, require less space, thus allowing for their tighter packaging. The conical springs provide a much higher natural frequencies than the other designs.

Pal et al. [43] stated that in most of the cam valvetrains applied in the IC engines, valve helical compression springs are critical components absorbing energy while opening the valves and releasing energy at the closing of them. Spring stiffness plays a significant role in the design of each helical valve spring.

Materials and design of classical valve springs were discussed, inter alia, in [17].

Interestingly, Shiao et al. [58] proposed a variable valve actuation device of compact design and comprising a magnetorheological (MR) valve, passive buffer spring, cam, and rocker arm. They reported that the MR valve could effectively provide functions of variable valve timing and variable valve lift (VVL) via a dynamical control of the external current in the magnetic coil.

As stated in [67] a compression spring can control the motion by maintaining contact between two elements. Particularly, in a cam-follower arrangement, a spring provides contact between such elements parallelly controlling their motion.

Chime and Ukwuaba [11] reported five major metallurgical classifications of wire spring materials including high carbon steel, alloy steel, stainless steel, Ni-based alloys, and Cu-based alloys.

According to [67] various compression springs can be made from the following materials:

- Hard-drawn wire – applied for low stresses and static loads. It cannot be used at sub-zero temperatures and at temperatures above 120 deg C.
- High carbon blue tempered and polished spring steel – applicable for springs operating in a protected environment, as carbon steel can corrode without lubrication or sealing against the atmosphere influence.

- Oil tempered wire (cold drawn, quenched, and tempered) – not suitable for springs exposed to fatigue or sudden loads as well as at sub-zero temperatures and at temperatures above 180 deg C.
- Alloy steels with Cr and V – applied for high stress conditions and at high temperature up to 220 deg C. Springs made of these materials exhibit a good fatigue resistance and long endurance for shock and impact loads.
- Alloy steels with Cr and Al – applied for highly stressed springs requiring for long life and operating under shock loading and at temperatures up to 250°C.
- Piano wire (made from tempered high carbon steel) – applied for small springs with a very high toughness and tensile strength, withstanding repeated loading at high stresses. They cannot be utilized at sub-zero temperature and the one above 120°C.
- Stainless steel (with at least 10% Cr) – for springs with a high corrosion resistance, staining and corroding very slowly in severe environment like a seawater. Springs made of this material are applicable for temperatures up to 288°C. These made from stainless steels of 18–8 composition can be utilized also for sub-zero temperatures.
- Phosphor bronze and brass – used as spring materials provide good corrosion resistance and electrical conductivity. They are normally used for contacts in electrical switches. Springs made of brass are applicable to sub-zero temperatures.

Wound wire springs are made of spring wire coiled hot or cold with ends configured within the limits of coil wire.

Boehm [7] reported that wire wound springs are usually made of medium and high strength steels, Ni alloys, Ti and stainless steels and undergone heat-treating and cold reduction. Machined springs use similar materials, however neither spring wire nor malleable bar can be applied for machined springs. A completed wound spring usually retains various amounts of residual stress despite the application of various stress relieving processes.

A machined spring with similar residual stress in the free state can exhibit unwanted free-state deformation. Low level of residual stress in such springs can be provided using martensitic corrosion resistant steels (CRES) and martensitic steels including moderate to high strength CRES, such as 17-4 PH per AMS5643, 15-5PH per AMS5659, CC455 per AMS5617, and very high strength steels like C300 per AMS6514.

The other appropriate group of materials for the machined springs comprises 7075-T6 Al (high strength), 7068-T6511 Al (very high strength), 38644 Beta C Ti (very high strength and corrosion resistant), Delrin 100 (machinable plastic), and Ultem 2300 (machinable plastic). The Al- and Ti-based cases are important from the point of view of the necessity to reducing movable masses in engine valvetrains.

Wound wire compression springs are often shot peened to increase the fatigue resistance. The gaps between the coils are usually wide enough to allow such a process related to the conditions allowing shot passing through and the surface exposure of coils.

Small coil slots of machined springs sometimes excluded possibility of shot passing through. In this case the fatigue resistance is providing by stress relief holes and slots added to the slot ends or by selection of high strength, fatigue-resistant materials.

Wire springs can be plated with Zn and Ni for corrosion protection. Plating machined springs is made harder by the sharp edge corners insufficient covered. Aluminum machined springs are typically anodized or coated to prevent corrosion.

Suda and Ibaraki [60] described trends in high strength steels for valve springs and development status of the super-high strength steels.

Boehm [7] noticed that although the machined springs function similarly to wire ones, they are manufactured starting usually from metal bar stocks. The latter are first machined into a thick wall tube form, from which a helical slot is cut revealing multiple coils. The final form when deflected, provides the desired elasticity.

The manufacturing of the machined springs is more expensive, involving more time and more specialized machines.

Valve spring usually posses round coils.

The machined compression springs can have square, or rectangular (radial or longitudinal) coils with an easily changeable sizes limited by no standard.

On wire wound compress springs, the space between the coils (slots) is uniform, with the end coils tending to taper to zero. These so called "closing" ends are obtainable in an additional forming process. Their optional grinding allows obtaining their nearly flatness.

Currently, machined springs can reach a minimum slot of about 0.51 mm. Wider slots, however, below 6.35 mm are also obtainable. The slot width can reach nearly zero value via a stress relieving process, but no pre-stressing is currently being met.

Machined springs has a limited number of coils up 30 coils depending on spring size, and commonly it is below 20.

Contrary to a wire spring, with the entire length of the wire contributing to the elasticity, for a machined one the flexure section providing the desired elasticity is captive between the end sections providing structure and attachment. The end sections possess infinite stiffness in comparison to the flexure. Additionally, the end slots do not taper to zero, but remain at the full or initial width visible under the free spring length conditions. Therefore, to reach the close elastic performance, machined springs should be longer than wire ones.

A dimension precision finer than 0.1% is not achievable available for wire wound springs but only for machined ones using post-processing techniques.

Because of the machining practicality the machining spring sizes are limited to the range 2.54–152 mm in diameter. The spring length can reach up to 610 mm, but this applies to the range 25.4–76 mm in diameter. For smaller or larger diameter springs should be shorter.

Compression springs are fully machined to make the ends flat and very perpendicular to the longitudinal axis of the spring.

While wire wound springs are limited to single start configurations, machined springs handle single and multiple starts allowing for a pure force reaction.

Multiple start springs allow for a pure force reaction. Hence, compression springs with multiple starts provide elastic motion without the need of corrective torques compensating these from compression forces occurring at the spring coil's width center shifted from the spring centerline. In multiple start springs these torques resolve to zero within the body of the spring. In single start springs, wound or machined, such torques need be resolved at the interface between the spring and the components providing the force and deflection.

Up to five starts can be used to unify the lateral reaction of machined springs. Multiple starts also add to the length of machined springs. Should a failure occur, the remaining coil(s) provide some functionality albeit degraded due to the missing coil.

Stresses in both machined and wire wound compression springs are dominantly torsional shear. The maximum stresses are located on the spring inner diameter and on the coil sides. Such stresses occur very rare on the spring outer diameter. Stresses at the sharp corners are very low.

The stress relief holes (SRH) or elongated holes at the slot ends are beneficial for compressed machined springs.

Linearity of compression springs depends on:

- geometric changes in the spring during elastic deformation from free length,
- residual stresses in the material,
- enhancing coil contact during deflection,
- boundary condition fixation,
- spring rotation during deflection.

When helical springs are compressed, end-to-end twisting occurs. To eliminate the torsional deformation in machined springs the following remedies can be utilized:

- fixing the end of the spring via any of the attachment techniques,
- constraining the spring end to enhance the elastic rate,
- the use of two concentric springs one with a right-hand flexure and the other a left hand. The twisting of the inner spring counteracts that of the outer one.
- placing of two flexures on a single spring blank, one right hand and the other left hand. Such a configuration allows the interface between the two flexures to twist, while the ends are in rest.

Compression machined springs with multiple starts are predestined to the systems operating at resonance, due to their low tolerance elasticity, continuous slot dimension (no touching at coil ends at any time guarantees clean and quiet operation), internally resolved moments and uniform cross axis stiffness.

The compression springs may be prone to buckling, especially as the number of coils enhances.

Tsubouchi et al. [70] proposed a new and inexpensive forming method of coil springs with a rectangle cross-section with a high rectangular ratio. The coil springs, formed by the proposed method, with a cross-section of a high rectangular ratio possessed the lower spring constant, compared to those with a circular cross-section. Additionally, the work-hardening enlarged the elastic limit, and thus also the safety level of the formed coil springs, compared to the machined ones.

Nama [42] numerically studied the linear static and modal analysis of a helical machined spring. The conventional helical springs of different index with rectangular cross section area were compared with two machined helical springs, one with different slot hole diameter and the other with different end extension length.

For the machined helical spring it was found that the tangent-to-machining path hole configuration is better than the center-to-machining hole configuration and changing the extension length has no significant effect on spring characteristics. The machined spring with any slot hole and any extension length was better than the identical helical spring with rectangular cross section.

The important aspect of the design of valve springs is the method used for the modelling of the valve springs.

During simulations carried out by Prabakar and Mangalaramanan [48], the valve springs were modeled as flexible bodies. Each coil of the springs was modeled as a separate flexible body and contact between these coils was established.

To study the influence of the spring on the dynamic behavior of the whole valvetrain, Frendo [18] proposed a multi-mass spring model in which the mass points are connected by two series of elastic and damping elements, one for the elasto-dynamic characteristics and the other for the possibility of the spring coils to reach contact with each other.

Iritani et al. [31] reported a valve spring model utilizing a beam to couple the displacement and shearing stress with gap elements. In this manner, both the same-pitch valve spring and the different-pitch valve spring can be modeled. Hsu and Pisano [75], Lee and Patterson [33] utilized the wave equation to describe the displacement of the spring elements. Pisano [45, 46], Hanachi and Freudenstein [57], Paranjpe [44], Jang and Park [59], Rego and Martins [53] modelled the valve spring as a distributed parameter system.

Guo et al. [23] modelled the valve spring using the surge-mode approach in which the displacement of each spring element was governed by the wave equation.

Zheng et al. [78] developed a multi-body dynamic model of the valve mechanism based on the key performance and the structure parameters of the valve spring. Via the optimization strategy utilizing such a model, the oscillation amplitude of the valve spring was weakened by about 63%.

4. Methods and materials

The analysis is carried out using models of:

- the electro-hydraulic drive of valve,
- valve assembly,
- valve spring.

The valve assembly contained valve, valve cap and valve stem locks. The geometry parameters were the same for all cases considered. The mass of valve cap and valve stem locks were also unchanged. The mass of valve depended on valve design and material. The classical valve spring geometry was the same for all cases considered. Its mass and characteristics depend on the material.

4.1. Model of electrohydraulic valve drive

Figure 3 shows diagram of the hydraulic drive with valve and valve spring. This drive is the single-acting drive. It consists of hydraulic distributor and hydraulic actuator. Between the engine valve 5 and the piston 3 there is the valve spring 4, which is responsible for closing the valve and maintains it in the closed position, providing a leakproof of the valve seat. Current in the electromagnet coil is the control signal forcing the movement of the valve. The engine oil is the working medium, which causes displacement of the piston to the bottom, and thus moves the engine valve. This oil flows into the space above the piston through oil channel O_2, from supply channel O_1 after turning on the current in the coil of the electromagnet 2 – Fig. 3b. Then slide of the distributor is moved to the right side and opens the gap, through which the oil flows from the supply channel O_1 to channel O_2. When changing the direction of current flow in the windings of the electromagnet, slider 1 moves to the left to its initial position, causing closure of the supply channel O_1 and the opening of the return channel O_3. The oil now flows from the oil space above piston 3, causing suddenly reduction of the pressure. This reduction of the oil pressure above the piston of the cylinder in combination with the force of the valve spring 4 moves the piston up and closes the engine valve 5 (Fig. 3a).

Prior to testing, the following assumptions were made:

- opening of the valve will last as short as possible,
- final phase of valve closing aim to slow down the valve speed, so that eventually it will shut down with as low speed as possible but without a significant extension of the whole closing phase,
- drive control will be limited to step signal.

This means that the controller can only change the duration of the bipolar signal depending on the angular velocity of the engine crankshaft.

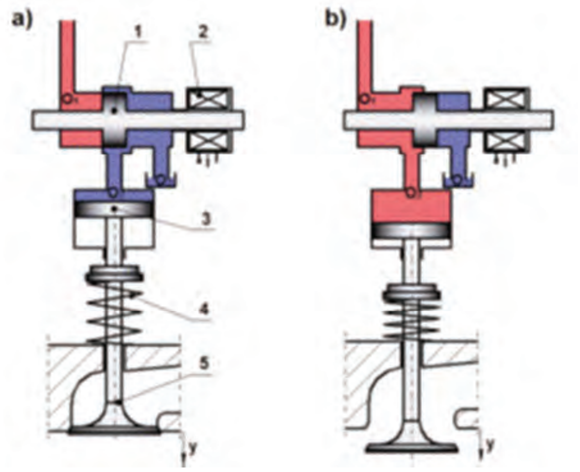

Fig. 3. The diagram of single-acting hydraulic drive: 1 – slider of electrovalve, 2 – electromagnet coil, 3 – piston of the actuator, 4 – actuator piston spring (valve spring), 5 – valve, O1, O2, O3 – oil channels

Considering the control of the electrohydraulic drive one must consider several important issues. First, start of movement of the valve is significantly delayed in opposition to the control signal, which results from the experimental research [9]. This delay time consists of:

time between start of control signal and beginning of the movement of the servo valve spool (1–2 ms) and the rise time of the corresponding actuator pressure, needed to move off the engine valve (1.5–3 ms). For this reason, the control of this valve drive cannot be done in real time, after start of the control signal at the time corresponding to one position of the crankshaft.

Therefore, to obtain the relevant moments of opening and closing of the valve (crankshaft angles), the control system should obtain a signal, for the time no less than equal to the delay time, before reaching the engine crankshaft position corresponding to the opening of the valve. This will be possible only, if the control system will solicit engine operation parameters in the form of feedback. These parameters, necessary for control signals, will include mainly the angular velocity of the engine crankshaft and the temperature of the working medium. If the control system will be the adaptive system, the angles of rotation of the crankshaft, which took place at the opening and closing of the valve and the actual valve lift must be taken into consideration, too.

Sample waveform of the valve lift is shown in Fig. 4. To obtain such a waveform, control signal with the following components is required:

1. the duration of the valve opening signal – t_o,
2. the duration of the valve closing signal – t_z,
3. the duration of the valve braking signal – t_h.

During valve lift the delay time of the drive was labeled as t_{zz}.

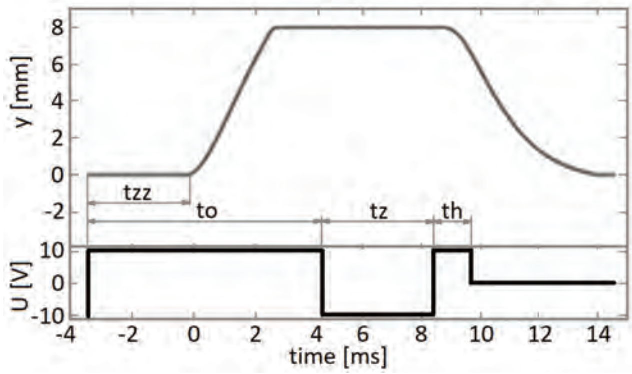

Fig. 4. Characteristic parameters of the control signal necessary to achieve the desired waveform of the valve lift

The duration of valve opening signal will depend mainly on the angular speed of the engine crankshaft. The duration of the closing signal and the braking signal will be fixed for specific ranges of supply pressures and speeds of the crankshaft, which will be achieved with the full opening of the valve, as demonstrated below.

Previous studies (mainly experimental) have shown that minimum valve closing speed for supply pressure 10 MPa was approximately 0.26 m/s. Such speed, from the viewpoint of valve subsidence in the seat, seems acceptable. Valve closing time for such speed, however, would be about 30 ms.

Full opening of the return gap allowed to reach for the valve closing speed is up to 3 m/s. Valve closing time for such speed would be about 3 ms. The aim of the simulation was, inter alia, propose such a method of controlling, to give as small as possible valve closing speed and not significantly increase valve closing time.

4.2. Model of electrohydraulic valve drive using the Rexroth servo valve

The concept and operating phases of the single-acting hydraulic drive with the Rexroth servo valve are shown in

Fig. 5. The basic element of the drive is the single-acting hydraulic cylinder 1, which opens the valve of the internal CE 2. The return spring 3 closes the valve. The operation of the drive is controlled by a distributor 4 (which connects the actuator either to the power supply or to the tank).

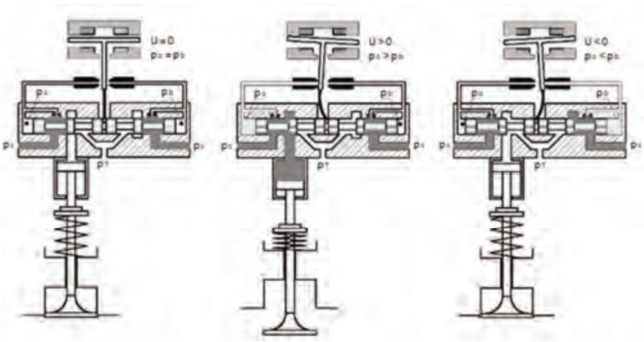

Fig. 5. Operating phases of electrohydraulic valve drive with the Rextrox servo valve

4.2.1. Mathematical model of the drive

Considering the complex structure of the model electro-hydraulic valve drive when developing its mathematical model, the whole system was divided into fragments (sub-models). For further considerations, the following model structure was adopted using the following markings:
SM – torque control motor model,
WH – hydraulic amplifier model,
SS – servo spool model,
RH – hydraulic distributor model,
SH – hydraulic cylinder model.

Initial condition related to the rest of all movable components. The boundary conditions were determined by the existing geometrical limits resulted from the design of the drive. Within such limits the related displacements were allowed between movable and immovable components, assumed to be rigid bodies.

4.2.1.1. Torque control actuator model

The servo control actuator converts the current signal to the proportional angular movement of the armature. The armature, made of magnetic material, is mounted elastically with a thin-walled tube in which the diaphragm is routed. The moment acting on the armature is proportional to the control current.

Considering the system of forces acting on the armature of the torque actuator according to Fig. 6, considering its small angular displacements, the equation of armature rotational motion relative to its axis of rotation assumes:

$$J_z \frac{d^2\varphi}{dt^2} = M_z - k_z \cdot \varphi - c_z \frac{d\phi}{dt} - F_h \cdot l_h - F_s \cdot l_s \qquad (1)$$

where: J_z – mass moment of inertia of the armature relative to its axis of rotation, φ – armature rotation angle, k_z – tube stiffness, c_z – armor viscosity resistance coefficient, M_z – armature torque, where: F_h – hydrodynamic force acting on the nozzle diaphragm, where: l_h – distance between the armature rotation axis and the nozzle axis,
$F_s = k_s \cdot (x + \varphi \cdot l_s)$ – spring force, where: k_s – spring elasticity coefficient, l_s – distance between the armature rotation axis and the end of the spring.

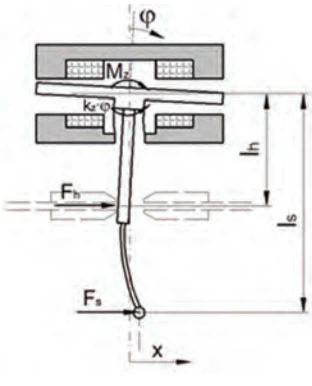

Fig. 6. Diagram of the torque control engine

The drive input control signal will be the voltage signal. Therefore, to assume small angular displacement of the armature, the relationship between the input voltage signal applied to the torque motor coils and the current can be described by the following equation:

$$L \cdot \frac{di}{dt} = U - R \cdot i \qquad (2)$$

where: L – inductance of coils, R – coil resistance, U – voltage.

4.2.1.2. Model of a hydraulic amplifier

Torque motor armature is rigidly connected to the nozzle diaphragm, which in functional terms belongs to a hydraulic amplifier. This is a nozzle-aperture amplifier. The angular movement of the armature causes the nozzle aperture to deflect and change its distance from the nozzles. This leads to a decrease in pressure before the exposure nozzle and an increase in pressure before the exposure nozzle – Fig. 7. The resulting pressure difference is used to change the position of the servo valve control spool.

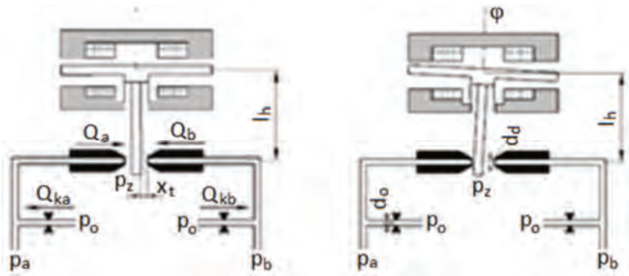

Fig. 7. Diagram of the electrohydraulic amplifier

The pressure connected to the supply system is p_0. These channels are separated by flanges with diameters d_0 connecting them with working channels a and b, in which pressures p_a and p_b prevail.

Therefore, the flow rate through the individual nozzles of the hydraulic amplifier is:

$$Q_{k_a} = Q_a + Q_{h_w} + Q_{cw} \qquad (3)$$

$$Q_{k_b} = Q_b - Q_{h_w} + Q_{cw} \qquad (4)$$

where: $Q_{ka} = c_q \cdot \frac{\pi \cdot d_0^2}{4} \cdot \sqrt{\frac{2 \cdot (p_0 - p_a)}{\rho}}$ – flow rate through the orifice 'a', where: c_q – flow factor, d_0 – diameter of the orifice, $Q_{kb} = c_q \cdot \frac{\pi \cdot d_0^2}{4} \cdot \sqrt{\frac{2 \cdot (p_0 - p_b)}{\rho}}$ – flow rate through orifice "b", $Q_a = c_q \cdot \pi \cdot d_d \cdot (x_t - \phi \cdot l_h) \cdot \sqrt{\frac{2 \cdot (p_a - p_z)}{\rho}}$ – flow rate through the nozzle 'a', where: d_d – nozzle diameter, x_t – distance between the aperture and the nozzle in the middle position of the armature, $Q_b = c_q \cdot \pi \cdot d_d \cdot (x_t + \phi \cdot l_h) \cdot \sqrt{\frac{2 \cdot (p_b - p_z)}{\rho}}$ – flow rate through the nozzle 'b', $Q_{hw} = A_s \frac{dx}{dt}$ – slider absorbency, where: $A_s = \frac{\pi \cdot d_s}{4}$ – slider face area, where: d_s – diameter of the four-edge slider, x – slider shift, $Q_c = \frac{V_k}{E_c} \cdot \frac{dp_{a/b}}{dt}$ – flow rate covering losses due to compressibility of the liquid, where: E_c – modulus of elasticity of liquids, V_k – chamber volume.

4.2.1.3. Servo valve slider model

The equation of motion of the four-edge slider has the form:

$$m_s \cdot \frac{d_s^2 x}{dt^2} = \Delta p_s \cdot A_s - F_s - F_{hd} - F_t \cdot \text{sgn}\left(\frac{dx}{dt}\right) - c_s \cdot \frac{dx}{dt} \quad (5)$$

where: m_s – mass of the four-edge slider, x – slider shift, Δp – differential pressure of front faces of the piston (nozzle inlets), $F_{hd} = \frac{0,72}{\sqrt{\xi}} \cdot \pi \cdot d_s \cdot x \cdot \Delta p_s = k_{hd} \cdot x \cdot \Delta p_s$ – hydrodynamic force acting on the slider, where: ξ – coefficient of flow resistance through the gap, Δp_s – pressure drop across the slider gap, F_t – static friction force, c_s – coefficient of viscosity of the slider.

4.2.1.4. Hydraulic distributor model

The movement of the four-edge slider opens and closes the gap connecting the cylinder chamber with the supply and drainage channel.

For the analyzed solution, the value of the flow rate through the working gap can be described by the relationship derived from the Bernoulli equation:

$$Q = c_q \cdot \sqrt{\frac{2}{\rho}} \cdot \pi \cdot d_s \cdot x_r \cdot \sqrt{\Delta p} = K_Q \cdot x_r \cdot \sqrt{\Delta p} \quad (6)$$

where: c_q – flow factor depending on Reynolds number, x_r – gap opening depends on the displacement of the four-edge slider, $K_Q = c_q \cdot \sqrt{\frac{2}{\rho}} \cdot \pi \cdot d_s$ – flow factor depending on the geometry of the gap, Reynolds number and density of the working medium, p – pressure drops across the gap.

The equation of flow through the servo valve takes the form:

$$Q_S = Q_T + Q_h + Q_p + Q_c \quad (7)$$

where: $Q_S = K_{QS} \cdot x_{rS} \cdot \sqrt{p_S - p_A}$ – supply flow rate, $Q_T = K_{QT} \cdot x_{rT} \cdot \sqrt{p_A - p_T}$ – drainage flow rate, where: p_S – supply pressure, p_A – pressure in the working chamber, p_T – pressure in the drainage channel, $Q_p = k_v \cdot p_A$ – leakage flow rate, where: k_v – leakage factor, $Q_h = A\frac{dy_p}{dt}$ – the absorber capacity of the actuator, where: A – working surface of the actuator piston, y_p – displacement of the gym piston rod $Q_c = \frac{V_0 + A \cdot y_p}{E_c} \cdot \frac{dp_A}{dt}$ – flow rate covering losses due to compressibility of the liquid, where: E_c – bulk modulus of liquids, V_0 – volume of the chamber.

4.2.1.5. Hydraulic distributor model

The equation of actuator valve movement can be presented in the following form:

$$\begin{cases} m \cdot \frac{d^2y}{dt^2} + C \cdot \frac{dy}{dt} + F_t \cdot \text{sign}\left(\frac{dy}{dt}\right) + k \cdot y \\ = A \cdot p_A + m \cdot g - k \cdot y_0 - F_g \text{ for } y < y_{pmax} \\ \\ m_v \cdot \frac{d^2y}{dt^2} + C_v \cdot \frac{dy}{dt} + F_{tv} \cdot \text{sign}\left(\frac{dy}{dt}\right) + k \cdot y \\ = m \cdot g - k \cdot y_0 - F_g \text{ for } y > y_{pmax} \end{cases} \quad (8)$$

where: m – sum of masses: piston with piston rod, engine valve and elements connected to it, m_v – mass of engine valve and components connected to it, y – motor valve displacement, y_0 – preload of the valve spring, C, C_v – coefficients of viscous friction, respectively for combined actuator and valve and the valve itself, F_t, F_{tv} – static friction forces, k – valve spring coefficient of elasticity, A – cylinder piston surface area, p_A – pressure in the actuator, $F_g = A_z \cdot p_s(t)$ – gas force acting on the valve head, where: A_z– surface area of the valve head, $p_s(t)$ – gas pressure in the engine cylinder.

4.3. Parameters of valve and classical valve spring

During analysis were used two valves: the full one made of steel (chosen as the reference one) and the full one made of Ti-Al alloy. The electro-hydraulically driven valve cooperated with a classical valve spring made of steel. Its parameters were presented in Table 1. Alternatively, valve can mate with the machined spring.

Table 1. Specifications of the analyzed vehicle

Parameter	Designation	Values
Steel valve mass	m_v [g]	41
TiAl valve mass		27
Valve stem lock mass	m_{vsl} [g]	1
Valve cap mass	m_{vc} [g]	6
Spring mass	m_s [g]	22
Valve seat diameter	D_{vs} [mm]	27.7
Valve stroke	H [mm]	8
Spring wire diameter	d [mm]	2.8
Inner diameter of spring	D_i [mm]	14.1
Outer diameter of spring	D_{out} [mm]	19.7
Initial length of spring	L_0 [mm]	46.9
Pre-tension displacement of spring	L_1 [mm]	12
Force relative to pre-tension displacement of spring	F_1 [N]	210
Maximum displacement of spring	L_2 [mm]	20
Force relative to maximal displacement of spring	F_2 [N]	370

4.4. The model of the machined spring

The model of machined spring was elaborated using the FEM. Geometry of such a model was presented in Fig. 8A. The grid of tetragonal elements was shown in Fig. 8B. The boundary conditions were following:

- bottom plane of spring was fixed,
- the top plane of spring was loaded by the force with a set value from the range 0–370 N.

During analysis, it was assumed, that reference machined spring rate was the same as for the classical steel valve spring. Also, its loads were assumed to be the same. The machined spring was obtained from single sleeve by removing material in the form of the coil with constant rectangular cross-section. The pitch of that coil was equal to 5 mm and number of its wings was equal to 8. It was assumed that Yield stress for the spring steel was equal to 1300 MPa.

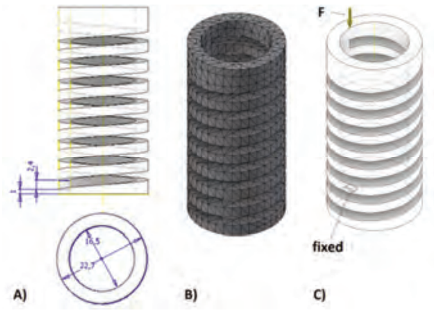

Fig. 8. Model of machined spring. A) geometry, B) grids of the finite elements, C) coundary conditions

5. Results

The obtained mass of the reference machined spring was equal to 39 g which was 72% higher than the mass of classical steel spring.

The obtained values of von-Misses stresses in of the steel machined spring with the removed coil pitch equal to 5 mm are presented in Fig. 9. The maximal value was higher only by 1.8% from the assumed Yield stress.

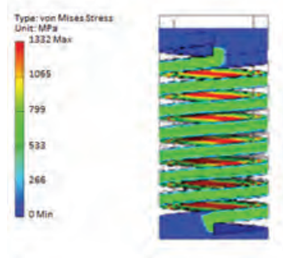

Fig. 9. von Misses stresses in the steel machined spring with the removed coil pitch equal to 5 mm

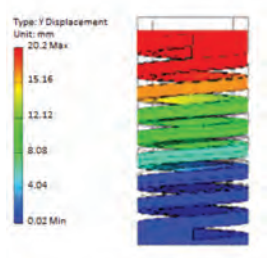

Fig. 10. Axial displacements of machined spring with the removed coil pitch equal to 5 mm

The obtained axial displacements for of the steel machined spring with the removed coil pitch equal to 5 mm were presented in Fig. 10. The maximal value differed by 1% from those of the classical steel spring.

The obtained values of von-Misses stresses in the steel machined spring with the removed coil pitch equal to 5.1 mm were presented in Fig. 11. The maximal value was lower by 3% from the assumed Yield stress.

The obtained axial displacements for of the steel machined spring with the removed coil pitch equal to 5.1 mm were presented in Fig. 12. The maximal value differed by 7% from those of the classical steel spring.

The obtained values of von-Misses stresses in the steel machined spring with the removed coil pitch equal to 4.9 mm were presented in Fig. 13. The maximal value was higher by 9% from the assumed Yield stress.

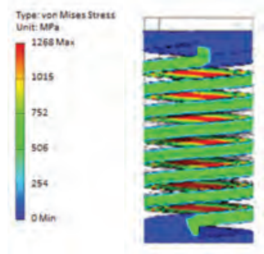

Fig. 11. von-Misses stresses in the steel machined spring von-Misses stresses in the steel machined spring with the removed coil pitch equal to 5.1 mm

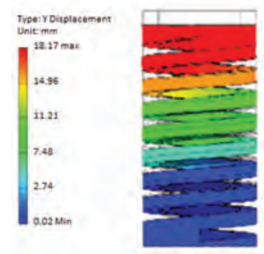

Fig. 12. Axial displacements of machined spring with the removed coil pitch equal to 5.1 mm

The obtained axial displacements for of the steel machined spring with the removed coil pitch equal to 4.9 mm were presented in Fig. 14. The maximal value differed by 10% from those of the classical steel spring.

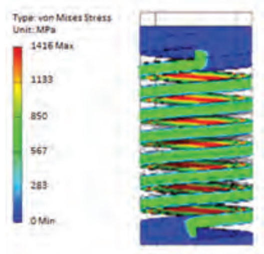

Fig. 13. von-Misses stresses in the steel machined spring von-Misses stresses in the steel machined spring with the removed coil pitch equal to 4.9 mm

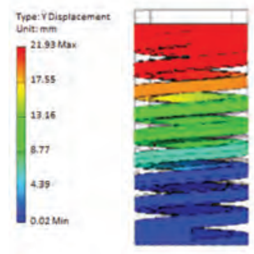

Fig. 14. Axial displacements of machined spring with the removed coil pitch equal to 4.9 mm

The obtained values of von-Misses stresses in the steel machined spring with the removed coil pitch equal to 5 mm and mean diameter increased by 1 mm were presented in Fig. 15. The maximal value was higher by 18% from the assumed Yield stress.

The obtained axial displacements for of the steel machined spring with the removed coil pitch equal to 5 mm and the mean diameter increased by 1 mm were presented in Fig. 16. The maximal value differed by 3% from those of the classical steel spring.

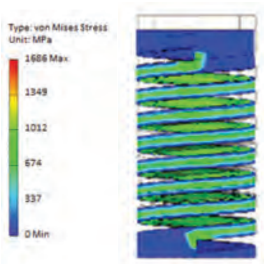

Fig. 15. von-Misses stresses in the steel machined spring von-Misses stresses in the steel machined spring with the removed coil pitch equal to 5 mm and mean diameter increased by 1 mm

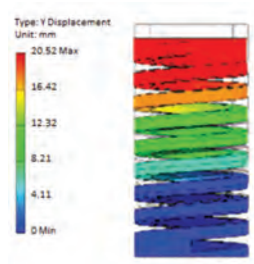

Fig. 16. Axial displacements of machined spring with the removed coil pitch equal to 5 mm and the mean diameter increased by 1 mm

The obtained values of von-Misses stresses in the steel machined spring with the removed coil pitch equal to 5 mm and mean diameter decreased by 1 mm were presented in Fig. 17. The maximal value was higher only by 1% from the assumed Yield stress.

The obtained axial displacements for of the steel machined spring with the removed coil pitch equal to 5 mm and the mean diameter decreased by 1 mm were presented in Fig. 18. The maximal value differed by 0.5% from those of the classical steel spring.

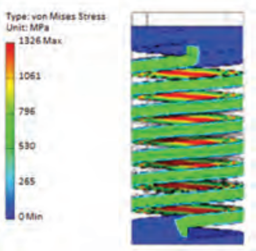

Fig. 17. von-Misses stresses in the steel machined spring von-Misses stresses in the steel machined spring with the removed coil pitch equal to 5 mm and mean d diameter increased by 1 mm

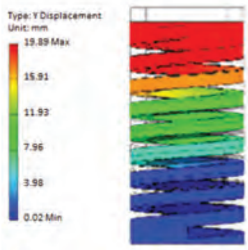

Fig. 18. Axial displacements of machined spring with the removed coil pitch equal to 5 mm and the mean diameter decreased by 1 mm

The obtained courses of valve lift versus time for analyzed vales and spring configurations were shown in Fig. 19. It was visible, that for the TiAl valve obtained maximal valve lifts were slightly higher than in case of the valve made of steel. Also, when using classic valve spring the valve lifts were slightly higher than in case of machined spring. The rising of valve was quicker when mating with the classic spring compared to the case of the machined spring. The falling of TiAl valve was quicker in the case of TiAl valve compared to the steel valve. The use of machined spring resulted in slightly longer falling period of TiAl valve, but in slightly shorter falling period of the steel valve compared to the case of classic valve spring.

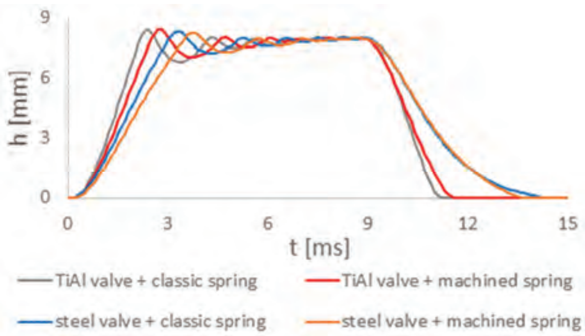

Fig. 19. The courses of engine valve lift versus time for the steel valve mating with the classic valve spring, the steel valve mating with the machined valve spring, the TiAL valve mating with the classic valve spring and the TiAl valve mating with the machined valve spring

For the 4-stroke engine speed equal to 3000 rpm, from the obtained courses of valve lifts versus time the relating values of valve angle-cross-sections were estimated. Calculations of the latter were carried out related to the camshaft rotates. The resulting values were presented in Table 2. Interestingly, the angle-cross-section obtained for the steel valve mating with machined valve spring was lower by 2.6% than that obtained in case of classical spring. The angle cross-sections for valve made of TiAl alloy were lower by 5.6% and 5.5% when mating with classical spring and machined one, respectively, compared to the case of steel valve mating with classical spring.

Table 2. The angle-cross-sections for valve driven electrohydraulically

Valve material	Type of valve spring	Angle-cross-section [deg·mm]
Ti-Al alloy	Classical	554.96
	Machined	554.41
Steel	Classical	587.45
	Machined	571.99

The obtained courses of related valve acceleration versus time for analyzed valves and spring configurations were shown in Fig. 20. It was seen that near the theoretical extreme positions of valve the damped vibration or/and impacts occurred. The amplitude of vibrations near the maximal valve lift was higher for the case of TiAl valve up to 3% compared to the case of the steel one. The highest amplitude of vibration occurred for the valve made of TiAl alloy mating with the classic valve spring. The smallest amplitude occurred for steel valve mating with the machined spring. The impact resulted in high amplitude of acceleration occurred during valve settling was much stronger for the valve made of TiAl alloy compared to the steel one. For the case of valve made of TiAl alloy the impact was stronger by up to 30% when it mated with classic spring compared to the case of the machined one. For the case of steel valve, the mentioned impact was stronger up to 50% in case of mating with the machined spring than in case of the classical spring.

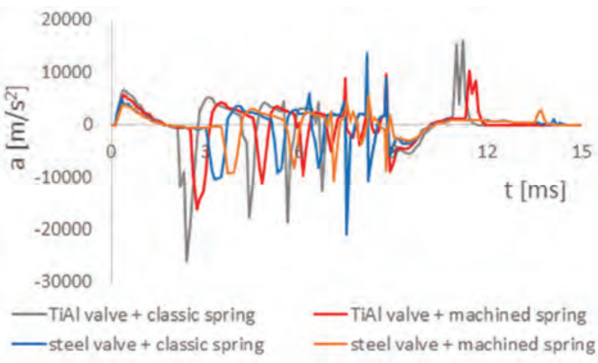

Fig. 20. The courses of engine valve acceleration versus time for the steel valve mating with the classic valve spring, the steel valve mating with the machined valve spring, the TiAl valve mating with the classic valve spring and the TiAl valve mating with the machined valve spring

The mentioned results of valve lifts and acceleration depended primarily on the total mass of valve and mating valve spring and by the relatively simple control scheme of medium pressure in the modelled drive. The geometry and material parameters of components in the modelled drive assembly and environmental parameters were not changed when analyzing individual configurations.

The simple control system used in the model of the currently existing research stand can be used to simulation tests of classic steel valves and machined springs. But it turned out to be not very effective for light valves made of TiAl alloy and classic springs. Therefore, it will be necessary to introduce changes in CE involving the use of stronger vibration dampers, and earlier additional braking of the valve. You will probably need to introduce a more effective negative feedback control valve based on tracking its current position and acceleration and their deviations from the allowable values.

6. Summary

Under the same characteristic of the machined spring as the classic valve spring, the mass of the machined spring is greater. The use of machined spring made longer valve rising period but differently influenced the valve falling period depending on the valve mass. The use of the lightweight valve made shorter both valve rising and falling periods. It also resulted in higher amplitude of vibrations occurring near maximal valve lift and much stronger impact during valve settling compared to the heavier steel valve. To obtain the smoother courses of the valve lifts versus time from the model of the existing research stand it is necessary to add stronger vibration dampers, and earlier braking of the valve before its close position.

Nomenclature

BP	bottom position
CE	combustion engine
CFD	computational fluid dynamics
EH-CEVA	electro-hydraulic camless engine valve actuator
GEV	gas exchange valve
IC	internal combustion
MR	magnetorheological
SI	spark ignition
SRH	stress relief holes
UP	upper position
VVA	variable valve actuation
VVL	variable valve lift

Bibliography

[1] AALTONEN, J., VILENIUS, M. Control and controllability of electrohydraulic valvetrain in high and medium speed diesels. *SAE Technical Paper* 2002-01-2175. 2002. https://doi.org/10.4271/2002-01-2175

[2] ALLEN, J., LAW, D. Advanced combustion using a Lotus active valve train. Internal exhaust gas recirculation promoted auto ignition. *IFP International Congress* 2001.

[3] ALLEN, J., LAW, D. Production electro-hydraulic variable valve-train for a new generation of I.C. engines. *SAE Technical Paper* 2002-01-1109. 2002. https://doi.org/10.4271/2002-01-1109

[4] ANDERSON, M., TSAO, T., LEVIN, M. Adaptive lift control for a camless electrohydraulic valvetrain. *SAE Technical Paper* 981029. 1998. https://doi.org/10.4271/981029

[5] BATTISTONI, M., MARIANI, F., FOSCHINI, L. A parametric optimization study of a hydraulic valve actuation system. *SAE Technical Paper* 2008-01-1356. 2008. https://doi.org/10.4271/2008-01-1356

[6] BERNARD, L., FERRARI, A., MICELLI, D. et al. Elektrohydraulische Ventilsteuerung mit dem "MultiAir" –Verfahren. *Motortechnische Zeitschrift*. 2009, **70**(12), 892-899.

[7] BOEHM, G.L. Wire Springs or Machined Springs? Design World, May 13, 2007. https://www.designworldonline.com/wire-springs-or-machined-springs/ (accessed on February 01, 2022).

[8] BOLETIS, E., KYRTATOS, A., YILDIRIM, T. et al. A new fuel injection and exhaust valve actuation system for a two-stroke engine family in the 30 to 50 cm bore segment. *CIMAC Congress* 2010. Paper No. 101, Bergen 2010.

[9] BRADER, J.S., ROCHELEAU, D.N. Development of a piezo electrically-controlled hydraulic actuator for a camless engine. Part 1. *Proceedings of the Institution of Mechanical Engineers, Part D: Journal of Automobile Engineering*. 2004, **218**(8), 817-822. https://doi.org/10.1243/0954407041581084

[10] CHEN, J. Electro-hydraulic fully flexible valve actuation system for engine test cell. *SAE Technical Paper* 2010-01-1200. 2010. https://doi.org/10.4271/2010-01-1200

[11] CHIME, R.O., UKWUABA, S.I. Design, modeling, simulation and analysis of compression spring. *International Journal of Engineering Science and Innovative Technology* (*IJESIT*). 2016, **5**(1), 1-13.

[12] DENGER, D., MISCHKER, K. The electro-hydraulic valvetrain system EHVS – system and potential. *SAE Technical Paper* 2005-01-0774. 2005. https://doi.org/10.4271/2005-01-0774

[13] DE OJEDA, W., FERNANDEZ, J. Hydraulic needle valve actuator and its application to a camless engine. *ASME, IMECE* 2003-43607. 2003, 39-44. https://doi.org/10.1115/IMECE2003-43607

[14] DI GAETA, A., VELASCO, C.I.H., GIGLIO, V. Modelling of an electro-hydraulic variable valve actuator for camless engines aimed at controlling valve lift parameters. *International Journal of Control*. 2021, **94**(10), 2857-2873. https://doi.org/10.1080/00207179.2020.1737333

[15] DITTRICH, P., PETER, F., HUBER, G. et al. Thermodynamic potentials of a fully variable valve actuation system for passenger-car diesel engines. *SAE Technical Paper* 2010-01-1199. 2010. https://doi.org/10.4271/2010-01-1199

[16] DRESNER, T., BARKAN, P. A review and classification of variable valve timing mechanisms. *SAE Technical Paper* 890674. 1989. https://doi.org/10.4271/890674

[17] EDWARDS, G.D. Valve-spring materials and design. *Industrial Lubrication and Tribology*. 1983, **35**(2), 44-51. https://doi.org/10.1108/eb053262

[18] FRENDO, F., VITALE, E., CARMIGNANI, L. et al. Development of a Lumped–parameter model for the dynamic analysis of valve train systems. *SAE Technical Paper* 2004-32-0051. 2004. https://doi.org/10.4271/2004-32-0051

[19] HERRANEN, M. Fully variable valve actuation in large bore diesel engines. *PhD Thesis*. Tampere University of Technology, Tampere 2014.

[20] GIARDIELLO, G., GIMELLI, A., DE NOLA, F. Engine valvetrain lift prediction using a physic-based model for the electronic control unit calibration. *E3S Web of Conferences*. 2020, **197**, 06015. https://doi.org/10.1051/e3sconf/202019706015

[21] GOLEBIOWSKI, W., WOLAK, A., ZAJAC, G. Definition of oil change intervals based on the analysis of selected

physicochemical properties of used engine oils. *Combustion Engines*. 2018, **172**(1), 44-50. https://doi.org/10.19206/CE-2018-105
[22] GU, Y., LI, H., LIU, F. et al. Study on modeling of electro-hydraulic variable valve mechanism based on CATIA. *International Conference on Future Power and Energy Engineering ICFPEE 2010*; June 26-27, 2010, Chenzen, China, 2010.
[23] GUO, J., ZHANG, W., ZOU, D. Investigation of dynamic characteristics of a valve train system. *Mechanism and Machine Theory*. 2011, **46**(12), 1950-1969. https://doi.org/10.1016/j.mechmachtheory.2011.07.014
[24] HERRANEN, M., HUHTALA, K., VILENIUS, M. et al. The electro-hydraulic valve actuation (EHVA) for medium speed diesel engines – development steps with simulations and measurements. *SAE Technical Paper* 2007-01-1289. 2007. https://doi.org/10.4271/2007-01-1289
[25] HERRANEN, M., VIRVALO, T., HUHTALA, K. et al. Comparison of control strategies of an electro-hydraulic valve actuation system. *SAE Technical Paper* 2009-01-0230. 2009. https://doi.org/10.4271/2009-01-0230
[26] HERRANEN, M., VIRVALO, T., HUHTALA, K. et al. Valve train with learning control features. *CIMAC Congress* 2010. Paper No. 68, Bergen 2010.
[27] http://www.jacobsvehiclesystems.com/files/media/Product/Evolve_production.pdf (accessed on February 01, 2022).
[28] http://sturmanindustries.com/Solutions/Products/HVACamless/HydraulicValveActuation/tabid/202/Default.aspx (accessed on February 01, 2022).
[29] http://www.schaeffler.com/remotemedien/media/_shared_media/08_media_library/01_publications/schaeffler_2/symposia_1/downloads_11/schaeffler_kolloquium_2010_18_en.pdf. (accessed on February 01, 2022).
[30] http://ic.daad.de/johannesburg/document/2013/extra2/NMMU3%20Becker%20Full%20variable%20valve%20train%20on%20a%20combustion%20engine.pdf (accessed on February 01, 2022).
[31] IRITANI, T., SHOZAKI, A., SHENG, B. et al. Prediction of the dynamic characteristics in valve train design of a diesel engine. *SAE Technical Paper* 2002-32-1839. 2002.
[32] LABORE, E. Valve spring tech: overview of valve spring design, dynamics. Chevy Hardcore, May 17, 2016. https://www.chevyhardcore.com/tech-stories/engine/valve-spring-tech-overview-of-valve-spring-design-dynamics/ (accessed on February 01, 2022).
[33] LEE, J., PATTERSON, D.J. Nonlinear valve train dynamics simulation with a distributed parameter model of valve springs. *ASME Journal of Engineering for Gas Turbines and Power*. 1997, **119**(3), 692-698. https://doi.org/10.1115/1.2817043
[34] LIU, J.R., JIN, B., XIE, Y.J. et al. Research on the electro-hydraulic variable valve actuation system based on a three-way proportional reducing valve. *International Journal of Automotive Technology*. 2009, **10**(1), 27-36.
[35] LIU, F., LI, H., GAO, F. et al. A new electro-hydraulic variable valve-train system for IC engine. *IEEE 2nd International Asia Conference on Informatics in Control, Automation and Robotics* (CAR) 6-7 March 2010, Wuhan 2010, 174-179.
[36] LOU, Z. Camless variable valve actuation designs with two-spring pendulum and electrohydraulic latching. *SAE Technical Paper* 2007-01-1295. 2007. https://doi.org/10.4271/2007-01-1295
[37] LOU, Z., DENG, Q., WEN, S. et al. Progress in camless variable valve actuation with two-spring pendulum and electrohydraulic latching. *SAE International Journal of Engines*. 2013, **6**(1), 319-326. https://doi.org/10.4271/2013-01-0590
[38] LOU, Z., WEN, S., QIAN, J. et al. Camless variable valve actuator with two discrete lifts. *SAE Technical Paper* 2015-01-0324. 2015. https://doi.org/10.4271/2015-01-0324
[39] MILOVANOVIC, N., TURNER, J., KENCHINGTON, S. et al. Active valvetrain for homogenous charge compression ignition. *International Journal of Engine Research*. 2005, **6**(4), 377-397. https://doi.org/10.1243/146808705X30396
[40] MURATA, Y., KUSAKA, J., ODAKA, M. et al. Achievement of medium engine speed and load premixed diesel combustion with variable valve timing. *SAE Technical Paper* 2006-01-0203, 2006. https://doi.org/10.4271/2006-01-0203
[41] NAM, K., CHO, K., PARK, S. et al. Design and performance evaluation of an electro-hydraulic camless engine valveactuator for future vehicle applications. *Sensors*. 2017, **17**, 2940. https://doi.org/10.3390/s17122940
[42] NAMA, S.A. Modeling and Analysis of a Helical Machined Springs. *The Iraqi Journal for Mechanical and Material Engineering*. 2015, **15**(2), 152-163.
[43] PAL, S., SINGH, S.K., BHARTI, S.K. et al. Design and analysis of engine valve spring. *International Journal of Scientific & Engineering Research*. 2020, **11**(6), 337-340.
[44] PARANJPE, R.S. Dynamic analysis of a valve spring with a Coulomb-friction damper. *ASME Journal of Mechanical Design*. 1990, **112**(4), 509-513. https://doi.org/10.1115/1.2912639
[45] PISANO, A.P. FREUDENSTEIN. F. An experimental and analytical investigation of the dynamic response of a high-speed cam-follower system. Part 1: experimental investigation. *ASME Journal of Mechanisms, Transmissions, and Automation in Design*. 1983, **105**(12), 692-698. https://doi.org/10.1115/1.3258538
[46] PISANO, A.P., FREUDENSTEIN, F. An experimental and analytical investigation of the dynamic response of a high-speed cam-follower system. Part 2: a combined, lumped/distributed parameter dynamic model. *ASME Journal of Mechanisms, Transmissions, and Automation in Design*. 1983, **105**(12), 699-704. https://doi.org/10.1115/1.3258539
[47] PLÖCKINGER, A. Comparison of three different concepts for a variable valvetrain for huge combustion engines. *Proceedings of the 3rd FPNI PhD symposium*. Terrassa 2004, 453-462.
[48] PRABAKAR, R., MANGALARAMANAN, S. Flexible multi-body dynamic analysis of multi-cylinder engine valve train. *SAE Technical Paper* 2011-26-0086. 2011. https://doi.org/10.4271/2011-26-0086
[49] POSTRIOTI, L., BATTISTONI, M., FOSCHINI, L. et al. Application of a fully flexible electrohydraulic camless system to a research SI engine. *SAE Technical Paper* 2009-24-0076, 2009. https://doi.org/10.4271/2009-24-0076
[50] POSTRIOTI, L., FOSCHINI, L., BATTISTONI, M. Experimental and numerical study of an electro-hydraulic camless VVA system. *SAE Technical Paper* 2008-01-1355, 2008. https://doi.org/10.4271/2008-01-1355
[51] POURNAZERI, M. Development of a new fully flexible hydraulic variable valve actuation system. *PhD Thesis*. University of Waterloo, Waterloo, Ontario 2012.
[52] RICHMAN, R., REYNOLDS, W. A computer-controlled poppet-valve actuation system for application on research engines. *SAE Technical Paper* 840340. 1984. https://doi.org/10.4271/840340
[53] REGO, R.A., MARTINS, J.G. Valve motion modelation for use in airflow engine simulation. *SAE Technical Paper* 2001-01-3958. 2001. https://doi.org/10.4271/2001-01-3958
[54] SCHECHTER, M., LEVIN, M. Camless engine. *SAE Technical Paper* 960581. 1996. https://doi.org/10.4271/960581

[55] SCHEIDL, R., WINKLER, B. Model relations between conceptual and detail design. *Mechatronics.* 2010, **20**, 842-849.

[56] SCHNEIDER, W. Fully variable, simple, and efficient electrohydraulic valve train for reciprocating engines. *12th International Fluid Power Conference*. Dresden 2020. **3**(3), 181-189. https://doi.org/10.25368/2020.107

[57] HANACHI, S, FREUDENSTEIN. F. The development of a predictive model for the optimization of high-speed cam-follower systems with Coulomb damping internal friction and elastic and fluidic elements. *Journal of Mechanisms Transmissions and Automation in Design.* 1986, **108**(12), 506-515. https://doi.org/10.1115/1.3258762

[58] SHIAO, Y., KANTIPUDI, M.B., JIANG, J.W. Novel spring-buffered variable valve train for an engine using magneto-rheological fluid technology. *Frontiers in Materials*. 2019, **6**, 95. https://doi.org/10.3389/fmats.2019.00095

[59] JANG, S., PARK, K. Dynamic EHL film thickness in cam and follower contacts of various valve lifts. *SAE Technical Paper* 2000-01-1789. 2000. https://doi.org/10.4271/2000-01-1789

[60] SUDA, S., IBARAKI, N. The past and future of high-strength steel for valve springs. *KOBELCO Technology Review*. 2005, **26**, 21-25.

[61] SUN, Z., KUO, T. Transient control of electro-hydraulic fully flexible engine valve actuation system. *IEEE Transactions on Control Systems Technology*. 2010, **18**(3), 613-621. https://doi.org/10.1109/TCST.2009.2025188

[62] SUN, Z. Electrohydraulic fully flexible valve actuation system with internal feedback. *Journal of Dynamic Systems, Measurement, and Control*. 2009, **131**(2), 024502. https://doi.org/10.1115/1.3072146

[63] SUN, Z., HE, X. Development and control of electro-hydraulic fully flexible valve actuation system for diesel combustion research. *SAE Technical Paper* 2007-01-4021. 2007. https://doi.org/10.4271/2007-01-4021

[64] SUN, Z., CLEARY, D. Dynamics and control of an electro-hydraulic fully flexible valve actuation system. *IEEE Proceedings of the American Control Conference*. 2003, **4**, 3119-3124.

[65] SZYDLOWSKI, T., SMOCZYNSKI, M. Model of hydraulic single acting drive for valves of internal combustion engines. *Journal of KONES Powertrain and Transport*. 2009, **16**(1), 465-472.

[66] SZYDLOWSKI, T. Experimental verification of the model of electrohydraulic drive for internal combustion engine valves. *Journal of KONES Powertrain and Transport*. 2009, **16**(3), 401-408.

[67] TABUÑARFORTUNADO, I., FORTUNADO, I. The spring as a simple machine. *IOSR Journal of Applied Physics.* 2019, **11**, 57-61. https://doi.org/10.9790/4861-1102025761

[68] The intelligent engine: Development status and prospects. http://www.mandieselturbo.com/files/news/filesof769/Int%20Eng%20Prospects.pdf (accessed on February 01, 2022).

[69] The Sulzer RT-flex common-rail system described. ftp://vk.od.ua/20011.pdf (accessed on February 01, 2022).

[70] TSUBOUCHI, T., TAKAHASHI, K., KUBOKI, T. Development of coiled springs with high rectangular ratio in cross-section. *Procedia Engineering*. 2014, **81**, 574-579. https://doi.org/10.1016/j.proeng.2014.10.04

[71] TURNER, C., BABBITT, G., BALTON, C. et al. Design and control of a two-stage electrohydraulic valve actuation system. *SAE Technical Paper* 2004-01-1265. 2004. https://doi.org/10.4271/2004-01-1265

[72] TURNER, J., KENCHINGTON, S., STRETCH, D. Production AVT development: Lotus and Eaton's electrohydraulic closed-loop fully variable valve train system. *25th International Vienna Motor Symposium*. Vienna 2004.

[73] VASILYEV, A.V., BAKHRACHEV, Y.S., STOROJAKOV, S.Y. Dynamics simulation model for the internal combustion engine valve gear. *Procedia Engineering*. 2016, **150**, 312-317. https://doi.org/10.1016/j.proeng.2016.07.017

[74] Wärtsilä RT-flex 50 technology review. http://engine.od.ua/ufiles/Wartsila-20041.pdf (accessed on February 01, 2022).

[75] HSU, W.S. PISANO, A.P. Modeling of a finger-follower cam system with verification in contact forces. *ASME Journal of Mechanical Design*. 1996, **118**(5), 132-137. https://doi.org/10.1115/1.2826844

[76] WU, H., CHEN, J., LI, M. et al. Iterative learning control for a fully flexible valve actuation in a test cell. *SAE Technical Paper* 2012-01-0162. 2012. https://doi.org/10.4271/2012-01-0162

[77] XIE, Y. GAO, Z., JIN, B. et al. Frequency response enhancement of variable valve system by employing peak and hold method. *Indian Journal of Engineering and Materials Sciences*. 2010, **17**(4), 275-281.

[78] ZHENG, H., YAN, F., LU, C. et al. Optimization design of the valve spring for abnormal noise control in a single-cylinder gasoline engine. *Proceedings of the Institution of Mechanical Engineers, Part D: Journal of Automobile Engineering.* 2017, **231**(2), 204-213. https://doi.org/10.1177/0954407016651180

[79] ZSIGA, N., OMANOVIC, A., SOLTIC, P. et al. Functionality and potential of a new electrohydraulic valve train. *MTZ Worldwide.* 2019, **80**, 18-27. https://doi.org/10.1007/s38313-019-0086-0

Tomasz Szydlowski, DEng. – Department of Vehicles and Fundamentals of Machine Design, Lodz University of Technology, Poland.

e-mail: *tomasz.szydlowski@p.lodz.pl*

Krzysztof Siczek, DSc., DEng. – Department of Vehicles and Fundamentals of Machine Design, Lodz University of Technology, Poland.

e-mail: *ks670907@p.lodz.pl*

Michał Głogowski, DEng. – Faculty of Process and Environmental Engineering, Lodz University of Technology, Poland

e-mail: *michal.glogowski@p.lodz.pl*


AIR FORCE INSTITUTE OF TECHNOLOGY
INSTYTUT TECHNICZNY WOJSK LOTNICZYCH
ul. Księcia Bolesława 6, 01-494 Warszawa, Poland
tel.: +48 261 851 300; fax: +48 261 851 313
www.itwl.pl e-mail: poczta@itwl.pl
SUPPORTING OPERATIONS & MAINTENANCE OF AERONAUTICAL ENGINEERING:
tribological diagnostics of lubrication systems in power units and hydraulic systems
endoscopic examinations of power units
measurements of operation parameters of power units using one's own and company systems and their analysis
DEVISING AND DEVELOPING NEW DIAGNOSTIC METHODS:
CT examinations – V/tome/X CT system
blade vibration measurements using the tip-timing method
NEW TECHNOLOGIES FOR UNMANNED AERIAL VEHICLES:
technical condition monitoring system of mini jet engine
hybrid drive of unmanned aerial vehicle

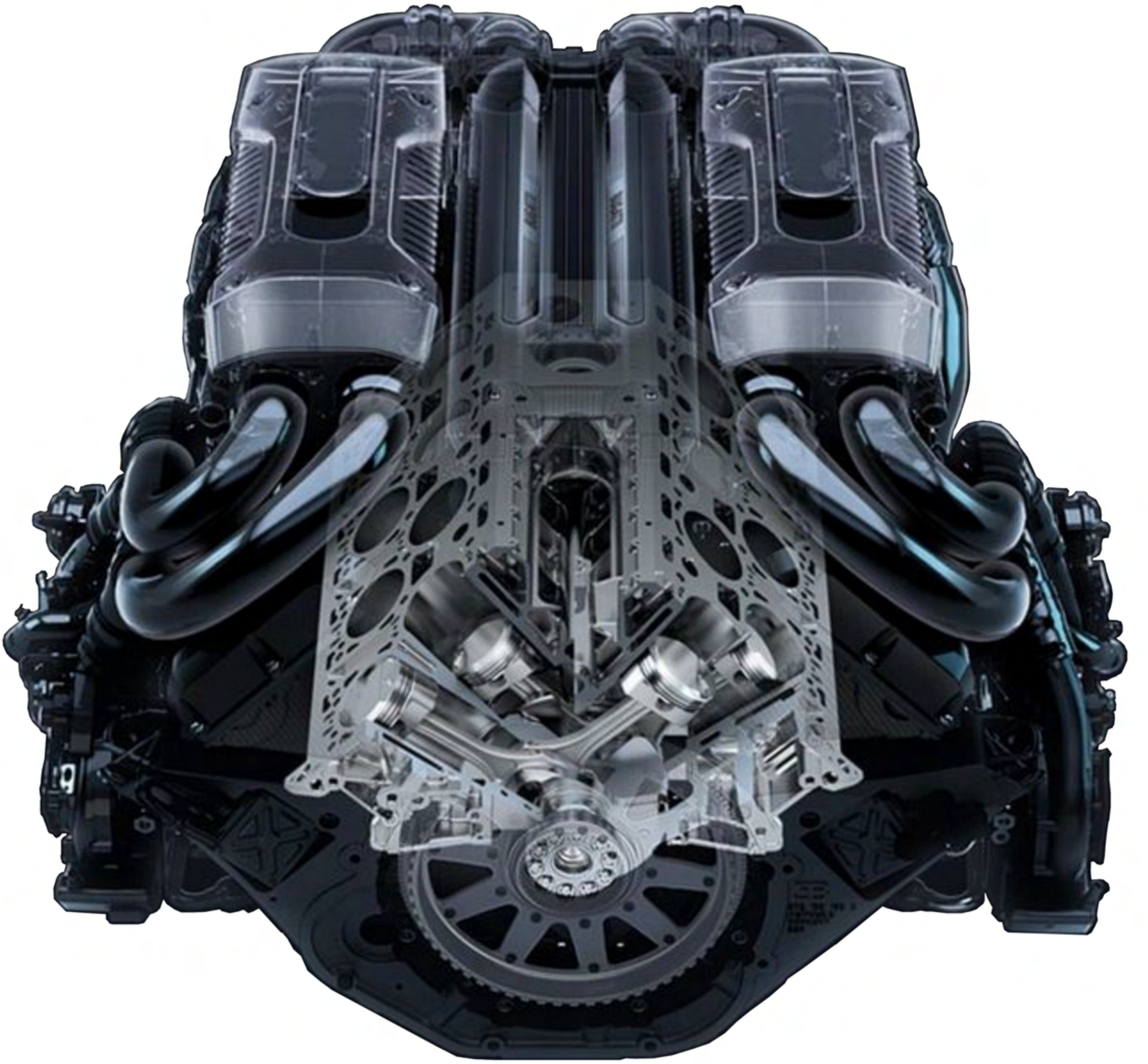

Publisher:

Polish Scientific Society of Combustion Engines

Combustion Engines

Polskie Towarzystwo Naukowe Silników Spalinowych

9772300989002

ISSN: 2300-9896
eISSN: 2658-1442

www.combustion-engines.eu